

Measurement of differential $t\bar{t}$ production cross sections in the full kinematic range using lepton+jets events from proton-proton collisions at $\sqrt{s} = 13$ TeV

The CMS Collaboration*

Abstract

Measurements of differential and double-differential cross sections of top quark pair ($t\bar{t}$) production are presented in the lepton+jets channels with a single electron or muon and jets in the final state. The analysis combines for the first time signatures of top quarks with low transverse momentum p_T , where the top quark decay products can be identified as separated jets and isolated leptons, and with high p_T , where the decay products are collimated and overlap. The measurements are based on proton-proton collision data at $\sqrt{s} = 13$ TeV collected by the CMS experiment at the LHC, corresponding to an integrated luminosity of 137 fb^{-1} . The cross sections are presented at the parton and particle levels, where the latter minimizes extrapolations based on theoretical assumptions. Most of the measured differential cross sections are well described by standard model predictions with the exception of some double-differential distributions. The inclusive $t\bar{t}$ production cross section is measured to be $\sigma_{t\bar{t}} = 791 \pm 25 \text{ pb}$, which constitutes the most precise measurement in the lepton+jets channel to date.

Submitted to Physical Review D

1 Introduction

Precision measurements of top quark pair ($t\bar{t}$) production are important tests of the standard model (SM) since the top quark plays an exceptional role; it is the heaviest known particle and the only quark that can be observed before hadronization. A detailed understanding of $t\bar{t}$ production is important for many searches for beyond-SM phenomena, where it often constitutes a major background. In addition, measurements of differential $t\bar{t}$ production can contribute significantly to the determination of parton distribution functions (PDFs), as well as the extraction of important SM parameters such as the top quark mass m_t , the strong coupling constant α_S [1], and the top quark Yukawa coupling [2, 3].

At the CERN LHC, measurements of differential cross sections have been performed in various $t\bar{t}$ decay channels at proton-proton (pp) center-of-mass energies of 7 [4, 5], 8 [6–12], and 13 [13–20] TeV. In this paper, measurements of differential $t\bar{t}$ production cross sections are presented by the CMS Collaboration using e/μ +jets events, i.e., with a single electron or muon and jets in the final state. This analysis is based on an integrated luminosity of 137 fb^{-1} at 13 TeV center-of-mass energy, where 35.9 fb^{-1} were recorded in 2016, 41.5 fb^{-1} in 2017, and 59.7 fb^{-1} in 2018. Since the running conditions and the CMS detector changed during this time period, detector performance and calibration measurements are carried out separately for each year.

We use resolved $t\bar{t}$ reconstruction techniques similar to those introduced in previous CMS analyses [16, 17]. These are applicable if all the $t\bar{t}$ decay products can be reconstructed as separated leptons and jets in the detector—typically for top quarks with transverse momenta $p_T < 500\text{ GeV}$. These results are extended by adding Lorentz-boosted top quarks with collimated and overlapping decay products. This is the first time that both the resolved and boosted techniques are used in a combined analysis. Techniques for the boosted and resolved reconstructions of t_h and t_ℓ are developed or improved, where t_h (t_ℓ) represents a top quark decaying into a b quark and a W boson with a subsequent hadronic (leptonic) decay of the W boson. The differential cross sections are extracted by performing a combined fit to various categories that are defined by the reconstruction methods, the lepton flavors, and the three years of data taking. The combination of the different categories provides constraints on the systematic uncertainties and results in an improved precision with respect to previous measurements.

The differential cross sections are presented at the parton and particle levels. The parton level represents a $t\bar{t}$ pair before decay. The cross sections are presented in the full phase space of the top quarks. This means for the parton-level measurements that all effects related to top quark decays, hadronization, and limited detector acceptance are corrected based on theoretical assumptions. The uncertainties due to these extrapolations are reduced in the measurements at the particle level, where the $t\bar{t}$ pair is defined based on jets and leptons that can be directly observed with the detector. The strong relation between particle- and detector-level objects also results in less bin-to-bin migrations and simplifies the unfolding. More details about the definitions of the parton and particle levels are given in Section 3.

At the parton and particle levels, we measure the differential cross sections as a function of the following variables: $p_T(t_h)$, $p_T(t_\ell)$, and their scalar sum S_T ; the higher $p_T(t_{\text{high}})$ and the lower $p_T(t_{\text{low}})$ transverse momenta of the top quarks; the rapidities $|y(t_h)|$, $|y(t_\ell)|$, and the rapidity differences $\Delta|y_{t/\bar{t}}| = |y(t) - y(\bar{t})|$, $|\Delta y_{t/\bar{t}}| = |y(t) - y(\bar{t})|$; and the angle between the top quarks in the transverse plane $\Delta\phi_{t/\bar{t}}$. For the $t\bar{t}$ system the differential cross sections are measured as a function of $|y(t\bar{t})|$, $p_T(t\bar{t})$, the invariant mass $m(t\bar{t})$, and $\cos(\theta^*)$, where θ^* is the angle between the t and the direction of flight of the $t\bar{t}$ system calculated in the $t\bar{t}$ rest frame. The identification of a t or \bar{t} is done using the charge of the electron or muon.

Double-differential cross sections are measured as a function of combinations of these variables: $p_T(t_h)$ vs. $|y(t_h)|$, $m(t\bar{t})$ vs. $|y(t\bar{t})|$, $m(t\bar{t})$ vs. $\cos(\theta^*)$, $m(t\bar{t})$ vs. $p_T(t_h)$, $p_T(t\bar{t})$ vs. $p_T(t_h)$, $m(t\bar{t})$ vs. $\Delta|y_{t/\bar{t}}|$, $|\Delta y_{t/\bar{t}}|$ vs. $m(t\bar{t})$, and $|y(t)|$ vs. $|y(\bar{t})|$. From the sum of cross sections in all bins of a distribution, a measurement of the inclusive $t\bar{t}$ production cross section is obtained. In addition, at the particle level the cross sections are determined as a function of the additional jet multiplicity and as a function of $p_T(t_h)$, $m(t\bar{t})$, and $p_T(t\bar{t})$ in bins of additional jet multiplicity, where additional jets are those that are not used in the reconstruction of the $t\bar{t}$ system. Finally, differential cross sections as a function of the scalar p_T sum of additional jets H_T , the invariant mass of the top quarks and all additional jets m_{evt} , and the p_T of the electrons and muons $p_T(\ell)$ are presented.

We begin with an overview of the theoretical calculations and simulations of the detector in Section 2, followed by a detailed discussion of the parton- and particle-level definitions in Section 3. After a short description of the CMS detector and the reconstruction and identification of the involved physics objects in Sections 4 and 5, respectively, the resolved and boosted reconstructions of t_h and t_ℓ are detailed in Sections 6–8. An overview of the event categorization based on the various reconstruction methods is presented in Section 9, before the methods of background subtraction are explained in Section 10 for the resolved reconstruction and in Section 11 for the boosted reconstruction. The extraction of the cross sections using a fit combining all categories is described in Section 12. In Section 13, detailed information about the systematic uncertainties are given. The results at the parton and particle levels are presented and discussed in Section 14, and a summary of the results is provided in Section 15. Tabulated results are provided in HEPData [21].

2 Signal and background modeling

The Monte Carlo event generator POWHEG [22–24] (version POWHEG-BOX-V2, process: hvq [25]) is used to simulate the production of $t\bar{t}$ events at next-to-leading-order (NLO) accuracy in quantum chromodynamics (QCD). The POWHEG output is combined with the parton shower (PS) simulation of PYTHIA [26] (version 8.2) using the underlying event (UE) tunes CUETP8M2T4 [27–29] for the 2016 simulations and CP5 [30] for the 2017 and 2018 simulations. The renormalization μ_R and factorization μ_F scales are set to the transverse mass $m_T = \sqrt{m_t^2 + p_T^2}$ of the top quark, where $m_t = 172.5$ GeV is used. The PDFs are NNPDF30_nlo_as_0118 [31] for 2016 and NNPDF31_nnlo_hessian_pdfas [32] for 2017–2018. The detector response is simulated using GEANT4 [33]. The simulations include multiple pp interactions per bunch crossing (pileup). The simulated distribution of the number of pileup interactions corresponds to the distribution in data for each year. Finally, the same reconstruction algorithms that are applied to the data are used for the simulated events. This POWHEG+PYTHIA simulation is taken as the default to obtain all corrections for the extraction of the differential cross sections.

To estimate systematic uncertainties, several variations in the default simulation are used, including simulations with m_t varied by ± 1 GeV and variations of the UE parameters representing the uncertainties in the tunes. In other simulations, the parton shower matching scales $h_{\text{damp}} = (1.58^{+0.66}_{-0.59})m_t$ (CUETP8M2T4) and $(1.38^{+0.92}_{-0.51})m_t$ (CP5) are varied within their uncertainties, which are obtained from the UE tunes. In addition, a simulation with a different color reconnection (CR) model [29] that allows interactions of colored particles from resonance decays with other particles, is used. Distributions corresponding to variations of the scales μ_R , μ_F , or the PS scales by factors of 0.5 and 2 are obtained by applying event weights to the default simulation. Event weights are also used for the estimation of PDF uncertainties.

The measured differential cross sections are compared to predictions obtained using POWHEG+HERWIG [34] (version 7.1) with tune CH3 [35]. The program MADGRAPH5_aMC@NLO [36] (version 2.2.2) (MG5_aMC@NLO) is used to simulate $t\bar{t}$ events with additional partons. All processes with up to two additional partons are calculated at NLO QCD and combined with the PYTHIA PS simulation using the FxFx [37] algorithm.

All $t\bar{t}$ simulations are normalized to the inclusive $t\bar{t}$ production cross section of 832_{-46}^{+40} pb calculated with TOP++ (version 2.0) [38]. This value is determined with next-to-NLO (NNLO) accuracy, including the resummation of next-to-next-to-leading-logarithmic (NNLL) soft-gluon terms, where $\mu_R = \mu_F = m_t$. Cross sections are calculated using the PDFs MSTW2008nnlo68cl [39], CT10nnlo [40], and NNPDF23_nnlo_FFNNF5 [41], and the midpoint of their envelopes is used. The uncertainty is evaluated by varying μ_R and μ_F and adding in quadrature the envelope of the uncertainties obtained for the various PDFs. Differential cross sections with NNLO QCD accuracy are obtained with MATRIX [42, 43], where $\mu_R = \mu_F = \frac{1}{2} \left[\sqrt{m_t^2 + p_T^2(t)} + \sqrt{m_t^2 + p_T^2(\bar{t})} \right]$ and the PDF set NNPDF31_nnlo_as_0118 is used.

The main backgrounds from SM processes are simulated applying the same techniques as used for the simulation of $t\bar{t}$ production. The MG5_aMC@NLO generator is used for the NLO QCD simulation of W boson production in association with jets, s -channel single top quark production, and Drell–Yan (DY) production in association with jets. The generator POWHEG [44] is used for the simulation of t -channel single top quark production and single top quark production associated with a W boson (tW). For the latter, contributions from $t\bar{t}$ production entering the NLO calculation are removed using the diagram removal scheme [45]. In all cases, the PS and the UE are described by PYTHIA. Multijet events, i.e., SM events comprised uniquely of jets produced through the strong interaction, are simulated using PYTHIA. The W boson and DY backgrounds are normalized to their NNLO cross sections calculated with FEWZ [46] (version 3.1). The t -channel single top quark production is normalized to the NLO calculation obtained from HATHOR [47] (version 2.1). The production of tW is normalized to the NLO calculation [48], and the multijet simulation is normalized to the leading-order calculation obtained with PYTHIA [49].

3 Definitions at the parton and particle levels

The parton level is represented by a $t\bar{t}$ pair before it decays. In other words, the top quarks are assumed to be stable and all effects related to their decays are corrected for in the measurement. Information from the decay is only used to identify t_h and t_ℓ , where a t_ℓ with a W boson decay involving a τ lepton, regardless of its decay mode, is excluded. The cross sections are presented in the full phase space of the top quarks. Results of a fixed-order $t\bar{t}$ calculation as obtained with MATRIX can be directly compared to the parton-level measurement after scaling by the branching fraction of $(28.77 \pm 0.32)\%$ for e/μ +jets events calculated using measured W boson branching fractions [50]. In calculations that combine matrix elements and PS, the top quark momenta are obtained after the combination, i.e., the PS affects the definition of the parton level.

Particle-level objects are constructed from simulated particles with a mean lifetime greater than 30 ps, obtained from the predictions of $t\bar{t}$ event generators before any detector simulation. The particle-level objects are further used to define particle-level top quarks. Detailed studies on particle-level definitions can be found in Ref. [51]. The exact definitions are summarized below.

- All simulated electrons and muons, including those from τ lepton decays but not originating from the decay of a hadron, are corrected for effects of bremsstrahlung

by adding the momentum of a photon to that of the closest lepton if their separation is $\Delta R < 0.1$, where $\Delta R = \sqrt{(\Delta\eta)^2 + (\Delta\phi)^2}$ with the differences in pseudorapidity $\Delta\eta$ and azimuthal angle $\Delta\phi$ between the directions of the photon and lepton. All photons are considered for the momentum correction. We require leptons to have $p_T > 15 \text{ GeV}$ and $|\eta| < 2.4$.

- Jets are clustered using the anti- k_T jet algorithm [52, 53] with a distance parameter of 0.4. All particles with the exception of neutrinos are clustered. Jets with $p_T > 25 \text{ GeV}$ and $|\eta| < 2.4$ are selected if there is no electron or muon, as defined above, within $\Delta R = 0.4$.
- Particle-level b jets are defined as those jets that contain a b hadron using the ghost-matching technique [54]: as a result of the short lifetime of b hadrons only their decay products are considered for the jet clustering. However, to allow their association with a jet, the b hadrons are also included with their momenta scaled down to a negligible value. This preserves the information of their directions, but removes their impact on the jet clustering.
- The magnitude of the neutrino four-momentum p_ν from the t_ℓ decay is calculated using all neutrinos, including those stemming from decays of hadrons. The vectorial sum of their transverse momenta is used as a proxy for the missing transverse momentum \vec{p}_T^{miss} . The longitudinal component $p_z(\nu)$ of p_ν is calculated using the W boson mass constraint $(p_\nu + p_\ell)^2 = m_W^2$, where \vec{p}_T^{miss} is taken as the transverse momentum of the neutrino, p_ℓ is the four-momentum of the lepton in the t_ℓ decay, and $m_W = 80.4 \text{ GeV}$ [50]. This results in a quadratic equation for the longitudinal component of the neutrino momentum $p_z(\nu)$. If no real solution exists, the two components of \vec{p}_T^{miss} are scaled separately to find a single solution under the condition of a minimum modification of p_T^{miss} . The scaled \vec{p}_T^{miss} , together with the calculated solution for $p_z(\nu)$, form the neutrino momentum. If two real solutions exist, the invariant masses of each of the neutrino solutions, together with the charged lepton and the b jet in the t_ℓ decay, are calculated, and the solution resulting in a mass closer to m_t is selected. The event is rejected if the invariant mass is not between 100 and 240 GeV. This method for calculating the neutrino momentum corresponds to the method used at the detector level.
- Candidates used to form a boosted t_ℓ are the b jets and any selected lepton within a cone of $\Delta R = 0.4$. The minimum p_T requirement is increased to 50 GeV for these leptons. The candidate momentum is calculated as the momenta sum of the jet, the lepton, and the calculated neutrino. It is ensured that the lepton momentum is not counted twice if it is a constituent of the jet. Finally, $p_T > 380 \text{ GeV}$, $|\eta| < 2.4$, and an invariant mass between 100 and 240 GeV are required for the boosted t_ℓ candidate.
- Candidates for a boosted t_h are b jets defined exactly as the b jets above but clustered with a distance parameter of 0.8. Those jets with $p_T > 380 \text{ GeV}$ and $|\eta| < 2.4$ are selected if there is no electron or muon, as defined above, within $\Delta R = 0.8$. In addition, the invariant mass of all constituents m_{jet} is required to be greater than 120 GeV.

Based on these objects, we construct a pair of particle-level top quarks in the e/μ +jets final state. Events with exactly one electron or muon with $p_T > 30 \text{ GeV}$ and $|\eta| < 2.4$ are selected. Simulated events with an additional particle-level electron or muon are rejected.

If one candidate for a boosted t_ℓ and at least one candidate for a boosted t_h exist that are separated at least by $\Delta R = 1.2$, the boosted t_h with m_{jet} closest to m_t is selected and the two form the

pair of particle-level top quarks. If there is a boosted t_ℓ but no candidate for a boosted t_h , the event is rejected. The combination of a boosted t_ℓ and a resolved reconstructed t_h is, in analogy to the detector-level reconstruction (cf. Section 9), not considered.

If there is no boosted t_ℓ , we find the permutation of jets that minimizes the quantity

$$[m(p_\nu + p_\ell + p_{b_\ell}) - m_t]^2 + [m(p_{j_{W1}} + p_{j_{W2}}) - m_W]^2 + [m(p_{j_{W1}} + p_{j_{W2}} + p_{b_h}) - m_t]^2, \quad (1)$$

where $p_{j_{W1}}$ and $p_{j_{W2}}$ are the four-momenta of two light-flavor jet candidates, considered as the decay products of the hadronically decaying W boson; and p_{b_ℓ} and p_{b_h} are the four-momenta of two b jet candidates. All jets with $p_T > 25$ GeV and $|\eta| < 2.4$ are considered. At least four jets are required, of which at least two must be b jets. The remaining jets with $p_T > 30$ GeV and $|\eta| < 2.4$ are defined as additional jets. The best permutation is only accepted if the reconstructed t_h invariant mass satisfies $100 < m(t_h) < 240$ GeV.

Alternatively, we also evaluate the possibility of a selection with a boosted t_h by minimizing

$$[m(p_\nu + p_\ell + p_{b_\ell}) - m_t]^2 + [m_{\text{jet}} - m_t]^2, \quad (2)$$

where separations of at least $\Delta R = 1.2$ between the t_h and both the ℓ and the b_ℓ are required. If both reconstruction methods for the resolved and the boosted t_h are successful, we select the reconstruction for which $m(t_h)$ is closer to m_t .

Events with a hadronically and a leptonically decaying particle-level top quark are not required to be e/μ +jets events at the parton level. Especially, τ +jets events with a leptonically decaying τ lepton can contribute, and also $t\bar{t}$ dilepton events with additional jets can be identified as e/μ +jets events at the particle level if one lepton fails to pass the selection.

As an example, the comparison between the $p_T(t_h)$ distributions at the particle and parton levels is shown in Fig. 1. About 60% of the t_h are in the same p_T bins at the parton and particle levels. At high p_T a particle-level t_h exists for up to 80% of the parton-level t_h , while only about 12% of the particle-level events do not fulfill the definition of parton-level events. This overall good correspondence between the particle and parton levels ensures that the observables are sensitive to the underlying physics of $t\bar{t}$ production.

4 The CMS detector

The central feature of the CMS detector is a superconducting solenoid of 6 m internal diameter, providing a magnetic field of 3.8 T. Within the solenoid volume are a silicon pixel and strip tracker, a lead tungstate crystal electromagnetic calorimeter (ECAL), and a brass and scintillator hadron calorimeter (HCAL), each composed of a barrel and two endcap sections. Forward calorimeters extend the η coverage provided by the barrel and endcap detectors. Muons are measured in gas-ionization detectors embedded in the steel flux-return yoke outside the solenoid. A more detailed description of the CMS detector, together with a definition of the coordinate system and relevant kinematic variables, can be found in Ref. [55].

Events of interest are selected using a two-tiered trigger system. The first level (L1), composed of custom hardware processors, uses information from the calorimeters and muon detectors to select events at a rate of around 100 kHz within a fixed latency of about 4 μ s [56]. The second level, known as the high-level trigger (HLT), consists of a farm of processors running a version of the full event reconstruction software optimized for fast processing, and reduces the event rate to around 1 kHz before data storage [57]. For this measurement events are selected using

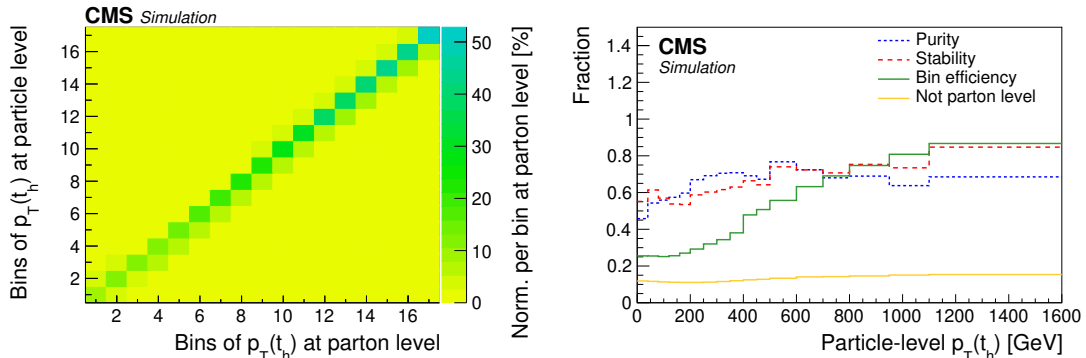


Figure 1: Comparison between the $p_T(t_h)$ distributions at the particle and parton levels, extracted from the POWHEG+PYTHIA simulation. Left: the percentage of p_T -bin migration between the particle and parton levels, shown using the color scale to the right of the plot. The bin boundaries are those shown in the right panel. Each column is normalized such that the sum of its entries corresponds to the fraction of particle-level events in this bin at the parton level in the full phase space. Right: fraction of parton-level top quarks in the same p_T bin at the particle level (purity), fraction of particle-level top quarks in the same p_T bin at the parton level (stability), ratio of the number of particle- to parton-level top quarks (bin efficiency), and the fraction of particle-level events that are not signal events at the parton level.

single electron and muon triggers with p_T thresholds below 34 GeV for isolated leptons and of 50 GeV for nonisolated leptons.

The particle-flow (PF) event algorithm [58] aims to reconstruct and identify each individual particle with an optimized combination of information from the various elements of the CMS detector. The energy of muons is obtained from the curvature of the corresponding track. The energy of electrons is determined from a combination of the electron momentum at the primary interaction vertex as determined by the tracker, the energy of the corresponding ECAL cluster, and the energy sum of all bremsstrahlung photons spatially compatible with originating from the electron track. The energy of photons is directly obtained from the ECAL measurement. The energy of charged hadrons is determined from a combination of their momentum measured in the tracker and the matching ECAL and HCAL energy deposits, corrected for zero-suppression effects and for the response function of the calorimeters to hadronic showers. Finally, the energy of neutral hadrons is obtained from the corresponding corrected ECAL and HCAL energy.

5 Physics object reconstruction

The measurements presented in this paper depend on the reconstruction and identification of electrons, muons, jets, and missing transverse momentum \vec{p}_T^{miss} associated with neutrinos. Electrons and muons are selected if they are compatible with originating from the primary vertex, which, among the reconstructed pp interaction vertices, is the one with the largest value of summed physics-object p_T^2 . The physics objects are the jets, clustered using the anti- k_T jet-finding algorithm [52, 53] with the tracks assigned to the primary vertex as inputs, and the associated missing transverse momentum, taken as the negative vectorial \vec{p}_T sum of those jets.

Isolated electrons [59] and muons [60] with $p_T > 30$ GeV and $|\eta| < 2.4$ are selected. In 2018 the minimum p_T of electrons was raised to 34 GeV due to increased trigger thresholds. Several quality criteria including isolation and compatibility with the primary vertex are required. The electron and muon reconstruction and selection efficiencies are measured in the data using the

“tag-and-probe” technique [61]. Depending on p_T and η , the overall reconstruction and selection efficiency is 50–80% for electrons and 75–85% for muons. Nonisolated electrons and muons are required to have $p_T > 50$ GeV due to the higher p_T thresholds for the lepton triggers without an isolation requirement. Apart from the p_T and isolation requirements, the nonisolated electrons and muons have to fulfill the same selection criteria as the isolated leptons. Their reconstruction and trigger efficiencies are measured using $t\bar{t}$ events in the $e\mu$ decay channel. The products of efficiencies for the nonisolated electrons and muons are about 80% and 90%, respectively. The trigger for nonisolated electrons also requires a jet with $p_T > 165$ GeV. The efficiency of this jet requirement reaches almost 100% for events with a boosted t_h candidate as selected in this analysis.

Jets are clustered from PF candidates using the anti- k_T jet algorithm with a distance parameter of 0.4 (AK4 jets) implemented in the FASTJET package [53]. Charged PF candidates originating from a pileup interaction vertex are excluded. The total energy of the jets is corrected for energy depositions from pileup. In addition, p_T - and η -dependent corrections are applied to correct for detector response effects [62]. If an isolated lepton with $p_T > 15$ GeV within $\Delta R = 0.4$ around a jet exists, the jet is assumed to represent the isolated lepton and is removed from further consideration to prevent counting the lepton momentum twice. The AK4 jets are considered for analysis if they fulfill the kinematic requirements $p_T > 30$ GeV and $|\eta| < 2.4$.

For the identification of b jets, the DeepCSV algorithm [63] is used. It is based on an artificial neural network (NN) that provides a discriminant to distinguish between b and other flavored jets using features of secondary vertices. An AK4 jet is identified as a b jet if the associated value of the discriminant exceeds a threshold criterion. Two different selection criteria are used: a tight one with an efficiency of about 70–75% and a rejection probability for c jets of about 88% and about 99% for other jets, and a loose one with corresponding values of 85–90, 55, and 90%.

Boosted t_h candidates are identified using anti- k_T jets with a distance parameter of 0.8 (AK8 jets), $p_T > 400$ GeV, $|\eta| < 2.4$, and a jet mass $m_{\text{jet}} > 120$ GeV. In contrast to the AK4 jets, the AK8 jets utilize the PUPPI [64] algorithm for pileup mitigation, and the p_T of all PF constituents are rescaled according to their PUPPI weights before clustering. Energy corrections are applied to account for detector response effects [62]. If an isolated lepton with $p_T > 15$ GeV within $\Delta R = 0.8$ of a jet exists, that jet is removed from further consideration.

The vector \vec{p}_T^{miss} is calculated as the negative vectorial \vec{p}_T sum of all PF candidates in the event. Jet energy corrections are also propagated to improve the measurement of \vec{p}_T^{miss} .

6 Reconstruction of the resolved $t\bar{t}$ system

For the resolved reconstruction exactly one isolated electron or muon and at least four AK4 jets are required. If at least two of the jets are identified as b jets by the tight criterion, the event is categorized as “2t”. If there is one jet passing the tight and another jet passing the loose b tagging criteria, the event is classified as “1t1l”. About 75% of the resolved reconstructed events fall into the 2t and the rest into the 1t1l category.

The reconstruction of the $t\bar{t}$ system in the resolved case follows closely the methods used in previous CMS analyses [16, 17]. The goal is the correct identification of detector-level objects as top quark decay products. For the optimization of the reconstruction algorithm, the following definitions of correct reconstructions based on generator-level information are used. For the particle-level measurements, the jets used to construct the top quarks are spatially matched to

detector-level jets within $\Delta R = 0.4$. For the parton-level measurements, the two b quarks from top quark decays and the two light quarks from the W boson decay are obtained from the event record of the simulation and spatially matched to detector-level jets with the highest p_T within $\Delta R = 0.4$.

All possible permutations of assigning detector-level jets to the corresponding $t\bar{t}$ decay products are tested and a likelihood that each permutation is correct is evaluated based on top quark and W boson mass constraints. Only the two jets with the highest b identification probabilities are tested as b_ℓ and b_h candidates. In each event, the permutation with the highest likelihood is selected.

For all tested permutations, p_ν is calculated using the W boson mass constraint $(p_\nu + p_\ell)^2 = m_W^2$, where \vec{p}_T^{miss} is taken as the transverse momentum of the neutrino. This results in a quadratic equation for the longitudinal component of the neutrino momentum $p_z(\nu)$. If no real solution exists, which can happen even in signal events due to the finite \vec{p}_T^{miss} resolution, the x and y components of \vec{p}_T^{miss} are scaled separately to find a single solution under the condition of a minimum modification of p_T^{miss} . The scaled \vec{p}_T^{miss} , together with the calculated solution for $p_z(\nu)$, form the neutrino momentum. If there are two solutions to the quadratic equation, the invariant mass is calculated using $m(t_\ell)^2 = (p_\nu + p_\ell + p_{b_\ell})^2$ for both p_ν values and the solution closer to m_t is selected. For each permutation, the p_ν calculation yields a value of $m(t_\ell)$, which is used to optimize the selection of b_ℓ , as explained below.

The information on $m(t_\ell)$ and the mass constraints on the hadronically decaying top quark are combined in a likelihood function λ , given by

$$-\log[\lambda] = -\log[P_h(m_2, m_3)] - \log[P_\ell(m(t_\ell))], \quad (3)$$

where P_h is the two-dimensional probability density found from simulation of the invariant masses of the hadronically decaying W bosons and top quarks that are correctly reconstructed. The value of λ is maximized to select the best permutation of jets. The probability density P_h is calculated as a function of the invariant mass m_2 of the two jets tested as the W boson decay products, and the invariant mass m_3 of the three jets tested as the decay products of the t_h . The distributions for the correct jets, taken from the POWHEG+PYTHIA simulation and normalized to unit area, are shown in Fig. 2 (left). This part of the likelihood function is sensitive to the correct reconstruction of the t_h . For the 2t (1t1l) category, $-\log[P_h(m_2, m_3)] < 11$ (9) is required. This selection rejects about 50% of the multijet, W boson, and single top quark backgrounds. For higher values of $-\log[P_h(m_2, m_3)]$, almost all $t\bar{t}$ events are reconstructed incorrectly and are then considered for a boosted reconstruction.

The probability density P_ℓ , also found from simulation, describes the distribution of $m(t_\ell)$ for a correctly selected b_ℓ . In Fig. 2 (right) the normalized distributions of P_ℓ for correctly selected b_ℓ and for other jets are shown. Permutations with $m(t_\ell) < 100$ GeV or $m(t_\ell) > 230$ GeV are rejected since they are very unlikely to originate from a correct b_ℓ association. This part of the likelihood function is sensitive to the correct reconstruction of the t_ℓ .

The distributions of $-\log(\lambda)$ in data and simulation are compared in Fig. 3 for the 2t and 1t1l categories. Here, the $t\bar{t}$ simulation is split into different categories based on the success of the reconstruction. The category “ $t\bar{t}$ correct” contains the events with all decay products correctly identified, “ $t\bar{t}$ incorrect” are incorrectly reconstructed but all decay products are available, and “ $t\bar{t}$ nonreconstructable” are events with at least one missing decay product caused by detector inefficiencies or acceptance losses. Finally, “ $t\bar{t}$ nonsignal” are $t\bar{t}$ background events, i.e., having no parton- or particle-level $t\bar{t}$ pair in the desired decay channel and phase space.

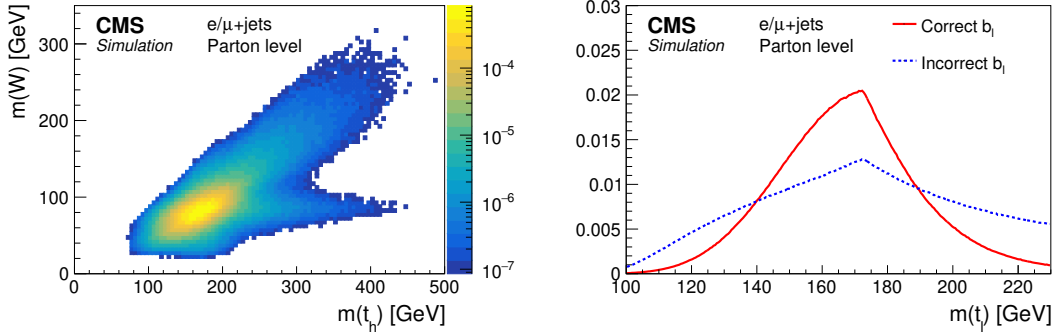


Figure 2: Normalized two-dimensional mass distribution of the correctly reconstructed hadronically decaying W bosons and the correctly reconstructed t_ℓ candidate (left). Normalized distributions of the reconstructed $m(t_\ell)$ for correctly (solid red curve) and incorrectly (dashed blue curve) selected b_ℓ (right). The distributions are taken from the POWHEG+PYTHIA $t\bar{t}$ simulation for the parton-level measurement.

7 Identification and reconstruction of boosted leptonically decaying top quarks

For $p_T(t_\ell) > 400$ GeV the separation in η and ϕ between the charged lepton and the b jet becomes increasingly small and the isolation cone for the lepton of $\Delta R = 0.4$ starts overlapping with the constituents of the b jets. In this case, the leptons do not fulfill the isolation criterion. Therefore, nonisolated leptons are used for the reconstruction of the boosted t_ℓ . We look for a loosely b-tagged AK4 jet within $\Delta R = 0.8$ around such a lepton. If the lepton is a constituent of the jet, its momentum is subtracted from the jet momentum to avoid double counting. Afterwards, p_ν is calculated using the m_W mass constraint as in the resolved reconstruction described in Section 6. The momentum of the boosted t_ℓ is calculated as the momentum sum of the lepton, b jet, and neutrino. If $p_T(t_\ell) > 400$ GeV, we consider this as a boosted t_ℓ candidate. The transverse and longitudinal momentum resolution is about 10% in the selected p_T range.

The reconstructed candidates might be jets containing a misreconstructed lepton, a lepton from a hadron decay, or from a leptonically decaying W boson produced within the jet. Based on the following variables, we use an NN to discriminate between a signal t_ℓ and background: the invariant mass of the lepton plus b jet system $m(\ell, \text{b jet})$, the ratios $m_{\text{b jet}}/m(\ell, \text{b jet})$, where $m_{\text{b jet}}$ is the invariant mass of the b jet, $p_T(\ell)/p_T(\ell + \text{b jet})$, I_{far}/I_0 , and I_{near}/I_0 , with the isolation variables $I = \sum_i p_T(o_i) \Delta R^q(\ell, o_i)$ and $q = -2, 0, 2$ for I_{near} , I_0 , and I_{far} , respectively, where o_i includes all charged, neutral, and photon-like PF objects within $\Delta R = 0.4$ around the lepton.

Separate NNs are used for $400 < p_T(t_\ell) < 650$ GeV and $p_T(t_\ell) > 650$ GeV. The muon and electron channels are combined. The NNs consist of a five-node input layer, three fully connected hidden layers with 20, 10, and 5 nodes, and a single output node. The activation function is hyperbolic tangent in all layers. The logistic loss function is minimized using stochastic gradient descent with the Adam algorithm [65]. Training samples of 2000 $t\bar{t}$ and 2000 multijet, DY, and W boson background events are used.

The distribution of the output variable L_{NN} of the NN is shown in Fig. 4. The largest uncertainties in the distribution of L_{NN} are those from the PS and the UE tune, since these affect the isolation variables. The discriminant L_{NN} is efficient in reducing the multijet background, whereas W bosons decaying into leptons and produced within a jet are more difficult to distinguish from the boosted t_ℓ candidate. We select t_ℓ candidates with $L_{\text{NN}} > 0.7$. The efficiency of this selection has been studied using $t\bar{t}$ events in the $e\mu$ decay channel with one isolated and

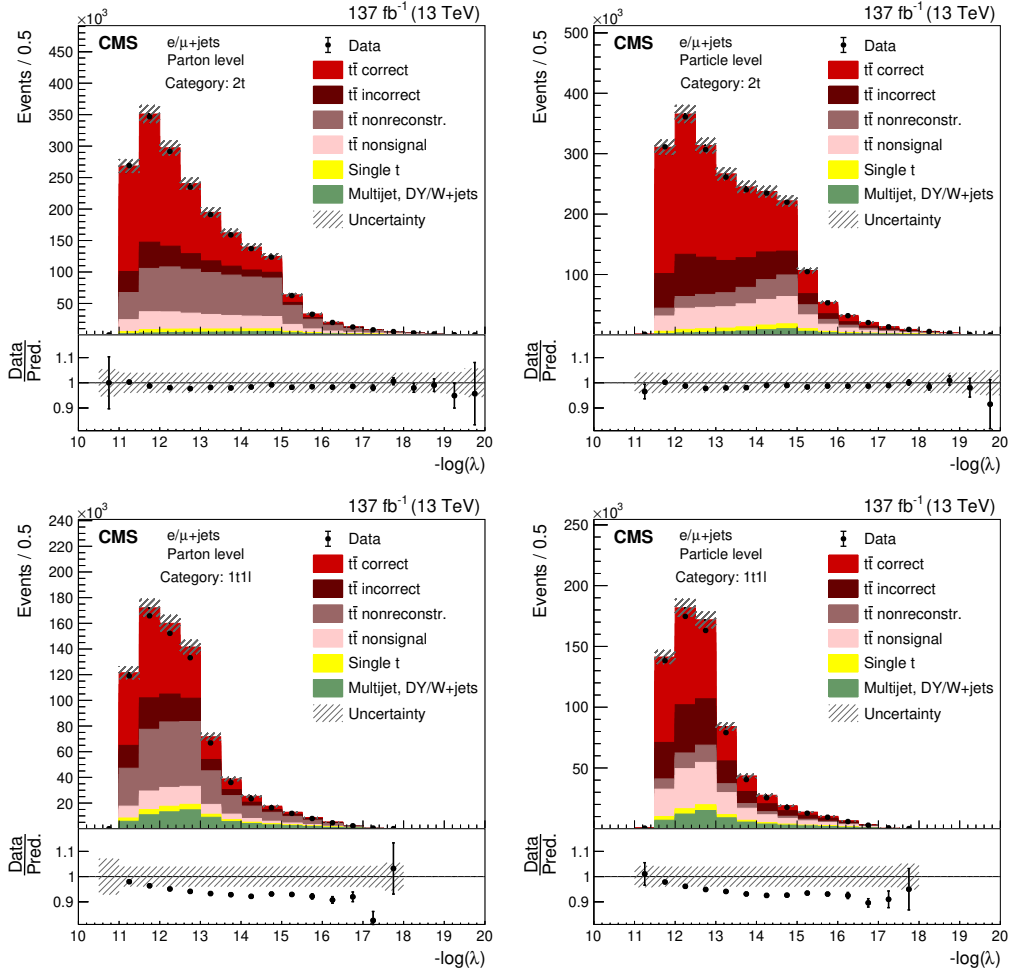


Figure 3: Distributions of the negative log-likelihood for the selected best permutation in the 2t (upper) and 1t1l (lower) categories. The comparisons of data (points) and predictions (colored histograms) are shown for the (left) parton- and (right) particle-level measurements. Events generated with POWHEG+PYTHIA describe $t\bar{t}$ production. The contribution of multijet, DY, and W boson background events is extracted from the data (cf. Section 10). Combined systematic (cf. Section 13) and statistical uncertainties (hatched area) are shown for the total predicted yields. The vertical bars on the points show the statistical uncertainty. The ratios of data to the sum of the predicted yields are provided in the lower panels.

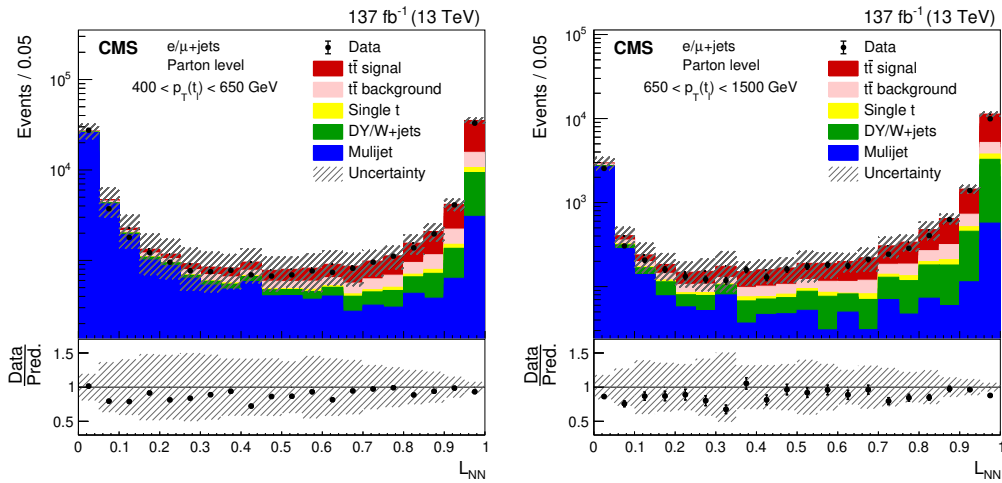


Figure 4: Distributions of the output discriminant L_{NN} used in the boosted t_ℓ identification for the low- $p_T(t_\ell)$ (left) and high- $p_T(t_\ell)$ (right) regions. The data (points) and predictions from simulation (colored histograms) are shown. The hatched area gives the combined statistical and systematic uncertainties in the prediction. The vertical bars on the points show the statistical uncertainty in the data. The ratio of the data to the sum of the individual predictions is displayed in the lower panels.

one nonisolated lepton and has a signal efficiency of about 90% over the entire p_T range.

8 Identification and reconstruction of boosted hadronically decaying top quarks

All selected AK8 jets are considered as t_h candidates. The pileup subtraction based on individual jet constituents, as performed with the PUPPI algorithm, results in a significant improvement in the reconstruction of the jet substructure used for the identification of the boosted t_h . To discriminate the candidates containing decay products of a t_h from other AK8 jets, several properties are combined using an NN. Most of these quantities are calculated after boosting the jet constituents into their center-of-mass system and clustering them with the anti- k_T jet algorithm with a distance parameter of 0.5 to obtain subjets. Since these subjets are clustered in the jet center-of-mass frame rather than in the laboratory frame, the energy and the angle between the objects are used in the jet definition instead of p_T and ΔR , which are invariant under longitudinal boosts. This boost into the center-of-mass system separates the top quark decay products and helps to identify the typical pattern of the three jets. The following NN input variables are used:

- the invariant masses of all combinations of two subjets are calculated, and the three highest values are used;
- the number of combinations of two subjets with invariant masses exceeding 40 GeV;
- the invariant masses of all combinations of three subjets are calculated, and the two highest values are used;
- the ratio of the highest invariant mass of three subjets to the invariant mass of all constituents;
- the ratios of N -jettiness [66] τ_2/τ_1 , τ_3/τ_2 , τ_4/τ_3 , and τ_5/τ_4 with $\tau_N = \sum_k \min(q_1 p_k, q_2 p_k, \dots, q_N p_k)$, where q_i with $1 \leq i \leq N$ are the momenta of the N

leading subjets and p_k are the momenta of all constituents in the jet rest frame;

- the energies of the four most-energetic subjets;
- the value of $|(\vec{p}_1 \times \vec{p}_2) \cdot \vec{p}_3|$, where \vec{p}_1 , \vec{p}_2 , and \vec{p}_3 are the three-momenta of the most-energetic subjets normalized to unity;
- the sphericity [67] $s = \frac{3}{2}(\lambda_2 + \lambda_3)$ of all subjets, with λ_2 and λ_3 the second- and third-highest eigenvalues of the tensor

$$s^{\alpha\beta} = \frac{\sum_i p_i^\alpha p_i^\beta / |p_i|}{\sum_i |p_i|}, \quad (4)$$

where p_i are the momenta of the subjets in the jet rest frame and α, β are the spatial indices;

- the three highest-momentum subjets are boosted back to the laboratory frame and their momentum fractions relative to the AK8 jet are calculated.

There are always at least three subjets in the t_h candidates. Variables relying on having four subjets are set to zero in the rare cases when only three subjets are found.

We use separate NNs for each of four different $p_T(t_h)$ regions: 400–500, 500–700, 700–1000, and >1000 GeV. The NNs consist of a 21-node input layer, four fully connected hidden layers with 63, 42, 42, and 21 nodes, and a single output node. We found that adding more nodes or layers does not improve the discriminating performance of the NN. The activation function is hyperbolic tangent in all layers. The logistic loss function is minimized using stochastic gradient descent with the Adam algorithm. Training samples of 100 000 $t\bar{t}$ signal and 100 000 $t\bar{t}$ background jets are used. The output discriminant is referred to as H_{NN} .

We consider as signal two types of top quark candidates, labeled 2Q and 3Q, where two and three of the quarks from the t_h decay are within $\Delta R = 0.8$, respectively. The 2Q candidates represent a significant contribution for $400 < p_T < 600$ GeV. These are, in general, more difficult to distinguish from background, but they do not provide a significantly worse momentum measurement of the top quarks than 3Q candidates. In Fig. 5 the performance of the NN is demonstrated, showing the background vs. signal selection efficiency for three different $p_T(t_h)$ ranges.

The definition of 2Q and 3Q candidates is based on the spatial matching of quarks to a jet, which is ambiguous. However, this definition is useful since the properties of two or three comparable hard structures within a jet allows us to identify a boosted t_h using the NN. We test the effect of the ambiguity by repeating the cross section measurement with $\Delta R = 0.7$ and 0.9 in the definition. Although this changes the number of events considered as signal and background, in combination with the altered response matrices, very similar cross sections are obtained and their differences are negligible compared with other uncertainties.

9 Event reconstruction and categorization

Depending on the event content, the various reconstruction algorithms are used, and the events are categorized in exclusive categories. The first attempt is the resolved reconstruction described in Section 6. If an event passes the required selection criteria of the 2t category, no further reconstruction is tried. The same is true for 1t1l, but in these events no boosted t_h candidate must exist. If a boosted t_h candidate exists, the boosted reconstruction methods are used on the event.

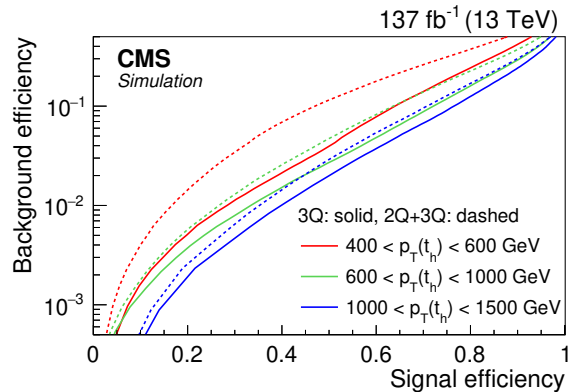


Figure 5: The selection efficiency for background jets as a function of the signal selection efficiency in three $p_T(t_h)$ ranges for 3Q (solid curves) and 2Q+3Q (dashed curves) jets from simulation. An efficiency of 100% corresponds to the preselection of $|\eta| < 2.4$ and $m_{\text{jet}} > 120$ GeV.

If the event is not categorized as 2t or 1t1l, but an isolated lepton, at least one b jet fulfilling the tight criterion, and at least one boosted t_h candidate are found, the event falls into the category BHRL (boosted t_h , resolved t_ℓ). The t_ℓ is reconstructed using the lepton and b jet for which $\Delta R(\ell, \text{b jet})$ is minimal. The neutrino momentum is determined using the m_W mass constraint introduced in Section 6. If such a t_ℓ can be reconstructed, all the t_h candidates with $\Delta R(t_h, \ell) > 1.2$ and $\Delta R(t_h, \text{b jet}) > 1.2$, are considered. The event is counted once for each available t_h candidate. Later, a fit of the H_{NN} distribution is performed to measure the signal yields.

If no isolated lepton exists but at least one boosted t_ℓ candidate with $L_{\text{NN}} > 0.7$ is found, the boosted t_ℓ candidate with the highest value of L_{NN} is used. The event is counted once for each boosted t_h candidate with $\Delta R(t_\ell, t_h) > 1.2$. We refer to this category as BHBL (boosted t_h , boosted t_ℓ). After combining with the BHRL category, the signal fraction is extracted from a fit of the H_{NN} distribution. The fitted signal yields corresponds to the number of signal events, since the definition of the boosted t_h signal does not allow for the presence of more than one signal candidate per event.

The category consisting of boosted t_ℓ and resolved t_h candidates is not used, since the fraction of these events is small. In addition, we find a low fraction of correctly reconstructed $t\bar{t}$ events in this category. Therefore, we consider these events as nonreconstructable.

An overview of the categories and how they are used in the course of the analysis is presented in Fig. 6. In Fig. 7 the contributions of the various reconstruction categories to the distributions of several kinematic variables are shown, and the predicted yields are compared to the data. The distributions are given for the parton-level measurements, but look very similar for the particle-level results.

10 Background subtraction in the resolved categories

In the resolved categories 2t and 1t1l, the multijet and DY/W boson backgrounds, which constitute a fraction of 1.5 and 5.5%, respectively, of the candidate events according to the simulation, are subtracted using combined templates that are obtained from a control region with a reduced $t\bar{t}$ contribution. In order to obtain the background templates, the resolved reconstruction is performed on events where the highest value of the b tagging discriminant is below the tight b tagging requirements. The exact range is optimized to obtain good agreement between

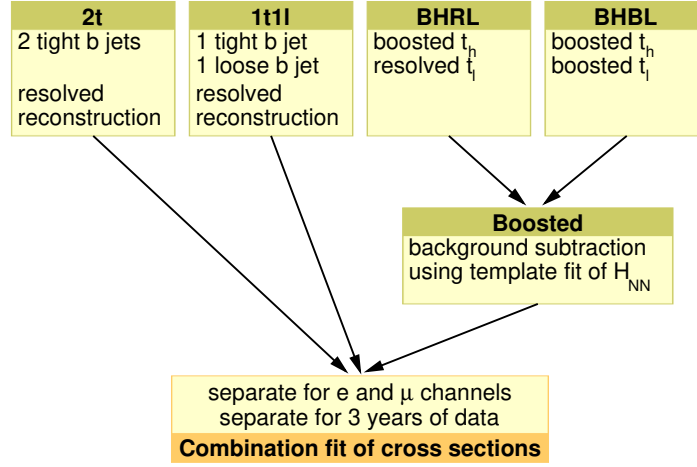


Figure 6: Schematic overview of the categories and how they are used in the analysis.

the distributions in the control region and the simulated prediction of the background in the signal region. Since the statistical precision of the background simulation is limited after applying all selection criteria, the agreement can only be assessed using a coarse binning, as shown in Fig. 8. In this figure, distributions from altered background estimations are also shown. These distributions are obtained by varying up and down the edges of the b tagging discriminant range used in the selection of the control region. The deviations of these distributions from those coming from the default range are used to estimate the systematic uncertainties. The variations in the range are chosen so that the obtained systematic uncertainties are comparable to the differences between the default background estimations and the simulated background predictions in the signal region.

The normalization of this background is obtained from the comparison of data and simulation in the control region. The normalization of the distributions in the control region as well as their shapes are well described by the simulation. After subtracting the predicted yield of $t\bar{t}$ events, the ratio of the observed and simulated yields is used to scale the predicted event yield in the signal region. The deviation of the scale factor from unity and the statistical uncertainty in the simulation are taken as uncertainties in the normalization of this background. The normalization uncertainty is about 50%.

The obtained background predictions with their shape and normalization uncertainties are included in the fits of the cross sections, as described in Section 12. Since the statistical uncertainties in the simulation are dominant, the background normalization is considered as uncorrelated among the three years of data taking. However, since the same method is used to derive the background distributions, the shape uncertainties are considered fully correlated among the years.

Another background contribution is single top quark production, which contributes about 2.5% in the 2t and 1t1l categories. It is subtracted during the cross section fits using SM expectations obtained from the simulation, where the following dominant uncertainties are included: variations of μ_R and μ_F , jet energy scales, and b tagging efficiency. The variations of μ_R and μ_F are treated independently from the corresponding variations of the $t\bar{t}$ simulation, whereas the experimental uncertainties are fully correlated among all processes.

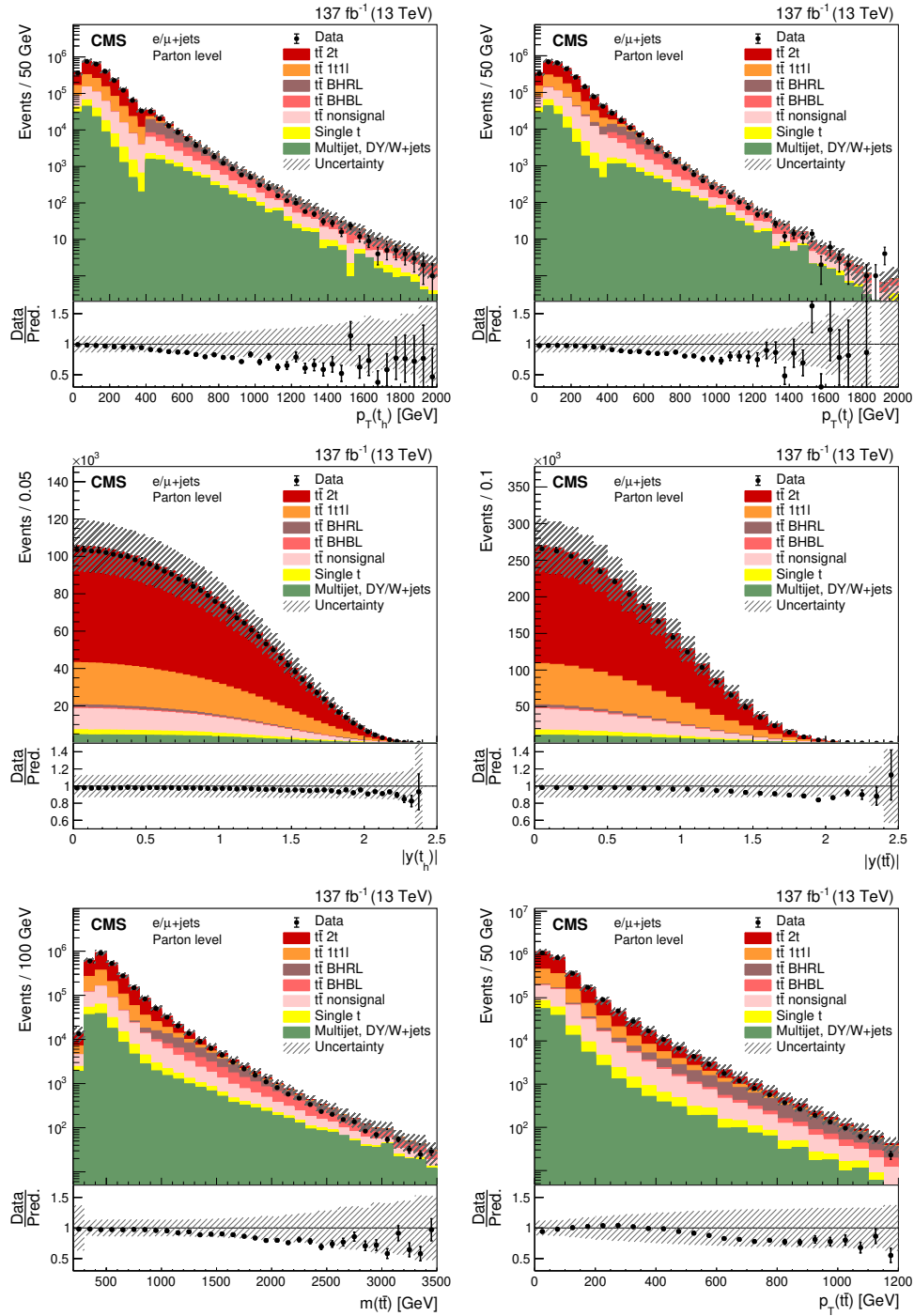


Figure 7: Comparisons of various reconstructed kinematic distributions between data (points) and predictions (colored histograms) obtained for the parton-level measurement. Contributions of the various reconstruction categories are obtained from the POWHEG+PYTHIA $t\bar{t}$ simulation. The contribution of multijet, DY, and W boson background events in the 2t and 1t1l categories are extracted from the data (cf. Section 10). All other background contributions are taken from simulation. Combined systematic (cf. Section 13) and statistical uncertainties (hatched area) are shown for the total predicted yields. The data points are shown with statistical uncertainties. The ratios of data to the sum of the predicted yields are provided in the lower panels.

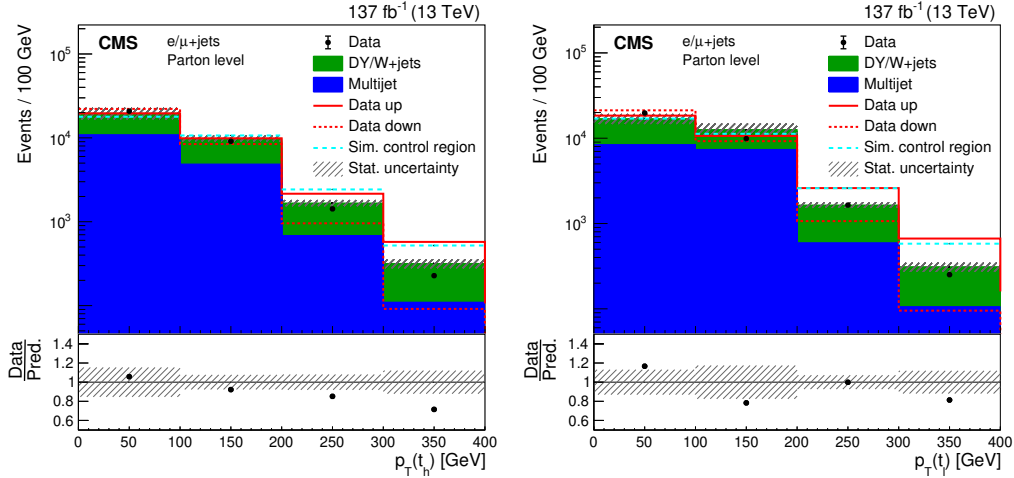


Figure 8: The $p_T(t_h)$ (left) and $p_T(t_l)$ (right) distributions for the multijet and DY/W boson backgrounds from data (points) in the control region and from simulation (colored histograms) in the signal region for the 1t1l category. The red lines show the variations in the control region distribution when shifting the discriminant selection range up (solid lines) and down (dotted lines). The blue dashed line gives the sum of the multijet and DY/W boson predictions in the control region. The hatched band shows the statistical uncertainties in the prediction. The data points are shown with statistical uncertainties. The ratios of data to the predicted yields are provided in the lower panels.

11 Background subtraction in the boosted categories

Events with a boosted t_h , i.e., the categories BHRL and BHBL, are combined for the background subtraction. Template fits based on the H_{NN} distribution are used to extract the yields of 2Q and 3Q events. Since the shape of the H_{NN} distribution depends on $p_T(t_h)$, the template fit is performed using the following bin boundaries in $p_T(t_h)$: 400, 450, 500, 550, 600, 700, 800, 900, 1000, and 7500 GeV. For each bin of a variable under consideration, we fit nine p_T bins. Because of kinematic restrictions, not all p_T bins are populated for each measured bin of the variable under consideration. In addition, we split the templates into three pseudorapidity regions: $|\eta(t_h)| < 0.8$, $0.8 < |\eta(t_h)| < 1.6$, and $1.6 < |\eta(t_h)| < 2.4$, corresponding to the barrel, barrel-endcap transition, and endcap regions, respectively. For each fitted bin the fractions in these three regions f_i are determined in data and the templates are composed as $f_1 T_1 + f_2 T_2 + f_3 T_3$, where the T_i represents the templates in the $|\eta(t_h)|$ regions. This takes into account the small $|\eta(t_h)|$ dependence of the templates without fitting in separate bins of $|\eta(t_h)|$. We verified in the simulation that the templates do not depend on any other of the measured variables. Therefore, the templates do not have to be adapted as a function of these variables.

The $t\bar{t}$ templates are taken from the simulation after applying the full event selections. The yields of 2Q and 3Q events are fitted separately using different templates for the two contributions. The $t\bar{t}$ background templates contain all other boosted t_h candidates that do not belong in the 2Q and 3Q categories, i.e., no or only a single quark from a $t\bar{t}$ decay points towards the candidate. The normalizations of these three templates are free parameters in the fit.

The single top quark background templates are taken from the simulation and normalized to their SM expectation. A Gaussian prior is used to represent the dominant normalization uncertainties in the μ_R and μ_F variations, jet energy scales, and b tagging efficiency. This corresponds to an overall normalization uncertainty of about 30%.

The common background templates for multijet and DY/W boson production are determined from a control region in data using events with at least one jet with $p_T > 400$ GeV and $|\eta| < 2.4$. In addition, events with an isolated electron or muon with $p_T > 15$ GeV are vetoed, and there must be no boosted t_ℓ candidate with $L_{\text{NN}} > 0.7$ in the event. The contribution of all-hadronic $t\bar{t}$ events is suppressed by discarding events with more than one t_h candidate with $H_{\text{NN}} > 0.4$.

For the multijet template we require at least one jet passing the tight b tagging criterion in the event. In such events, we select all t_h candidates that do not overlap with at least one of the b jets. The selection of these events with a t_h candidate and a b jet is like the signal selection but without a lepton.

For the DY/W boson template a quark jet enhanced region is needed. Therefore, we require an isolated photon with $p_T > 35$ GeV and $|\eta| < 2.4$ in the event. The additional requirement, that the photon must be separated from all AK4 jets by $\Delta R(\gamma, \text{jet}) > 0.5$, increases the fraction of photons not stemming from hadron decays. However, these photons are dominantly produced close to jets, where they are radiated from quarks. This selection enhances the overall fraction of quark jets in the event. In such events, we select all t_h candidates that do not overlap with the photon to construct the background templates.

To verify that the selected t_h candidates from the control regions provide accurate background templates, we compare the templates obtained from simulation in the signal region to the templates obtained from simulation in the control region and find these in reasonable agreement. In addition, the simulation is able to describe the data in the control region.

The multijet and DY/W boson backgrounds have slightly different shapes due to different compositions of quark flavors and gluon jets. The yields are constrained to the SM predictions using Gaussian priors with an uncertainty of 50%. These 50% uncertainties are meant to guide the fit to a minimum similar to the SM expectation. Since these background shapes are very similar, the obtained fraction of the background components is somewhat arbitrary if the constraints are removed. However, this gives the fit the freedom to cope with backgrounds of different parton compositions and does not affect the extracted signal yields, since the signal is well distinguished from the backgrounds.

Systematic uncertainties that affect the H_{NN} distribution in the simulation are included in the fit for the corresponding templates. These are the uncertainties in the final-state PS scale, m_t , UE tune, CR model, pileup, and energy response and resolution of the t_h candidates. In addition, the effect of the energy scale uncertainty in the individual subjects is estimated. To assess this, we boost the subjects into the laboratory frame and vary their energies by the uncertainty obtained for PUPPI jets with a distance parameter of 0.4. For the up- and down-varied subjects we recalculate H_{NN} taking into account the change of the center-of-mass system of the AK8 jet. In this way we modify the substructure of the jet according to the typical energy-dependent uncertainty in the jet energy scale. These are the only sources that affect the substructure of jets and hence the H_{NN} distribution. A more detailed discussion of these uncertainties is presented in Section 13.

The various contributions, especially the signal yields for 2Q and 3Q, are obtained by performing a binned maximum likelihood fit simultaneously to all bins of a measurement. The effects of uncertainties in the H_{NN} templates are parameterized by nuisance parameters and consistently varied in all bins. To reduce statistical fluctuations in the descriptions of the uncertainties, a smoothing algorithm [68] is applied to the shape of their relative contributions. The fits are performed separately for the electron and muon channels for each of the three years. As a consistency test, the simulation is fitted, and the extracted event yields are found

to be unbiased. As examples, several postfit H_{NN} distributions in bins of $p_T(t_h)$ and $m(t\bar{t})$ are shown in Fig. 9. For the $m(t\bar{t})$ measurement, the results are summed over the $p_T(t_h)$ bins that are fitted separately for each $m(t\bar{t})$ bin. However, to obtain the input for the cross section extractions discussed in Section 12, we do not use the signal yields with profiled uncertainties. Instead, we perform the fit using the default simulation and repeat it for all relevant up and down variations of the simulation to estimate the systematic uncertainties.

To obtain the signal yields as a function of the variable of interest, we add the extracted yields of 2Q and 3Q events in the $p_T(t_h)$ bins. In Fig. 10 the extracted yields are compared to the simulation. For comparison these plots also show the yields in the 2t and 1t1l categories that use the resolved reconstruction. The backgrounds in the resolved categories are subtracted using the techniques discussed in Section 10. The ratio of data to the prediction as a function of $p_T(t_h)$ in the upper-left plot of Fig. 10 shows a smooth transition between the boosted and resolved reconstructions.

12 Extraction of the differential and inclusive cross sections

As explained in Section 11, the BHRL and BHBL categories are combined in the boosted category for the background subtraction fit. The distributions in the 2t, 1t1l, and boosted categories are combined in the fit to extract the differential cross sections. Each of the three categories are measured separately in the electron and muon channels for each of the three years of data taking. This results in 18 categories entering the fit.

For the extraction of the cross sections, the response matrices R are needed. These map a vector of cross sections σ in bins of the measured distribution to the corresponding event yields at the detector level. After adding a vector \mathbf{b} giving the non- $t\bar{t}$ background events in each bin, the prediction for the number of events at detector level

$$\mathbf{s} = R\sigma + \mathbf{b} \quad (5)$$

is obtained, which can be compared to the measured event yields. Since non- $t\bar{t}$ backgrounds are already subtracted in the boosted category, the components of \mathbf{b} for that category are all zero. However, the systematic uncertainties in the background subtraction, as discussed in Section 11, are taken into account. There are also backgrounds in all categories from $t\bar{t}$ production. Since these backgrounds scale with the $t\bar{t}$ cross section, their contributions are encoded in the response matrix R_{ij} , whose elements are calculated from the simulated $t\bar{t}$ events through the equation:

$$R_{ij} = L \sum_m \sum_n \frac{\delta_{ni}(r_n + M_{n:})}{M_{n:}} M_{nm} \frac{\delta_{mj}}{g_m + M_{:m}}, \quad (6)$$

where M_{nm} is the two-dimensional distribution of the parton- or particle-level vs. detector-level quantity. The first index n corresponds to a bin at the detector level, the second index m to a bin at the parton/particle level. This distribution is only filled if the quantity can be calculated at both levels. As abbreviations, we define the quantities M_i , ($M_{:i}$) as the sum of entries in the i -th row (column) of M . Events that can be reconstructed but do not contain a defined $t\bar{t}$ signal are considered as $t\bar{t}$ background events and enter the distribution \mathbf{r} . The first ratio in Eq. (6) corrects for these $t\bar{t}$ background events. Events with a defined $t\bar{t}$ signal at the parton/particle level, but no $t\bar{t}$ at the detector level, are filled into distribution \mathbf{g} , entering the second ratio in Eq. (6), which represents the losses due to inefficiencies and acceptance. Individual elements of \mathbf{r} (\mathbf{g}) are referred to as r_i (g_i). To convert cross sections into event yields, the expression is multiplied by the integrated luminosity L . In this analysis, the same binning

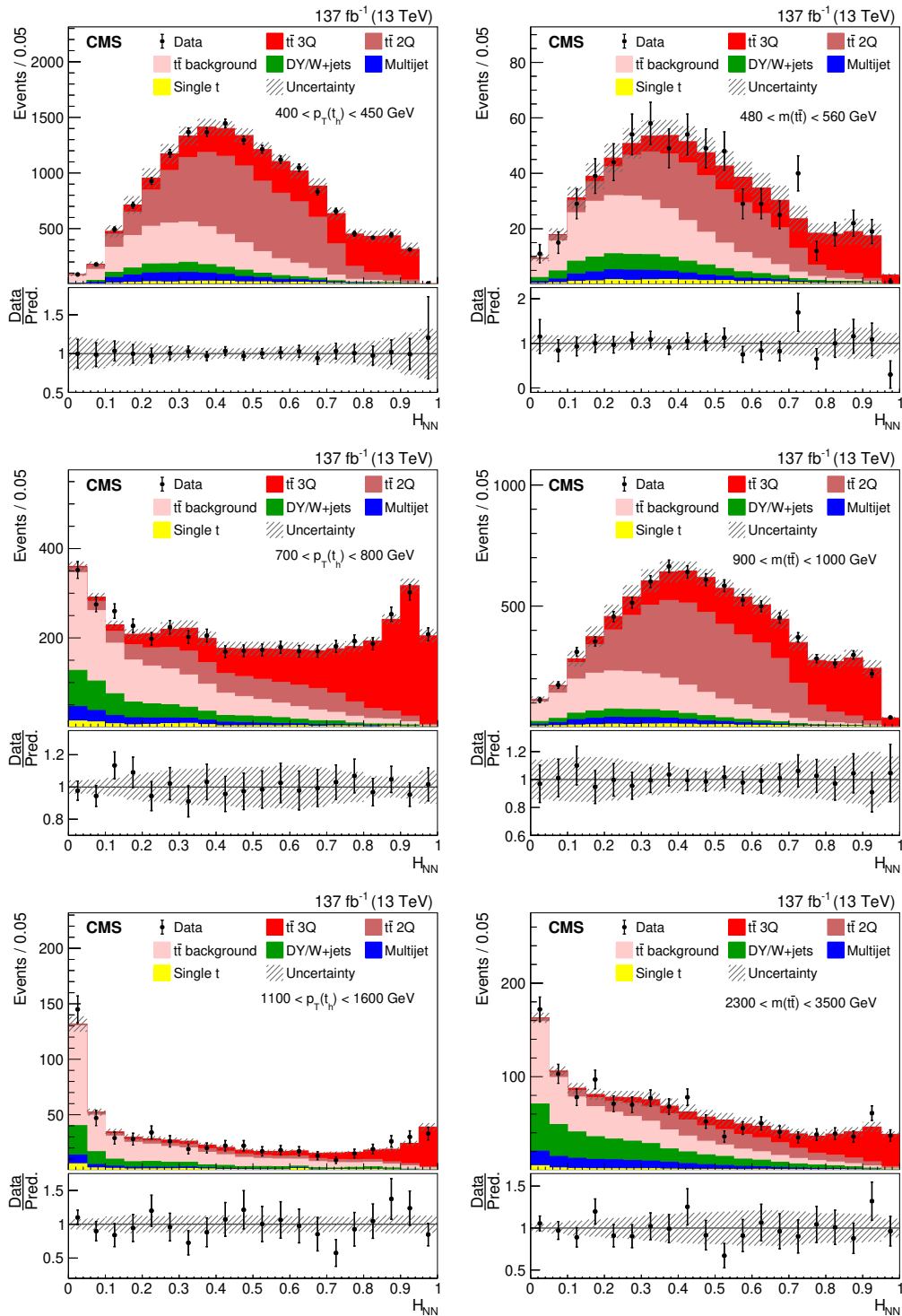


Figure 9: The postfit H_{NN} distributions in bins of $p_T(t_h)$ (left) and $m(t\bar{t})$ (right) for the data (points) and simulation (colored histograms). The electron and muon events and all three years of data taking have been combined. The hatched area shows the total uncertainties from the fit. The vertical bars on the points represent the statistical uncertainty in the data. The ratios of data to the sum of the fitted yields are provided in the lower panels.

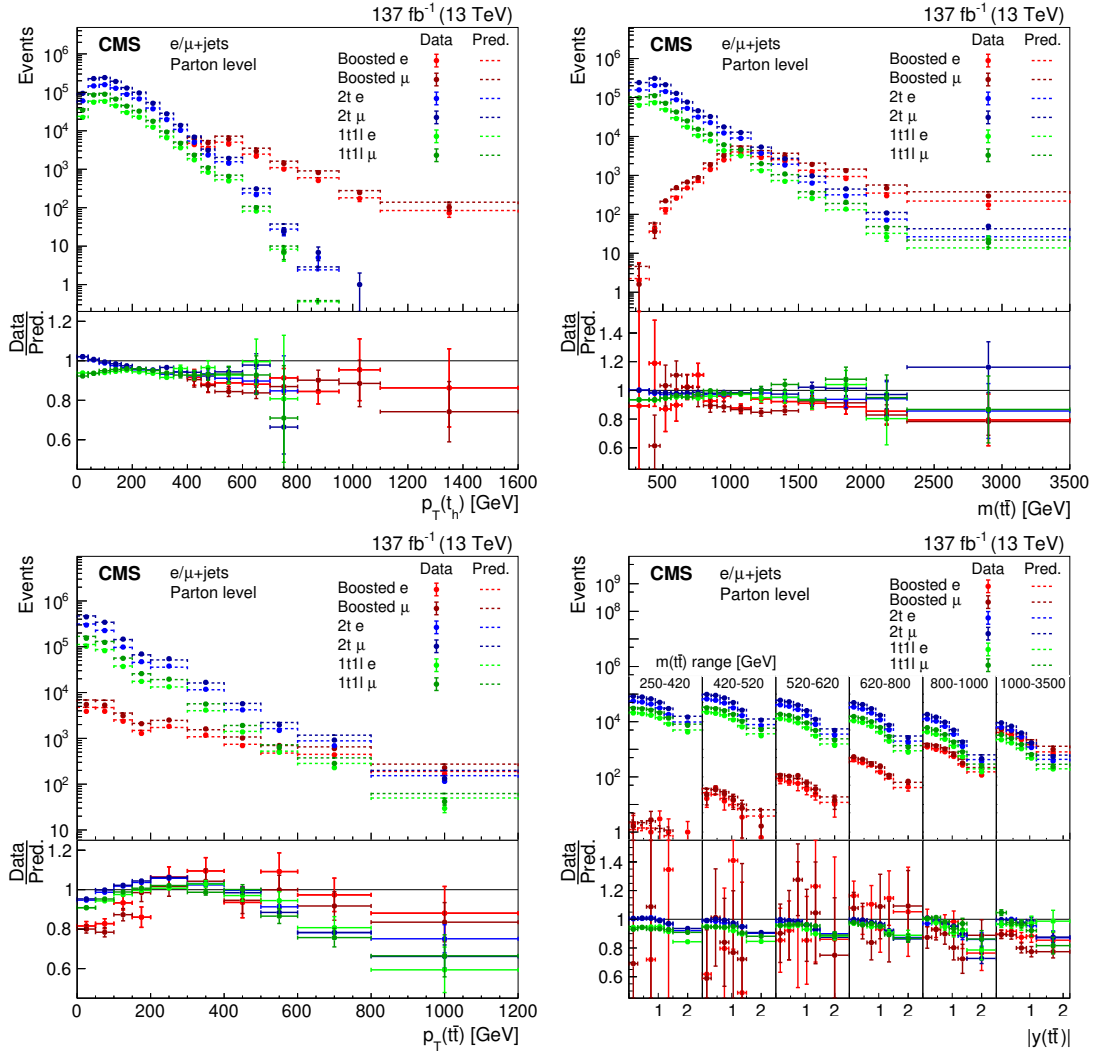


Figure 10: Distributions of $p_T(t_h)$ (upper left), $m(t\bar{t})$ (upper right), $p_T(t\bar{t})$ (lower left), and $m(t\bar{t})$ vs. $|y(t\bar{t})|$ (lower right) after background subtraction. The points show the data and the dashed lines the predictions for the various events types. The lower panels give the ratio of the data to the predictions. The vertical bars on the points give the statistical uncertainties, and the horizontal bars the bin widths.

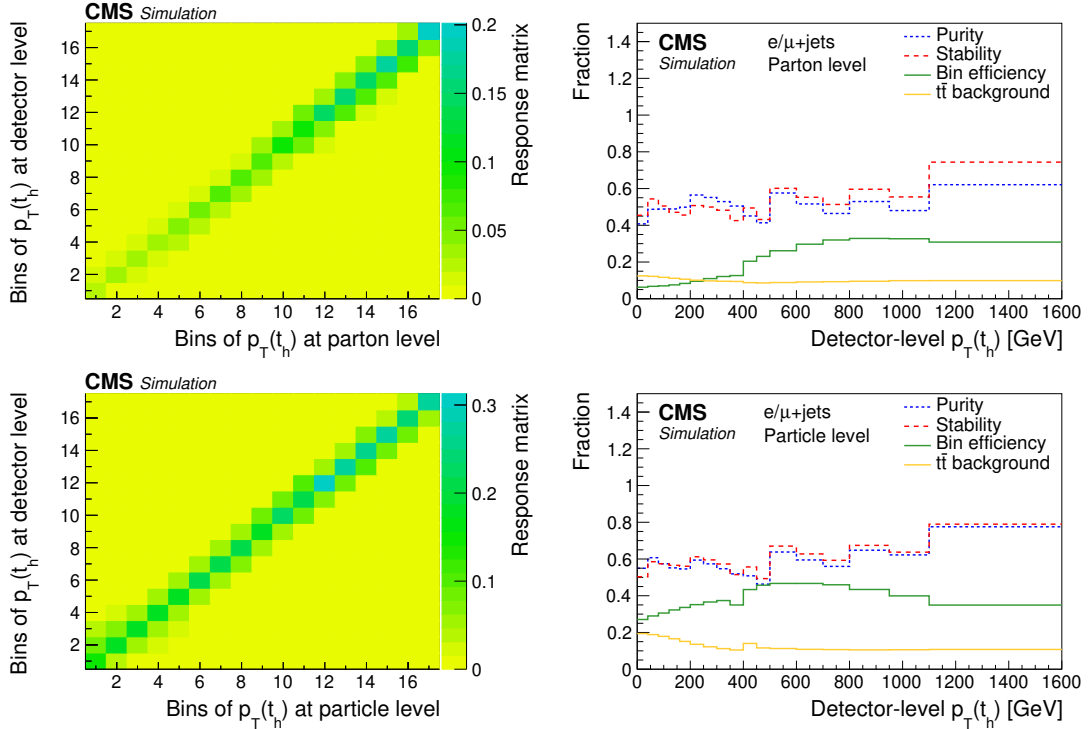


Figure 11: Combined response matrices of all reconstruction categories for the measurements of $p_T(t_h)$ at parton (upper left) and particle (lower left) levels from the POWHEG+PYTHIA simulation. The purity (fraction of parton-/particle-level events that are reconstructed in the same bin at the detector level), stability (fraction of detector-level events that belong in the same bin at the parton/particle level), the efficiency per bin, and the fraction of $t\bar{t}$ background for the corresponding parton and particle levels are shown in the right plots.

is used at the parton/particle and detector levels. In Fig. 11 we show the response matrices of the $p_T(t_h)$ measurements obtained from the POWHEG+PYTHIA simulation, together with their purities (fraction of parton-/particle-level events that are reconstructed in the same bin at the detector level) and stabilities (fraction of detector-level events that belong in the same bin at the parton/particle level). For illustration the combinations of the matrices in the individual categories are shown. The reconstruction performances are very similar for the three years of data taking.

Defining \mathbf{o} as the observed event yield vector, we calculate the χ^2 of the fit using:

$$\chi^2(\boldsymbol{\sigma}, \boldsymbol{\nu}) = \sum_y \sum_c \sum_\ell (\mathbf{o}_{ycl} - \mathbf{s}_{ycl}(\boldsymbol{\sigma}, \boldsymbol{\nu}))^T C_{ycl}^{-1} (\mathbf{o}_{ycl} - \mathbf{s}_{ycl}(\boldsymbol{\sigma}, \boldsymbol{\nu})) + \boldsymbol{\nu}^T Q^{-1} \boldsymbol{\nu}, \quad (7)$$

where we sum over the years ($y = 2016, 2017, \text{ and } 2018$), the reconstruction categories ($c = 2t, 1t1l, \text{ and } \text{boosted}$), and the lepton channels ($\ell = e, \mu$). In the resolved categories, the covariance matrix C is a diagonal matrix with the numbers of observed events per bin, while in the boosted category, since the background was already subtracted, the covariance matrix is the diagonal matrix of the squared statistical uncertainties obtained from the background fits, as described in Section 11. In each category, only bins with at least four events are used, i.e., very low-content and unpopulated bins are not included in the fit. For such bins a χ^2 fit is not well defined. However, since the combined event yields of all categories are from several hundred to thousands of events per bin, this does not affect the results.

The σ values are free parameters of the fit. The systematic uncertainties affecting s are param-

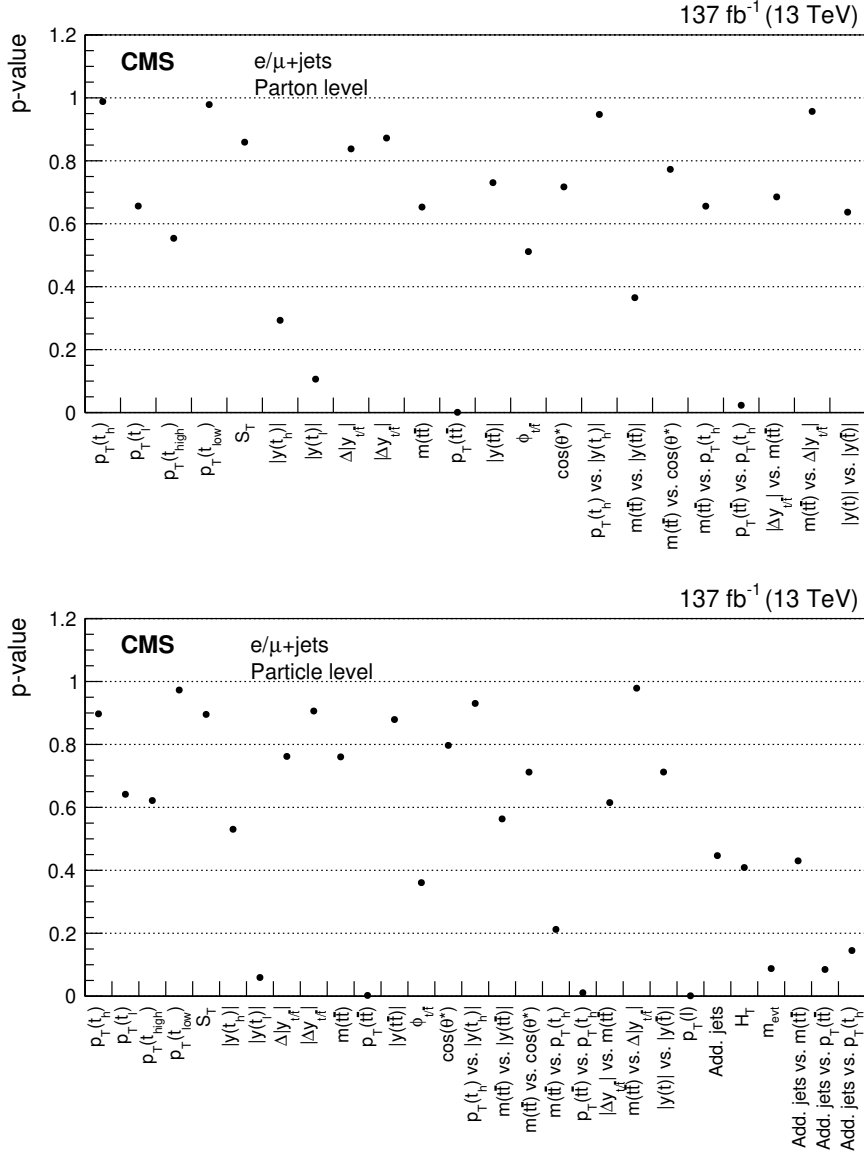


Figure 12: The p -values of the χ^2 fits for the listed variables are shown for the parton- (upper) and particle- (lower) level measurements.

eterized as functions of the nuisance parameters ν . These are constrained by the last term in Eq. (7), where the matrix Q is the correlation matrix of the nuisance parameters. The correlations of the uncertainty sources among the measurements from different years are important. They are discussed in detail in Section 13. The goodness of fit is calculated from the minimized χ^2 and the number of degrees of freedom, which is obtained by subtracting the number of bins in σ from the used detector-level bins. The corresponding p -values, shown in Fig. 12, are reasonable. They follow approximately a uniform distribution between 0 and 1, with a minimum value of 0.2%. Thus, the differential cross sections are able to describe the data in all categories simultaneously. In all the differential cross sections fits, the nuisance parameter values are not pulled more than two standard deviations. Most of them are either not constrained or only moderately constrained, and their uncertainties are typically reduced by about 30%.

13 Systematic uncertainties

In the cross section fits, several sources of systematic uncertainties affect the response matrix. These sources can be split into two main categories: theoretical and experimental uncertainties. The theoretical ones are listed below.

- The effects of higher-order contributions to the cross section calculations are estimated by varying μ_R and μ_F separately by a factor of two. Distributions for these variations are obtained using event weights in the POWHEG+PYTHIA simulation. The two scale variations are included as two separate uncertainties in the fit. Since the POWHEG calculation is the same for all three years, these uncertainties are considered to be fully correlated.
- Since the μ_R and μ_F variations barely account for the differences in the shape of the p_T spectrum from POWHEG at NLO QCD and from MATRIX at NNLO QCD precision, an additional uncertainty is introduced, which corresponds to the difference in the p_T spectra of the two calculations. This uncertainty is correlated among measurements in the three years.
- With the PDF parameterizations NNPDF30_nlo_as_0118 in the CUETP8M2T4 tune of the 2016 simulations and NNPDF31_nnlo_hessian_pdfas in the CP5 tune of the 2017 and 2018 simulations, different PDFs are used. The PDF sets provide 100 variations representing their uncertainty. For each variation a nuisance parameter enters the fit. In addition, a variation of α_S by 0.002 in the PDF parameterizations is taken into account. The distributions are obtained using the corresponding event weights. Only the uncertainties in the 2017 and 2018 measurements are treated as correlated, whereas the uncertainties in the 2016 measurement, which uses different PDFs, is assumed to be uncorrelated.
- The uncertainty in the initial-state PS is estimated by varying the shower scale by factors of 0.5 and 2. The corresponding distributions are obtained using event weights. With $\alpha_S = 0.1108$ (0.118) for CUETP8M2T4 (CP5), the values are very similar, and we assume that this uncertainty is fully correlated among the measurements in all years.
- The uncertainty in the final-state PS is estimated by varying the shower scale by factors of 0.5 and 2. The corresponding distributions are obtained using event weights. With $\alpha_S = 0.1365$ (0.118) for CUETP8M2T4 (CP5), we assume that this uncertainty is uncorrelated for the two tunes.
- In POWHEG, the matching between the matrix element calculation and the PS is controlled by the parameter h_{damp} . The values used with the CUETP8M2T4 and CP5 tunes are $(1.58^{+0.66}_{-0.59})m_t$ and $(1.38^{+0.92}_{-0.51})m_t$, respectively. Since the values are similar, the uncertainty is taken as fully correlated among the measurements in different years. Separate samples produced with the uncertainty variations of h_{damp} are used to obtain these uncertainties.
- Separate samples produced with $m_t = 171.5 \text{ GeV}$ and $m_t = 173.5 \text{ GeV}$ are used to conservatively estimate the uncertainty due to the m_t measurement. This $\pm 1 \text{ GeV}$ variation is fully correlated among the measurements in different years.
- The uncertainty in the UE modeling is estimated using separate samples that represent the envelope of uncertainties in the tunes. This uncertainty is fully correlated between the measurements in 2017 and 2018, but taken as uncorrelated with the 2016 measurement, where a different tune is used.

- The fraction of leptonically decaying b hadrons is changed according to the known precision of the corresponding branching fractions [50] using event-based reweighting. This uncertainty is fully correlated among the measurements in different years.
- The uncertainty in the CR is assessed using an alternative model where the reconnection of colored particles from resonance decays, which is deactivated by default in PYTHIA, is activated. The difference between these two is taken as a symmetric uncertainty. We assume that the amount of CR is fully correlated among the measurements in the three years.

The following experimental uncertainties are assessed.

- The uncertainties in the integrated luminosity are 2.5, 2.3, and 2.5% for 2016, 2017, and 2018, respectively. Their correlations are between 20 and 30% [69–71]. These uncertainties and their correlations are directly used in the cross section fits.
- The uncertainty in the pileup estimation is divided into two sources: one in the inelastic cross section of about 4.5% [72] and another in the instantaneous luminosities. Since the former is dominant and fully correlated among the years, a high correlation of about 85% is estimated. Response matrices for enhanced and reduced pileup are obtained by applying event weights to alter the distribution of the number of pileup interactions in the simulation.
- The jet energy scale uncertainty is split into 20 different sources. The combined uncertainties are p_T - and η -dependent, with a magnitude that varies between 0.3 and 1.8% for the relevant jets. The correlation among the years is evaluated for each source. The sources affect the AK4 and AK8 jets simultaneously, but in different ways. The differences in the response matrices are obtained by rescaling the jet momenta in the simulation.
- The uncertainty in the subjet energy scale of boosted t_h candidates is considered, where subjets with $p_T < 30$ GeV have energy scale uncertainties up to 3%. This uncertainty has a correlation of 50% among the years.
- For AK4 and PUPPI AK8 jets, separate uncertainties in the energy resolutions are introduced because the different methods of pileup corrections have large effects on the resolutions. The uncertainties are considered uncorrelated among the measurements in different years. The response matrices for different jet resolutions are obtained by rescaling the jet resolution in the simulation.
- The dominant source of uncertainty in p_T^{miss} is the uncertainty in the jet energy calibration. Therefore, p_T^{miss} is also recalculated whenever the jet momenta are rescaled for uncertainty estimations. An additional contribution to the uncertainty comes from PF particles that do not belong to any of the selected jets. A 50% correlation of this uncertainty among the years is assumed.
- Uncertainties in the tagging and mistagging efficiencies of various b tagging requirements have been studied [63]. In this analysis, tight and loose b tagging requirements are used. To simulate the variations of the efficiencies, event weights are calculated according to the probability to find the combination of correctly and wrongly identified jets under the assumption of altered efficiencies. We alter separately the efficiencies of the loose and tight requirements, and in addition, the efficiency of passing the loose but not the tight requirement. Each of the three variations introduces a nuisance parameter related to the tagging and mistagging efficiencies. We assume a 50% correlation among the years.

- For electrons and muons, uncertainties in the trigger and reconstruction efficiencies are included. Since the same methods for measuring these efficiencies in data are used in all years, the corresponding uncertainties are likely to have a common origin, and we assume a correlation of 50% for these uncertainties among the years.
- During the 2016 and 2017 data taking, a gradual shift in the timing of the inputs of the ECAL L1 trigger in the region of $|\eta| > 2.0$ caused a trigger inefficiency. For events containing an electron (a jet) with p_T larger than ≈ 50 GeV (≈ 100 GeV), in the region $2.5 < |\eta| < 3.0$ the efficiency loss is ≈ 10 – 20% , depending on p_T , η , and time. Correction factors were computed from data and applied to the acceptance evaluated by simulation. The uncertainties in these correction factors are propagated to the cross section measurements.

The description of uncertainties estimated from separate simulations (h_{damp} , m_t , UE tune, and CR model) suffers from statistical fluctuations despite several tens of millions of simulated events. With a two-dimensional smoothing algorithm [68] applied to the relative uncertainties in the response matrices, we recover a meaningful description that is consistent among the different channels.

In addition, we estimate the effect of the limited event count in the simulations by repeating the entire fit 100 times with varied response matrices. From these results we calculate the covariance matrix, which is added to the covariance matrix of the other uncertainties obtained from the fits with the default response matrices. The response matrices are varied randomly taking into account statistical uncertainties in the default POWHEG+PYTHIA simulation and in the simulations used for the uncertainty estimations in m_t , h_{damp} , the UE tune, and the CR model. For the uncertainties estimated based on event weights or rescaling of object momenta, the correlations between the default bin contents and the altered bin contents are taken into account when the random variations are generated. Overall, the uncertainty due to limited event count in the simulations is on the order of other leading systematic uncertainties. It becomes a dominant systematic uncertainty only in a few bins, but is always small compared to the statistical uncertainty in the data.

In Fig. 13, the uncertainties in the measurements of a few differential cross sections are shown, split into individual sources. The statistical uncertainty in the data becomes dominant only in the tails of the distributions, while the bulk is dominated by the systematic uncertainties. The main contributions are from the uncertainty in the jet energy scale and the integrated luminosity. The leading theoretical uncertainties are the variations of μ_R , μ_F , and the uncertainty that reflects the difference in $p_T(t)$ between the NLO and NNLO calculations.

14 Results at the parton and particle levels

In Fig. 14 the results of χ^2 tests comparing the measurements with several predictions are shown. To magnify the regions of low and high p -values, they are converted into Z -scores using the relation

$$p\text{-value} = 1 - \int_{-\infty}^{Z\text{-score}} \text{norm}(x) dx, \quad (8)$$

where the integrand is the normal distribution with mean 0 and standard deviation 1. For the comparison the covariance matrices of the measurements and the predictions are taken into account. For the POWHEG+PYTHIA simulations all theoretical uncertainties are considered. For the MATRIX, POWHEG+HERWIG, and MG5_aMC@NLO+PYTHIA simulations, we consider

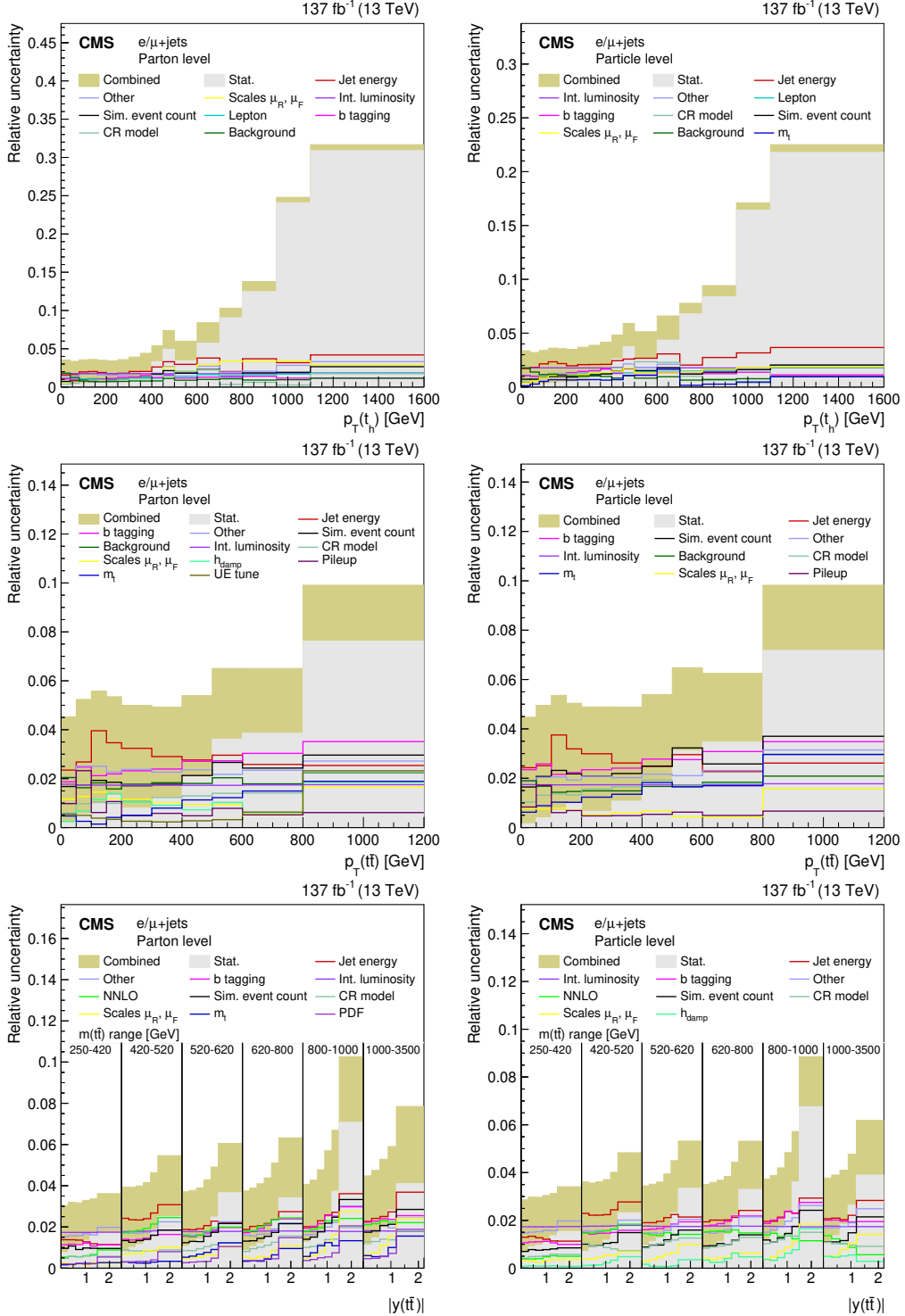


Figure 13: The individual sources of systematic uncertainties in the various parton (left) and particle (right) measurements and their relative contributions to the overall uncertainty. Sources with a maximum uncertainty below 1.5% are combined in the category “Other”.

the dominant sources of matrix element scales and PDF uncertainties. In addition, the PS scale uncertainties are evaluated for MG5_aMC@NLO+PYTHIA. The PDF uncertainties for MATRIX are obtained as the envelope of the differences obtained with the CT14 [73], HERA [74], and MMHT [75] PDF sets. In all predictions, the individual uncertainty sources are assumed to be correlated among the bins, while the sources themselves are uncorrelated. Most of the distributions are well described by the predictions, and the uncertainty in the NNLO MATRIX calculation is significantly smaller than in the NLO predictions. For the parton-level measurements, similar p -values are obtained for POWHEG+PYTHIA with the CUETP8M2T4 and CP5 tunes and POWHEG+HERWIG, while the description by MG5_aMC@NLO+PYTHIA is slightly worse. For the particle-level measurements similar agreements are obtained for POWHEG+PYTHIA with the CUETP8M2T4 and CP5 tunes. In most cases, the p -values of the MG5_aMC@NLO+PYTHIA and POWHEG+HERWIG predictions are lower. At both levels, the distributions of $m(t\bar{t})$ vs. $p_T(t_h)$, $p_T(t\bar{t})$ vs. $p_T(t_h)$, and $|\Delta y_{t/\bar{t}}|$ vs. $m(t\bar{t})$ are not well described by any of the tested predictions. The corresponding distributions are shown in Figs. 27–32. The one-dimensional distributions of $p_T(t_h)$, $m(t\bar{t})$, and $p_T(t\bar{t})$ are consistent with the predictions at the level of two standard deviations, which calls for further investigations to improve the understanding of the kinematic relations between these variables. In addition, at the particle level the kinematic distributions in bins of jet multiplicity are not well described.

The measurements at the parton level are compared to the POWHEG+PYTHIA (CP5), POWHEG+HERWIG, MG5_aMC@NLO+PYTHIA, and the MATRIX predictions. For the particle-level measurements, the MATRIX prediction is replaced by POWHEG+PYTHIA (CUETP8M2T4). In general, when comparing the distributions in data and simulation, very similar trends are observed at both levels.

The differential cross sections as a function of $p_T(t_h)$, $p_T(t_\ell)$, $p_T(t_{\text{high}})$, $p_T(t_{\text{low}})$, and S_T are presented in Figs. 15 and 16 at the parton and particle levels, respectively. In these and most of the following figures of the differential cross sections, the displayed width of the last bin is reduced. The exact boundaries of these bins are indicated by the axis labels. For better visibility, the horizontal marker positions of the predictions are shifted with respect to the bin centers.

Compared with the previous CMS measurement [17] the precision is significantly improved, e.g., for a top quark $p_T < 500$ GeV the uncertainty is reduced by about 50%. Since it is easier to perform the background subtraction (cf. Section 11) in bins of $p_T(t_h)$, the measurement as a function of $p_T(t_h)$ is extended towards higher p_T compared to the measurement as a function of $p_T(t_\ell)$. The p_T spectra are softer than predicted by the NLO calculations at low p_T . For $p_T > 500$ GeV the predictions overestimate the measured cross sections by about 20%. However, the NNLO QCD calculation performed with MATRIX describes the data significantly better, with the exception of $p_T(t_{\text{low}})$. As discussed in Ref. [43], $p_T(t_{\text{high}})$ and $p_T(t_{\text{low}})$ cannot be accurately described by fixed-order calculations; resummation effects of the Sudakov type have to be taken into account. At the parton level the differential cross sections as a function exclusively of t_h or t_ℓ should be the same, and this is used to check the consistency of the results obtained with the different top quark decays.

Figures 17 and 18 show the distributions of $|y(t_h)|$, $|y(t_\ell)|$, and the differences $\Delta|y_{t/\bar{t}}|$ and $|\Delta y_{t/\bar{t}}|$. They are all well described by the simulations.

In Figs. 19 and 20 the differential cross sections are shown as a function of the $t\bar{t}$ kinematic variables $m(t\bar{t})$, $p_T(t\bar{t})$, $|y(t\bar{t})|$, $\Delta\phi_{t/\bar{t}}$, and $\cos(\theta^*)$. A small modulation is observed in the $p_T(t\bar{t})$ distribution, i.e., the data are underestimated at about 300 GeV and overestimated at very high values. A discrepancy also occurs at high values of $|y(t\bar{t})|$, where all simulations predict a higher cross section than observed. Despite these small deviations, there is no significant dis-

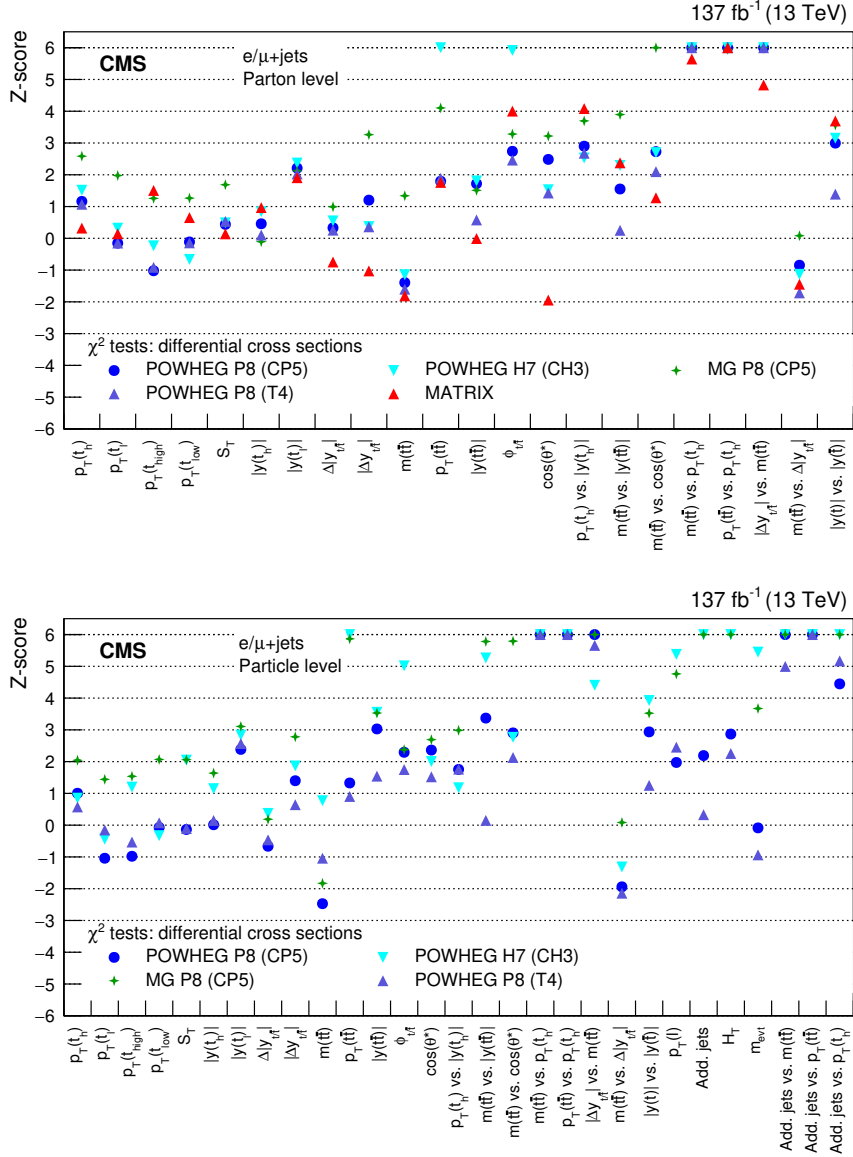


Figure 14: The Z-scores from the corresponding χ^2 tests comparing the measured differential cross sections for the shown variables at the parton (upper) and particle (lower) levels to the predictions of POWHEG+PYTHIA (P8) for the CP5 and CUETP8M2T4 (T4) tunes, POWHEG+HERWIG (H7), the multiparton simulation MG5_aMC@NLO (MG)+PYTHIA FxFx, and the NNLO QCD calculations obtained with MATRIX. The Z-scores are truncated at an upper limit of six. The uncertainties in the measurements and the predictions are taken into account in the χ^2 calculation.

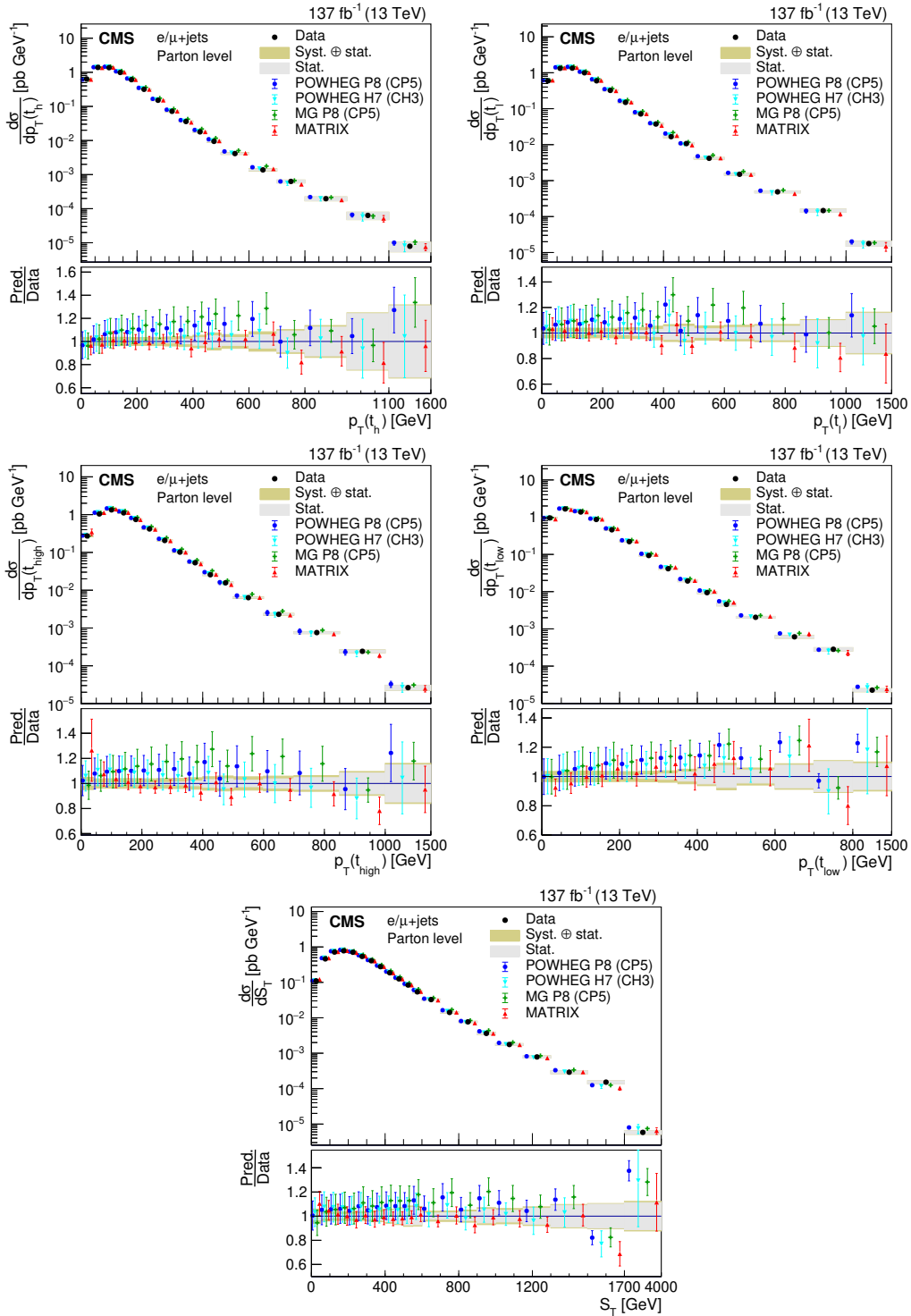


Figure 15: Differential cross sections at the parton level as a function of $p_T(t_h)$, $p_T(t_l)$, $p_T(t_{\text{high}})$, $p_T(t_{\text{low}})$, and S_T . The data are shown as points with gray (yellow) bands indicating the statistical (statistical and systematic) uncertainties. The cross sections are compared to the predictions of POWHEG combined with PYTHIA (P8) or HERWIG (H7), the multiparton simulation MG5_aMC@NLO (MG)+PYTHIA FxFx, and the NNLO QCD calculations obtained with MATRIX. The ratios of the various predictions to the measured cross sections are shown in the lower panels.

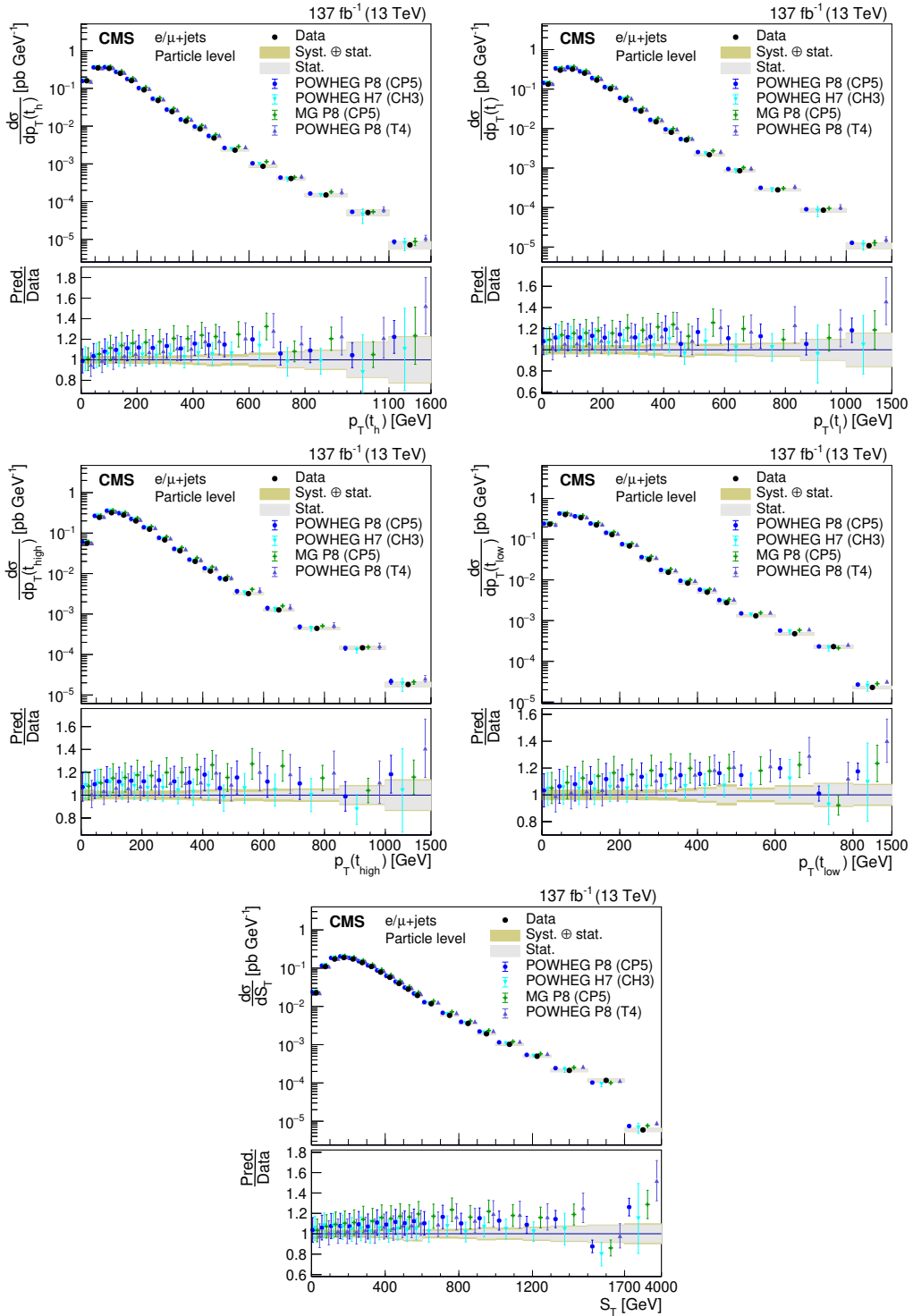


Figure 16: Differential cross sections at the particle level as a function of $p_T(t_h)$, $p_T(t_l)$, $p_T(t_{\text{high}})$, $p_T(t_{\text{low}})$, and S_T . The data are shown as points with gray (yellow) bands indicating the statistical (statistical and systematic) uncertainties. The cross sections are compared to the predictions of POWHEG+PYTHIA (P8) for the CP5 and CUETP8M2T4 (T4) tunes, POWHEG+HERWIG (H7), and the multiparton simulation MG5_aMC@NLO (MG)+PYTHIA. The ratios of the various predictions to the measured cross sections are shown in the lower panels.

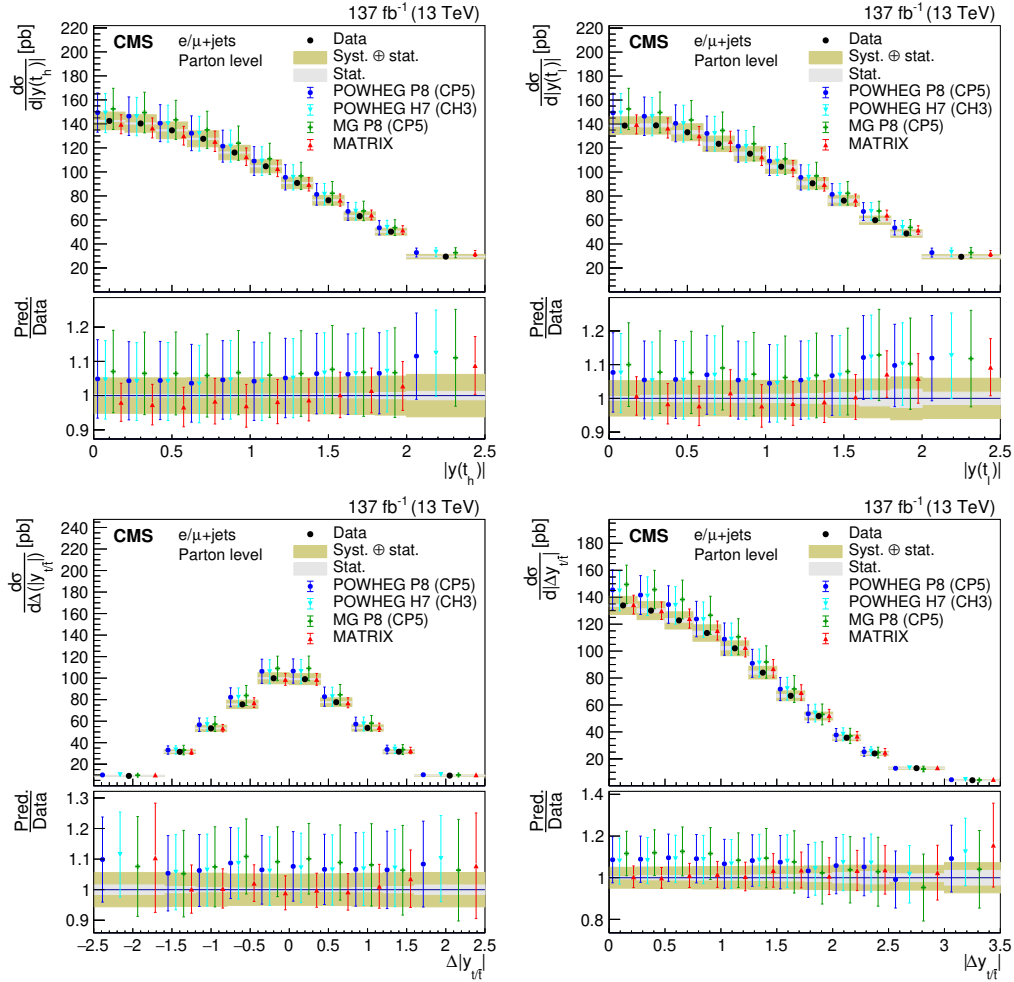


Figure 17: Differential cross sections at the parton level as a function of $|y(t_h)|$, $|y(t_l)|$, and the differences $\Delta|y_{t/\bar{t}}|$ and $|\Delta y_{t/\bar{t}}|$. The data are shown as points with gray (yellow) bands indicating the statistical (statistical and systematic) uncertainties. The cross sections are compared to the predictions of POWHEG combined with PYTHIA (P8) or HERWIG (H7), the multiparton simulation MG5_aMC@NLO (MG)+PYTHIA FxFx, and the NNLO QCD calculations obtained with MATRIX. The ratios of the various predictions to the measured cross sections are shown in the lower panels.

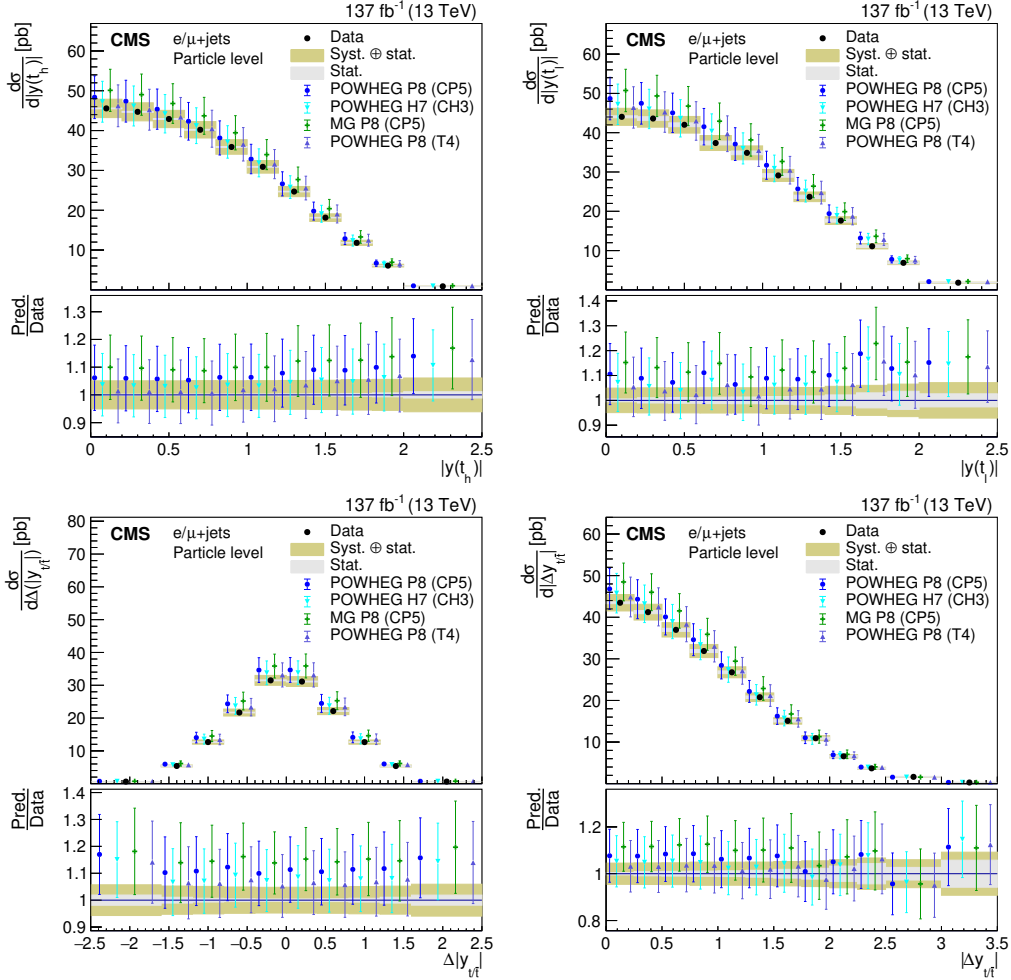


Figure 18: Differential cross sections at the particle level as a function of $|y(t_h)|$, $|y(t_\ell)|$, and the differences $\Delta|y_{t/\bar{t}}|$ and $|\Delta y_{t/\bar{t}}|$. The data are shown as points with gray (yellow) bands indicating the statistical (statistical and systematic) uncertainties. The cross sections are compared to the predictions of POWHEG+PYTHIA (P8) for the CP5 and CUETP8M2T4 (T4) tunes, POWHEG+HERWIG (H7), and the multiparton simulation MG5_aMC@NLO (MG)+PYTHIA. The ratios of the various predictions to the measured cross sections are shown in the lower panels.

agreement between data and predictions.

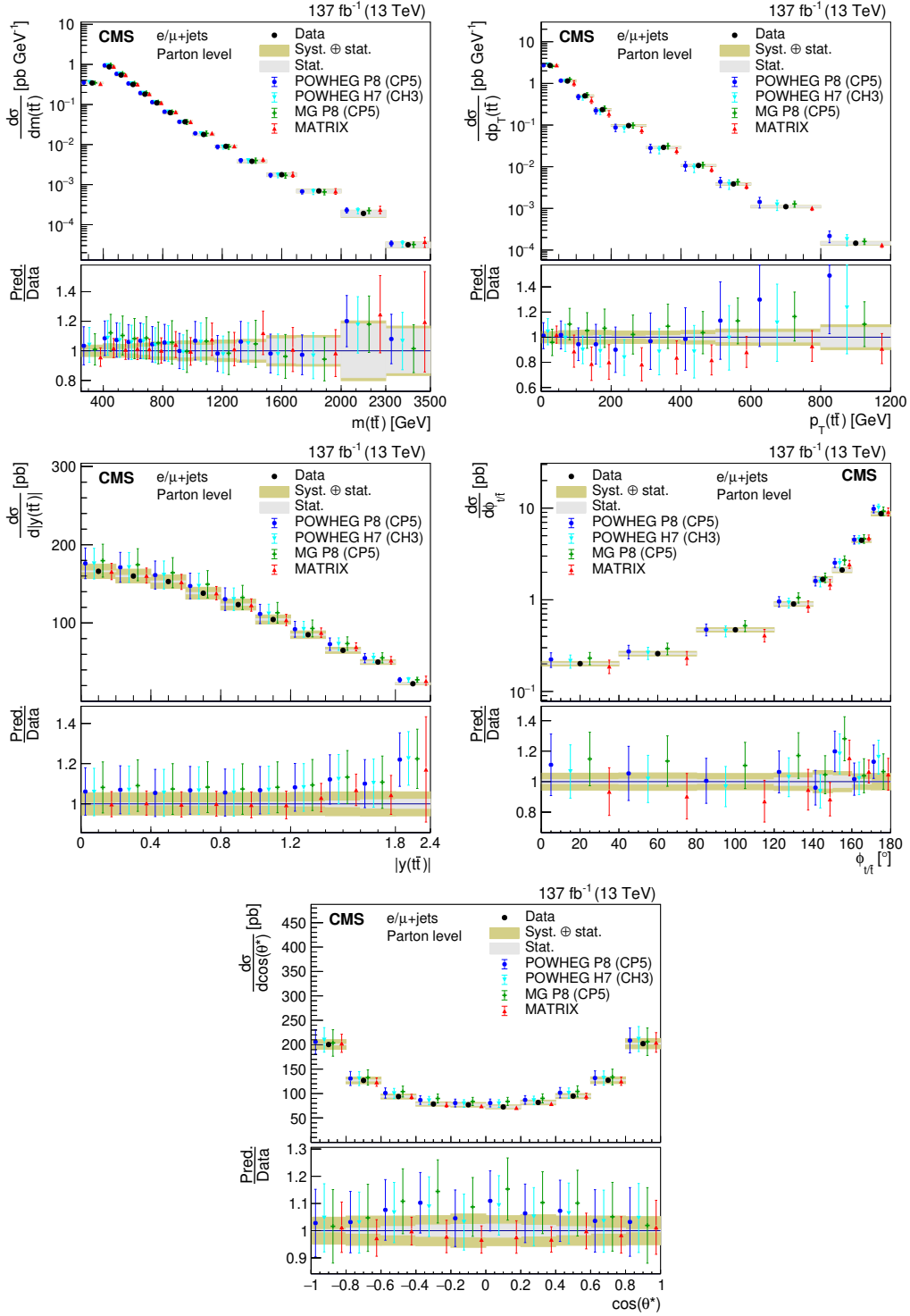


Figure 19: Differential cross sections at the parton level as a function of kinematic variables of the $t\bar{t}$ system. The data are shown as points with gray (yellow) bands indicating the statistical (statistical and systematic) uncertainties. The cross sections are compared to the predictions of POWHEG combined with PYTHIA (P8) or HERWIG (H7), the multiparton simulation MG5_aMC@NLO (MG)+PYTHIA FxFx, and the NNLO QCD calculations obtained with MATRIX. The ratios of the various predictions to the measured cross sections are shown in the lower panels.

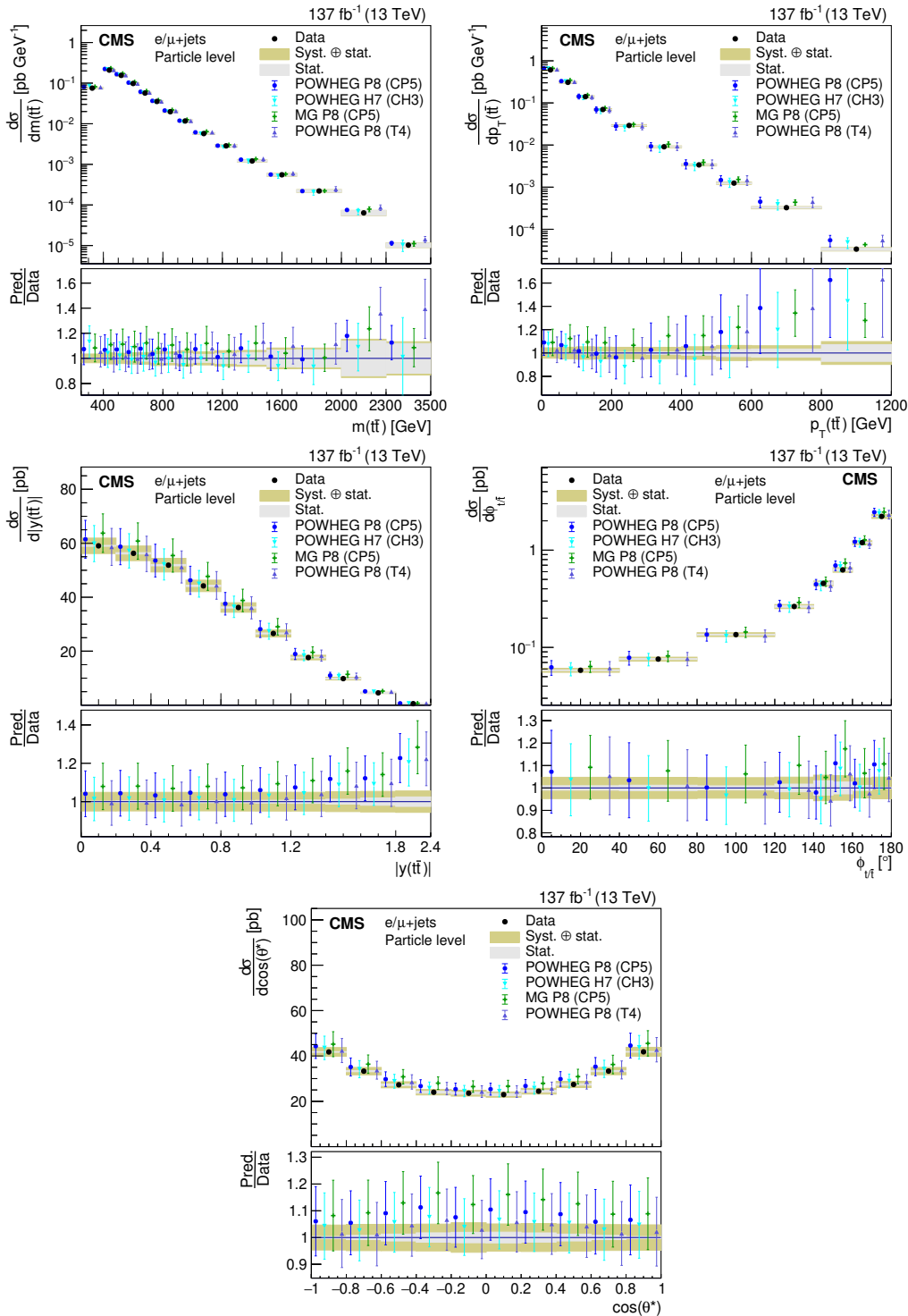


Figure 20: Differential cross sections at the particle level as a function of kinematic variables of the $t\bar{t}$ system. The data are shown as points with gray (yellow) bands indicating the statistical (statistical and systematic) uncertainties. The cross sections are compared to the predictions of POWHEG+PYTHIA (P8) for the CP5 and CUETP8M2T4 (T4) tunes, POWHEG+HERWIG (H7), and the multiparton simulation MG5_aMC@NLO (MG)+PYTHIA. The ratios of the various predictions to the measured cross sections are shown in the lower panels.

The double-differential cross sections are shown in Figs. 21–36. The distributions of $p_T(t_h)$ vs. $|y(t_h)|$ shown in Figs. 21 and 22 are well described by most of the predictions. The NLO calculations overestimate the cross sections in all $|y(t_h)|$ bins in the high- $p_T(t_h)$ region. The corresponding distributions for t_ℓ are not shown, since the information they add is marginal. However, we measure consistent distributions of t_h and t_ℓ at the parton level.

As mentioned earlier, a higher cross section is predicted than seen in the data at high values of $|y(t\bar{t})|$. This effect persists in different regions of $m(t\bar{t})$, as shown in the $m(t\bar{t})$ vs. $|y(t\bar{t})|$ measurements in Figs. 23 and 24.

In Figs. 25 and 26 the measurements of $m(t\bar{t})$ vs. $\cos(\theta^*)$ are shown. These double-differential cross sections are well described by the simulations.

The measurements of $m(t\bar{t})$ vs. $p_T(t_h)$, shown in Figs. 27 and 28, are not well described by any of the predictions, as indicated by the χ^2 tests given in Fig. 14. While the measured p_T spectra are in agreement or even harder than predicted at low $m(t\bar{t})$, the spectra are softer at high $m(t\bar{t})$. Such an opposite trend in the different $m(t\bar{t})$ regions, along with the bin-by-bin correlations of uncertainties, results in low p -values. The mismodeling is even more apparent in the normalized differential cross sections in Figs. A.13 and A.14.

The measurements of $p_T(t\bar{t})$ vs. $p_T(t_h)$ are shown in Figs. 29 and 30. Compared to the various predictions, the softer measured $p_T(t_h)$ spectrum is most evident in the low- $p_T(t\bar{t})$ region, while at high $p_T(t\bar{t})$ the measurements are well described.

The measurements of $|\Delta y_{t/\bar{t}}|$ vs. $m(t\bar{t})$ are displayed in Figs. 31 and 32. This distribution is known to be sensitive to electroweak corrections, especially to the top quark Yukawa coupling [2, 3]. The NNLO calculation results in an improved description of this distribution.

In Figs. 33 and 34 the measurements of $m(t\bar{t})$ vs. $|\Delta y_{t/\bar{t}}|$ are presented. They are well described by all predictions. Note that it is problematic to use these measurements of $|\Delta y_{t/\bar{t}}|$ to extract information on the charge asymmetry of $t\bar{t}$ production in pp collisions because the acceptance corrections introduce a significant asymmetry in these measurements.

In Figs. 35 and 36 the double-differential cross sections as a function of $|y(t)|$ vs. $|y(\bar{t})|$ are shown. They are used to calculate the ratio of cross sections of t and \bar{t} as a function of rapidity when the bin-by-bin correlations are taken into account correctly. These ratios are displayed in the lower-right plots of Figs. 35 and 36. Differences in the rapidity of t and \bar{t} are a direct consequence of the charge asymmetry, where on average $|y(t)|$ is less central than $|y(\bar{t})|$. In contrast to measurements based on $|\Delta y_{t/\bar{t}}|$, the acceptance correction of this double-differential measurement does not depend on the asymmetry in the simulation. However, no significant difference between $|y(t)|$ and $|y(\bar{t})|$ is observed. The simulation predicts that the main effect of the charge asymmetry is expected at high rapidities, where the measurement is limited by the statistical accuracy and detector acceptance.

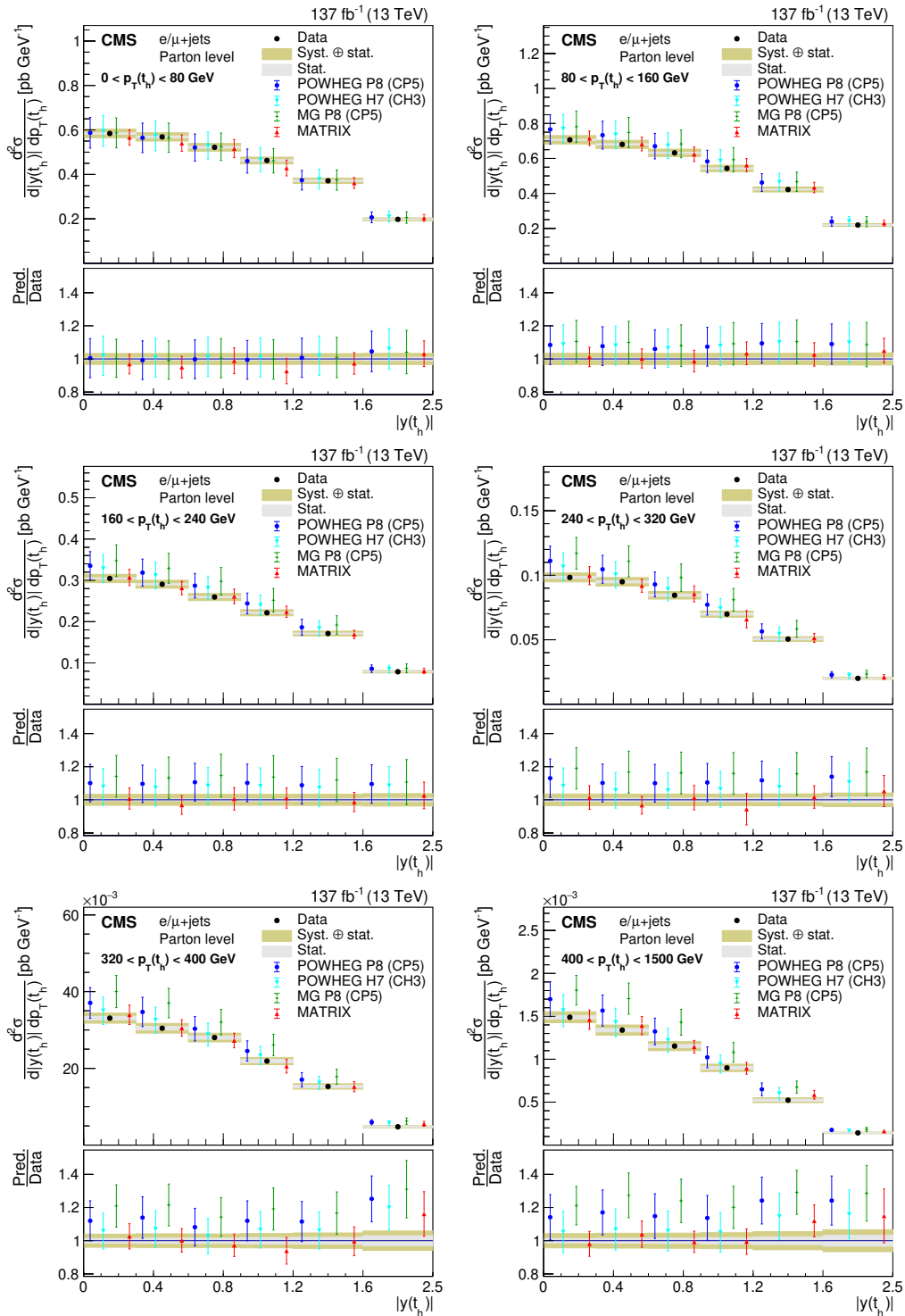


Figure 21: Double-differential cross section at the parton level as a function of $p_T(t_h)$ vs. $|y(t_h)|$. The data are shown as points with gray (yellow) bands indicating the statistical (statistical and systematic) uncertainties. The cross sections are compared to the predictions of POWHEG combined with PYTHIA (P8) or HERWIG (H7), the multiparton simulation MG5_aMC@NLO (MG)+PYTHIA FxFx, and the NNLO QCD calculations obtained with MATRIX. The ratios of the various predictions to the measured cross sections are shown in the lower panels.

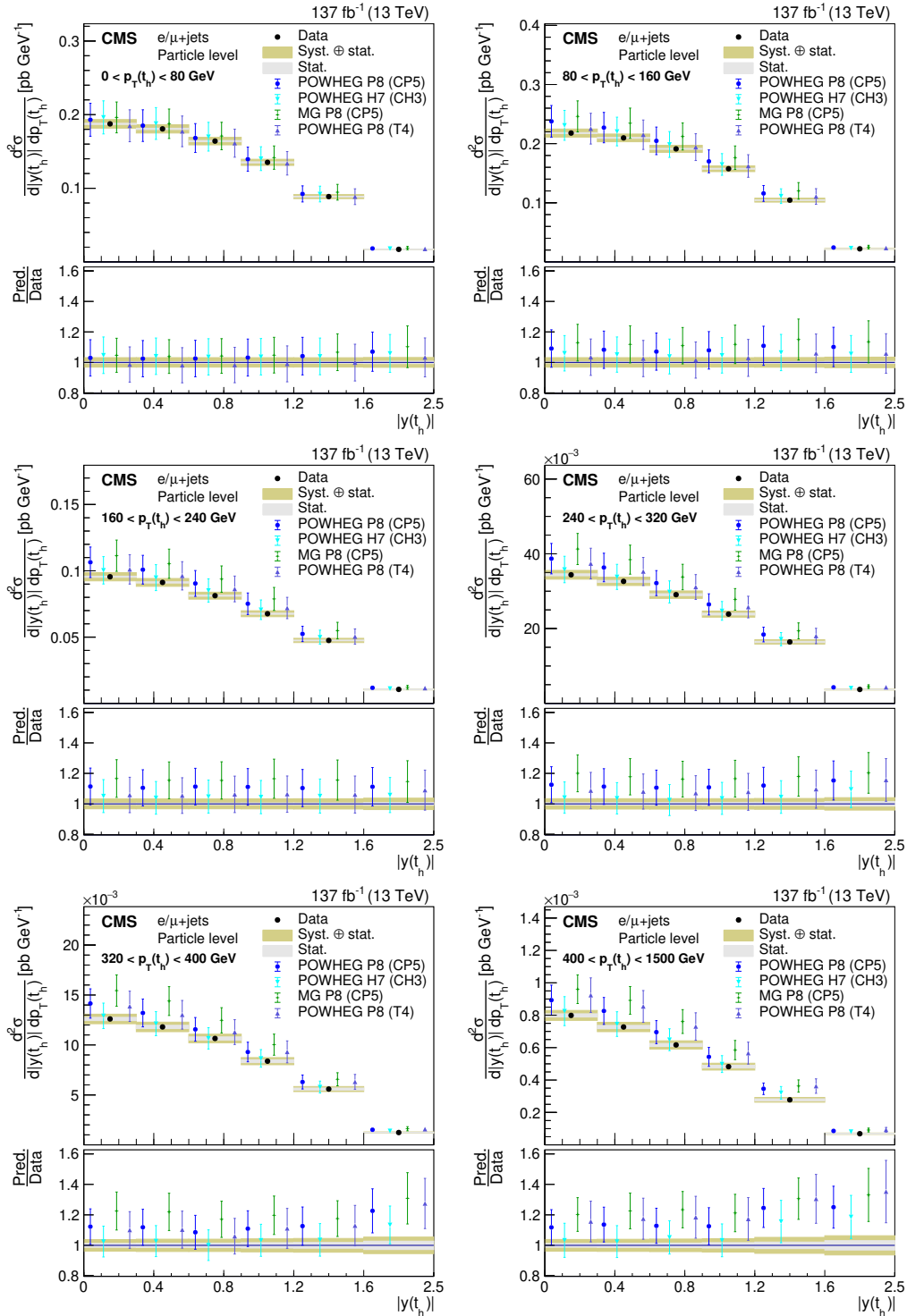


Figure 22: Double-differential cross section at the particle level as a function of $p_T(t_h)$ vs. $|y(t_h)|$. The data are shown as points with gray (yellow) bands indicating the statistical (statistical and systematic) uncertainties. The cross sections are compared to the predictions of POWHEG+PYTHIA (P8) for the CP5 and CUETP8M2T4 (T4) tunes, POWHEG+HERWIG (H7), and the multiparton simulation MG5_aMC@NLO (MG)+PYTHIA. The ratios of the various predictions to the measured cross sections are shown in the lower panels.

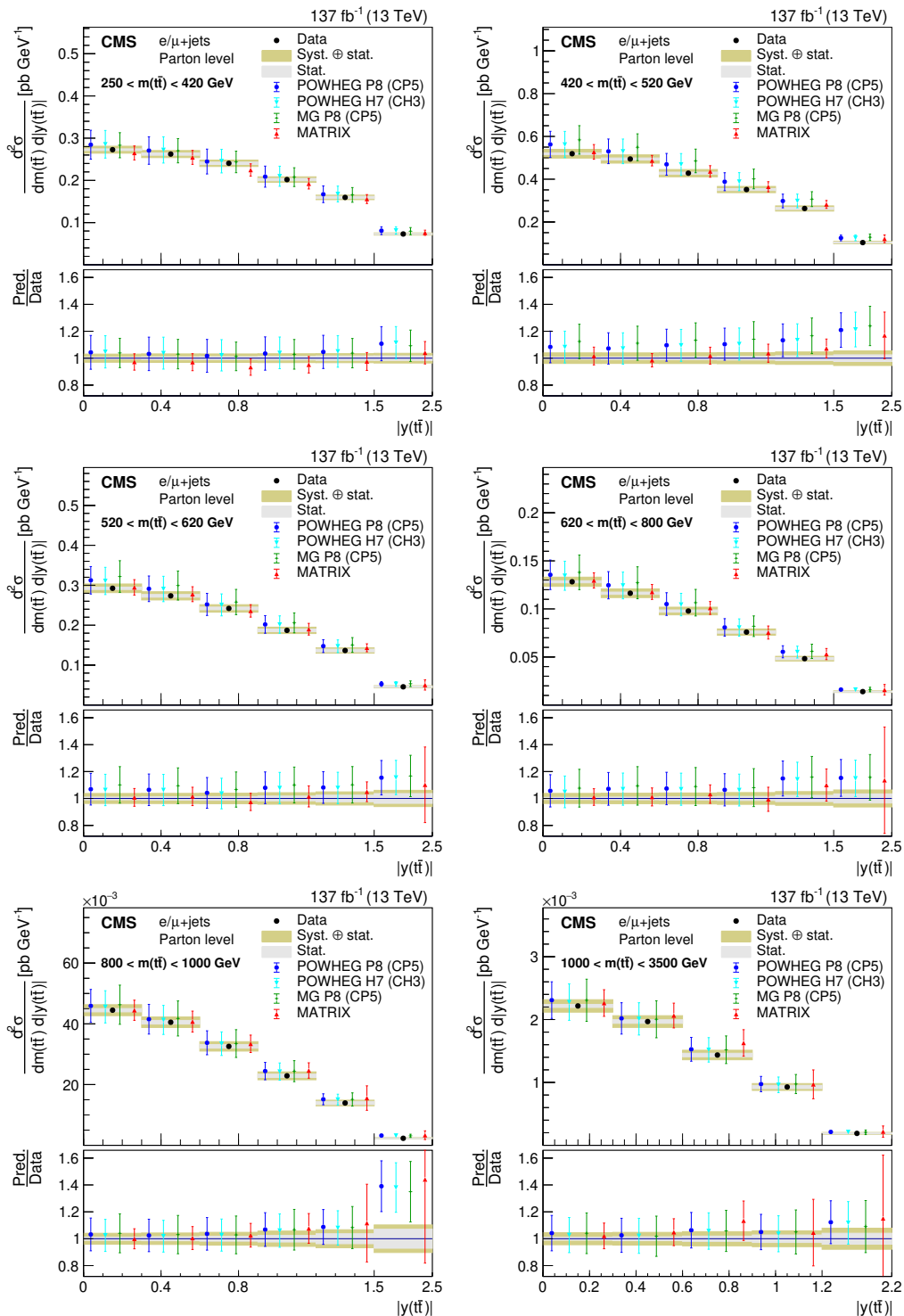


Figure 23: Double-differential cross section at the parton level as a function of $m(t\bar{t})$ vs. $|y(t\bar{t})|$. The data are shown as points with gray (yellow) bands indicating the statistical (statistical and systematic) uncertainties. The cross sections are compared to the predictions of POWHEG combined with PYTHIA (P8) or HERWIG (H7), the multiparton simulation MG5_aMC@NLO (MG)+PYTHIA FxFx, and the NNLO QCD calculations obtained with MATRIX. The ratios of the various predictions to the measured cross sections are shown in the lower panels.

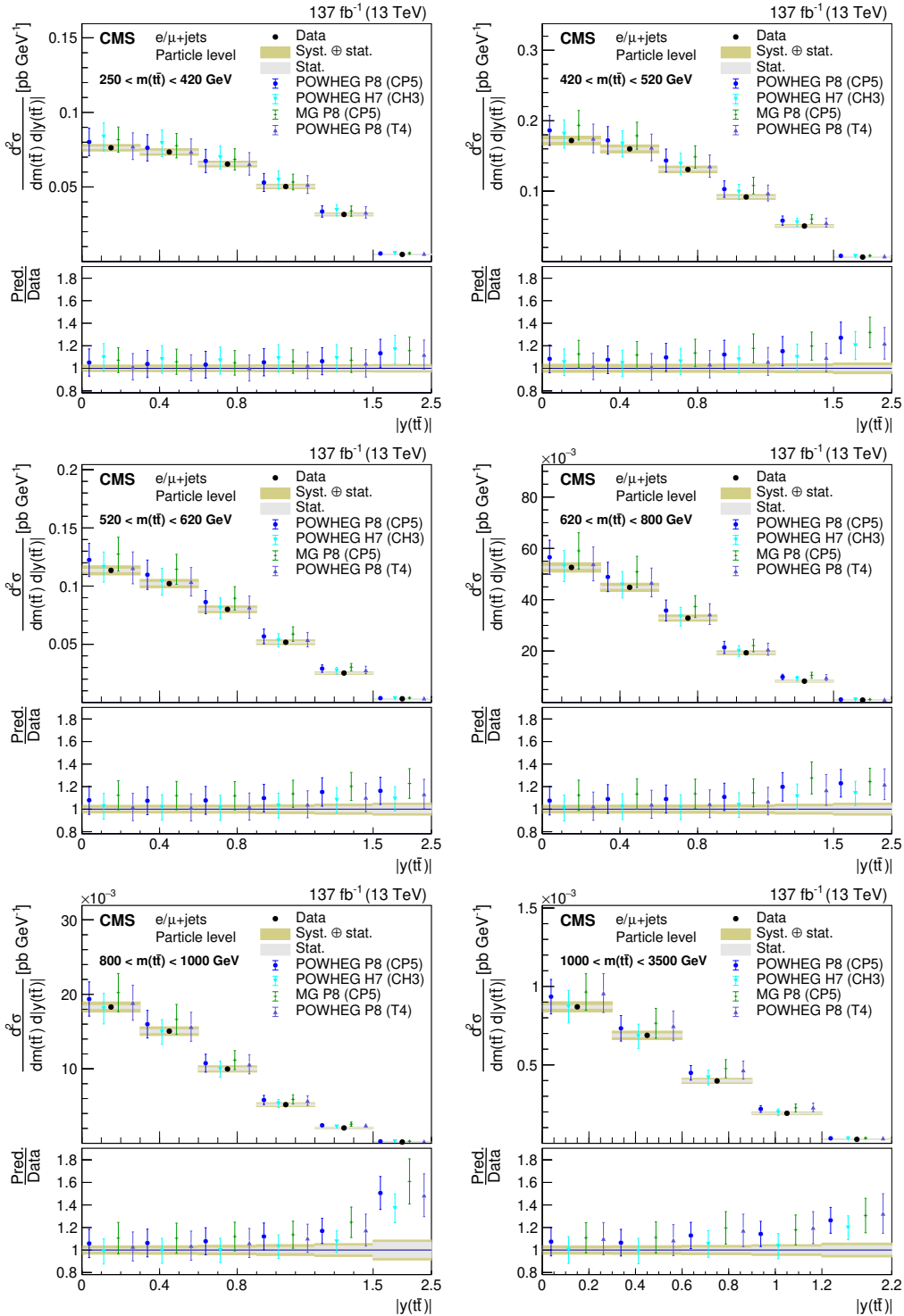


Figure 24: Double-differential cross section at the particle level as a function of $m(t\bar{t})$ vs. $|y(t\bar{t})|$. The data are shown as points with gray (yellow) bands indicating the statistical (statistical and systematic) uncertainties. The cross sections are compared to the predictions of POWHEG+PYTHIA (P8) for the CP5 and CUETP8M2T4 (T4) tunes, POWHEG+HERWIG (H7), and the multiparton simulation MG5_aMC@NLO (MG)+PYTHIA. The ratios of the various predictions to the measured cross sections are shown in the lower panels.

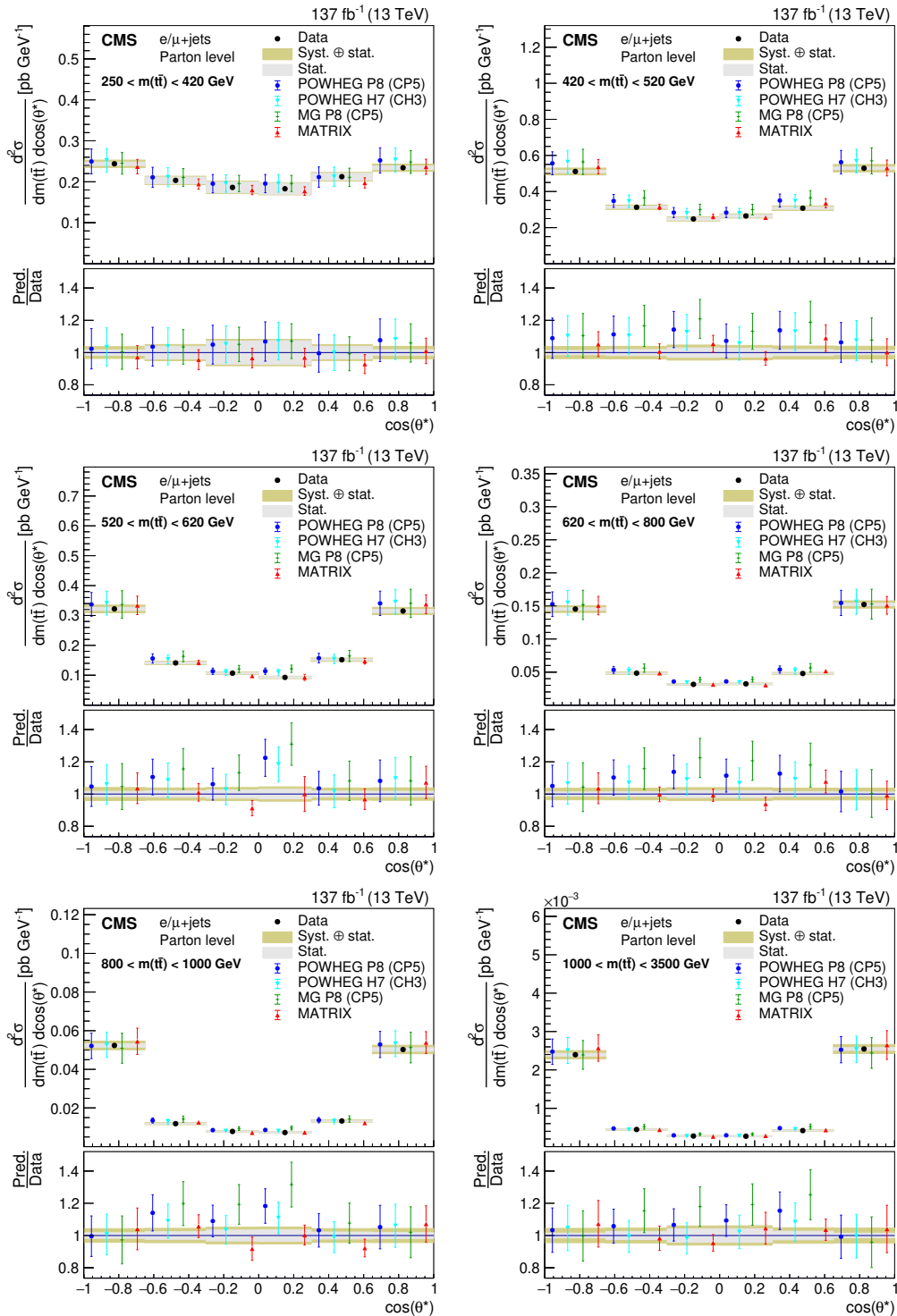


Figure 25: Double-differential cross section at the parton level as a function of $m(\bar{t}t)$ vs. $\cos(\theta^*)$. The data are shown as points with gray (yellow) bands indicating the statistical (statistical and systematic) uncertainties. The cross sections are compared to the predictions of POWHEG combined with PYTHIA (P8) or HERWIG (H7), the multiparton simulation MG5_aMC@NLO (MG)+PYTHIA FxFx, and the NNLO QCD calculations obtained with MATRIX. The ratios of the various predictions to the measured cross sections are shown in the lower panels.

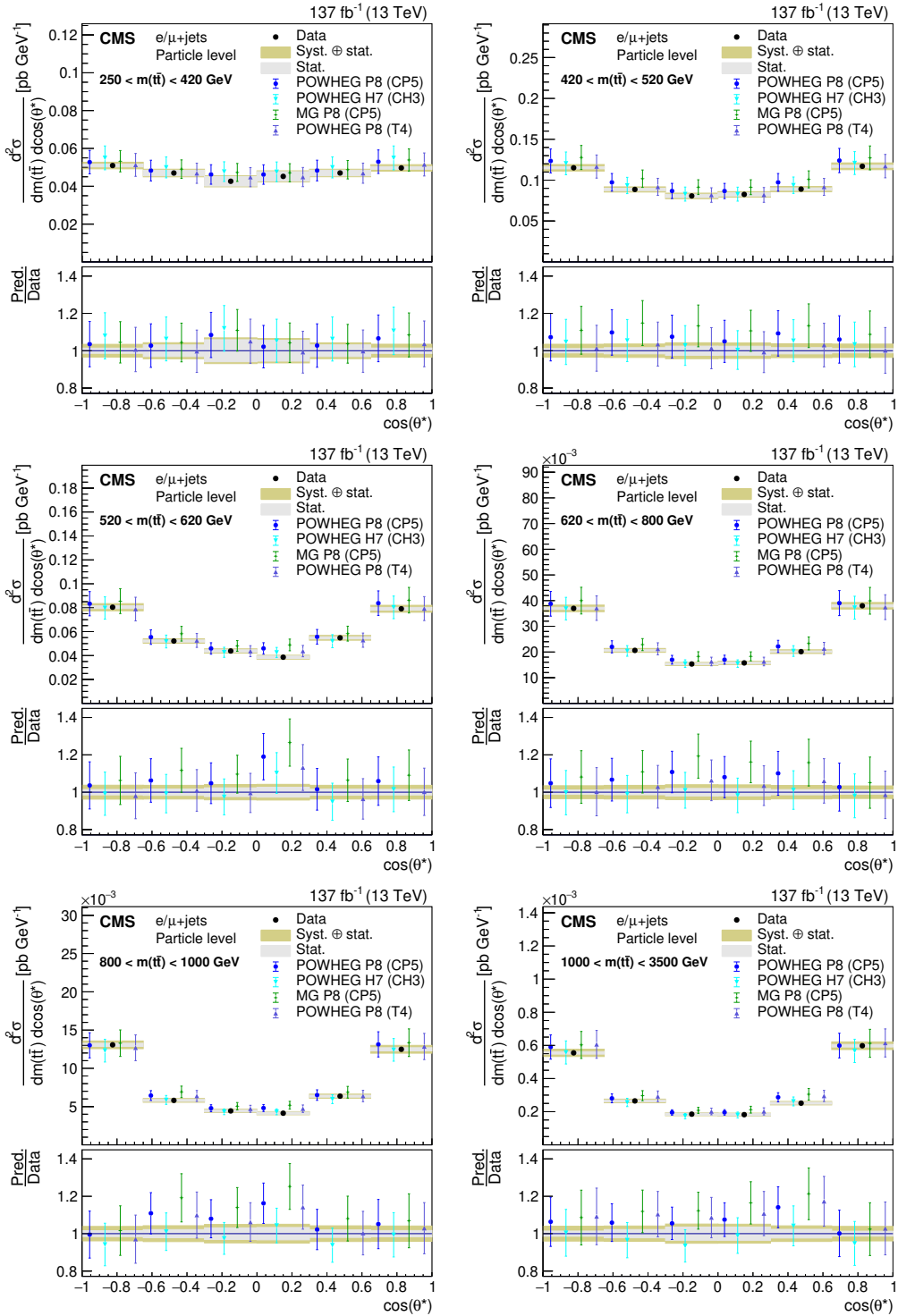


Figure 26: Double-differential cross section at the particle level as a function of $m(t\bar{t})$ vs. $\cos(\theta^*)$. The data are shown as points with gray (yellow) bands indicating the statistical (stat.) and systematic (Syst.) uncertainties. The cross sections are compared to the predictions of POWHEG+PYTHIA (P8) for the CP5 and CUETP8M2T4 (T4) tunes, POWHEG+HERWIG (H7), and the multiparton simulation MG5_aMC@NLO (MG)+PYTHIA. The ratios of the various predictions to the measured cross sections are shown in the lower panels.

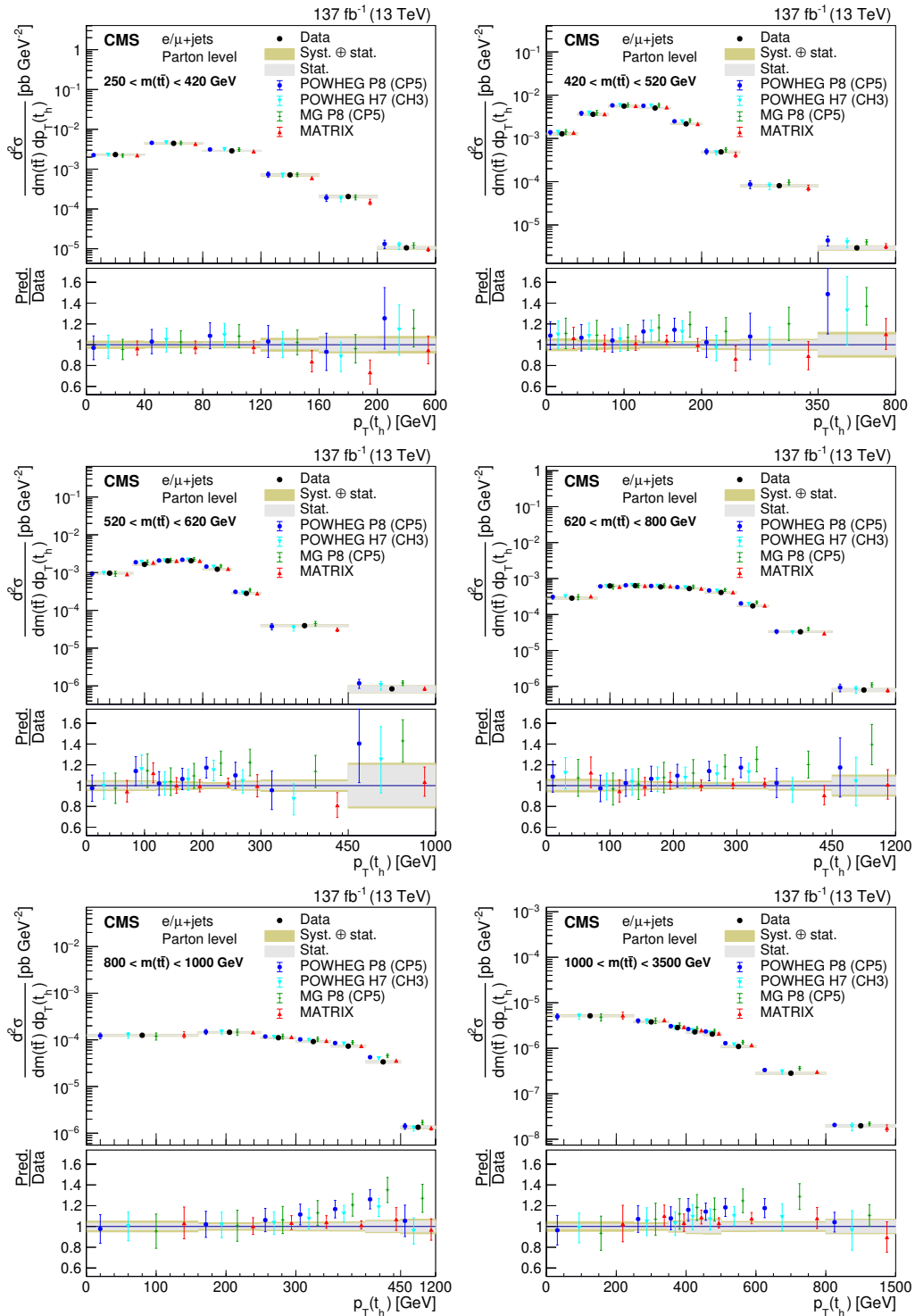


Figure 27: Double-differential cross section at the parton level as a function of $m(t\bar{t})$ vs. $p_T(t_h)$. The data are shown as points with gray (yellow) bands indicating the statistical (statistical and systematic) uncertainties. The cross sections are compared to the predictions of POWHEG combined with PYTHIA (P8) or HERWIG (H7), the multiparton simulation MG5_aMC@NLO (MG)+PYTHIA FxFx, and the NNLO QCD calculations obtained with MATRIX. The ratios of the various predictions to the measured cross sections are shown in the lower panels.

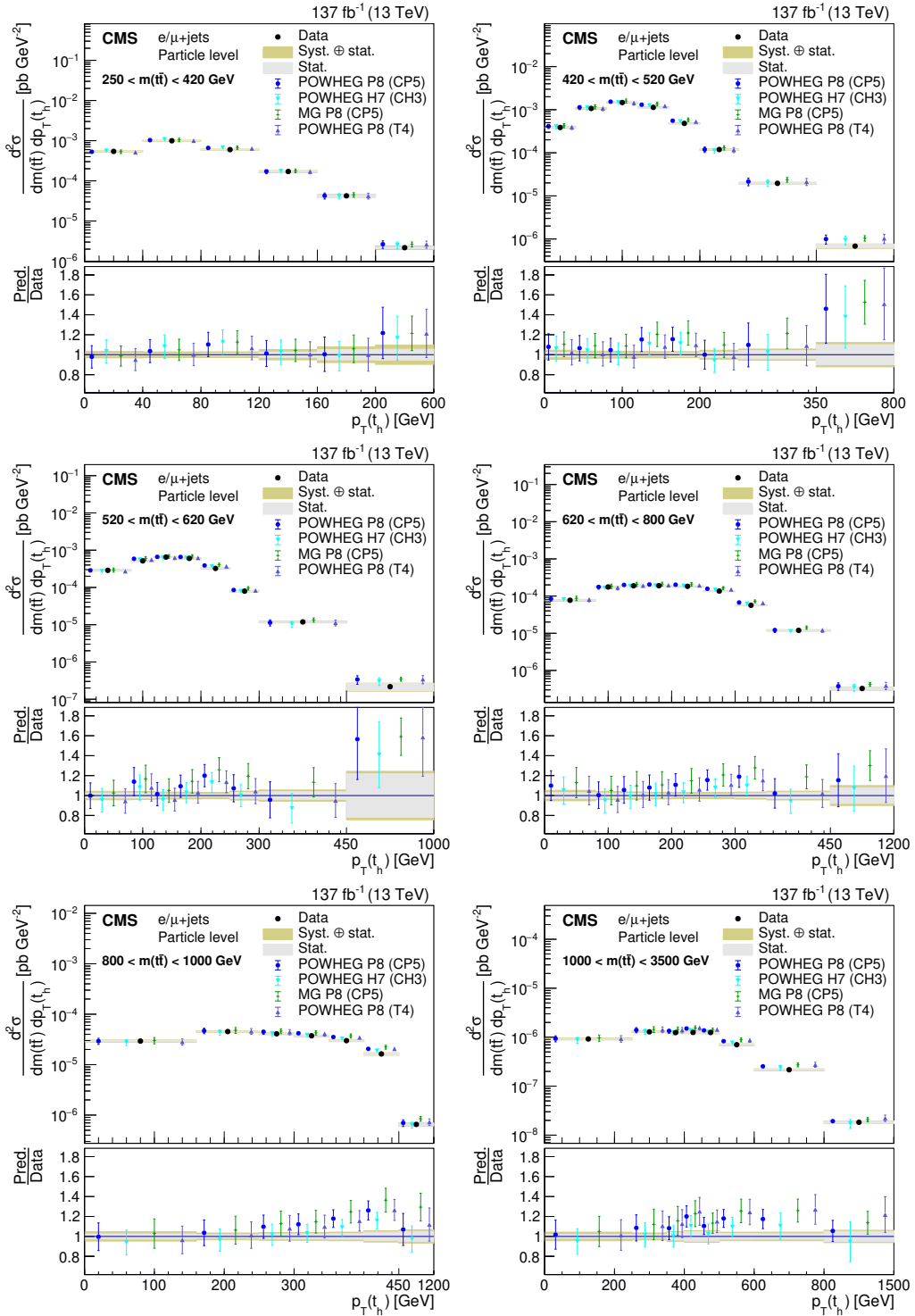


Figure 28: Double-differential cross section at the particle level as a function of $m(t\bar{t})$ vs. $p_T(t_h)$. The data are shown as points with gray (yellow) bands indicating the statistical (statistical and systematic) uncertainties. The cross sections are compared to the predictions of POWHEG+PYTHIA (P8) for the CP5 and CUETP8M2T4 (T4) tunes, POWHEG+HERWIG (H7), and the multiparton simulation MG5_aMC@NLO (MG)+PYTHIA. The ratios of the various predictions to the measured cross sections are shown in the lower panels.

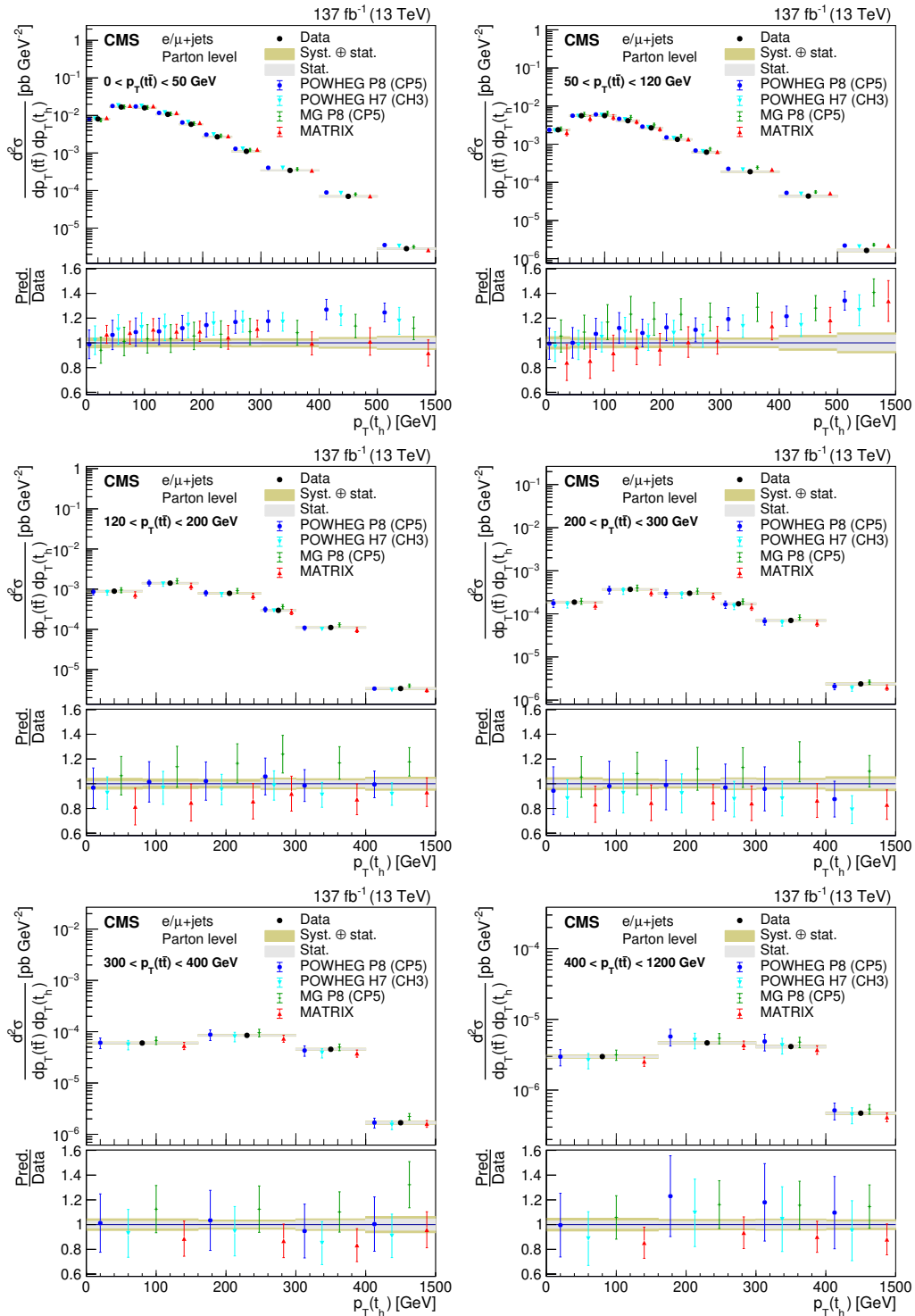


Figure 29: Double-differential cross section at the parton level as a function of $p_T(\bar{t}t)$ vs. $p_T(t_h)$. The data are shown as points with gray (yellow) bands indicating the statistical (statistical and systematic) uncertainties. The cross sections are compared to the predictions of POWHEG combined with PYTHIA (P8) or HERWIG (H7), the multiparton simulation MG5_aMC@NLO (MG)+PYTHIA FxFx, and the NNLO QCD calculations obtained with MATRIX. The ratios of the various predictions to the measured cross sections are shown in the lower panels.

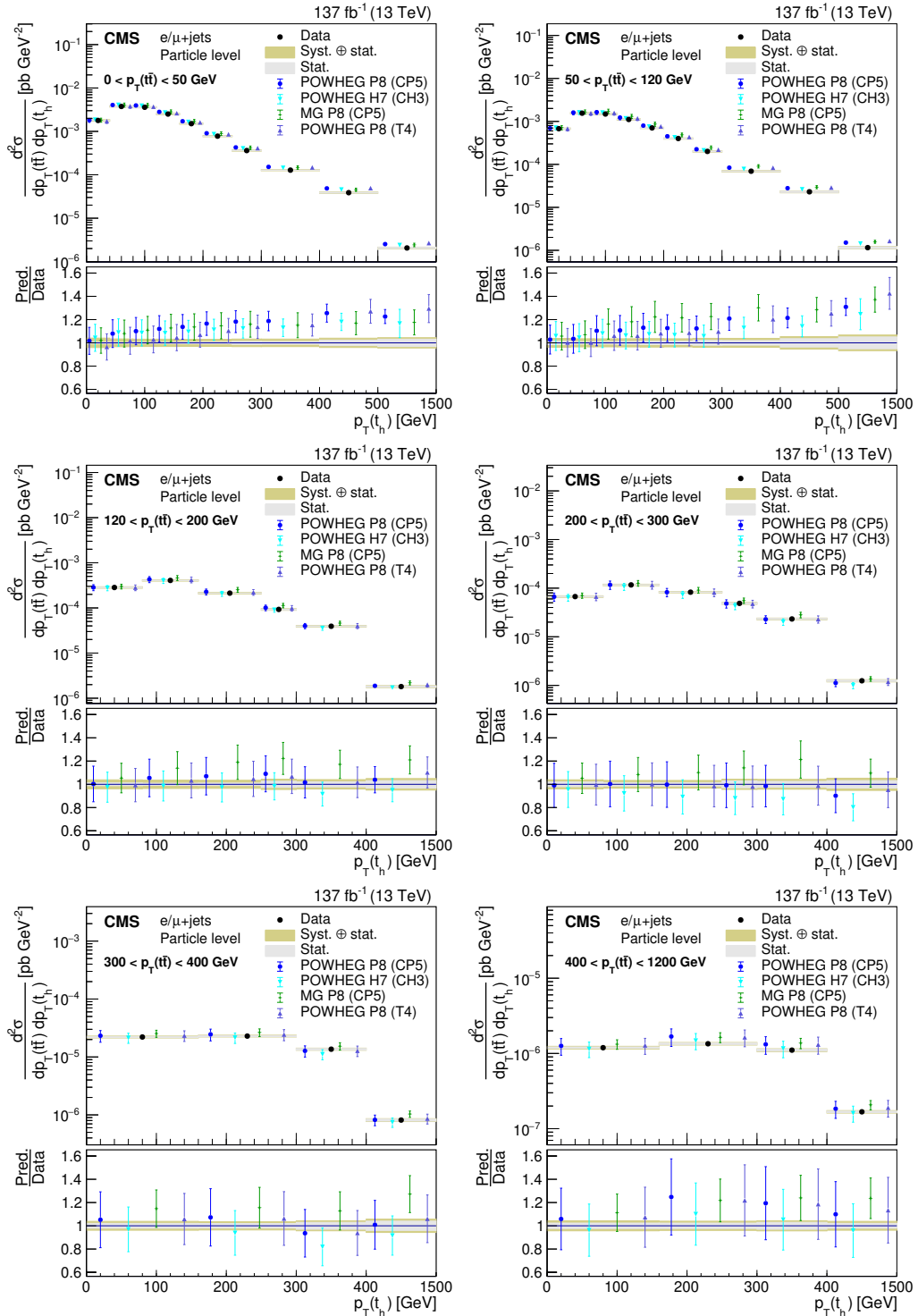


Figure 30: Double-differential cross section at the particle level as a function of $p_T(\bar{t}\bar{t})$ vs. $p_T(t_h)$. The data are shown as points with gray (yellow) bands indicating the statistical (statistical and systematic) uncertainties. The cross sections are compared to the predictions of POWHEG+PYTHIA (P8) for the CP5 and CUETP8M2T4 (T4) tunes, POWHEG+HERWIG (H7), and the multiparton simulation MG5_aMC@NLO (MG)+PYTHIA. The ratios of the various predictions to the measured cross sections are shown in the lower panels.

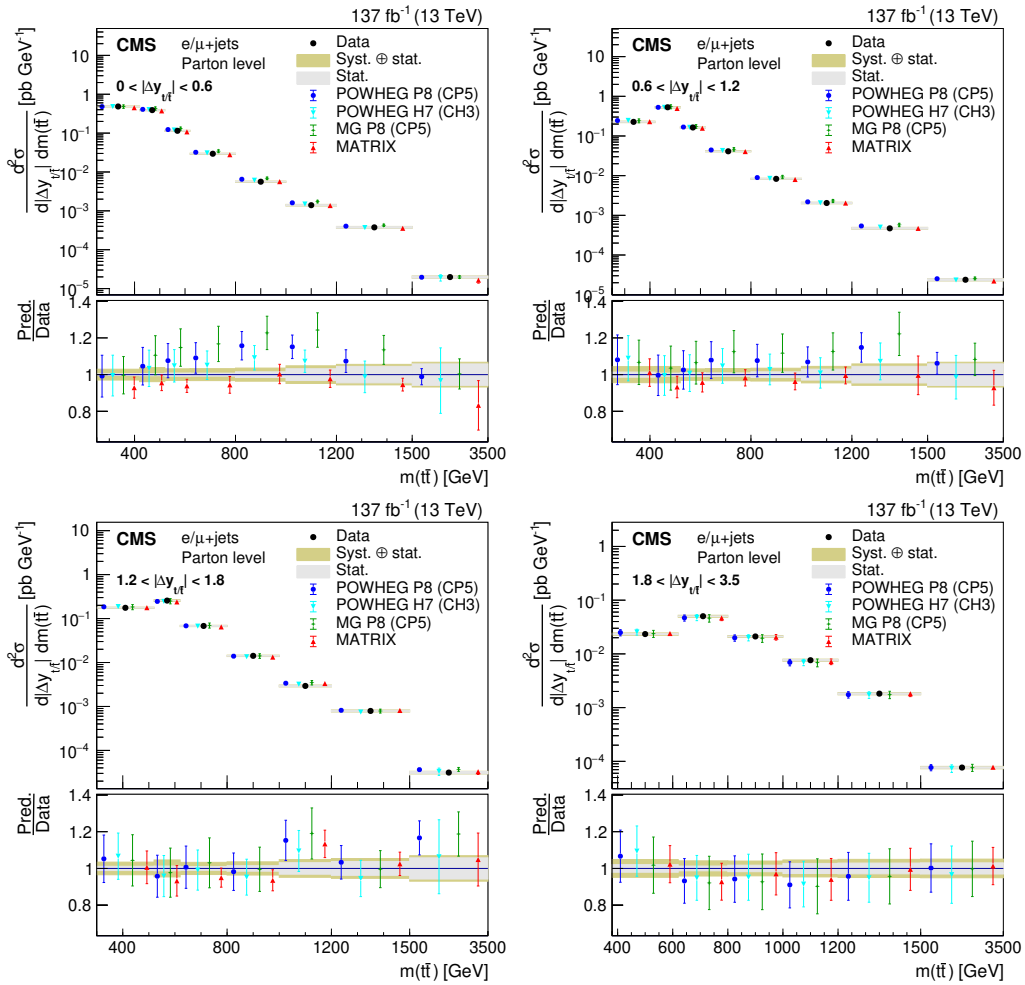


Figure 31: Double-differential cross section at the parton level as a function of $|\Delta y_{t/\bar{t}}|$ vs. $m(t\bar{t})$. The data are shown as points with gray (yellow) bands indicating the statistical (statistical and systematic) uncertainties. The cross sections are compared to the predictions of POWHEG combined with PYTHIA (P8) or HERWIG (H7), the multiparton simulation MG5_aMC@NLO (MG)+PYTHIA FxFx, and the NNLO QCD calculations obtained with MATRIX. The ratios of the various predictions to the measured cross sections are shown in the lower panels.

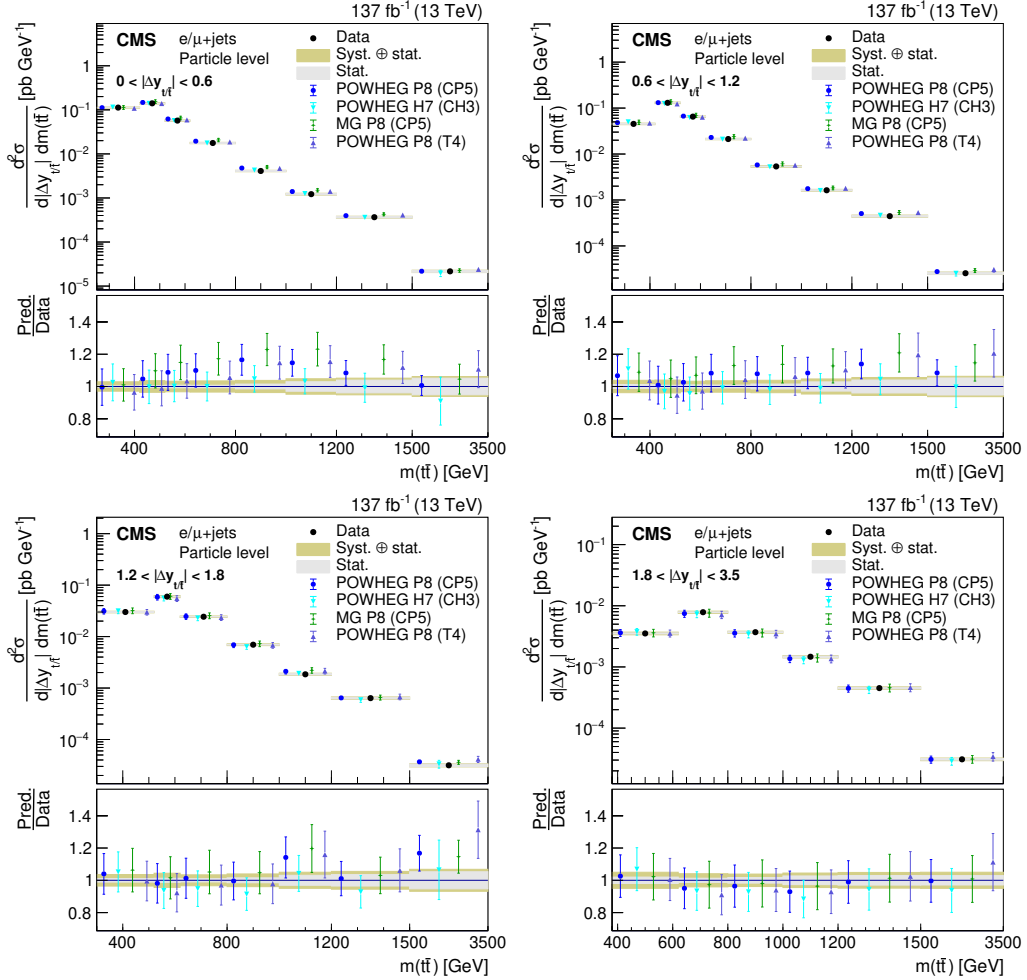


Figure 32: Double-differential cross section at the particle level as a function of $|\Delta y_{t/\bar{t}}|$ vs. $m(t\bar{t})$. The data are shown as points with gray (yellow) bands indicating the statistical (statistical and systematic) uncertainties. The cross sections are compared to the predictions of POWHEG+PYTHIA (P8) for the CP5 and CUETP8M2T4 (T4) tunes, POWHEG+HERWIG (H7), and the multiparton simulation MG5_aMC@NLO (MG)+PYTHIA. The ratios of the various predictions to the measured cross sections are shown in the lower panels.

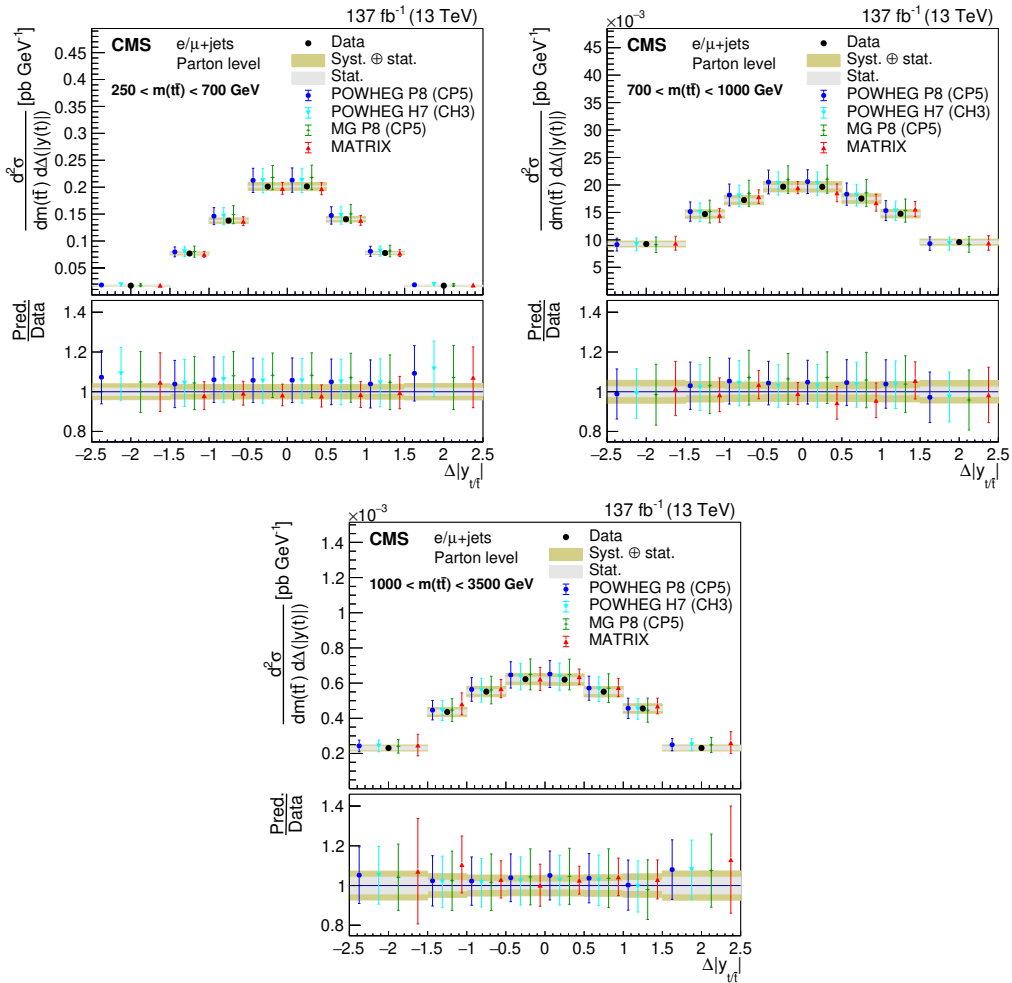


Figure 33: Double-differential cross section at the parton level as a function of $m(t\bar{t})$ vs. $\Delta|y_{t/\bar{t}}|$. The data are shown as points with gray (yellow) bands indicating the statistical (statistical and systematic) uncertainties. The cross sections are compared to the predictions of POWHEG combined with PYTHIA (P8) or HERWIG (H7), the multiparton simulation MG5_aMC@NLO (MG)+PYTHIA FxFx, and the NNLO QCD calculations obtained with MATRIX. The ratios of the various predictions to the measured cross sections are shown in the lower panels.

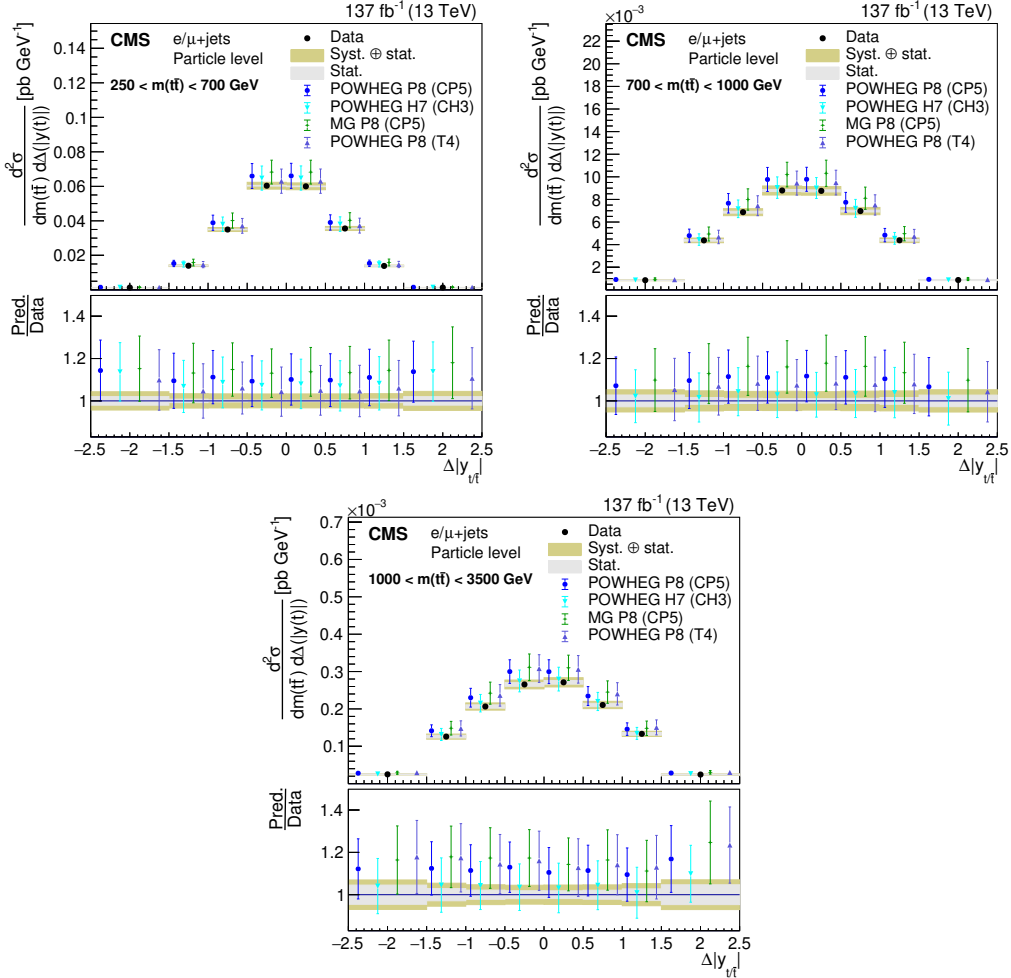


Figure 34: Double-differential cross section at the particle level as a function of $m(t\bar{t})$ vs. $\Delta|y_{t/\bar{t}}|$. The data are shown as points with gray (yellow) bands indicating the statistical (statistical and systematic) uncertainties. The cross sections are compared to the predictions of POWHEG+PYTHIA (P8) for the CP5 and CUETP8M2T4 (T4) tunes, POWHEG+HERWIG (H7), and the multiparton simulation MG5_aMC@NLO (MG)+PYTHIA. The ratios of the various predictions to the measured cross sections are shown in the lower panels.

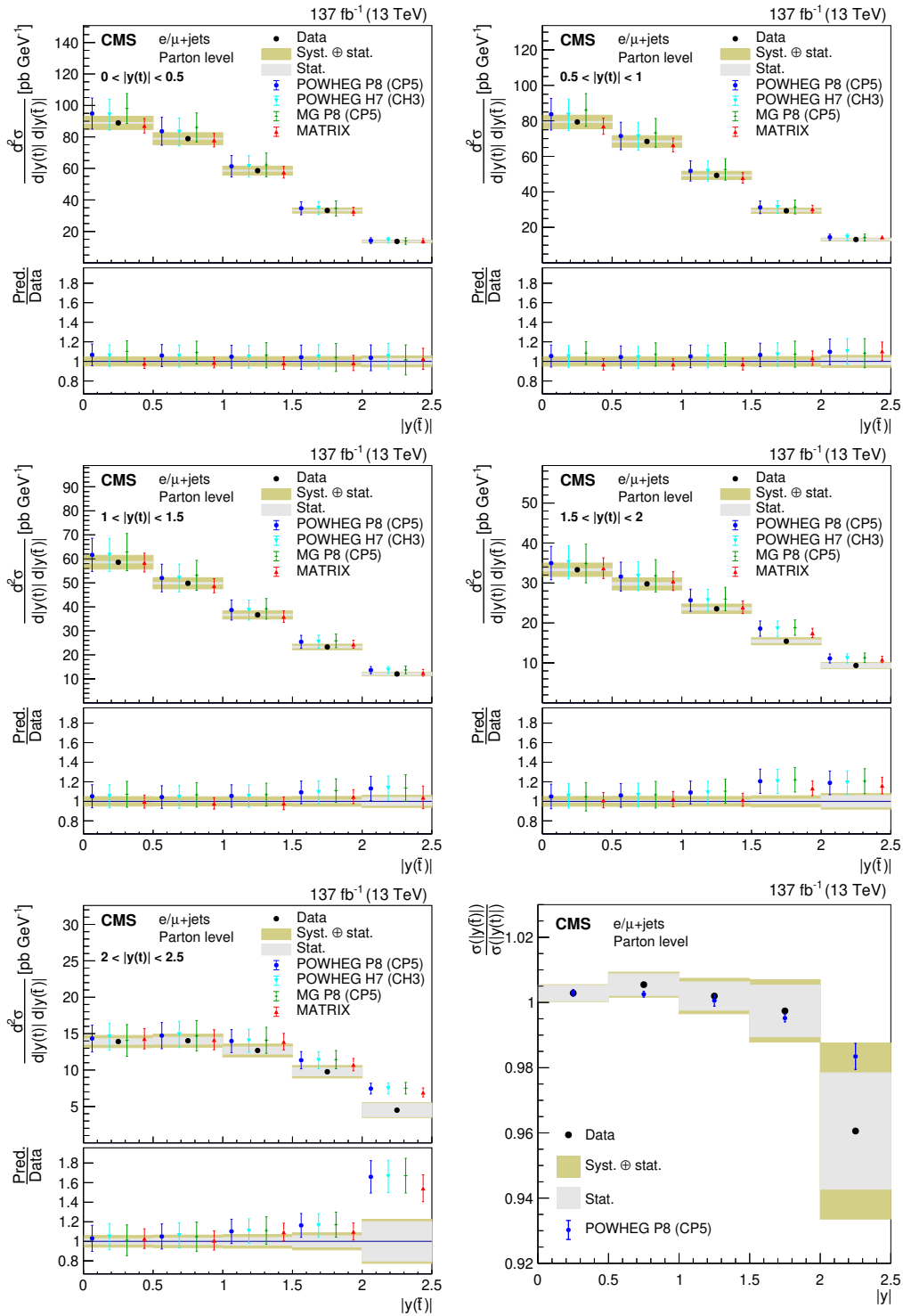


Figure 35: Double-differential cross section at the parton level as a function of $|y(t)|$ vs. $|y(\bar{t})|$. The data are shown as points with gray (yellow) bands indicating the statistical (statistical and systematic) uncertainties. The cross sections are compared to the predictions of POWHEG combined with PYTHIA (P8) or HERWIG (H7), the multiparton simulation MG5_aMC@NLO (MG)+PYTHIA FxFx, and the NNLO QCD calculations obtained with MATRIX. The ratios of the various predictions to the measured cross sections are shown in the lower panels. Lower right: ratio of $|y(\bar{t})|/|y(t)|$.

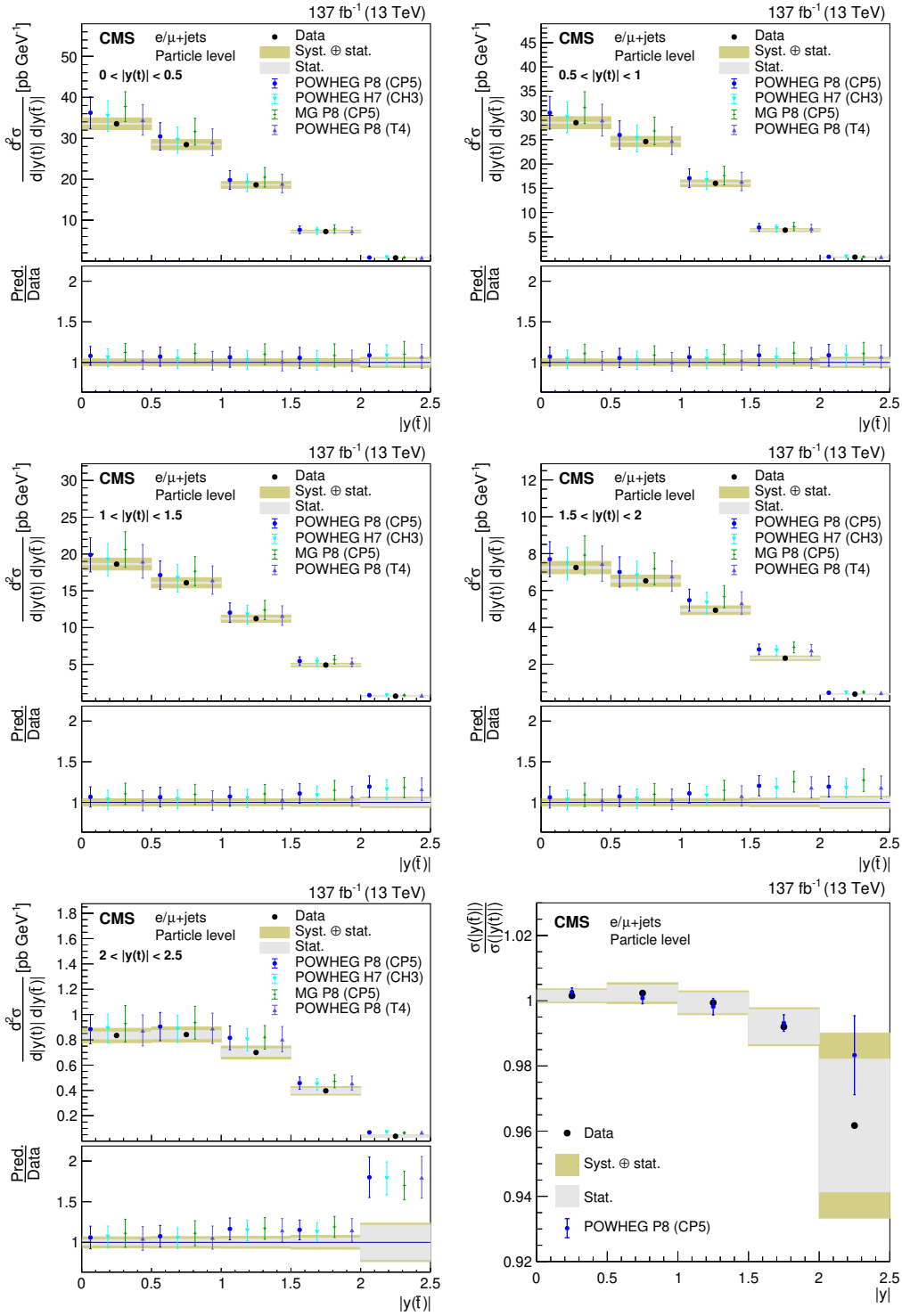


Figure 36: Double-differential cross section at the particle level as a function of $|y(t)|$ vs. $|y(\bar{t})|$. The data are shown as points with gray (yellow) bands indicating the statistical (statistical and systematic) uncertainties. The cross sections are compared to the predictions of POWHEG+PYTHIA (P8) for the CP5 and CUETP8M2T4 (T4) tunes, POWHEG+HERWIG (H7), and the multiparton simulation MG5_aMC@NLO (MG)+PYTHIA. The ratios of the various predictions to the measured cross sections are shown in the lower panels. Lower right: ratio of $|y(\bar{t})|/|y(t)|$

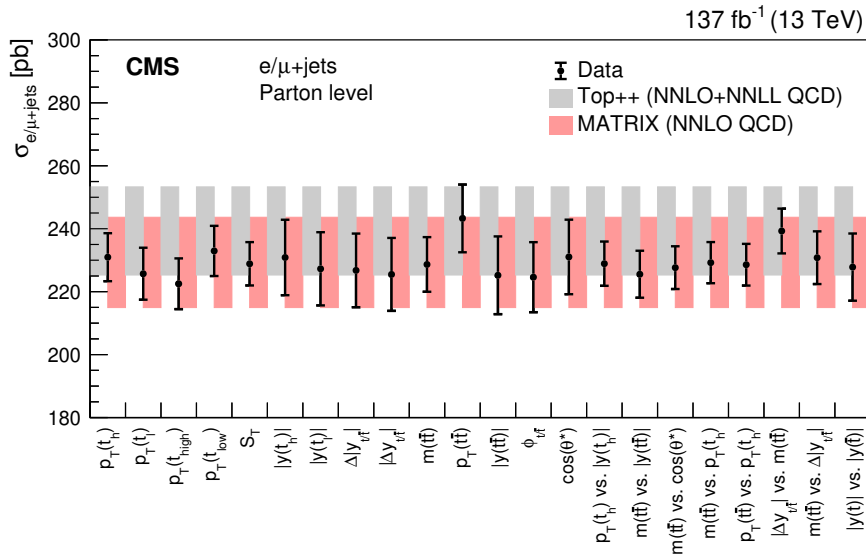


Figure 37: Measurements of the $t\bar{t}$ production cross sections $\sigma_{e/\mu+jets}$ with their total uncertainty obtained as the sum of the cross sections in all bins of a distribution as a function of the kinematic variable used in the determination. The results are compared to the TOP++ and the MATRIX predictions with their corresponding uncertainties.

The sum of the cross sections in all bins of a distribution at the parton level corresponds to the $t\bar{t}$ production cross section in the $e/\mu+jets$ channel. The cross sections outside the measured ranges are predicted from the simulation to be negligibly small. Only for the rapidity-related distributions there is a contribution of up to 3% estimated from the simulation. These corrections are taken into account to determine the different measurements of the total cross section shown in Fig. 37.

All cross section values are similar, although it is difficult to judge the degree of agreement because they do not represent independent measurements since several of the observables are strongly correlated. We choose for our final result the cross section obtained from the measurement of $m(t\bar{t})$ vs. $\cos(\theta^*)$. According to the simulation, this is expected to be the most precise measurement because its response matrix is little affected by systematic uncertainties, and the measurement can most effectively constrain those uncertainties. This expectation is confirmed and we find a value of

$$\sigma_{e/\mu+jets} = 227.6 \pm 6.8 \text{ pb.} \quad (9)$$

Only the measurement of $m(t\bar{t})$ vs. $p_T(t_h)$ has a marginally smaller uncertainty in data. With a branching fraction of $(28.77 \pm 0.32)\%$ [50] for the decay of $t\bar{t}$ to $e/\mu+jets$, the total $t\bar{t}$ production cross section becomes

$$\sigma_{t\bar{t}} = 791 \pm 25 \text{ pb.} \quad (10)$$

When breaking down the uncertainty into different sources, we find

$$\sigma_{t\bar{t}} = 791 \pm 1 \text{ (stat)} \pm 21 \text{ (syst)} \pm 14 \text{ (lumi)} \text{ pb,} \quad (11)$$

where the last uncertainty comes from that in the integrated luminosity.

All individual sources of systematic uncertainty and their values are given in Table 1. This result is in good agreement with the SM expectation of 797^{+39}_{-51} (scale) ± 39 (PDF) pb obtained with MATRIX, and 832^{+40}_{-46} pb obtained with TOP++ [38], as discussed in Section 2.

Table 1: The sources of systematic uncertainty and their absolute and relative values in the measurement of $\sigma_{t\bar{t}}$.

Source	Uncertainty	
	[pb]	[%]
Jet energy	11	1.38
Branching fraction	8.8	1.11
Lepton	7.8	0.98
NNLO	7.6	0.96
b tagging	7.0	0.88
Sim. event count	6.5	0.82
Background	6.1	0.77
CR model	5.5	0.69
Jet energy resolution	3.4	0.43
Scales μ_R, μ_F	3.2	0.41
Initial-state PS scale	3.2	0.40
Final-state PS scale	2.7	0.34
Subjet energy	2.4	0.31
b mistagging	2.2	0.28
UE tune	2.2	0.27
m_t	2.1	0.26
PDF	1.9	0.25
h_{damp}	1.5	0.19
L1 trigger	0.5	0.07
Pileup	0.4	0.05
Total syst.	21	2.66
Total stat.	0.6	0.07
Int. luminosity	14	1.75

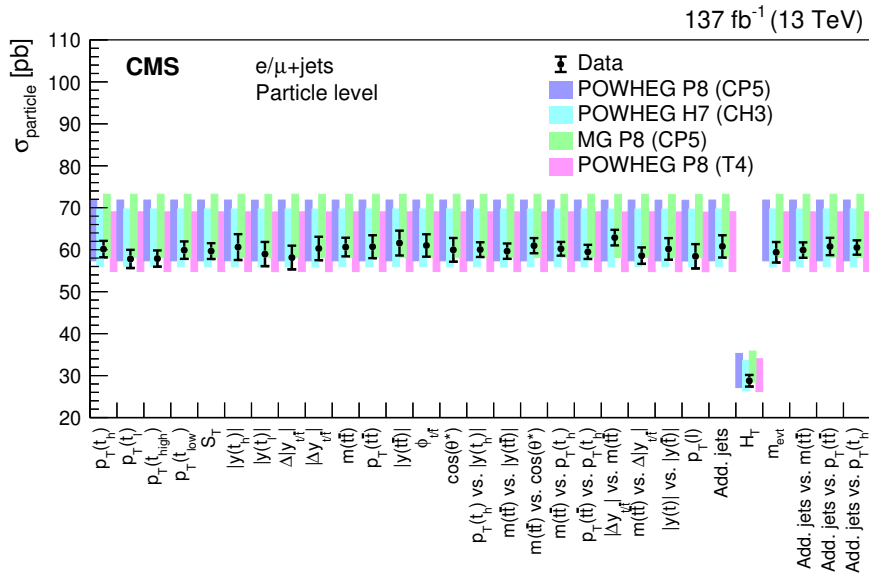


Figure 38: Measurements of the $t\bar{t}$ production cross sections σ_{particle} at the particle level and their total uncertainties as a function of the kinematic variable used in the determination. The results are compared to the predictions of POWHEG+PYTHIA (P8) for the CP5 and CUETP8M2T4 (T4) tunes, POWHEG+HERWIG (H7), and the multiparton simulation MG5_aMC@NLO (MG)+PYTHIA.

By adding the cross sections in all bins of a distribution at the particle level, the inclusive cross section σ_{particle} is obtained. The exception is the cross section at the parton level as a function of H_T , where events with zero additional jets do not contribute. This leads to a significantly smaller cross section. As shown in Fig. 38, the σ_{particle} values are similar for all the other distributions. The simulations predict that the cross section the cross section obtained from the measurement of $m(t\bar{t})$ vs. $\cos(\theta^*)$ to be the most precise. This is confirmed in data, and the measured value is

$$\sigma_{\text{particle}} = 61.0 \pm 1.8 \text{ pb.} \quad (12)$$

The individual sources of systematic uncertainty in this measurement and their values are given in Table 2.

Table 2: The sources of systematic uncertainty and their absolute and relative values in the measurement of σ_{particle} .

Source	Uncertainty	
	[pb]	[%]
Jet energy	0.85	1.40
b tagging	0.67	1.11
Sim. event count	0.63	1.03
Lepton	0.59	0.96
Background	0.47	0.78
CR model	0.44	0.72
NNLO	0.32	0.52
m_t	0.27	0.45
Scales μ_R, μ_F	0.27	0.45
Jet energy resolution	0.19	0.31
b mistagging	0.19	0.31
UE tune	0.18	0.30
PDF	0.15	0.24
Subjet energy	0.12	0.20
Final-state PS scale	0.08	0.13
h_{damp}	0.07	0.11
Pileup	0.05	0.08
L1 trigger	0.05	0.08
Initial-state PS scale	0.03	0.05
Total syst.	1.46	2.39
Total stat.	0.04	0.06
Int. luminosity	1.06	1.74

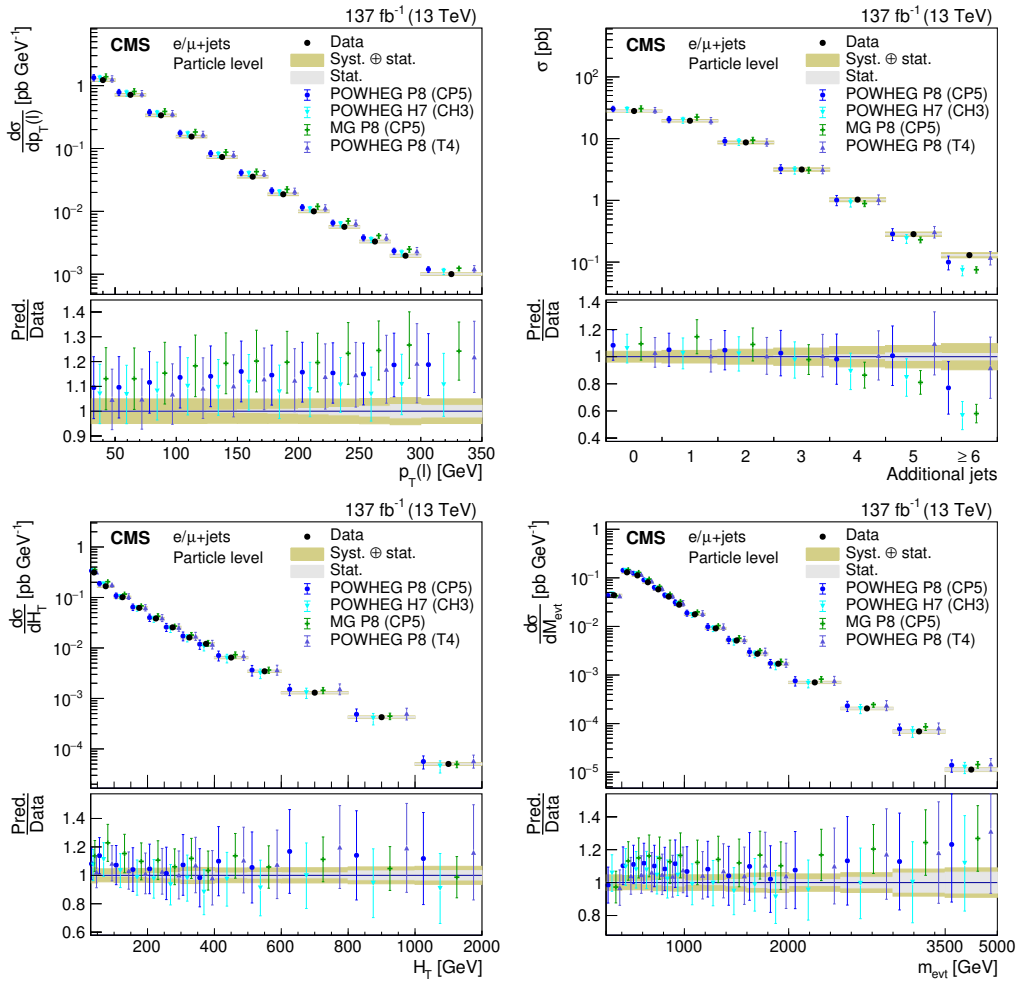


Figure 39: Differential cross sections at the particle level as a function of $p_T(\ell)$, jet multiplicity, H_T , and m_{evt} . The data are shown as points with gray (yellow) bands indicating the statistical (statistical and systematic) uncertainties. The cross sections are compared to the predictions of POWHEG+PYTHIA (P8) for the CP5 and CUETP8M2T4 (T4) tunes, POWHEG+HERWIG (H7), and the multiparton simulation MG5_aMC@NLO (MG)+PYTHIA. The ratios of the various predictions to the measured cross sections are shown in the lower panels.

In Figs. 39–42 the differential cross sections that are only measured at the particle level are shown. Of special note in Fig. 39 is the softer $p_T(\ell)$ spectrum in data, compared to the prediction, a quantity that is not directly affected by the modeling of jets. Also, the number of additional jets with $p_T > 30 \text{ GeV}$ and $|\eta| < 2.4$ is higher in data compared to most of the predictions. Only POWHEG+PYTHIA with the CUETP8M2T4 tune makes a correct prediction of the jet multiplicity. The distributions of H_T and m_{evt} are well described. Figure 40 shows that the measured $p_T(t_h)$ spectrum is only softer than the predictions if there is no or, to a smaller extent, one additional jet. For the higher multiplicities the spectrum is better described. Good agreement between data and predictions is observed for the differential cross sections as a function of $m(t\bar{t})$ and $p_T(t\bar{t})$ measured for different numbers of additional jets, as given in Figs. 41 and 42, respectively. In Appendix A, all the measured differential cross sections are presented normalized to unity.

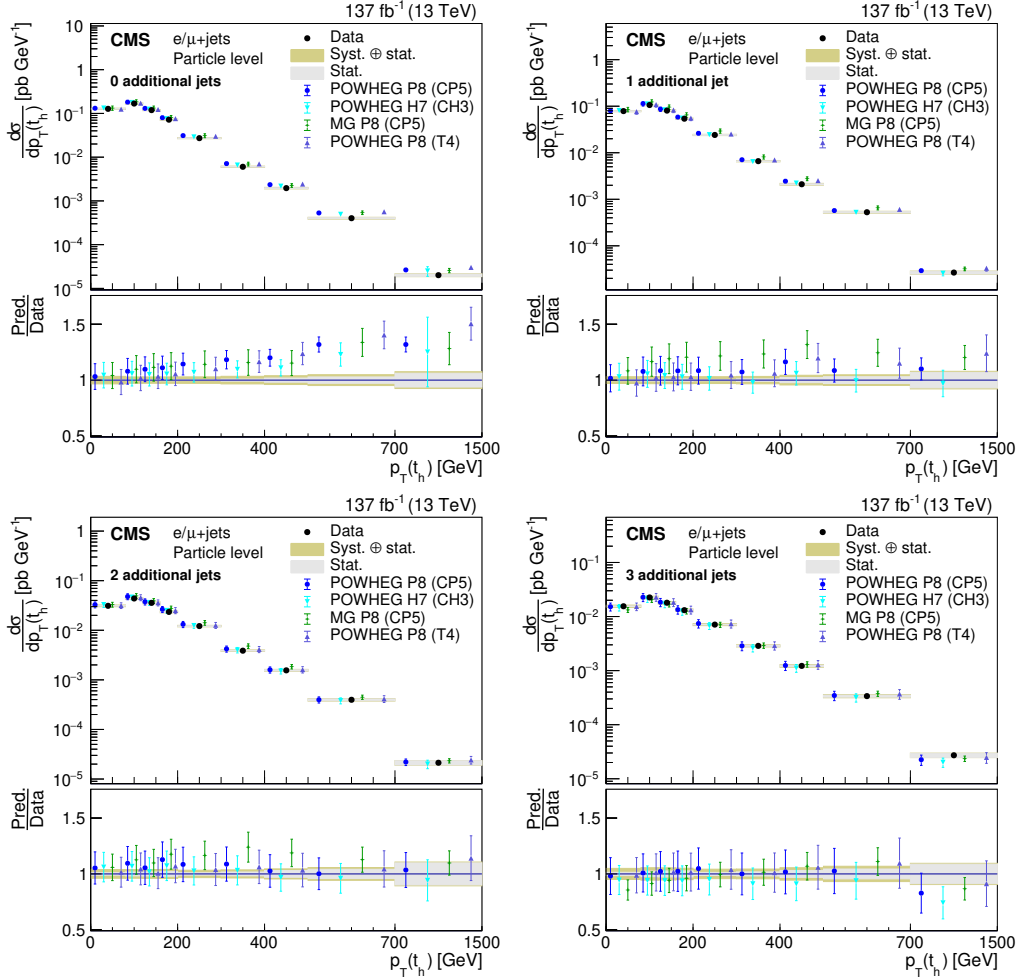


Figure 40: Differential cross section at the particle level as a function of $p_T(t_h)$ in bins of jet multiplicity. The data are shown as points with gray (yellow) bands indicating the statistical (stat.) and systematic (Syst.) uncertainties. The cross sections are compared to the predictions of POWHEG+PYTHIA (P8) for the CP5 and CUETP8M2T4 (T4) tunes, POWHEG+HERWIG (H7), and the multiparton simulation MG5_aMC@NLO (MG)+PYTHIA. The ratios of the various predictions to the measured cross sections are shown in the lower panels.

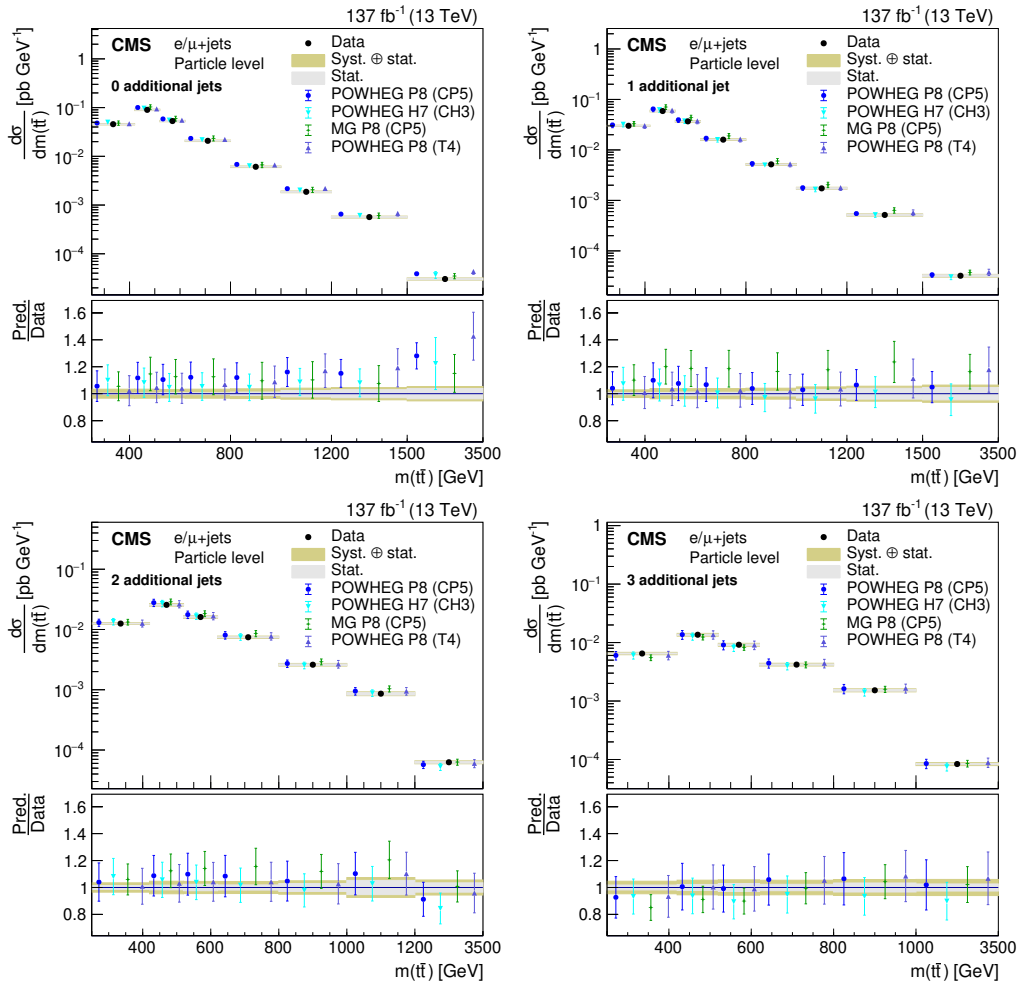


Figure 41: Differential cross section at the particle level as a function of $m(t\bar{t})$ in bins of jet multiplicity. The data are shown as points with gray (yellow) bands indicating the statistical (statistical and systematic) uncertainties. The cross sections are compared to the predictions of POWHEG+PYTHIA (P8) for the CP5 and CUETP8M2T4 (T4) tunes, POWHEG+HERWIG (H7), and the multiparton simulation MG5_aMC@NLO (MG)+PYTHIA. The ratios of the various predictions to the measured cross sections are shown in the lower panels.

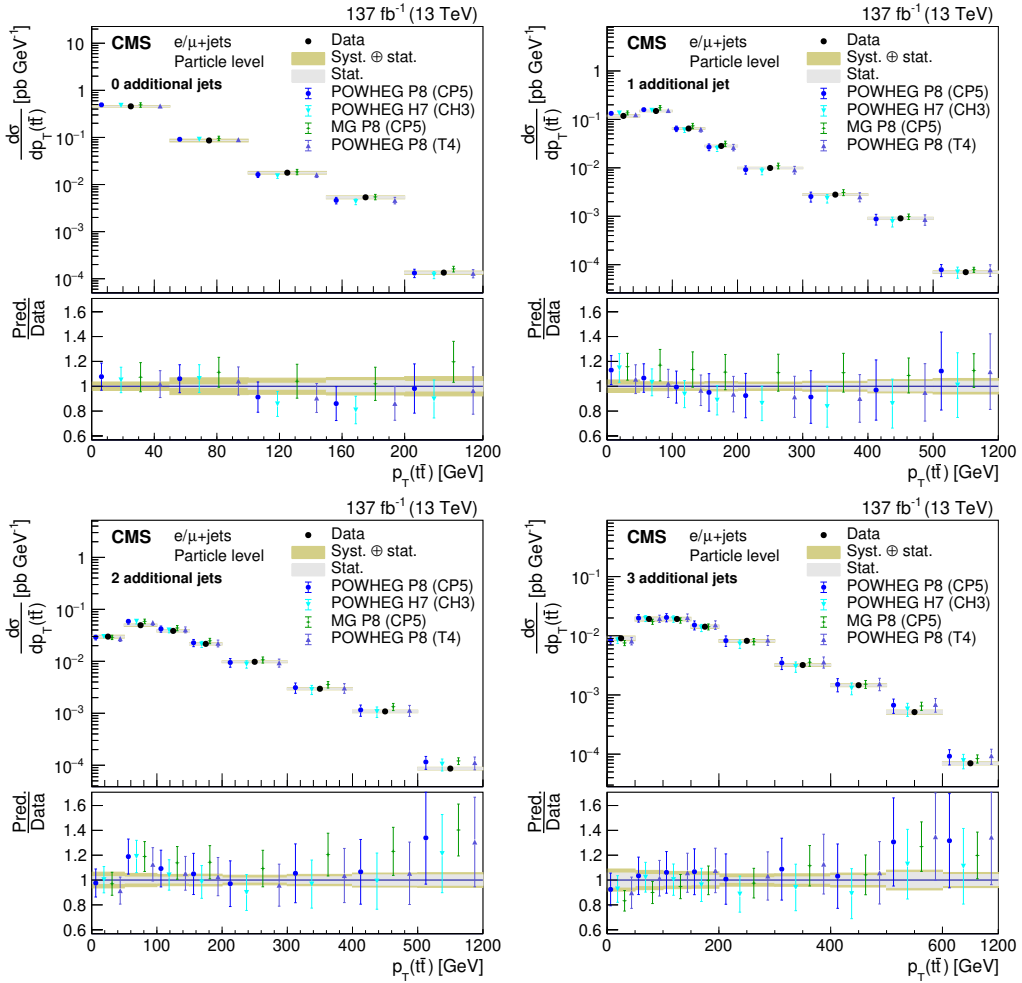


Figure 42: Differential cross section at the particle level as a function of $p_T(t\bar{t})$ in bins of jet multiplicity. The data are shown as points with gray (yellow) bands indicating the statistical (statistical and systematic) uncertainties. The cross sections are compared to the predictions of POWHEG+PYTHIA (P8) for the CP5 and CUETP8M2T4 (T4) tunes, POWHEG+HERWIG (H7), and the multiparton simulation MG5_aMC@NLO (MG)+PYTHIA. The ratios of the various predictions to the measured cross sections are shown in the lower panels.

15 Summary

Measurements of differential and double-differential top quark pair ($t\bar{t}$) production cross sections have been presented as a function of many kinematic properties of the top quarks and the $t\bar{t}$ system at the parton and particle levels, where the latter reduces extrapolations based on theoretical assumptions. In addition, the number of additional jets and kinematic variables in bins of jet multiplicities have been measured at the particle level. The data correspond to an integrated luminosity of 137 fb^{-1} recorded by the CMS experiment at the LHC in proton-proton collisions at $\sqrt{s} = 13 \text{ TeV}$. The $t\bar{t}$ cross sections are measured in the e/μ +jets channels with a single electron or muon and jets in the final state. For the first time the full spectra of differential cross sections are determined using a combination of resolved and boosted $t\bar{t}$ topologies, in which the $t\bar{t}$ decay products can be either identified as separated jets and isolated leptons or as collimated and overlapping jets, respectively. The combination of multiple reconstruction categories provides constraints on the systematic uncertainties and results in a significantly improved precision with respect to previous measurements. For a top quark transverse momentum $p_T < 500 \text{ GeV}$ the uncertainty is reduced by about 50% compared with the previous CMS measurement [17]. The dominant sources of systematic uncertainties are the jet energy scale, integrated luminosity, and $t\bar{t}$ modeling.

Most differential distributions are found to be compatible with the standard model predictions of the event generators POWHEG+PYTHIA, POWHEG+HERWIG, and MG5_aMC@NLO+PYTHIA. In addition, the parton-level cross sections are compared to the next-to-next-to-leading-order quantum chromodynamics calculations obtained with MATRIX that comes with a significantly reduced theoretical uncertainty. A softer top quark p_T spectrum is observed compared to most of the next-to-leading-order predictions. Deviations between the predictions and data are observed when the top quark p_T is measured in bins of the $t\bar{t}$ invariant mass and p_T . The POWHEG+HERWIG and MG5_aMC@NLO+PYTHIA simulations do not give a good description of the observed jet multiplicities and related observables such as the scalar p_T sum of additional jets. The total $t\bar{t}$ production cross section is measured to be

$$\sigma_{t\bar{t}} = 791 \pm 25 \text{ pb.} \quad (13)$$

When breaking down the uncertainty into different sources, we find

$$\sigma_{t\bar{t}} = 791 \pm 1 \text{ (stat)} \pm 21 \text{ (syst)} \pm 14 \text{ (lumi)} \text{ pb,} \quad (14)$$

where the last uncertainty comes from that in the integrated luminosity. The measured value of $\sigma_{t\bar{t}}$ is in good agreement with the standard model expectation.

Acknowledgments

We congratulate our colleagues in the CERN accelerator departments for the excellent performance of the LHC and thank the technical and administrative staffs at CERN and at other CMS institutes for their contributions to the success of the CMS effort. In addition, we gratefully acknowledge the computing centers and personnel of the Worldwide LHC Computing Grid and other centers for delivering so effectively the computing infrastructure essential to our analyses. Finally, we acknowledge the enduring support for the construction and operation of the LHC, the CMS detector, and the supporting computing infrastructure provided by the following funding agencies: the Austrian Federal Ministry of Education, Science and Research and the Austrian Science Fund; the Belgian Fonds de la Recherche Scientifique, and Fonds voor Wetenschappelijk Onderzoek; the Brazilian Funding Agencies (CNPq, CAPES,

FAPERJ, FAPERGS, and FAPESP); the Bulgarian Ministry of Education and Science; CERN; the Chinese Academy of Sciences, Ministry of Science and Technology, and National Natural Science Foundation of China; the Ministerio de Ciencia Tecnología e Innovación (MIN-CIENCIAS), Colombia; the Croatian Ministry of Science, Education and Sport, and the Croatian Science Foundation; the Research and Innovation Foundation, Cyprus; the Secretariat for Higher Education, Science, Technology and Innovation, Ecuador; the Ministry of Education and Research, Estonian Research Council via PRG780, PRG803 and PRG445 and European Regional Development Fund, Estonia; the Academy of Finland, Finnish Ministry of Education and Culture, and Helsinki Institute of Physics; the Institut National de Physique Nucléaire et de Physique des Particules / CNRS, and Commissariat à l'Énergie Atomique et aux Énergies Alternatives / CEA, France; the Bundesministerium für Bildung und Forschung, the Deutsche Forschungsgemeinschaft (DFG), under Germany's Excellence Strategy – EXC 2121 “Quantum Universe” – 390833306, and under project number 400140256 - GRK2497, and Helmholtz-Gemeinschaft Deutscher Forschungszentren, Germany; the General Secretariat for Research and Innovation, Greece; the National Research, Development and Innovation Fund, Hungary; the Department of Atomic Energy and the Department of Science and Technology, India; the Institute for Studies in Theoretical Physics and Mathematics, Iran; the Science Foundation, Ireland; the Istituto Nazionale di Fisica Nucleare, Italy; the Ministry of Science, ICT and Future Planning, and National Research Foundation (NRF), Republic of Korea; the Ministry of Education and Science of the Republic of Latvia; the Lithuanian Academy of Sciences; the Ministry of Education, and University of Malaya (Malaysia); the Ministry of Science of Montenegro; the Mexican Funding Agencies (BUAP, CINVESTAV, CONACYT, LNS, SEP, and UASLP-FAI); the Ministry of Business, Innovation and Employment, New Zealand; the Pakistan Atomic Energy Commission; the Ministry of Science and Higher Education and the National Science Center, Poland; the Fundação para a Ciência e a Tecnologia, Portugal; JINR, Dubna; the Ministry of Education and Science of the Russian Federation, the Federal Agency of Atomic Energy of the Russian Federation, Russian Academy of Sciences, the Russian Foundation for Basic Research, and the National Research Center “Kurchatov Institute”; the Ministry of Education, Science and Technological Development of Serbia; the Secretaría de Estado de Investigación, Desarrollo e Innovación, Programa Consolider-Ingenio 2010, Plan Estatal de Investigación Científica y Técnica y de Innovación 2017–2020, research project IDI-2018-000174 del Principado de Asturias, and Fondo Europeo de Desarrollo Regional, Spain; the Ministry of Science, Technology and Research, Sri Lanka; the Swiss Funding Agencies (ETH Board, ETH Zurich, PSI, SNF, UniZH, Canton Zurich, and SER); the Ministry of Science and Technology, Taipei; the Thailand Center of Excellence in Physics, the Institute for the Promotion of Teaching Science and Technology of Thailand, Special Task Force for Activating Research and the National Science and Technology Development Agency of Thailand; the Scientific and Technical Research Council of Turkey, and Turkish Atomic Energy Authority; the National Academy of Sciences of Ukraine; the Science and Technology Facilities Council, UK; the US Department of Energy, and the US National Science Foundation.

Individuals have received support from the Marie-Curie program and the European Research Council and Horizon 2020 Grant, contract Nos. 675440, 724704, 752730, 758316, 765710, 824093, and COST Action CA16108 (European Union) the Leventis Foundation; the Alfred P. Sloan Foundation; the Alexander von Humboldt Foundation; the Belgian Federal Science Policy Office; the Fonds pour la Formation à la Recherche dans l'Industrie et dans l'Agriculture (FRIA-Belgium); the Agentschap voor Innovatie door Wetenschap en Technologie (IWT-Belgium); the F.R.S.-FNRS and FWO (Belgium) under the “Excellence of Science – EOS” – be.h project n. 30820817; the Beijing Municipal Science & Technology Commission, No. Z191100007219010; the Ministry of Education, Youth and Sports (MEYS) of the Czech Republic; the Lendület (“Mo-

mentum”) Program and the János Bolyai Research Scholarship of the Hungarian Academy of Sciences, the New National Excellence Program ÚNKP, the NKfIA research grants 123842, 123959, 124845, 124850, 125105, 128713, 128786, and 129058 (Hungary); the Council of Scientific and Industrial Research, India; the Latvian Council of Science; the National Science Center (Poland), contracts Opus 2014/15/B/ST2/03998 and 2015/19/B/ST2/02861; the National Priorities Research Program by Qatar National Research Fund; the Ministry of Science and Higher Education, project no. 0723-2020-0041 (Russia); the Programa de Excelencia María de Maeztu, and the Programa Severo Ochoa del Principado de Asturias; the Stavros Niarchos Foundation (Greece); the Rachadapisek Sompot Fund for Postdoctoral Fellowship, Chulalongkorn University, and the Chulalongkorn Academic into Its 2nd Century Project Advancement Project (Thailand); the Kavli Foundation; the Nvidia Corporation; the SuperMicro Corporation; the Welch Foundation, contract C-1845; and the Weston Havens Foundation (USA).

References

- [1] CMS Collaboration, “Measurement of $t\bar{t}$ normalised multi-differential cross sections in pp collisions at $\sqrt{s} = 13$ TeV and simultaneous determination of the strong coupling strength, top quark pole mass, and parton distribution functions”, *Eur. Phys. J. C* **80** (2020) 658, doi:10.1140/epjc/s10052-020-7917-7, arXiv:1904.05237.
- [2] CMS Collaboration, “Measurement of the top quark Yukawa coupling from $t\bar{t}$ kinematic distributions in the lepton+jets final state in proton-proton collisions at $\sqrt{s} = 13$ TeV”, *Phys. Rev. D* **100** (2019) 072007, doi:10.1103/PhysRevD.100.072007, arXiv:1907.01590.
- [3] CMS Collaboration, “Measurement of the top quark Yukawa coupling from $t\bar{t}$ kinematic distributions in the dilepton final state in proton-proton collisions at $\sqrt{s} = 13$ TeV”, *Phys. Rev. D* **102** (2020) 092013, doi:10.1103/PhysRevD.102.092013, arXiv:2009.07123.
- [4] CMS Collaboration, “Measurement of differential top-quark pair production cross sections in pp collisions at $\sqrt{s} = 7$ TeV”, *Eur. Phys. J. C* **73** (2013) 2339, doi:10.1140/epjc/s10052-013-2339-4, arXiv:1211.2220.
- [5] ATLAS Collaboration, “Differential top-antitop cross-section measurements as a function of observables constructed from final-state particles using pp collisions at $\sqrt{s} = 7$ TeV in the ATLAS detector”, *JHEP* **06** (2015) 100, doi:10.1007/JHEP06(2015)100, arXiv:1502.05923.
- [6] CMS Collaboration, “Measurement of the differential cross section for top quark pair production in pp collisions at $\sqrt{s} = 8$ TeV”, *Eur. Phys. J. C* **75** (2015) 542, doi:10.1140/epjc/s10052-015-3709-x, arXiv:1505.04480.
- [7] ATLAS Collaboration, “Measurements of top-quark pair differential cross-sections in the lepton+jets channel in pp collisions at $\sqrt{s} = 8$ TeV using the ATLAS detector”, *Eur. Phys. J. C* **76** (2016) 538, doi:10.1140/epjc/s10052-016-4366-4, arXiv:1511.04716.
- [8] ATLAS Collaboration, “Measurement of the differential cross-section of highly boosted top quarks as a function of their transverse momentum in $\sqrt{s} = 8$ TeV proton-proton collisions using the ATLAS detector”, *Phys. Rev. D* **93** (2016) 032009, doi:10.1103/PhysRevD.93.032009, arXiv:1510.03818.

-
- [9] CMS Collaboration, “Measurement of the $t\bar{t}$ production cross section in the all-jets final state in pp collisions at $\sqrt{s} = 8$ TeV”, *Eur. Phys. J. C* **76** (2016) 128, doi:10.1140/epjc/s10052-016-3956-5, arXiv:1509.06076.
- [10] CMS Collaboration, “Measurement of the integrated and differential $t\bar{t}$ production cross sections for high- p_T top quarks in pp collisions at $\sqrt{s} = 8$ TeV”, *Phys. Rev. D* **94** (2016) 072002, doi:10.1103/PhysRevD.94.072002, arXiv:1605.00116.
- [11] ATLAS Collaboration, “Measurement of top quark pair differential cross-sections in the dilepton channel in pp collisions at $\sqrt{s} = 7$ and 8 TeV with ATLAS”, *Phys. Rev. D* **94** (2016) 092003, doi:10.1103/PhysRevD.94.092003, arXiv:1607.07281.
- [12] CMS Collaboration, “Measurement of double-differential cross sections for top quark pair production in pp collisions at $\sqrt{s} = 8$ TeV and impact on parton distribution functions”, *Eur. Phys. J. C* **77** (2017) 459, doi:10.1140/epjc/s10052-017-4984-5, arXiv:1703.01630.
- [13] ATLAS Collaboration, “Measurement of jet activity produced in top-quark events with an electron, a muon and two b-tagged jets in the final state in pp collisions at $\sqrt{s} = 13$ TeV with the ATLAS detector”, *Eur. Phys. J. C* **77** (2017) 220, doi:10.1140/epjc/s10052-017-4766-0, arXiv:1610.09978.
- [14] ATLAS Collaboration, “Measurements of top-quark pair differential cross-sections in the $e\mu$ channel in pp collisions at $\sqrt{s} = 13$ TeV using the ATLAS detector”, *Eur. Phys. J. C* **77** (2017) 292, doi:10.1140/epjc/s10052-017-4821-x, arXiv:1612.05220.
- [15] CMS Collaboration, “Measurement of normalized differential $t\bar{t}$ cross sections in the dilepton channel from pp collisions at $\sqrt{s} = 13$ TeV.”, *JHEP* **04** (2018) 60, doi:10.1007/JHEP04(2018)060, arXiv:1708.07638.
- [16] CMS Collaboration, “Measurement of differential cross sections for top quark pair production using the lepton+jets final state in proton-proton collisions at 13 TeV”, *Phys. Rev. D* **95** (2017) 092001, doi:10.1103/PhysRevD.95.092001, arXiv:1610.04191.
- [17] CMS Collaboration, “Measurement of differential cross sections for the production of top quark pairs and of additional jets in lepton+jets events from pp collisions at 13 TeV”, *Phys. Rev. D* **97** (2018) 112003, doi:10.1103/PhysRevD.97.112003, arXiv:1803.08856.
- [18] ATLAS Collaboration, “Measurements of $t\bar{t}$ differential cross-sections of highly boosted top quarks decaying to all-hadronic final states in pp collisions at $\sqrt{s} = 13$ TeV using the ATLAS detector”, *Phys. Rev. D* **98** (2018) 012003, doi:10.1103/PhysRevD.98.012003, arXiv:1801.02052.
- [19] ATLAS Collaboration, “Measurements of top-quark pair differential and double-differential cross-sections in the ℓ +jets channel with pp collisions at $\sqrt{s} = 13$ TeV using the ATLAS detector”, *Eur. Phys. J. C* **79** (2019) 1028, doi:10.1140/epjc/s10052-019-7525-6, arXiv:1908.07305.
- [20] ATLAS Collaboration, “Measurement of the $t\bar{t}$ production cross-section and lepton differential distributions in $e\mu$ dilepton events from pp collisions at $\sqrt{s} = 13$ TeV with the ATLAS detector”, *Eur. Phys. J. C* **80** (2020) 528, doi:10.1140/epjc/s10052-020-7907-9, arXiv:1910.08819.

- [21] “HEPData record for this analysis”, 2021. doi:10.17182/hepdata.102956.
- [22] P. Nason, “A new method for combining NLO QCD with shower Monte Carlo algorithms”, *JHEP* **11** (2004) 40, doi:10.1088/1126-6708/2004/11/040, arXiv:hep-ph/0409146.
- [23] S. Frixione, P. Nason, and C. Oleari, “Matching NLO QCD computations with parton shower simulations: the POWHEG method”, *JHEP* **11** (2007) 70, doi:10.1088/1126-6708/2007/11/070, arXiv:0709.2092.
- [24] S. Alioli, P. Nason, C. Oleari, and E. Re, “A general framework for implementing NLO calculations in shower Monte Carlo programs: the POWHEG BOX”, *JHEP* **06** (2010) 043, doi:10.1007/JHEP06(2010)043, arXiv:1002.2581.
- [25] S. Frixione, P. Nason, and G. Ridolfi, “A positive-weight next-to-leading-order Monte Carlo for heavy flavour hadroproduction”, *JHEP* **09** (2007) 126, doi:10.1088/1126-6708/2007/09/126, arXiv:0707.3088.
- [26] T. Sjöstrand et al., “An Introduction to PYTHIA 8.2”, *Comput. Phys. Commun.* **191** (2015) 159, doi:10.1016/j.cpc.2015.01.024, arXiv:1410.3012.
- [27] P. Skands, S. Carrazza, and J. Rojo, “Tuning PYTHIA 8.1: the Monash 2013 tune”, *Eur. Phys. J. C* **74** (2014) 3024, doi:10.1140/epjc/s10052-014-3024-y, arXiv:1404.5630.
- [28] CMS Collaboration, “Event generator tunes obtained from underlying event and multiparton scattering measurements”, *Eur. Phys. J. C* **76** (2016) 155, doi:10.1140/epjc/s10052-016-3988-x, arXiv:1512.00815.
- [29] CMS Collaboration, “Investigations of the impact of the parton shower tuning in PYTHIA 8 in the modelling of $t\bar{t}$ at $\sqrt{s} = 8$ and 13 TeV”, CMS Physics Analysis Summary CMS-PAS-TOP-16-021, 2016.
- [30] CMS Collaboration, “Extraction and validation of a new set of CMS PYTHIA8 tunes from underlying-event measurements”, *Eur. Phys. J. C* **80** (2020) 4, doi:10.1140/epjc/s10052-019-7499-4, arXiv:1903.12179.
- [31] NNPDF Collaboration, “Parton distributions for the LHC Run II”, *JHEP* **04** (2015) 040, doi:10.1007/JHEP04(2015)040, arXiv:1410.8849.
- [32] NNPDF Collaboration, “Parton distributions from high-precision collider data”, *Eur. Phys. J. C* **77** (2017) 663, doi:10.1140/epjc/s10052-017-5199-5, arXiv:1706.00428.
- [33] GEANT4 Collaboration, “GEANT4—a simulation toolkit”, *Nucl. Instrum. Meth. A* **506** (2003) 250, doi:10.1016/S0168-9002(03)01368-8.
- [34] M. Bähr et al., “HERWIG++ physics and manual”, *Eur. Phys. J. C* **58** (2008) 639, doi:10.1140/epjc/s10052-008-0798-9, arXiv:0803.0883.
- [35] CMS Collaboration, “Development and validation of HERWIG 7 tunes from CMS underlying-event measurements”, *Eur. Phys. J. C* **81** (2021) 312, doi:10.1140/epjc/s10052-021-08949-5, arXiv:2011.03422.

-
- [36] J. Alwall et al., “The automated computation of tree-level and next-to-leading order differential cross sections, and their matching to parton shower simulations”, *JHEP* **07** (2014) 079, doi:10.1007/JHEP07(2014)079, arXiv:1405.0301.
- [37] R. Frederix and S. Frixione, “Merging meets matching in MC@NLO”, *JHEP* **12** (2012) 061, doi:10.1007/JHEP12(2012)061, arXiv:1209.6215.
- [38] M. Czakon and A. Mitov, “Top++: A program for the calculation of the top-pair cross-section at hadron colliders”, *Comput. Phys. Commun.* **185** (2014) 2930, doi:10.1016/j.cpc.2014.06.021, arXiv:1112.5675.
- [39] A. D. Martin, W. J. Stirling, R. S. Thorne, and G. Watt, “Parton distributions for the LHC”, *Eur. Phys. J. C* **63** (2009) 189, doi:10.1140/epjc/s10052-009-1072-5, arXiv:0901.0002.
- [40] J. Gao et al., “CT10 next-to-next-to-leading order global analysis of QCD”, *Phys. Rev. D* **89** (2014) 033009, doi:10.1103/PhysRevD.89.033009, arXiv:1302.6246.
- [41] R. D. Ball et al., “Parton distributions with LHC data”, *Nucl. Phys. B* **867** (2013) 244, doi:10.1016/j.nuclphysb.2012.10.003, arXiv:1207.1303.
- [42] S. Catani et al., “Top-quark pair hadroproduction at next-to-next-to-leading order in QCD”, *Phys. Rev. D* **99** (2019) 051501, doi:10.1103/PhysRevD.99.051501, arXiv:1901.04005.
- [43] S. Catani et al., “Top-quark pair production at the LHC: Fully differential QCD predictions at NNLO”, *JHEP* **07** (2019) 100, doi:10.1007/JHEP07(2019)100, arXiv:1906.06535.
- [44] E. Re, “Single-top Wt-channel production matched with parton showers using the POWHEG method”, *Eur. Phys. J. C* **71** (2011) 1547, doi:10.1140/epjc/s10052-011-1547-z, arXiv:1009.2450.
- [45] C. D. White, S. Frixione, E. Laenen, and F. Maltoni, “Isolating Wt production at the LHC”, *JHEP* **11** (2009) 074, doi:10.1088/1126-6708/2009/11/074, arXiv:0908.0631.
- [46] Y. Li and F. Petriello, “Combining QCD and electroweak corrections to dilepton production in FEWZ”, *Phys. Rev. D* **86** (2012) 094034, doi:10.1103/PhysRevD.86.094034, arXiv:1208.5967.
- [47] P. Kant et al., “HatHor for single top-quark production: Updated predictions and uncertainty estimates for single top-quark production in hadronic collisions”, *Comput. Phys. Commun.* **191** (2015) 74, doi:10.1016/j.cpc.2015.02.001, arXiv:1406.4403.
- [48] N. Kidonakis, “NNLL threshold resummation for top-pair and single-top production”, *Phys. Part. Nucl.* **45** (2014) 714, doi:10.1134/S1063779614040091, arXiv:1210.7813.
- [49] T. Sjöstrand, S. Mrenna, and P. Skands, “A brief introduction to PYTHIA 8.1”, *Comput. Phys. Commun.* **178** (2008) 852, doi:10.1016/j.cpc.2008.01.036, arXiv:0710.3820.
- [50] Particle Data Group, P. A. Zyla et al., “Review of particle physics”, *Prog. Theor. Exp. Phys.* **2020** (2020) 083C01, doi:10.1093/ptep/ptaa104.

- [51] CMS Collaboration, “Object definitions for top quark analyses at the particle level”, CMS Note CERN-CMS-NOTE-2017-004, 2017.
- [52] M. Cacciari, G. P. Salam, and G. Soyez, “The anti- k_T jet clustering algorithm”, *JHEP* **04** (2008) 063, doi:10.1088/1126-6708/2008/04/063, arXiv:0802.1189.
- [53] M. Cacciari, G. P. Salam, and G. Soyez, “FastJet user manual”, *Eur. Phys. J. C* **72** (2012) 1896, doi:10.1140/epjc/s10052-012-1896-2, arXiv:1111.6097.
- [54] M. Cacciari, G. P. Salam, and G. Soyez, “The catchment area of jets”, *JHEP* **04** (2008) 005, doi:10.1088/1126-6708/2008/04/005, arXiv:0802.1188.
- [55] CMS Collaboration, “The CMS experiment at the CERN LHC”, *JINST* **3** (2008) S08004, doi:10.1088/1748-0221/3/08/S08004.
- [56] CMS Collaboration, “Performance of the CMS Level-1 trigger in proton-proton collisions at $\sqrt{s} = 13$ TeV”, *JINST* **15** (2020) P10017, doi:10.1088/1748-0221/15/10/P10017, arXiv:2006.10165.
- [57] CMS Collaboration, “The CMS trigger system”, *JINST* **12** (2017) P01020, doi:10.1088/1748-0221/12/01/P01020, arXiv:1609.02366.
- [58] CMS Collaboration, “Particle-flow reconstruction and global event description with the CMS detector”, *JINST* **12** (2017) P10003, doi:10.1088/1748-0221/12/10/P10003, arXiv:1706.04965.
- [59] CMS Collaboration, “Electron and photon reconstruction and identification with the CMS experiment at the CERN LHC”, *JINST* **16** (2021) P05014, doi:10.1088/1748-0221/16/05/P05014, arXiv:2012.06888.
- [60] CMS Collaboration, “Performance of the CMS muon detector and muon reconstruction with proton-proton collisions at $\sqrt{s} = 13$ TeV”, *JINST* **13** (2018) P06015, doi:10.1088/1748-0221/13/06/P06015, arXiv:1804.04528.
- [61] CMS Collaboration, “Measurements of inclusive W and Z cross sections in pp collisions at $\sqrt{s} = 7$ TeV”, *JHEP* **01** (2011) 080, doi:10.1007/JHEP01(2011)080, arXiv:1012.2466.
- [62] CMS Collaboration, “Jet energy scale and resolution in the CMS experiment in pp collisions at 8 TeV”, *JINST* **12** (2017) P02014, doi:10.1088/1748-0221/12/02/P02014, arXiv:1607.03663.
- [63] CMS Collaboration, “Identification of heavy-flavour jets with the CMS detector in pp collisions at 13 TeV”, *JINST* **13** (2018) P05011, doi:10.1088/1748-0221/13/05/P05011, arXiv:1712.07158.
- [64] D. Bertolini, P. Harris, M. Low, and N. Tran, “Pileup per particle identification”, *JHEP* **10** (2014) 59, doi:10.1007/JHEP10(2014)059, arXiv:1407.6013.
- [65] D. Kingma and J. Ba, “Adam: a method for stochastic optimization”, in *Proceedings of the 3rd Int. Conf. on Learning Representations, ICLR 2015*. 2015. arXiv:1412.6980.
- [66] I. W. Stewart, F. J. Tackmann, and W. J. Waalewijn, “N-jettiness: an inclusive event shape to veto jets”, *Phys. Rev. Lett.* **105** (2010) 092002, doi:10.1103/PhysRevLett.105.092002, arXiv:1004.2489.

- [67] J. D. Bjorken and S. J. Brodsky, "Statistical model for electron-positron annihilation into hadrons", *Phys. Rev. D* **1** (1970) 1416, doi:10.1103/PhysRevD.1.1416.
- [68] W. S. Cleveland, "Robust locally weighted regression and smoothing scatterplots", *J. Am. Stat. Assoc.* **74** (1979) 829, doi:10.1080/01621459.1979.10481038.
- [69] CMS Collaboration, "Precision luminosity measurement in proton-proton collisions at $\sqrt{s} = 13$ TeV in 2015 and 2016 at CMS", 2021. arXiv:2104.01927. Submitted to *Eur. Phys. J. C*.
- [70] CMS Collaboration, "CMS Luminosity measurement for the 2017 data-taking period", CMS Physics Analysis Summary CMS-PAS-LUM-17-004, 2017.
- [71] CMS Collaboration, "CMS Luminosity measurement for the 2018 data-taking period", CMS Physics Analysis Summary CMS-PAS-LUM-18-002, 2018.
- [72] ATLAS Collaboration, "Measurement of the inelastic proton-proton cross section at $\sqrt{s} = 13$ TeV with the ATLAS detector at the LHC", *Phys. Rev. Lett.* **117** (2016) 182002, doi:10.1103/PhysRevLett.117.182002, arXiv:1606.02625.
- [73] S. Dulat et al., "New parton distribution functions from a global analysis of quantum chromodynamics", *Phys. Rev. D* **93** (2016) 033006, doi:10.1103/PhysRevD.93.033006, arXiv:1506.07443.
- [74] H1 and ZEUS Collaborations, "Combination of measurements of inclusive deep inelastic $e^\pm p$ scattering cross sections and QCD analysis of HERA data", *Eur. Phys. J. C* **12** (2015) 580, doi:10.1140/epjc/s10052-015-3710-4, arXiv:1506.06042.
- [75] L. A. Harland-Lang, A. D. Martin, P. Motylinski, and R. S. Thorne, "Parton distributions in the LHC era: MMHT 2014 PDFs", *Eur. Phys. J. C* **75** (2015) 204, doi:10.1140/epjc/s10052-015-3397-6, arXiv:1412.3989.

A Normalized cross sections at the parton and particle levels

In Figs. A.1–A.26, all differential cross sections are presented normalized to unity. This has the advantage of canceling out the systematic uncertainties affecting only the overall normalization, and the differences in the shapes between data and predictions are more apparent. For this purpose the differential cross sections are divided by the $t\bar{t}$ cross sections σ_{norm} , which are obtained for each measurement as the sum of the cross sections in all bins of the corresponding kinematic observable or observables in the one- or two-dimensional range. The uncertainties in the normalized distributions are evaluated using error propagation and take into account the correlations between uncertainties in the individual measurements and σ_{norm} . The results of the χ^2 tests, comparing the normalized differential cross sections to the various predictions, are shown in Fig. A.27. The p -values are very similar to those obtained without normalization. This confirms that the normalizations are well predicted and that the χ^2 tests are sensitive to differences in the shapes.

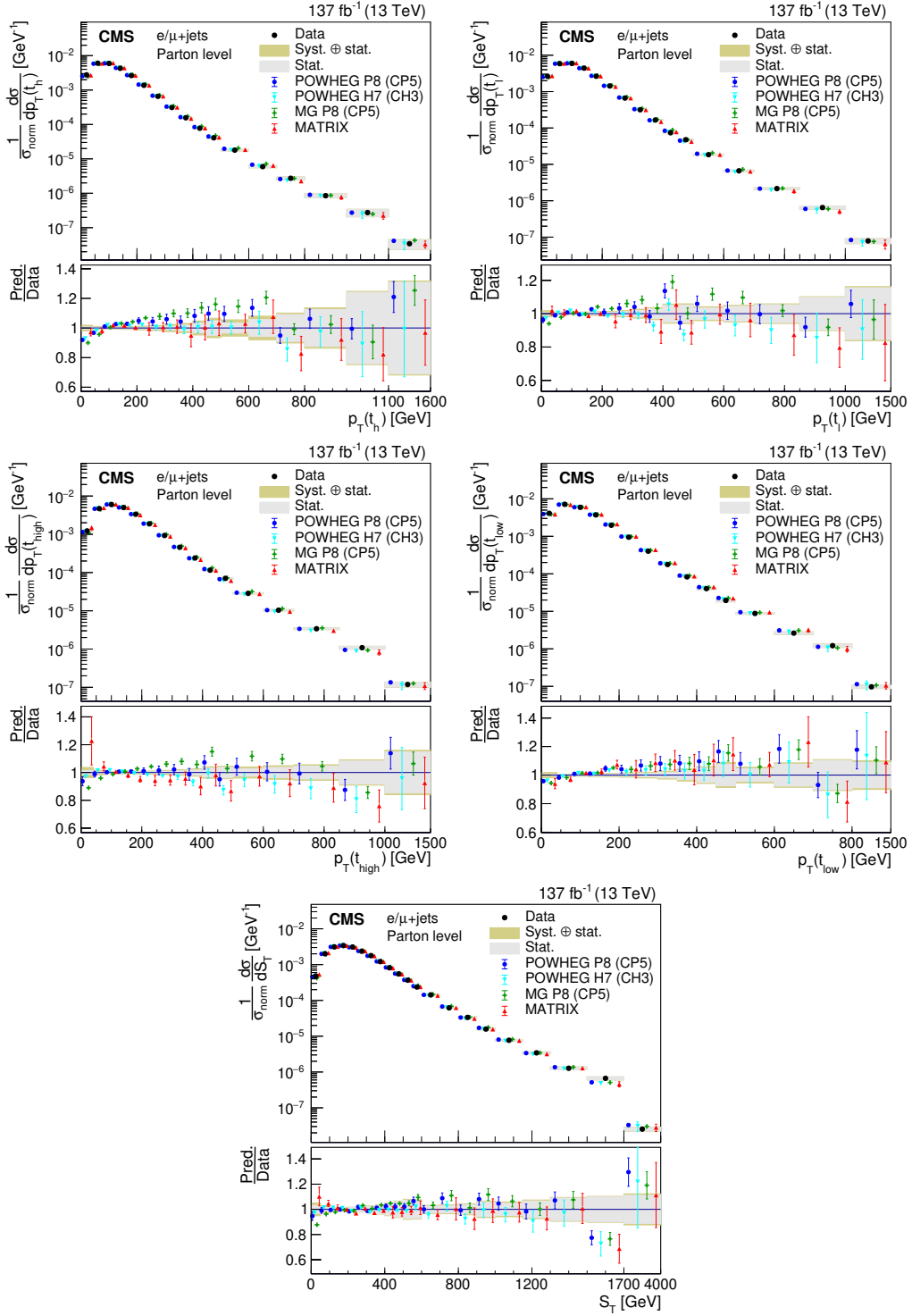


Figure A.1: Normalized differential cross sections at the parton level as a function of $p_T(t_h)$, $p_T(t_\ell)$, $p_T(t_{\text{high}})$, $p_T(t_{\text{low}})$, and S_T . The data are shown as points with gray (yellow) bands indicating the statistical (statistical and systematic) uncertainties. The cross sections are compared to the predictions of POWHEG combined with PYTHIA (P8) or HERWIG (H7), the multiparton simulation MG5_aMC@NLO (MG)+PYTHIA FxFx, and the NNLO QCD calculations obtained with MATRIX. The ratios of the various predictions to the measured cross sections are shown in the lower panels.

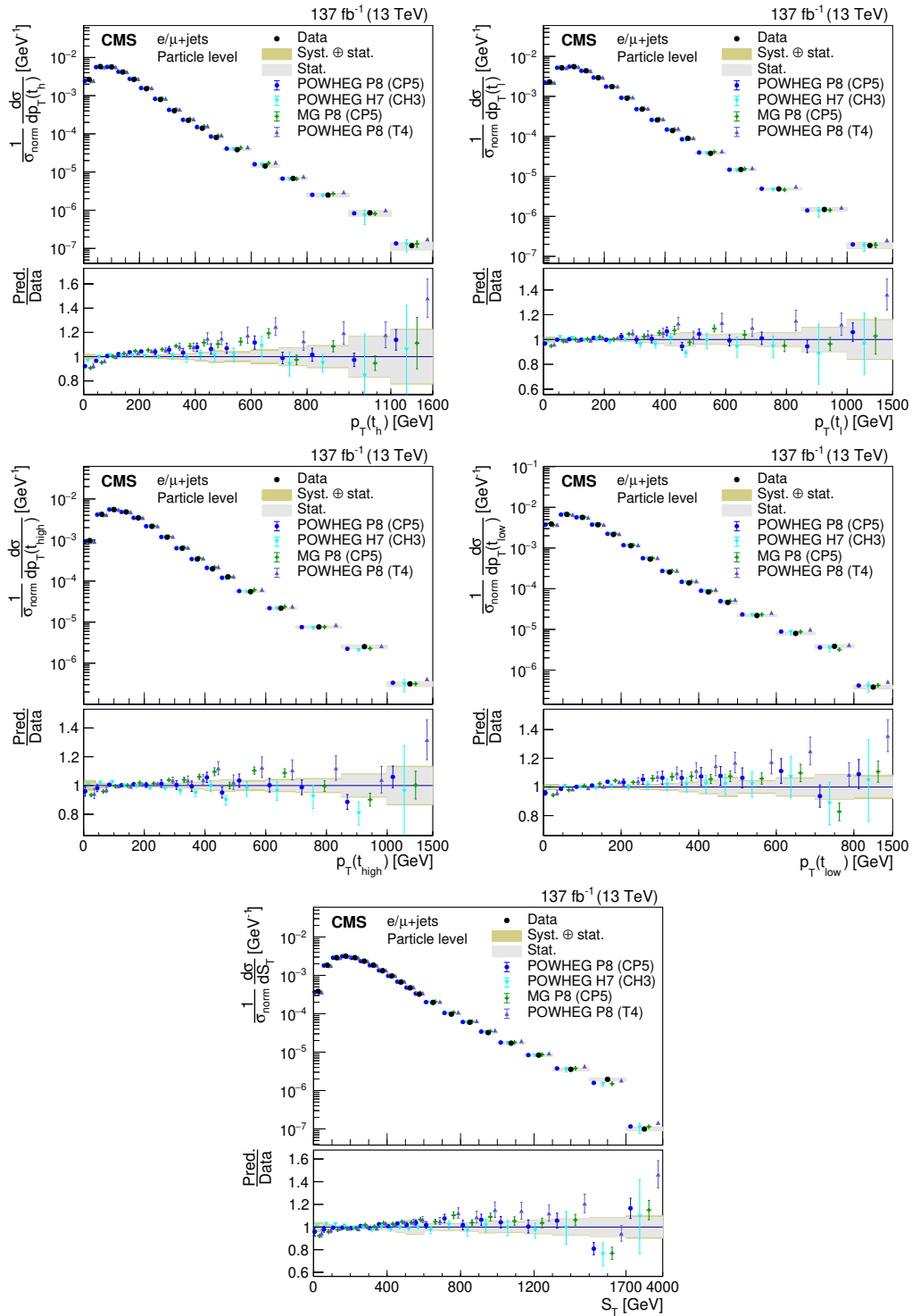


Figure A.2: Normalized differential cross sections at the particle level as a function of $p_T(t_h)$, $p_T(t_l)$, $p_T(t_{\text{high}})$, $p_T(t_{\text{low}})$, and S_T . The data are shown as points with gray (yellow) bands indicating the statistical (statistical and systematic) uncertainties. The cross sections are compared to the predictions of POWHEG+PYTHIA (P8) for the CP5 and CUETP8M2T4 (T4) tunes, POWHEG+HERWIG (H7), and the multiparton simulation MG5_aMC@NLO (MG)+PYTHIA. The ratios of the various predictions to the measured cross sections are shown in the lower panels.

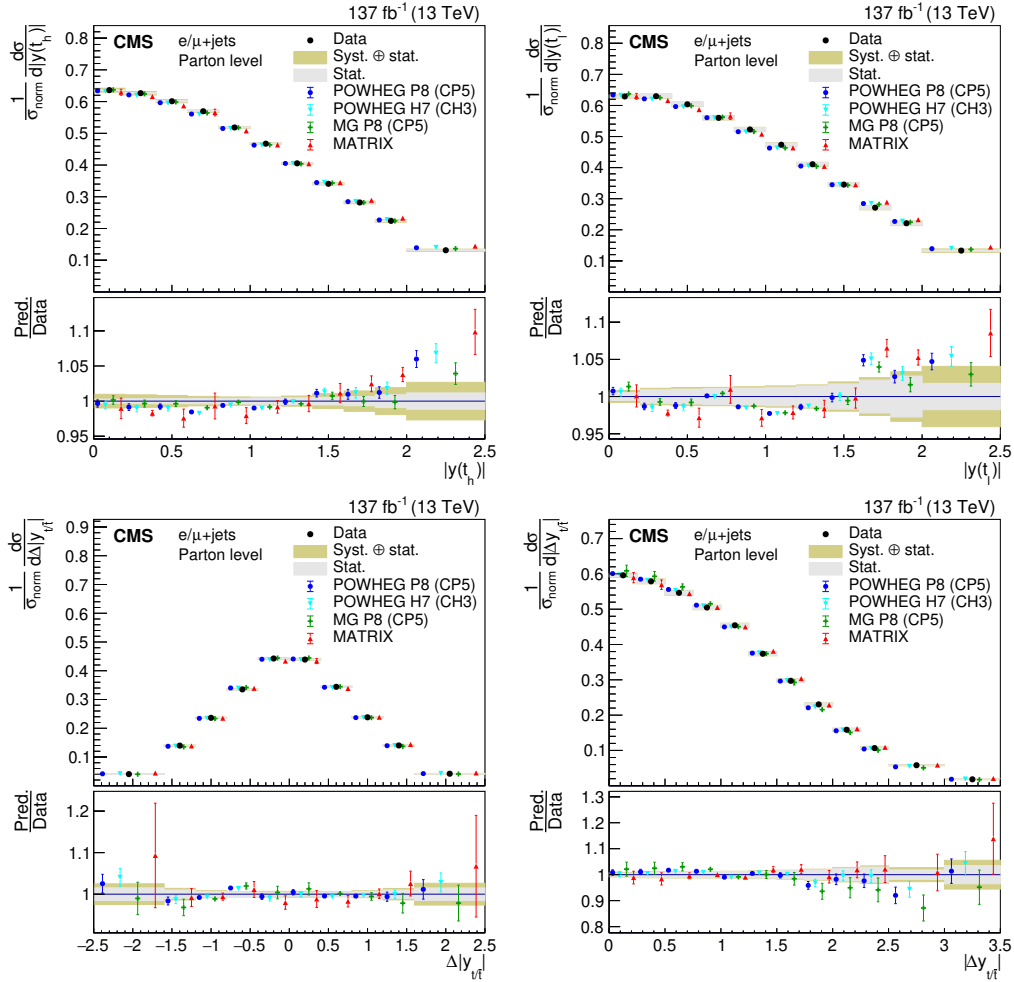


Figure A.3: Normalized differential cross sections at the parton level as a function of $|y(t_h)|$, $|y(t_l)|$, and the differences $\Delta|y_{t/\bar{t}}|$ and $|\Delta y_{t/\bar{t}}|$. The data are shown as points with gray (yellow) bands indicating the statistical (statistical and systematic) uncertainties. The cross sections are compared to the predictions of POWHEG combined with PYTHIA (P8) or HERWIG (H7), the multiparton simulation MG5_aMC@NLO (MG)+PYTHIA FxFx, and the NNLO QCD calculations obtained with MATRIX. The ratios of the various predictions to the measured cross sections are shown in the lower panels.

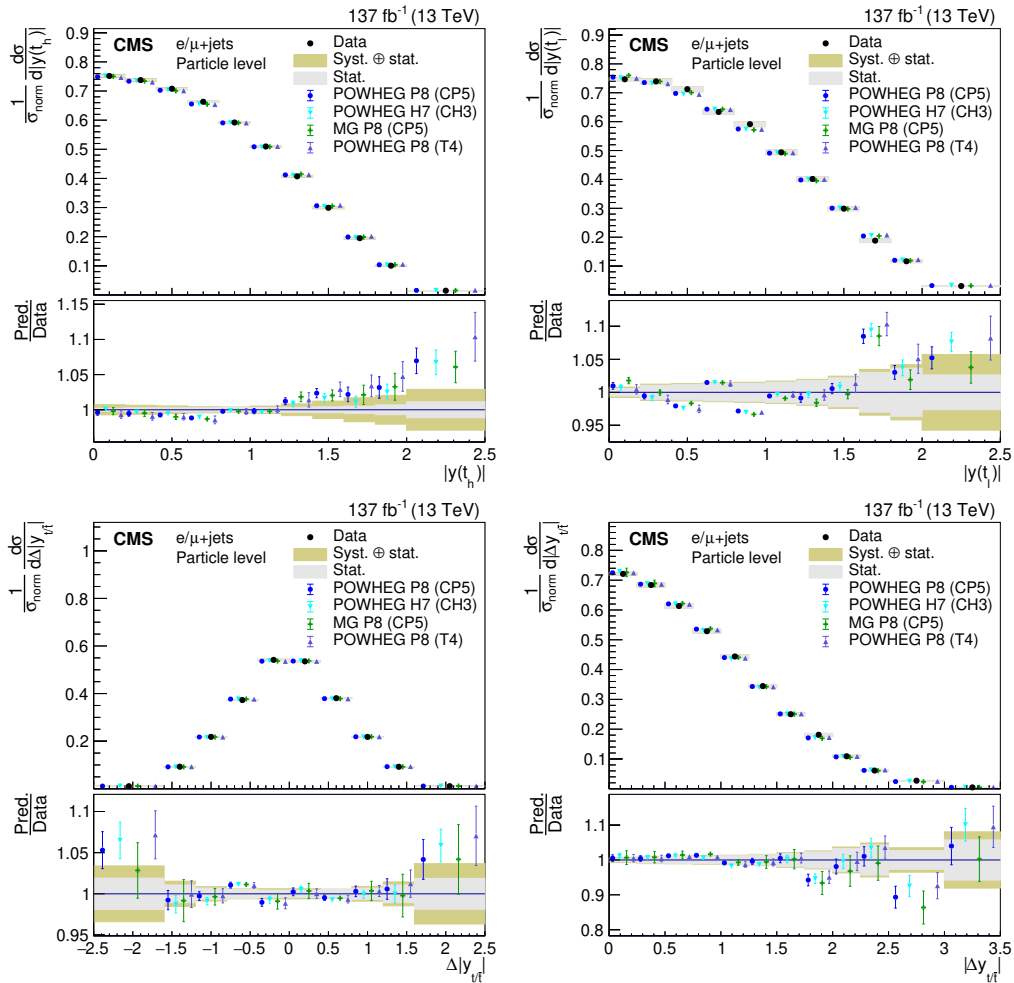


Figure A.4: Normalized differential cross sections at the particle level as a function of $|y(t_h)|$, $|y(t_l)|$, and the differences $\Delta|y_{t/\bar{t}}|$ and $|y_{t/\bar{t}}|$. The data are shown as points with gray (yellow) bands indicating the statistical (statistical and systematic) uncertainties. The cross sections are compared to the predictions of POWHEG+PYTHIA (P8) for the CP5 and CUETP8M2T4 (T4) tunes, POWHEG+HERWIG (H7), and the multiparton simulation MG5_aMC@NLO (MG)+PYTHIA. The ratios of the various predictions to the measured cross sections are shown in the lower panels.

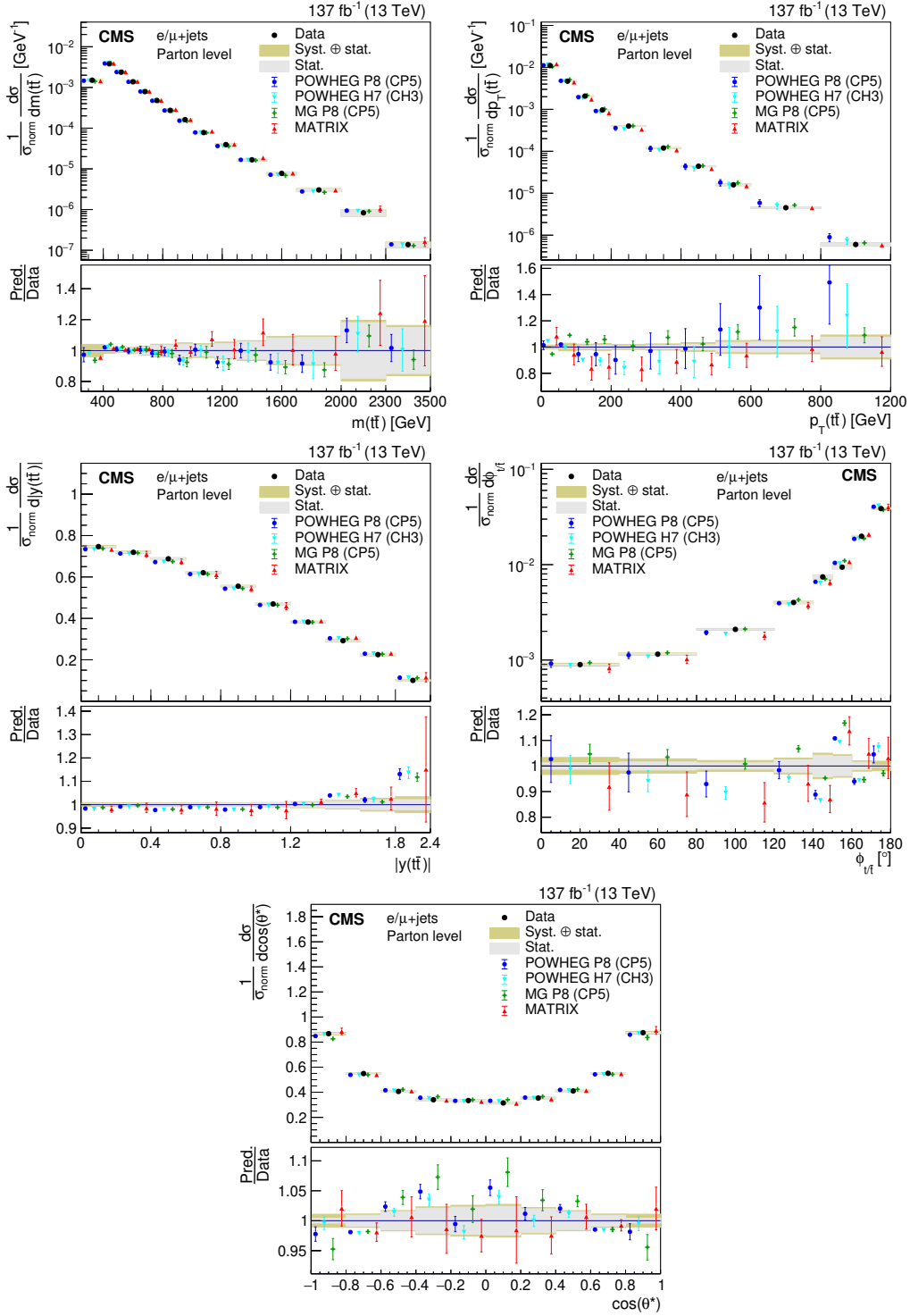


Figure A.5: Normalized differential cross sections at the parton level as a function of kinematic variables of the $t\bar{t}$ system. The data are shown as points with gray (yellow) bands indicating the statistical (statistical and systematic) uncertainties. The cross sections are compared to the predictions of POWHEG combined with PYTHIA (P8) or HERWIG (H7), the multiparton simulation MG5_aMC@NLO (MG)+PYTHIA FxFx, and the NNLO QCD calculations obtained with MATRIX. The ratios of the various predictions to the measured cross sections are shown in the lower panels.

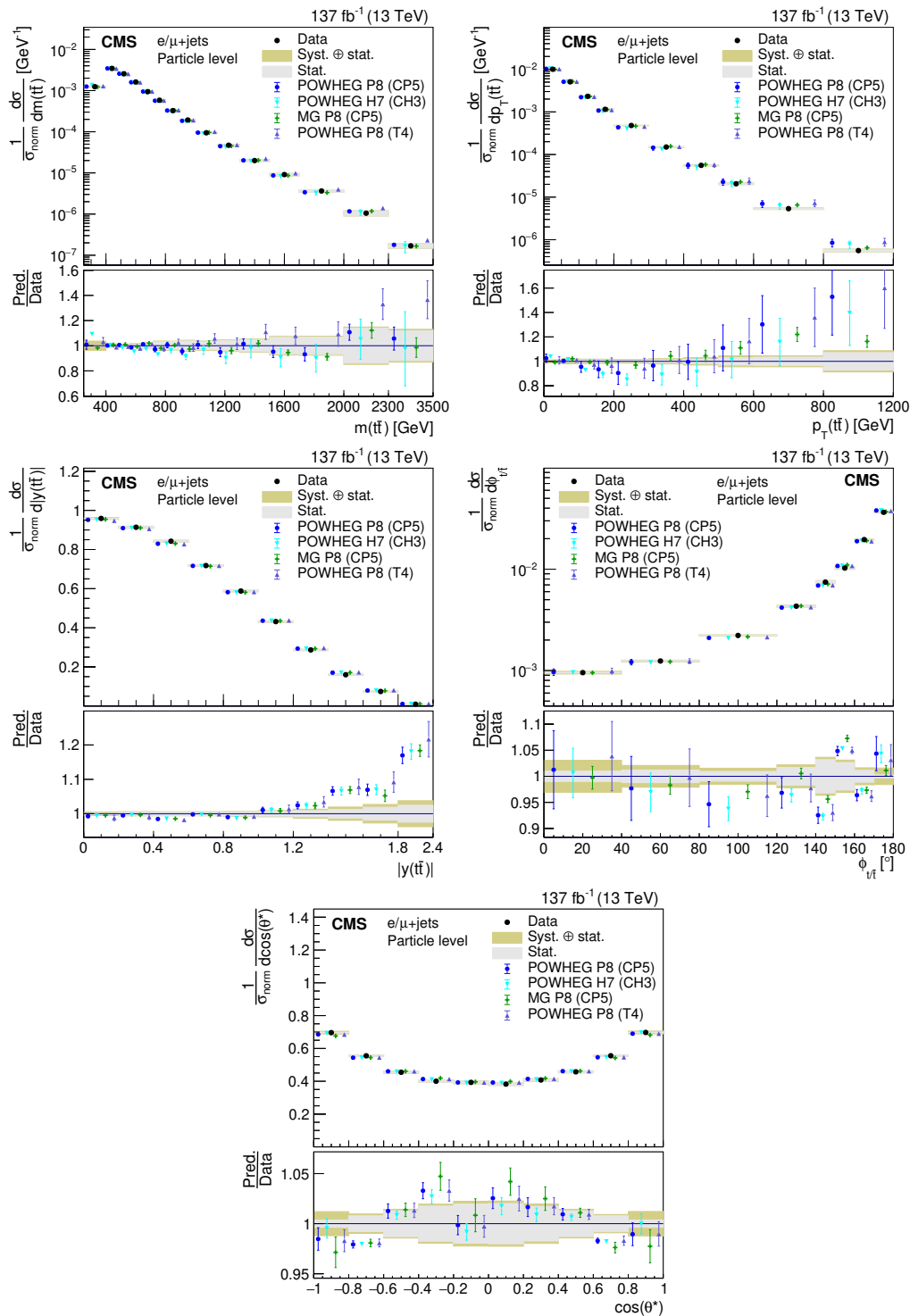


Figure A.6: Normalized differential cross sections at the particle level as a function of kinematic variables of the $t\bar{t}$ system. The data are shown as points with gray (yellow) bands indicating the statistical (statistical and systematic) uncertainties. The cross sections are compared to the predictions of POWHEG+PYTHIA (P8) for the CP5 and CUETP8M2T4 (T4) tunes, POWHEG+HERWIG (H7), and the multiparton simulation MG5_aMC@NLO (MG)+PYTHIA. The ratios of the various predictions to the measured cross sections are shown in the lower panels.

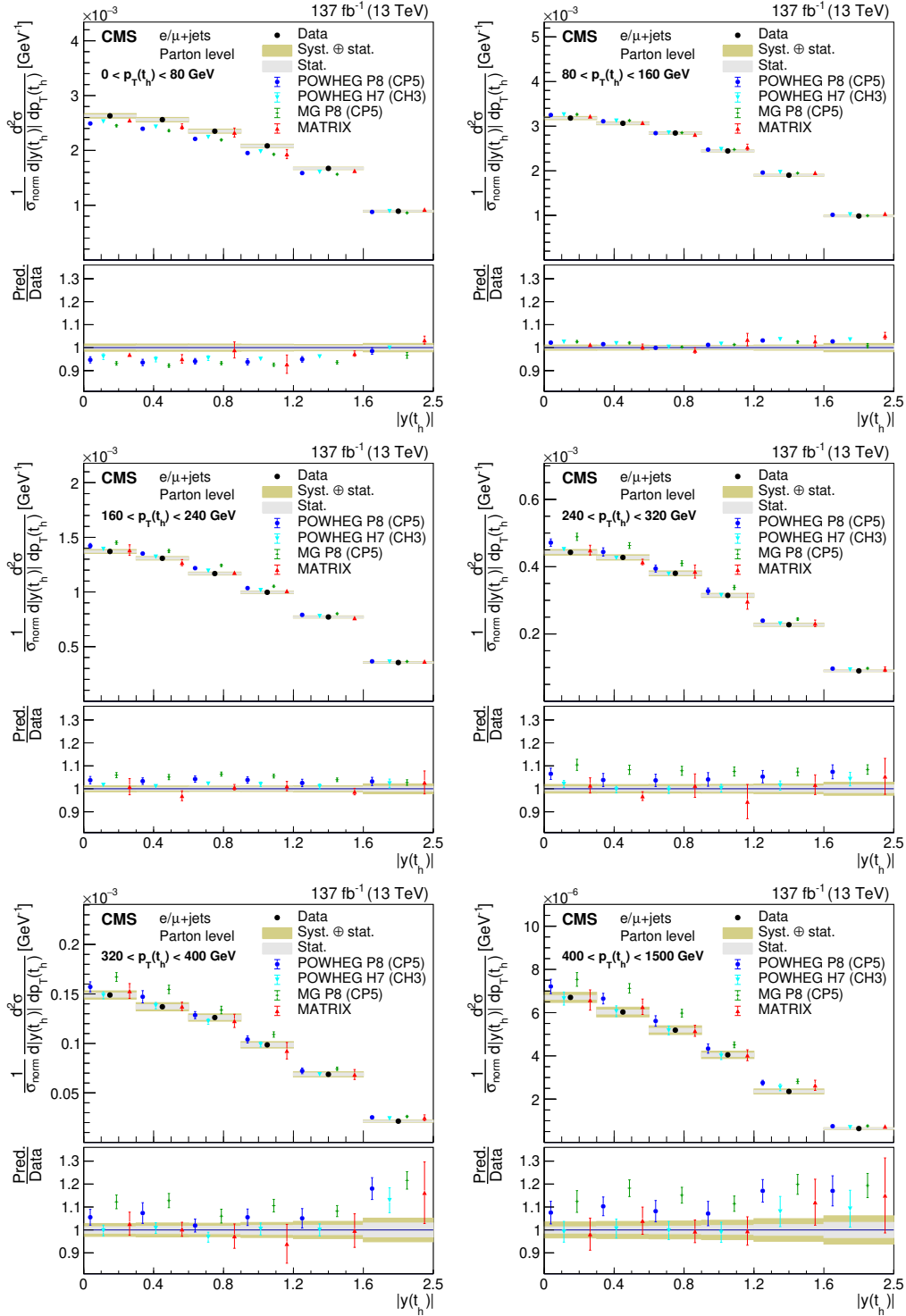


Figure A.7: Normalized double-differential cross section at the parton level as a function of $p_T(t_h)$ vs. $|y(t_h)|$. The data are shown as points with gray (yellow) bands indicating the statistical (systematic) uncertainties. The cross sections are compared to the predictions of POWHEG combined with PYTHIA (P8) or HERWIG (H7), the multiparton simulation MG5_aMC@NLO (MG)+PYTHIA FxFx, and the NNLO QCD calculations obtained with MATRIX. The ratios of the various predictions to the measured cross sections are shown in the lower panels.

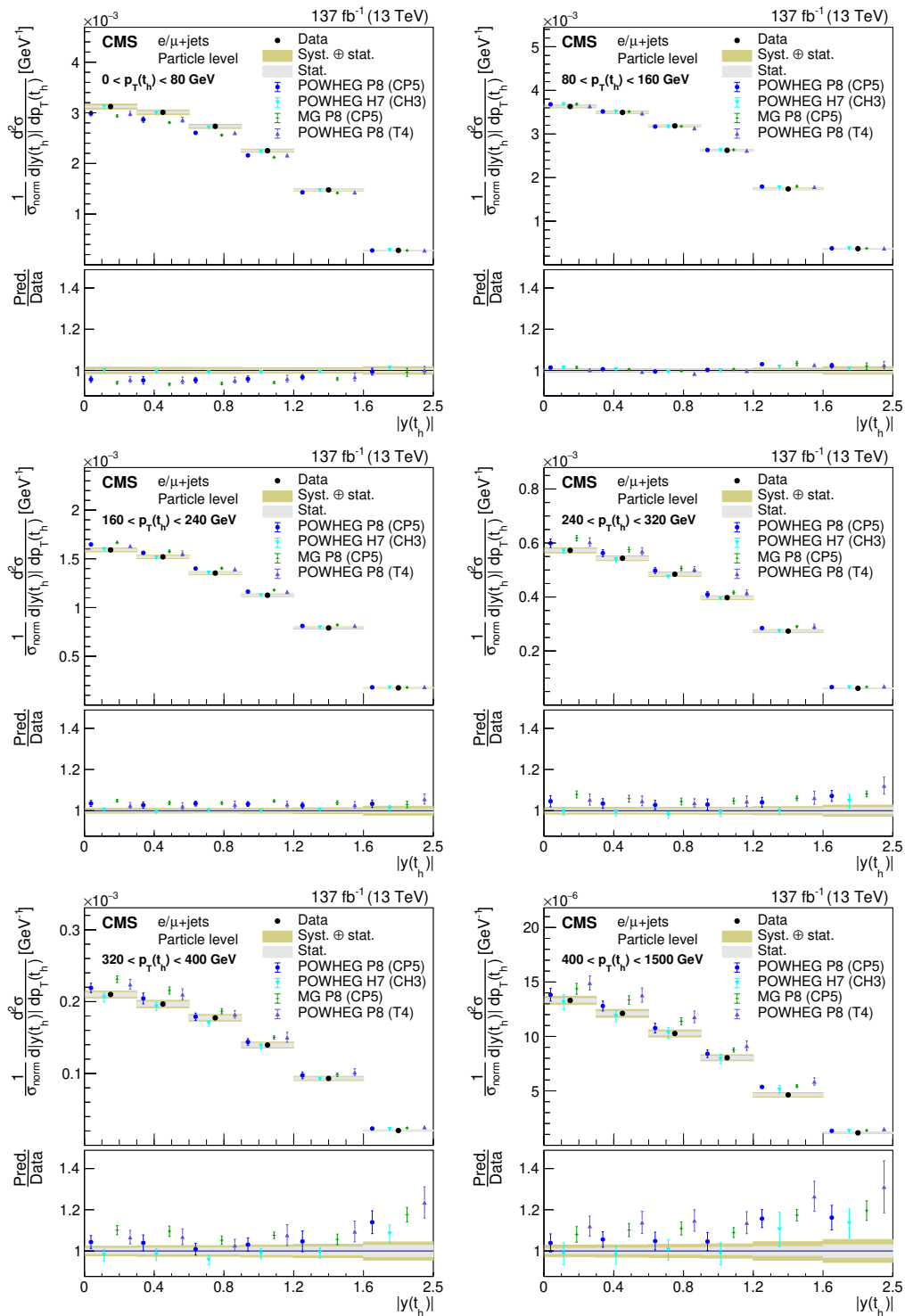


Figure A.8: Normalized double-differential cross section at the particle level as a function of $p_T(t_h)$ vs. $|y(t_h)|$. The data are shown as points with gray (yellow) bands indicating the statistical (statistical and systematic) uncertainties. The cross sections are compared to the predictions of POWHEG+PYTHIA (P8) for the CP5 and CUETP8M2T4 (T4) tunes, POWHEG+HERWIG (H7), and the multiparton simulation MG5_aMC@NLO (MG)+PYTHIA. The ratios of the various predictions to the measured cross sections are shown in the lower panels.

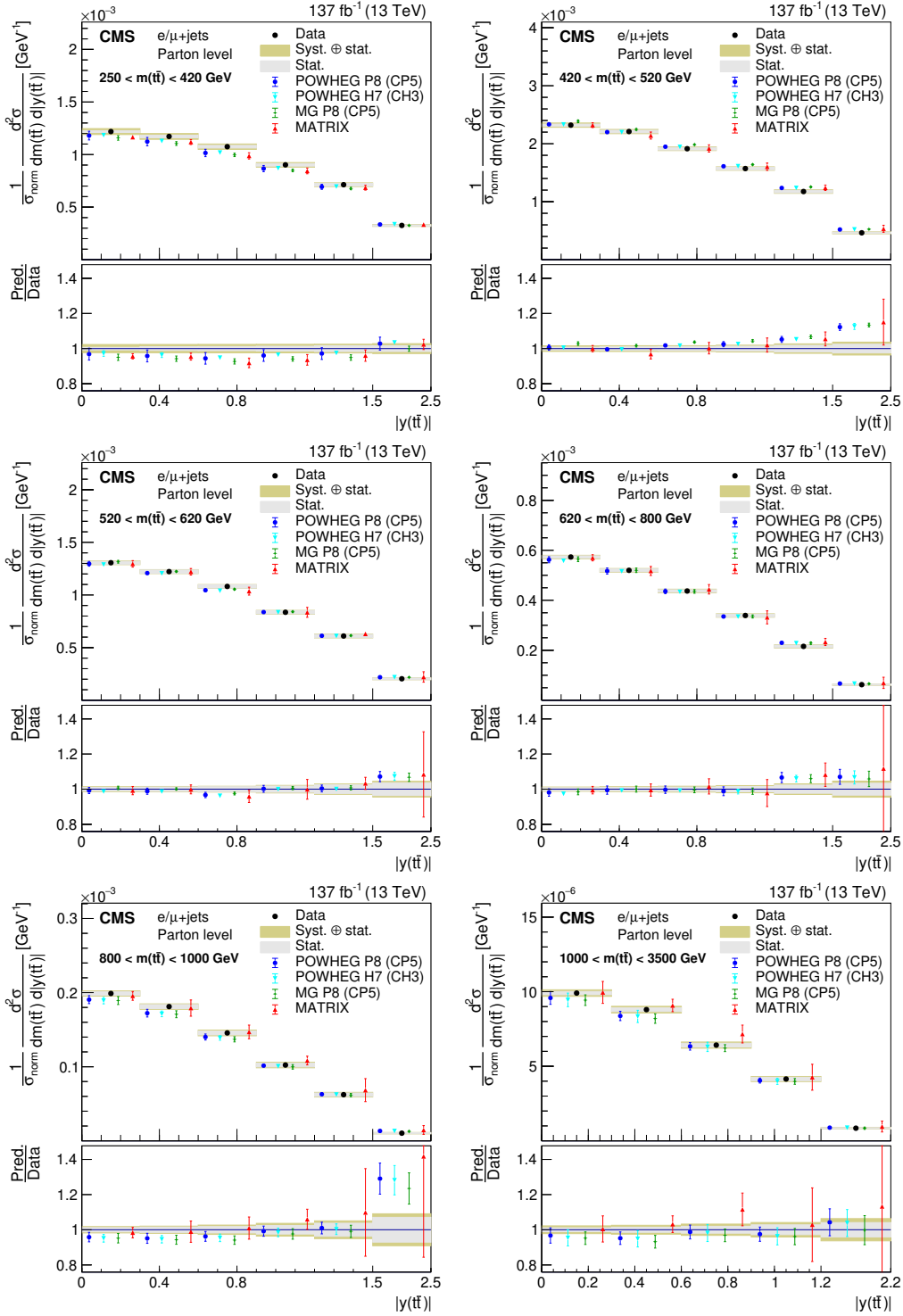


Figure A.9: Normalized double-differential cross section at the parton level as a function of $m(\bar{t}t)$ vs. $|y(\bar{t}t)|$. The data are shown as points with gray (yellow) bands indicating the statistical (statistical and systematic) uncertainties. The cross sections are compared to the predictions of POWHEG combined with PYTHIA (P8) or HERWIG (H7), the multiparton simulation MG5_aMC@NLO (MG)+PYTHIA FxFx, and the NNLO QCD calculations obtained with MATRIX. The ratios of the various predictions to the measured cross sections are shown in the lower panels.

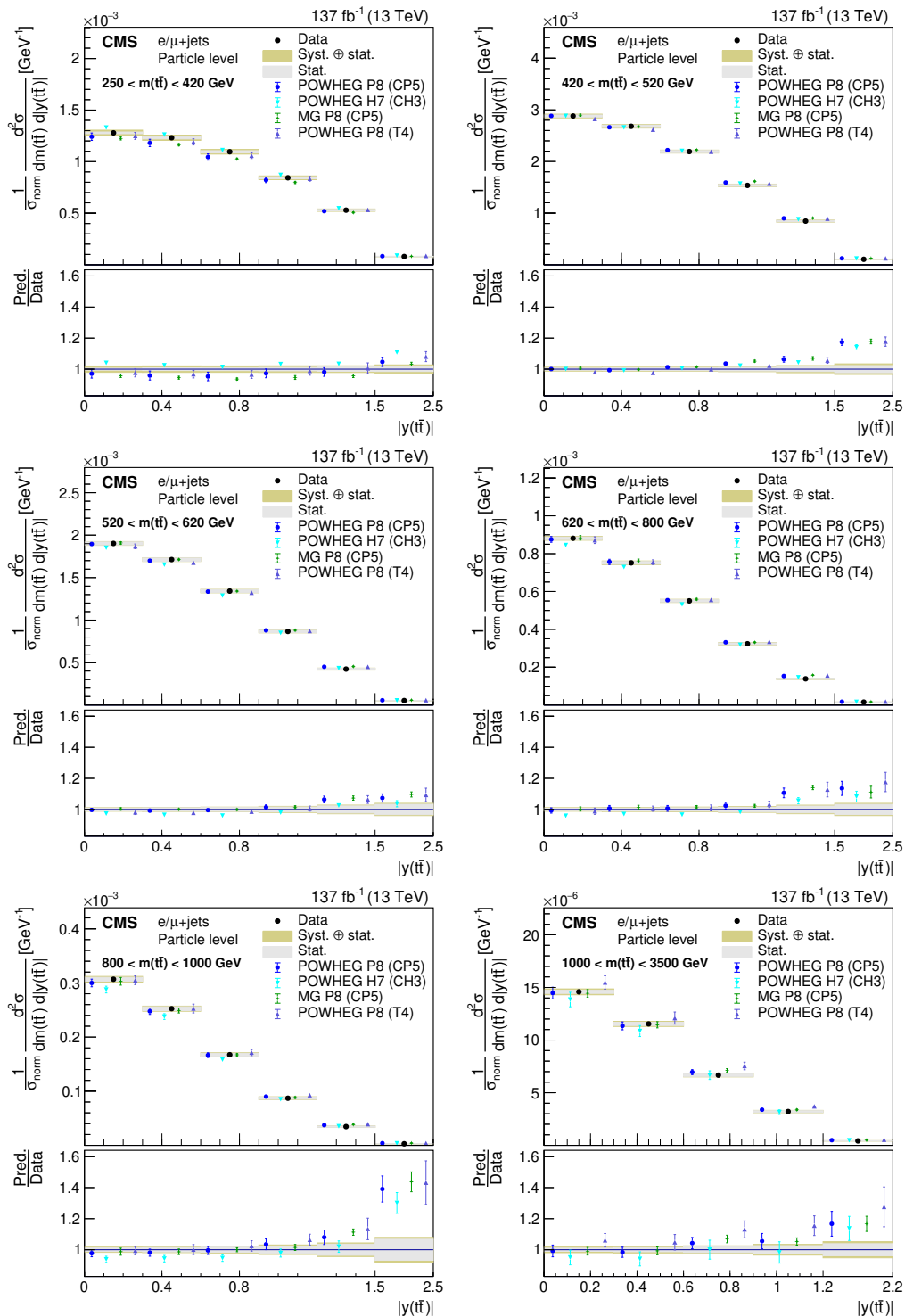


Figure A.10: Normalized double-differential cross section at the particle level as a function of $m(\bar{t}t)$ vs. $|y(\bar{t}t)|$. The data are shown as points with gray (yellow) bands indicating the statistical (statistical and systematic) uncertainties. The cross sections are compared to the predictions of POWHEG+PYTHIA (P8) for the CP5 and CUETP8M2T4 (T4) tunes, POWHEG+HERWIG (H7), and the multiparton simulation MG5_aMC@NLO (MG)+PYTHIA. The ratios of the various predictions to the measured cross sections are shown in the lower panels.

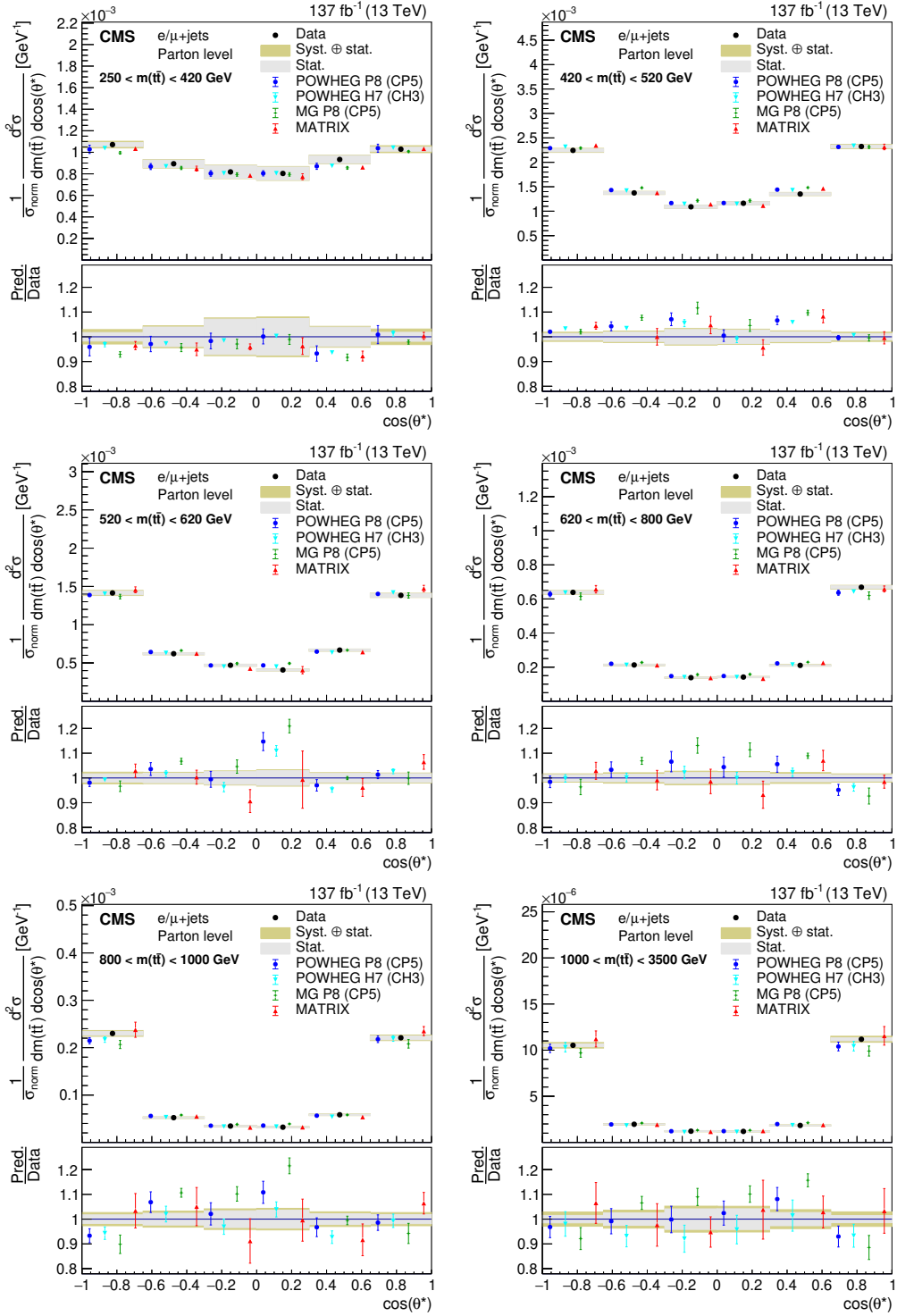


Figure A.11: Normalized double-differential cross section at the parton level as a function of $m(\bar{t}t)$ vs. $\cos(\theta^*)$. The data are shown as points with gray (yellow) bands indicating the statistical (statistical and systematic) uncertainties. The cross sections are compared to the predictions of POWHEG combined with PYTHIA (P8) or HERWIG (H7), the multiparton simulation MG5_aMC@NLO (MG)+PYTHIA FxFx, and the NNLO QCD calculations obtained with MATRIX. The ratios of the various predictions to the measured cross sections are shown in the lower panels.

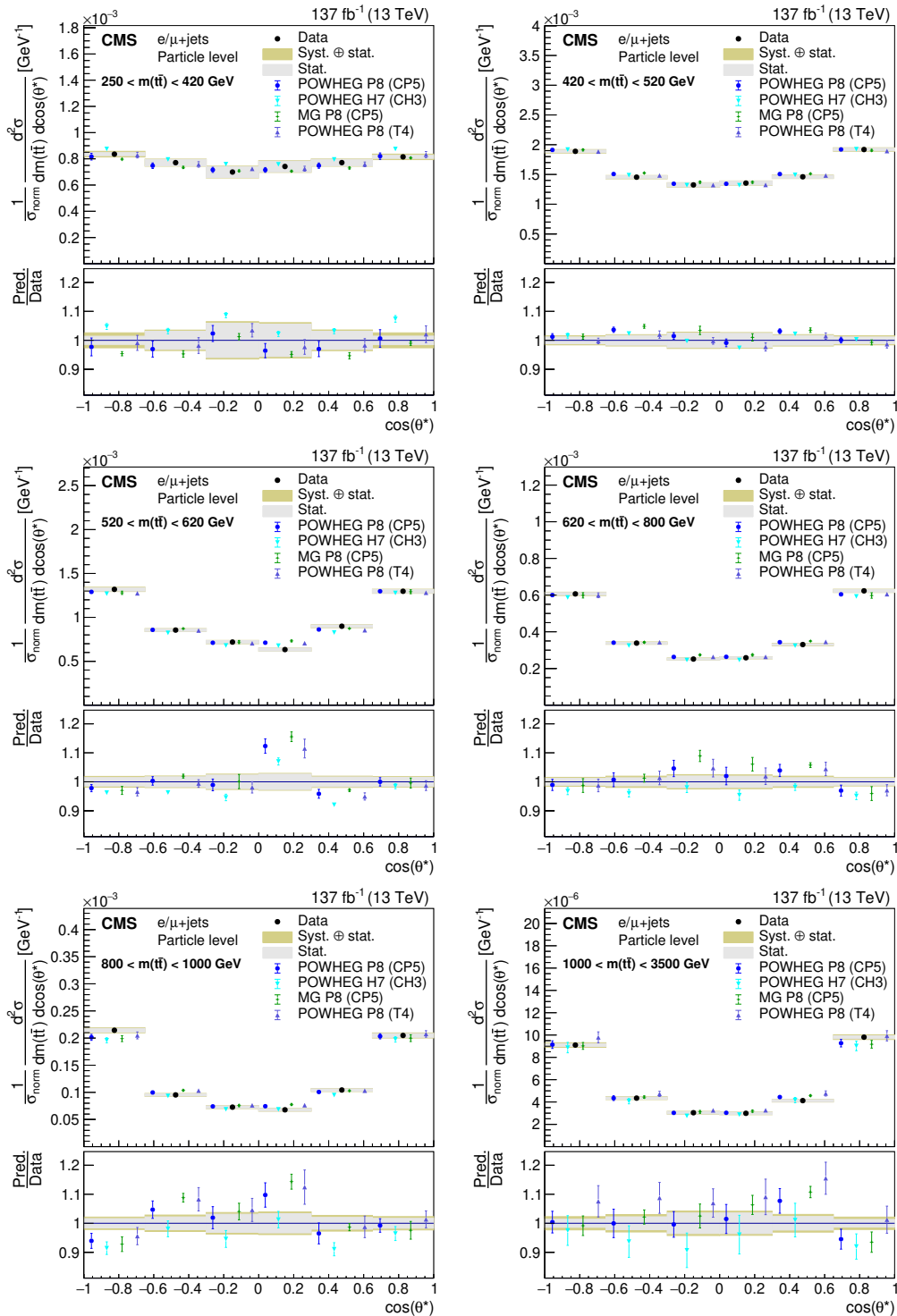


Figure A.12: Normalized double-differential cross section at the particle level as a function of $m(t\bar{t})$ vs. $\cos(\theta^*)$. The data are shown as points with gray (yellow) bands indicating the statistical (statistical and systematic) uncertainties. The cross sections are compared to the predictions of POWHEG+PYTHIA (P8) for the CP5 and CUETP8M2T4 (T4) tunes, POWHEG+HERWIG (H7), and the multiparton simulation MG5_aMC@NLO (MG)+PYTHIA. The ratios of the various predictions to the measured cross sections are shown in the lower panels.

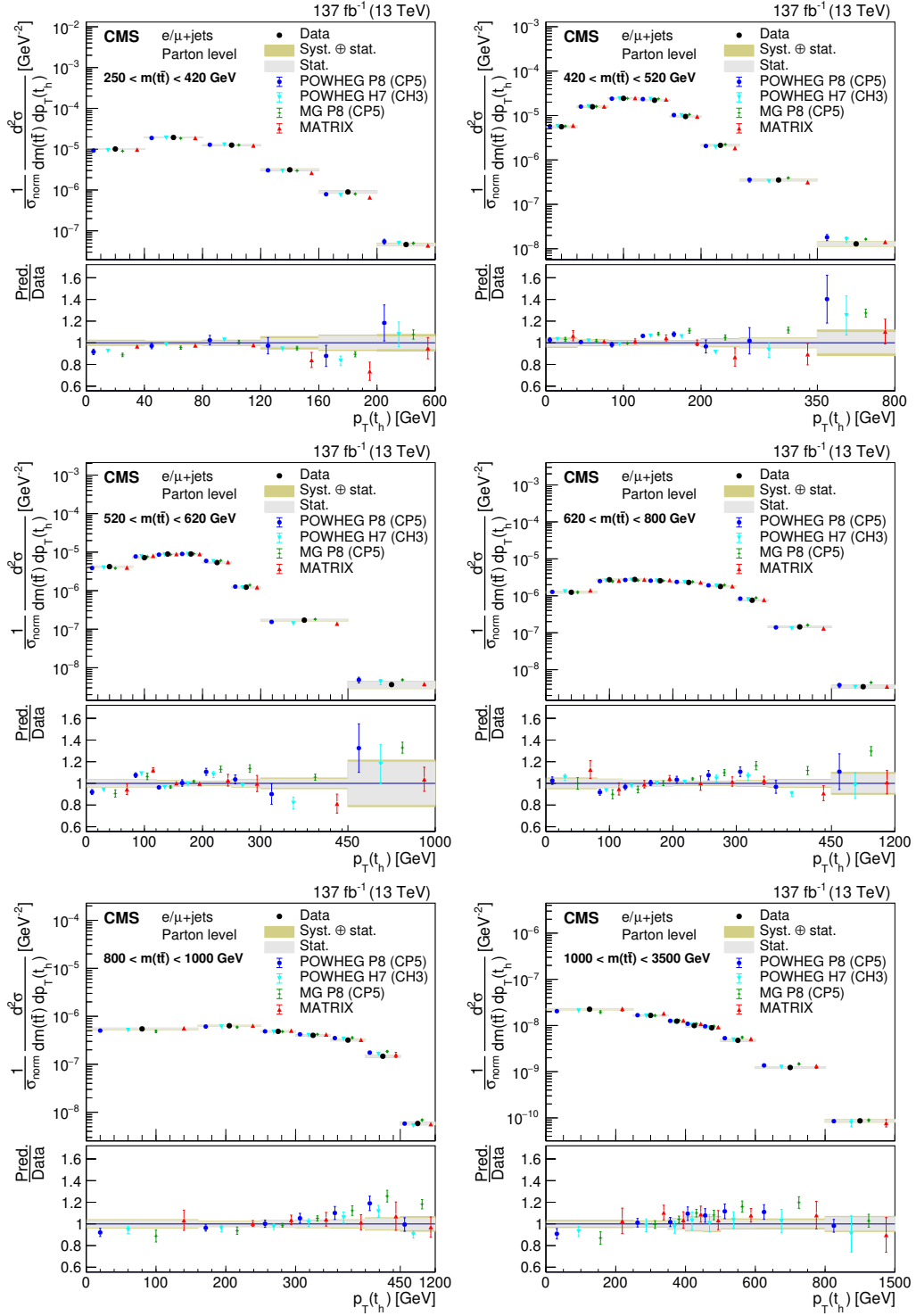


Figure A.13: Normalized double-differential cross section at the parton level as a function of $m(\bar{t}t)$ vs. $p_T(t_h)$. The data are shown as points with gray (yellow) bands indicating the statistical (systematic) uncertainties. The cross sections are compared to the predictions of POWHEG combined with PYTHIA (P8) or HERWIG (H7), the multiparton simulation MG5_aMC@NLO (MG)+PYTHIA FxFx, and the NNLO QCD calculations obtained with MATRIX. The ratios of the various predictions to the measured cross sections are shown in the lower panels.

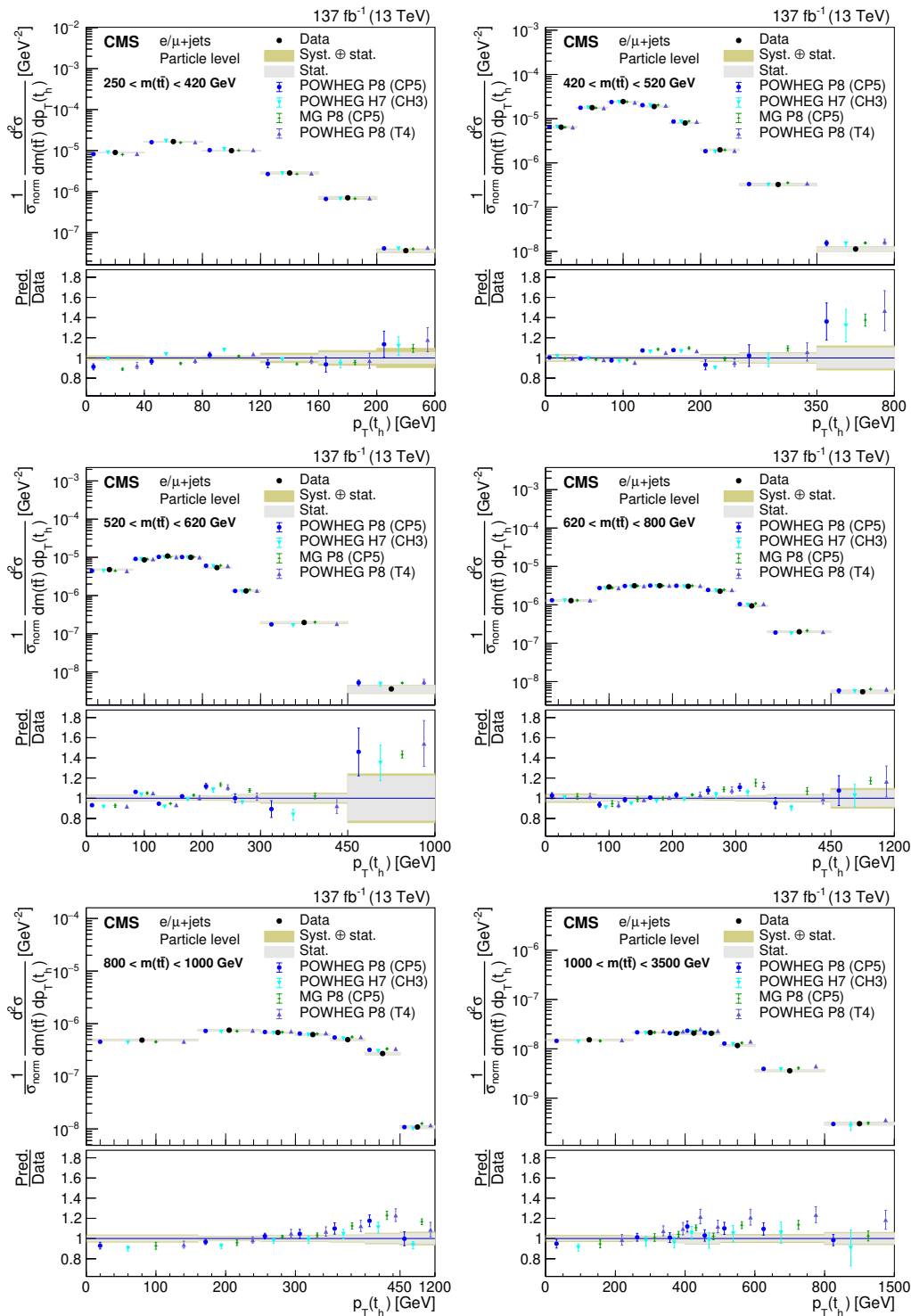


Figure A.14: Normalized double-differential cross section at the particle level as a function of $m(\bar{t}t)$ vs. $p_T(t_h)$. The data are shown as points with gray (yellow) bands indicating the statistical (statistical and systematic) uncertainties. The cross sections are compared to the predictions of POWHEG+PYTHIA (P8) for the CP5 and CUETP8M2T4 (T4) tunes, POWHEG+HERWIG (H7), and the multiparton simulation MG5_aMC@NLO (MG)+PYTHIA. The ratios of the various predictions to the measured cross sections are shown in the lower panels.

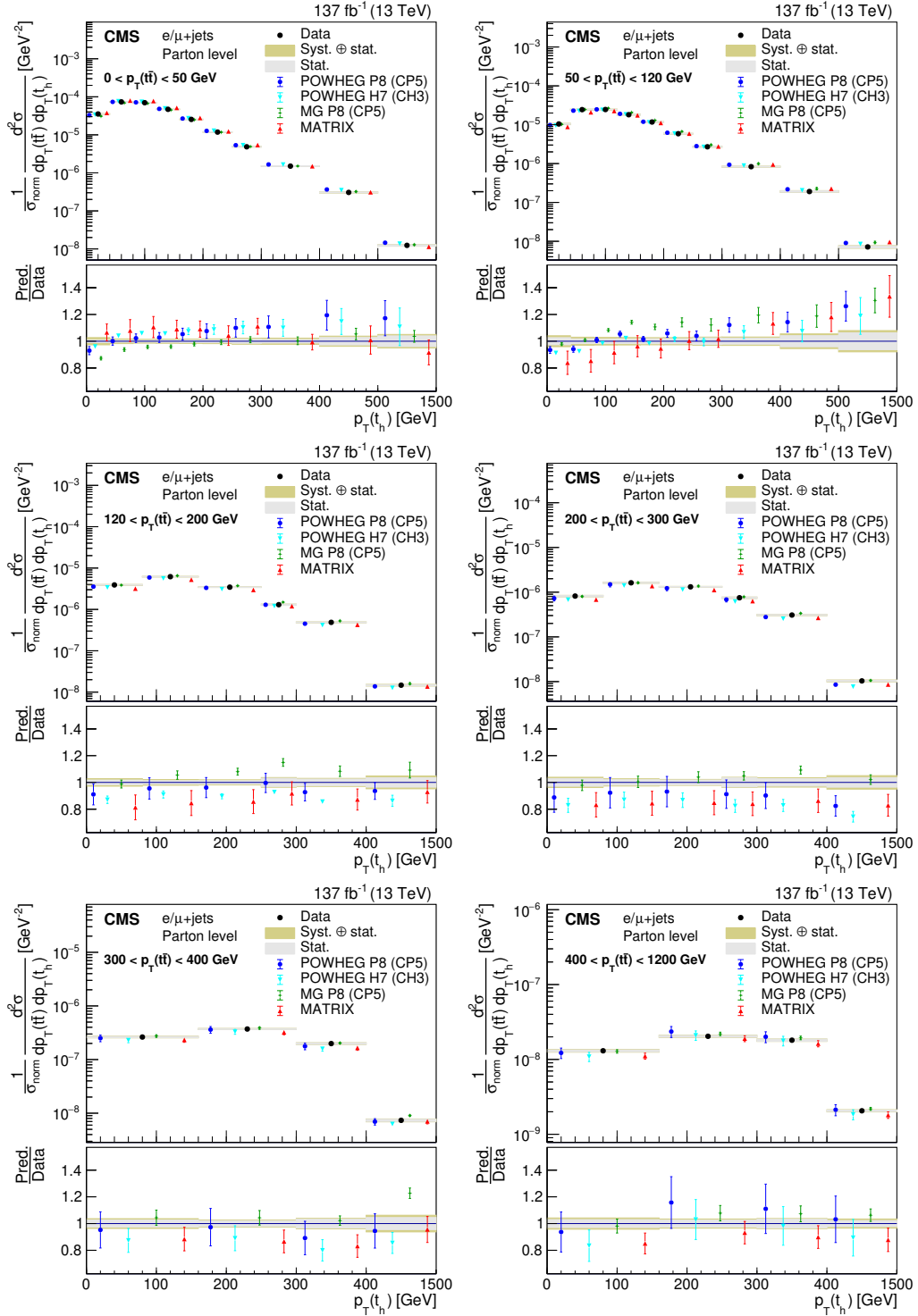


Figure A.15: Normalized double-differential cross section at the parton level as a function of $p_T(\bar{t})$ vs. $p_T(t_h)$. The data are shown as points with gray (yellow) bands indicating the statistical (systematic) uncertainties. The cross sections are compared to the predictions of POWHEG combined with PYTHIA (P8) or HERWIG (H7), the multiparton simulation MG5_aMC@NLO (MG)+PYTHIA FxFx, and the NNLO QCD calculations obtained with MATRIX. The ratios of the various predictions to the measured cross sections are shown in the lower panels.

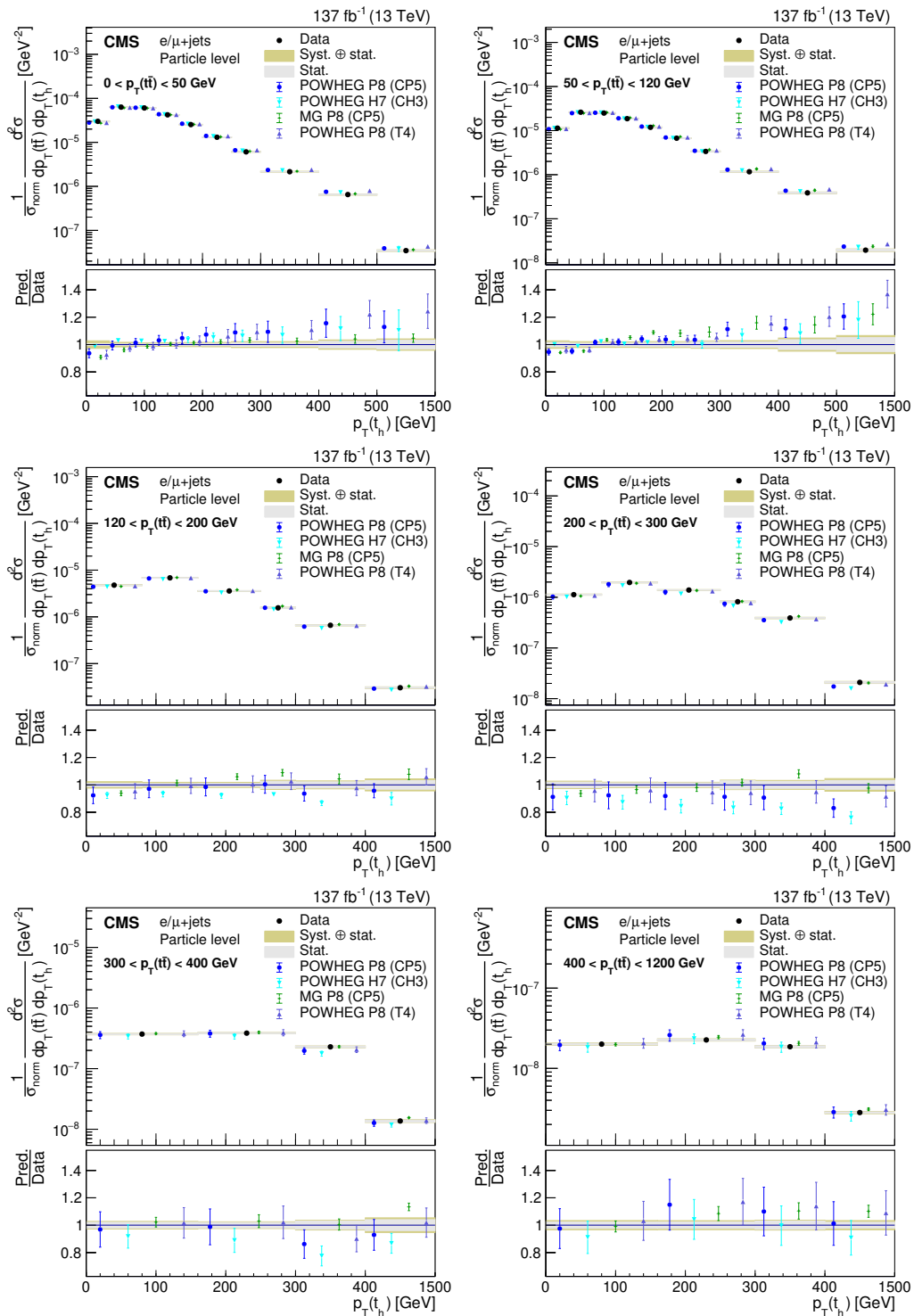


Figure A.16: Normalized double-differential cross section at the particle level as a function of $p_T(\bar{t}\bar{t})$ vs. $p_T(t_h)$. The data are shown as points with gray (yellow) bands indicating the statistical (statistical and systematic) uncertainties. The cross sections are compared to the predictions of POWHEG+PYTHIA (P8) for the CP5 and CUETP8M2T4 (T4) tunes, POWHEG+HERWIG (H7), and the multiparton simulation MG5_aMC@NLO (MG)+PYTHIA. The ratios of the various predictions to the measured cross sections are shown in the lower panels.

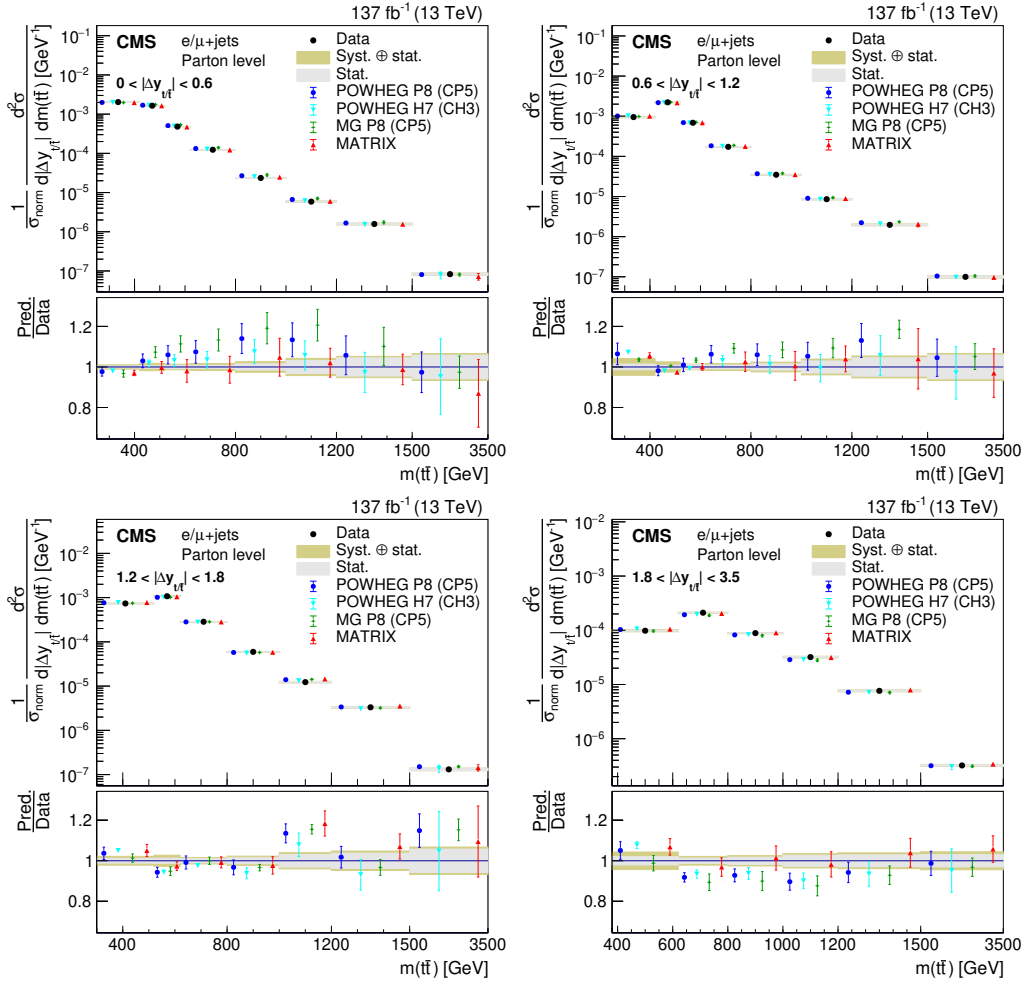


Figure A.17: Normalized double-differential cross section at the parton level as a function of $|\Delta y_{t/\bar{t}}|$ vs. $m(t\bar{t})$. The data are shown as points with gray (yellow) bands indicating the statistical (statistical and systematic) uncertainties. The cross sections are compared to the predictions of POWHEG combined with PYTHIA (P8) or HERWIG (H7), the multiparton simulation MG5_aMC@NLO (MG)+PYTHIA FxFx, and the NNLO QCD calculations obtained with MATRIX. The ratios of the various predictions to the measured cross sections are shown in the lower panels.

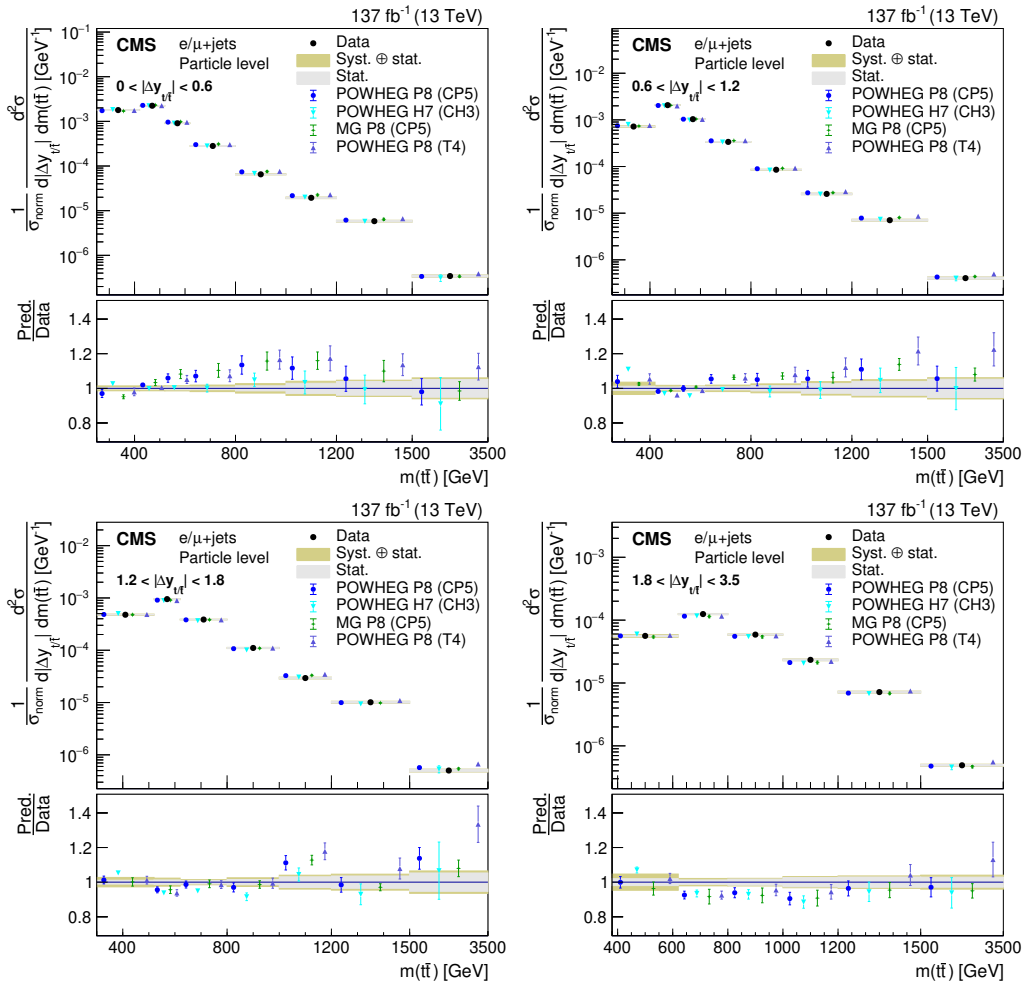


Figure A.18: Normalized double-differential cross section at the particle level as a function of $|\Delta y_{t\bar{t}}|$ vs. $m(t\bar{t})$. The data are shown as points with gray (yellow) bands indicating the statistical (statistical and systematic) uncertainties. The cross sections are compared to the predictions of POWHEG+PYTHIA (P8) for the CP5 and CUETP8M2T4 (T4) tunes, POWHEG+HERWIG (H7), and the multiparton simulation MG5_aMC@NLO (MG)+PYTHIA. The ratios of the various predictions to the measured cross sections are shown in the lower panels.

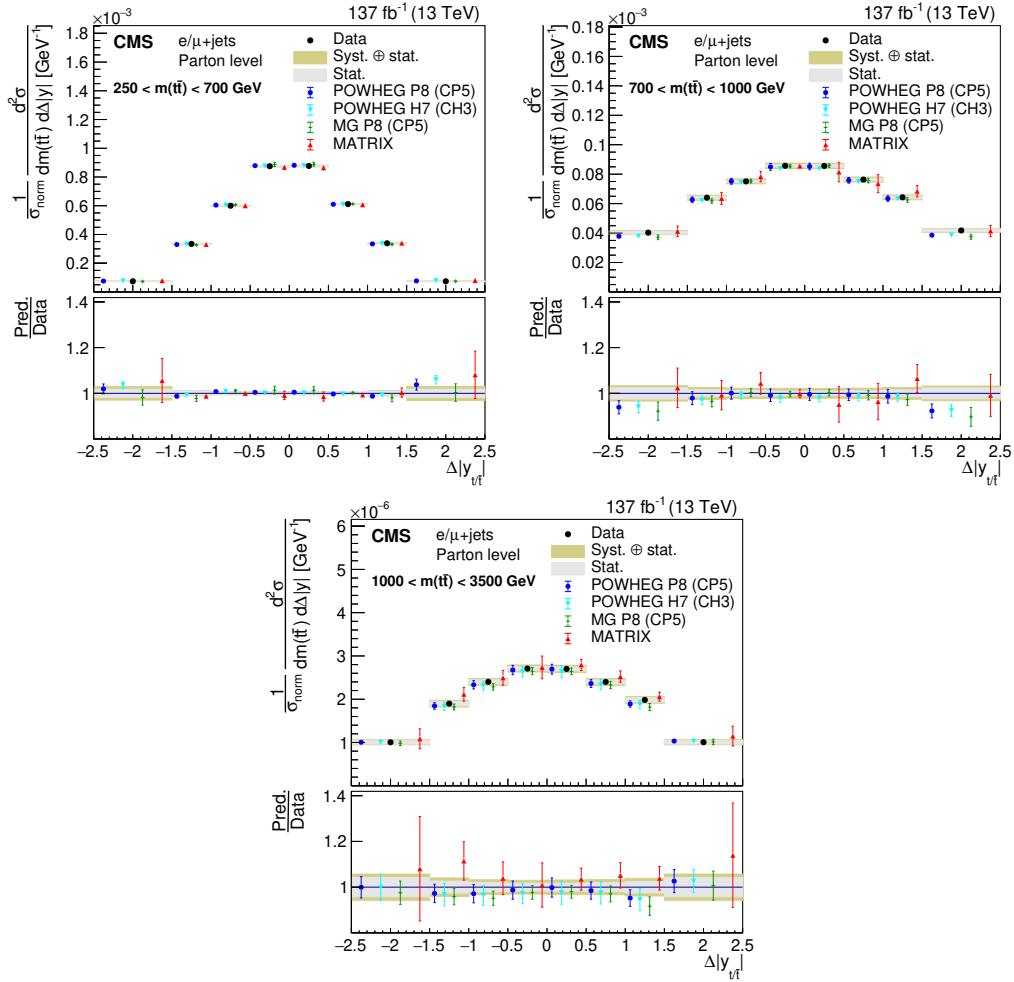


Figure A.19: Normalized double-differential cross section at the parton level as a function of $m(t\bar{t})$ vs. $\Delta|y_{t/\bar{t}}|$. The data are shown as points with gray (yellow) bands indicating the statistical (statistical and systematic) uncertainties. The cross sections are compared to the predictions of POWHEG combined with PYTHIA (P8) or HERWIG (H7), the multiparton simulation MG5_aMC@NLO (MG)+PYTHIA FxFx, and the NNLO QCD calculations obtained with MATRIX. The ratios of the various predictions to the measured cross sections are shown in the lower panels.

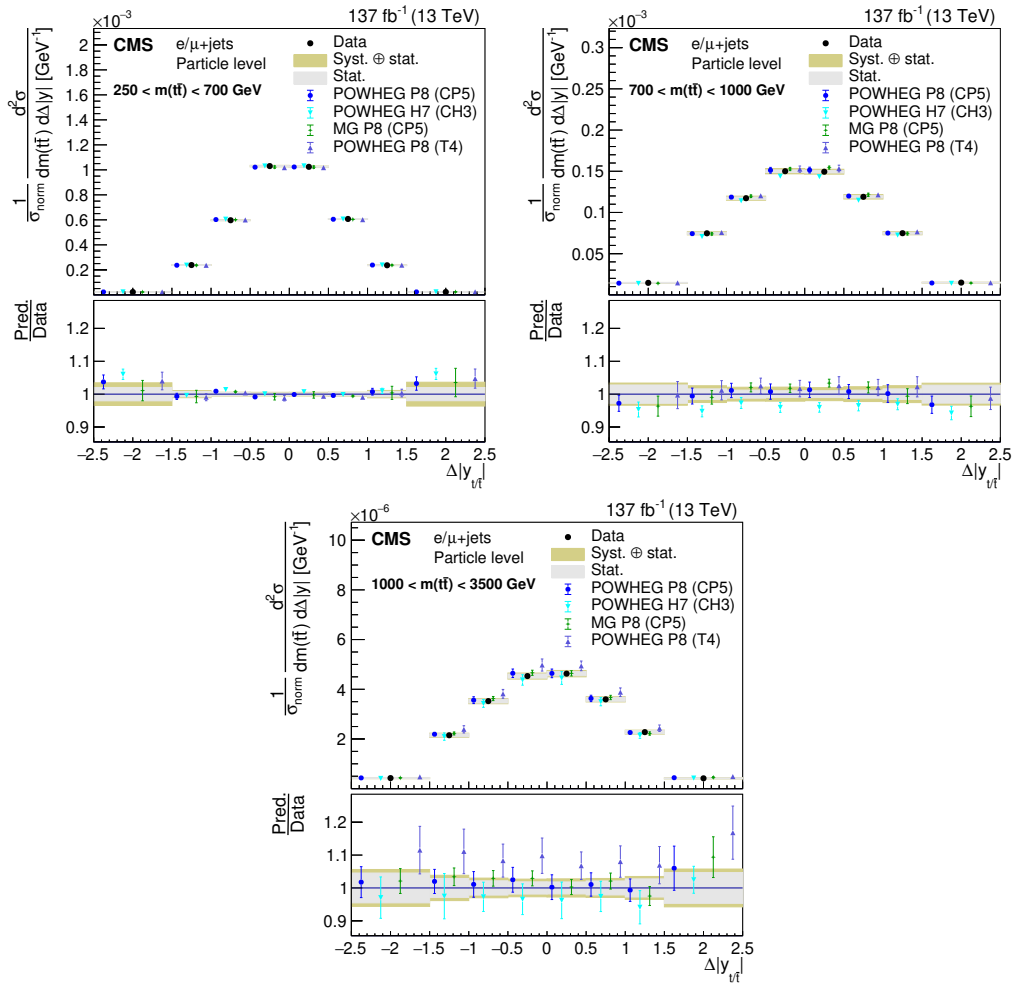


Figure A.20: Normalized double-differential cross section at the particle level as a function of $m(t\bar{t})$ vs. $|\Delta y_{t/\bar{t}}|$. The data are shown as points with gray (yellow) bands indicating the statistical (statistical and systematic) uncertainties. The cross sections are compared to the predictions of POWHEG+PYTHIA (P8) for the CP5 and CUETP8M2T4 (T4) tunes, POWHEG+HERWIG (H7), and the multiparton simulation MG5_aMC@NLO (MG)+PYTHIA. The ratios of the various predictions to the measured cross sections are shown in the lower panels.

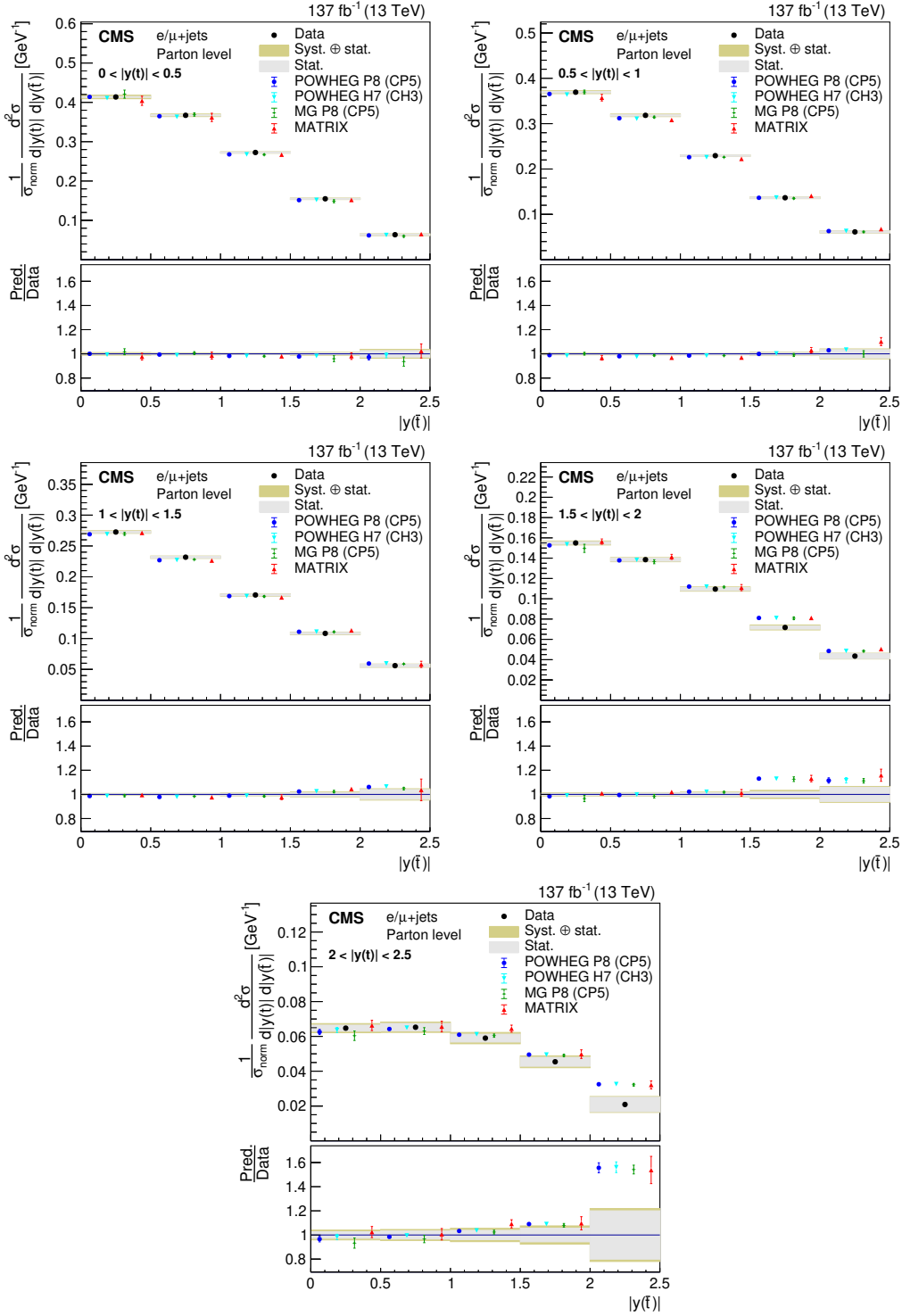


Figure A.21: Normalized double-differential cross section at the parton level as a function of $|y(t)|$ vs. $|y(\bar{t})|$. The data are shown as points with gray (yellow) bands indicating the statistical (statistical and systematic) uncertainties. The cross sections are compared to the predictions of POWHEG combined with PYTHIA (P8) or HERWIG (H7), the multiparton simulation MG5_aMC@NLO (MG)+PYTHIA FxFx, and the NNLO QCD calculations obtained with MATRIX. The ratios of the various predictions to the measured cross sections are shown in the lower panels.

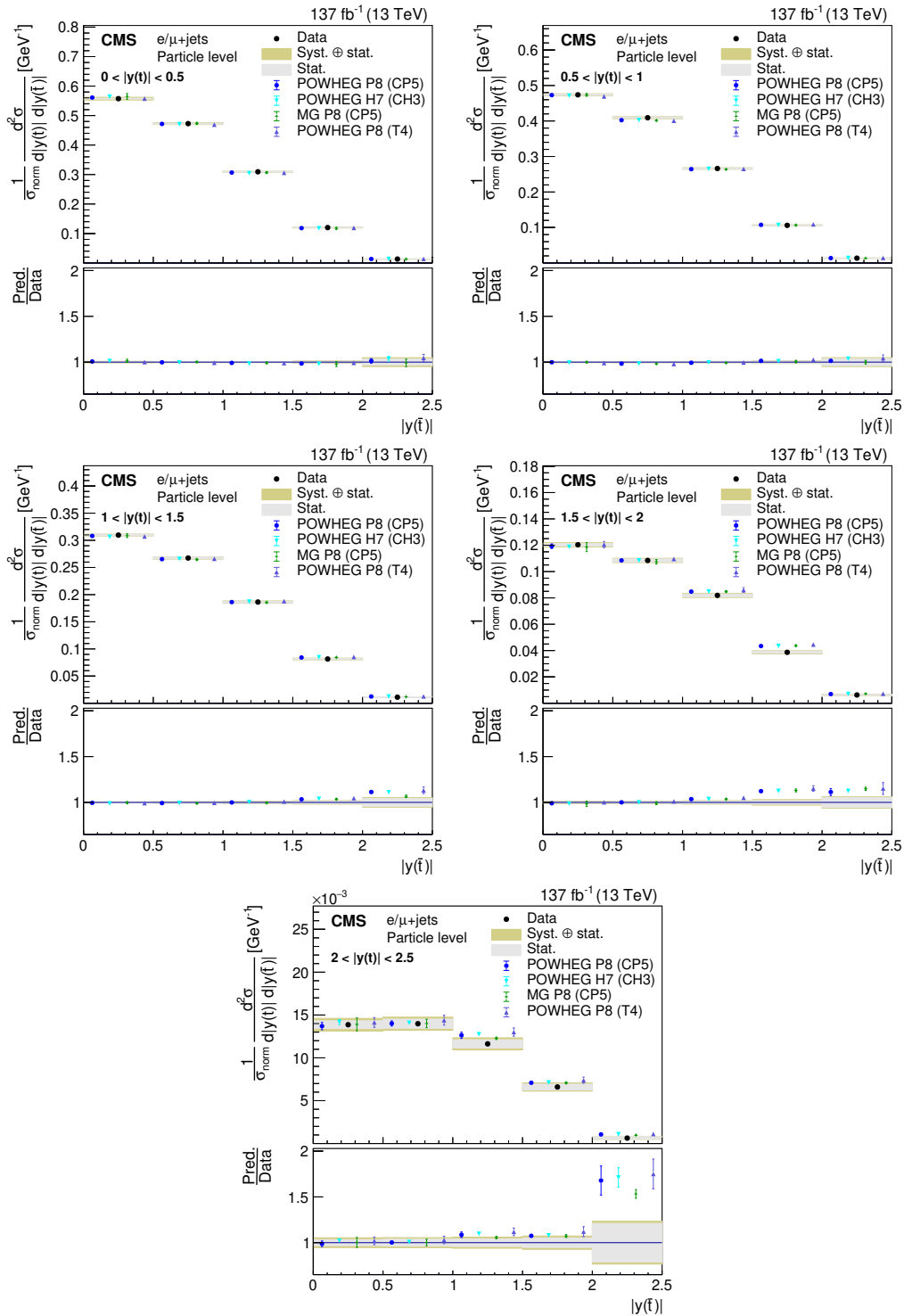


Figure A.22: Normalized double-differential cross section at the particle level as a function of $|y(t)|$ vs. $|y(\bar{t})|$. The data are shown as points with gray (yellow) bands indicating the statistical (stat.) and systematic (Syst.) uncertainties. The cross sections are compared to the predictions of POWHEG+PYTHIA (P8) for the CP5 and CUETP8M2T4 (T4) tunes, POWHEG+HERWIG (H7), and the multiparton simulation MG5_aMC@NLO (MG)+PYTHIA. The ratios of the various predictions to the measured cross sections are shown in the lower panels.

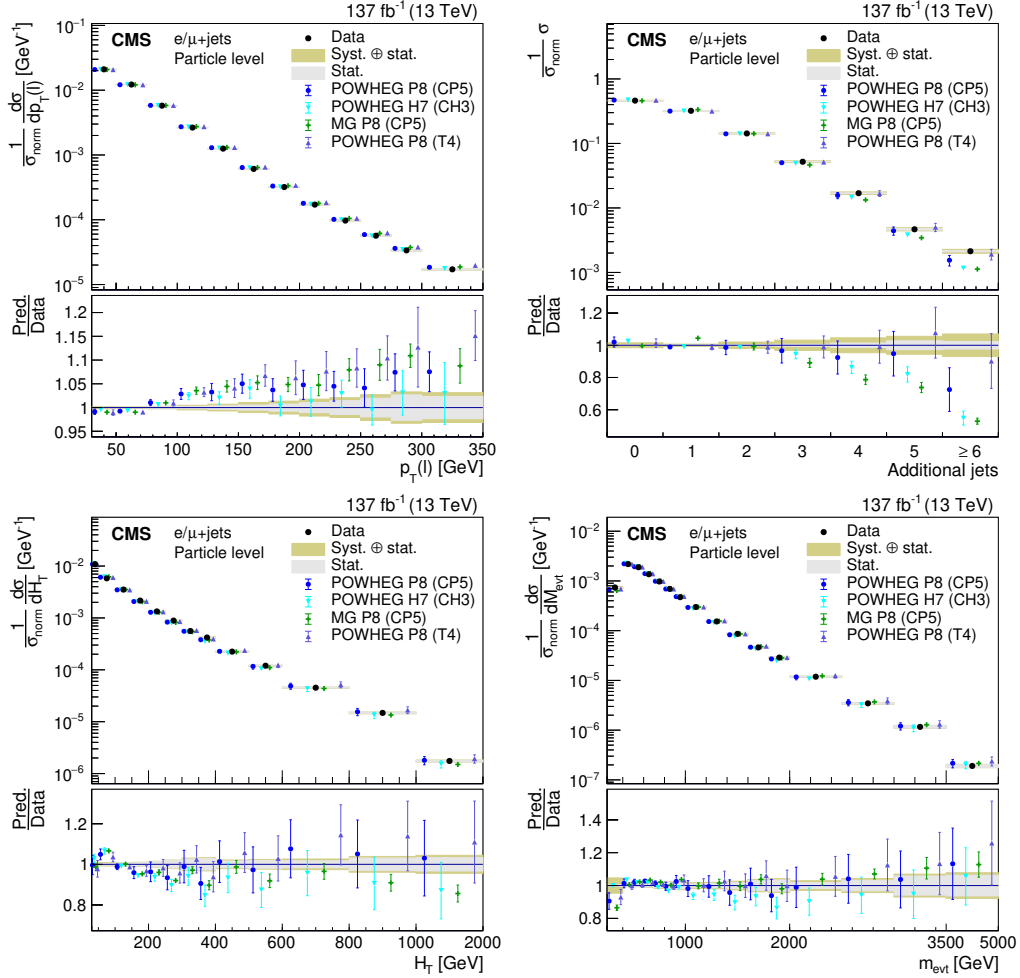


Figure A.23: Normalized differential cross sections at the particle level as a function of $p_T(\ell)$, jet multiplicity, H_T , and m_{evt} . The data are shown as points with gray (yellow) bands indicating the statistical (statistical and systematic) uncertainties. The cross sections are compared to the predictions of POWHEG+PYTHIA (P8) for the CP5 and CUETP8M2T4 (T4) tunes, POWHEG+HERWIG (H7), and the multiparton simulation MG5_aMC@NLO (MG)+PYTHIA. The ratios of the various predictions to the measured cross sections are shown in the lower panels.

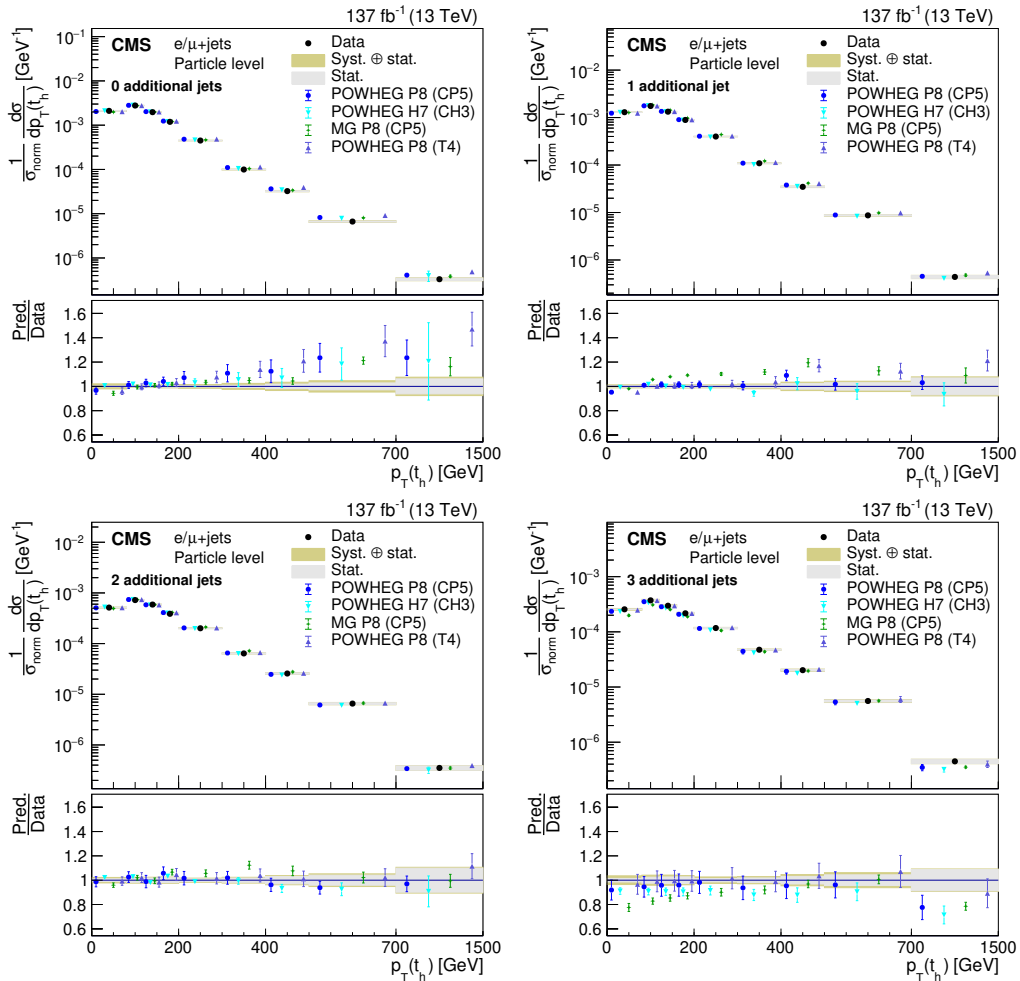


Figure A.24: Normalized differential cross section at the particle level as a function of $p_T(t_h)$ in bins of jet multiplicity. The data are shown as points with gray (yellow) bands indicating the statistical (statistical and systematic) uncertainties. The cross sections are compared to the predictions of POWHEG+PYTHIA (P8) for the CP5 and CUETP8M2T4 (T4) tunes, POWHEG+HERWIG (H7), and the multiparton simulation MG5_aMC@NLO (MG)+PYTHIA. The ratios of the various predictions to the measured cross sections are shown in the lower panels.

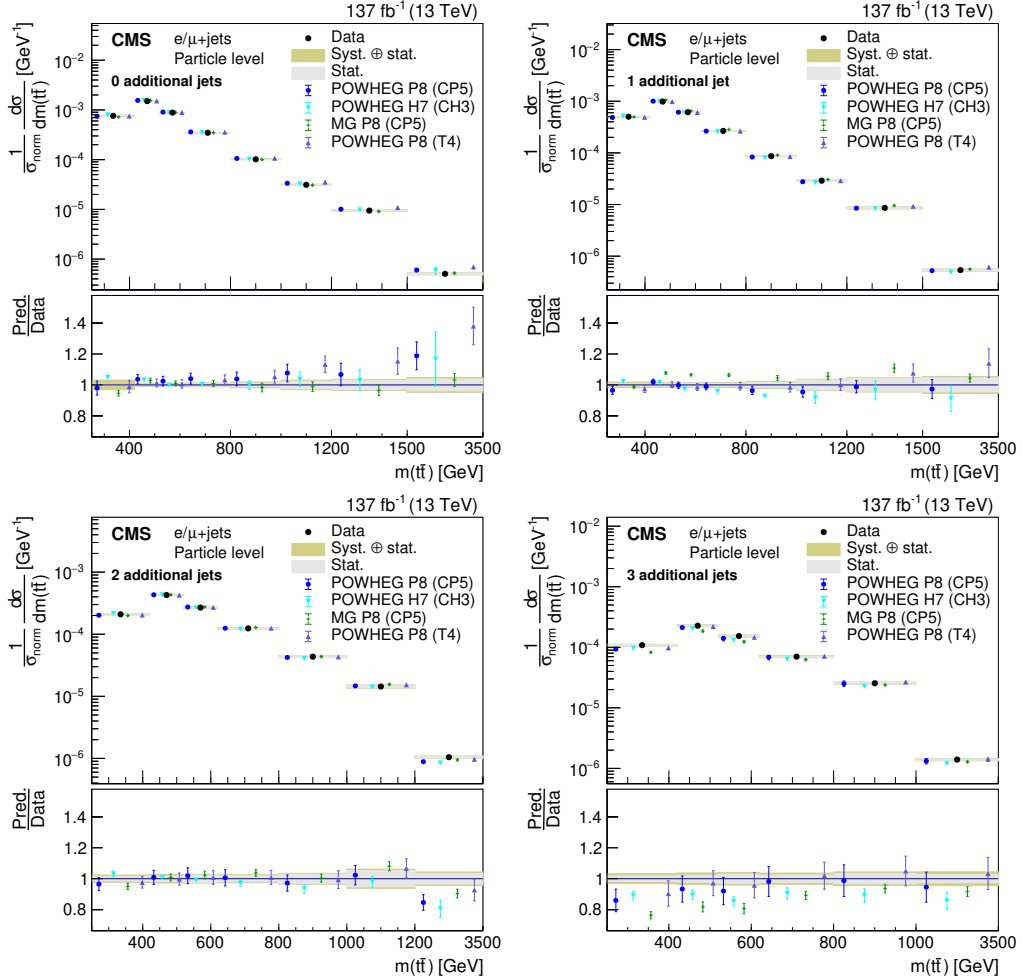


Figure A.25: Normalized differential cross section at the particle level as a function of $m(t\bar{t})$ in bins of jet multiplicity. The data are shown as points with gray (yellow) bands indicating the statistical (statistical and systematic) uncertainties. The cross sections are compared to the predictions of POWHEG+PYTHIA (P8) for the CP5 and CUETP8M2T4 (T4) tunes, POWHEG+HERWIG (H7), and the multiparton simulation MG5_aMC@NLO (MG)+PYTHIA. The ratios of the various predictions to the measured cross sections are shown in the lower panels.

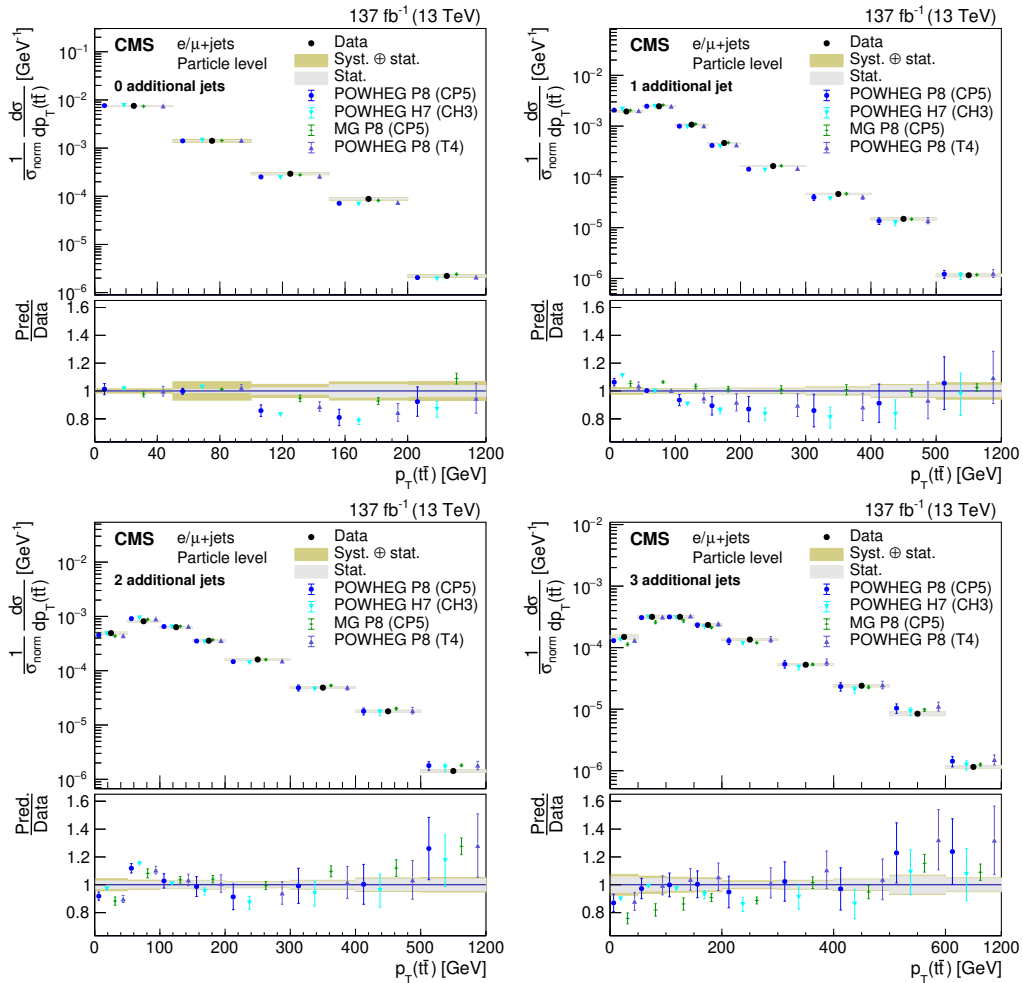


Figure A.26: Normalized differential cross section at the particle level as a function of $p_T(t\bar{t})$ in bins of jet multiplicity. The data are shown as points with gray (yellow) bands indicating the statistical (statistical and systematic) uncertainties. The cross sections are compared to the predictions of POWHEG+PYTHIA (P8) for the CP5 and CUETP8M2T4 (T4) tunes, POWHEG+HERWIG (H7), and the multiparton simulation MG5_aMC@NLO (MG)+PYTHIA. The ratios of the various predictions to the measured cross sections are shown in the lower panels.

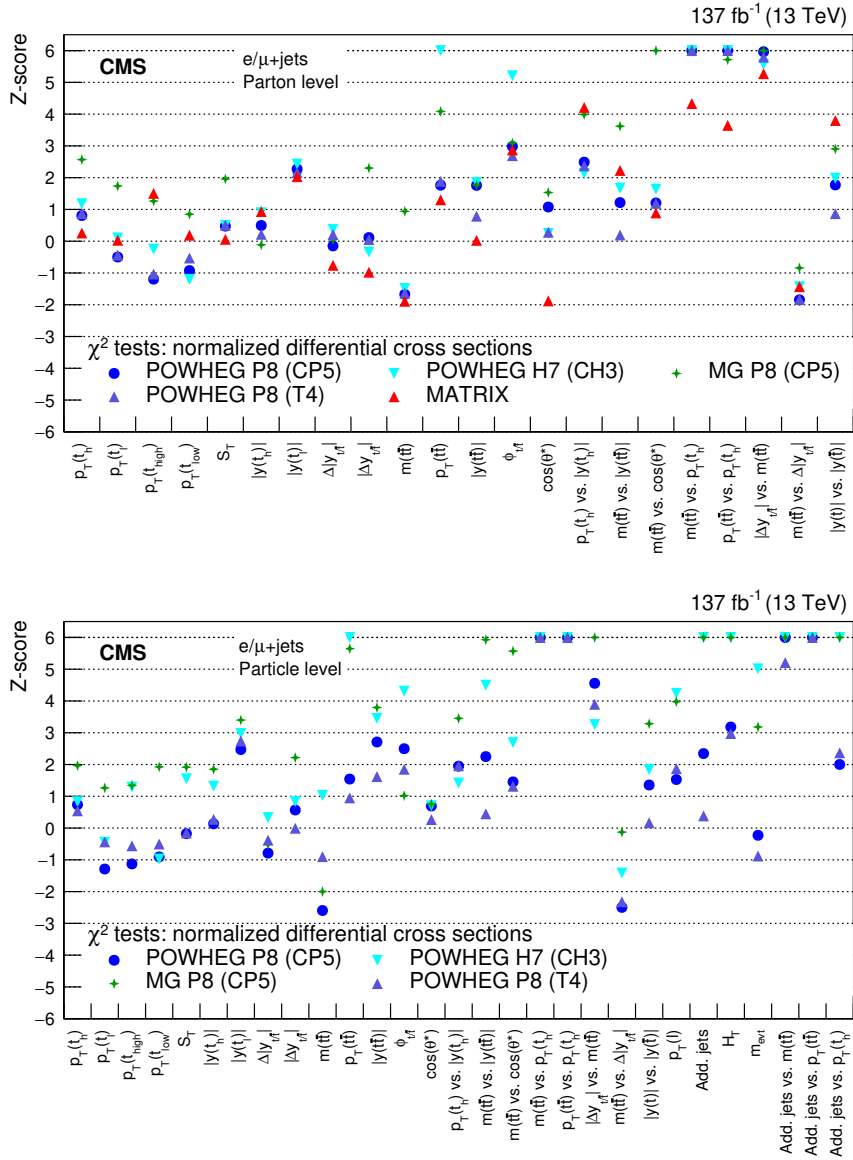


Figure A.27: Results of χ^2 tests in Z-scores comparing the measured normalized cross sections at the parton (upper) and particle (lower) levels to the predictions of POWHEG+PYTHIA (P8) for the CP5 and CUETP8M2T4 (T4) tunes, POWHEG+HERWIG (H7), the multiparton simulation MG5_aMC@NLO (MG)+PYTHIA FxFx, and the NNLO QCD calculations obtained with MATRIX. The Z-scores are truncated at an upper limit of six. The uncertainties in the measurements and the predictions are taken into account for the calculation of the χ^2 .

B The CMS Collaboration

Yerevan Physics Institute, Yerevan, Armenia

A. Tumasyan

Institut für Hochenergiephysik, Vienna, Austria

W. Adam, J.W. Andrejkovic, T. Bergauer, S. Chatterjee, M. Dragicevic, A. Escalante Del Valle, R. Frühwirth¹, M. Jeitler¹, N. Krammer, L. Lechner, D. Liko, I. Mikulec, P. Paulitsch, F.M. Pitters, J. Schieck¹, R. Schöfbeck, M. Spanring, S. Templ, W. Waltenberger, C.-E. Wulz¹

Institute for Nuclear Problems, Minsk, Belarus

V. Chekhovsky, A. Litomin, V. Makarenko

Universiteit Antwerpen, Antwerpen, Belgium

M.R. Darwish², E.A. De Wolf, T. Janssen, T. Kello³, A. Lelek, H. Rejeb Sfar, P. Van Mechelen, S. Van Putte, N. Van Remortel

Vrije Universiteit Brussel, Brussel, Belgium

F. Blekman, E.S. Bols, J. D'Hondt, M. Delcourt, H. El Faham, S. Lowette, S. Moortgat, A. Morton, D. Müller, A.R. Sahasransu, S. Tavernier, W. Van Doninck, P. Van Mulders

Université Libre de Bruxelles, Bruxelles, Belgium

D. Beghin, B. Bilin, B. Clerbaux, G. De Lentdecker, L. Favart, A. Grebenyuk, A.K. Kalsi, K. Lee, M. Mahdavihorrani, I. Makarenko, L. Moureaux, L. Pétré, A. Popov, N. Postiau, E. Starling, L. Thomas, M. Vanden Bemden, C. Vander Velde, P. Vanlaer, D. Vannerom, L. Wezenbeek

Ghent University, Ghent, Belgium

T. Cornelis, D. Dobur, J. Knolle, L. Lambrecht, G. Mestdach, M. Niedziela, C. Roskas, A. Samalan, K. Skovpen, M. Tytgat, B. Vermassen, M. Vit

Université Catholique de Louvain, Louvain-la-Neuve, Belgium

A. Bethani, G. Bruno, F. Bury, C. Caputo, P. David, C. Delaere, I.S. Donertas, A. Giammanco, K. Jaffel, Sa. Jain, V. Lemaitre, K. Mondal, J. Prisciandaro, A. Taliercio, M. Teklishyn, T.T. Tran, P. Vischia, S. Wertz

Centro Brasileiro de Pesquisas Fisicas, Rio de Janeiro, Brazil

G.A. Alves, C. Hensel, A. Moraes

Universidade do Estado do Rio de Janeiro, Rio de Janeiro, Brazil

W.L. Aldá Júnior, M. Alves Gallo Pereira, M. Barroso Ferreira Filho, H. BRANDAO MALBOUISSON, W. Carvalho, J. Chinellato⁴, E.M. Da Costa, G.G. Da Silveira⁵, D. De Jesus Damiao, S. Fonseca De Souza, D. Matos Figueiredo, C. Mora Herrera, K. Mota Amarilo, L. Mundim, H. Nogima, P. Rebello Teles, A. Santoro, S.M. Silva Do Amaral, A. Sznajder, M. Thiel, F. Torres Da Silva De Araujo, A. Vilela Pereira

Universidade Estadual Paulista ^a, Universidade Federal do ABC ^b, São Paulo, Brazil

C.A. Bernardes^{a,a,5}, L. Calligaris^a, T.R. Fernandez Perez Tomei^a, E.M. Gregores^{a,b}, D.S. Lemos^a, P.G. Mercadante^{a,b}, S.F. Novaes^a, Sandra S. Padula^a

Institute for Nuclear Research and Nuclear Energy, Bulgarian Academy of Sciences, Sofia, Bulgaria

A. Aleksandrov, G. Antchev, R. Hadjiiska, P. Iaydjiev, M. Misheva, M. Rodozov, M. Shopova, G. Sultanov

University of Sofia, Sofia, Bulgaria

A. Dimitrov, T. Ivanov, L. Litov, B. Pavlov, P. Petkov, A. Petrov

Beihang University, Beijing, China

T. Cheng, Q. Guo, T. Javaid⁶, M. Mittal, H. Wang, L. Yuan

Department of Physics, Tsinghua University

M. Ahmad, G. Bauer, C. Dozen⁷, Z. Hu, J. Martins⁸, Y. Wang, K. Yi^{9,10}

Institute of High Energy Physics, Beijing, China

E. Chapon, G.M. Chen⁶, H.S. Chen⁶, M. Chen, F. Iemmi, A. Kapoor, D. Leggat, H. Liao, Z.-A. LIU⁶, V. Milosevic, F. Monti, R. Sharma, J. Tao, J. Thomas-wilsker, J. Wang, H. Zhang, S. Zhang⁶, J. Zhao

State Key Laboratory of Nuclear Physics and Technology, Peking University, Beijing, China

A. Agapitos, Y. An, Y. Ban, C. Chen, A. Levin, Q. Li, X. Lyu, Y. Mao, S.J. Qian, D. Wang, Q. Wang, J. Xiao

Sun Yat-Sen University, Guangzhou, China

M. Lu, Z. You

Institute of Modern Physics and Key Laboratory of Nuclear Physics and Ion-beam Application (MOE) - Fudan University, Shanghai, China

X. Gao³, H. Okawa

Zhejiang University, Hangzhou, China

Z. Lin, M. Xiao

Universidad de Los Andes, Bogota, Colombia

C. Avila, A. Cabrera, C. Florez, J. Fraga

Universidad de Antioquia, Medellin, Colombia

J. Mejia Guisao, F. Ramirez, J.D. Ruiz Alvarez, C.A. Salazar González

University of Split, Faculty of Electrical Engineering, Mechanical Engineering and Naval Architecture, Split, Croatia

D. Giljanovic, N. Godinovic, D. Lelas, I. Puljak

University of Split, Faculty of Science, Split, Croatia

Z. Antunovic, M. Kovac, T. Sculac

Institute Rudjer Boskovic, Zagreb, Croatia

V. Brigljevic, D. Ferencek, D. Majumder, M. Roguljic, A. Starodumov¹¹, T. Susa

University of Cyprus, Nicosia, Cyprus

A. Attikis, K. Christoforou, E. Erodoutou, A. Ioannou, G. Kole, M. Kolosova, S. Konstantinou, J. Mousa, C. Nicolaou, F. Ptochos, P.A. Razis, H. Rykaczewski, H. Saka

Charles University, Prague, Czech Republic

M. Finger¹², M. Finger Jr.¹², A. Kveton

Escuela Politecnica Nacional, Quito, Ecuador

E. Ayala

Universidad San Francisco de Quito, Quito, Ecuador

E. Carrera Jarrin

Academy of Scientific Research and Technology of the Arab Republic of Egypt, Egyptian Network of High Energy Physics, Cairo, Egypt

H. Abdalla¹³, S. Elgammal¹⁴

Center for High Energy Physics (CHEP-FU), Fayoum University, El-Fayoum, Egypt

A. Lotfy, M.A. Mahmoud

National Institute of Chemical Physics and Biophysics, Tallinn, Estonia

S. Bhowmik, R.K. Dewanjee, K. Ehataht, M. Kadastik, S. Nandan, C. Nielsen, J. Pata, M. Raidal, L. Tani, C. Veelken

Department of Physics, University of Helsinki, Helsinki, Finland

P. Eerola, L. Forthomme, H. Kirschenmann, K. Osterberg, M. Voutilainen

Helsinki Institute of Physics, Helsinki, Finland

S. Bharthuar, E. Brücken, F. Garcia, J. Havukainen, M.S. Kim, R. Kinnunen, T. Lampén, K. Lassila-Perini, S. Lehti, T. Lindén, M. Lotti, L. Martikainen, M. Myllymäki, J. Ott, H. Siikonen, E. Tuominen, J. Tuominiemi

Lappeenranta University of Technology, Lappeenranta, Finland

P. Luukka, H. Petrow, T. Tuuva

IRFU, CEA, Université Paris-Saclay, Gif-sur-Yvette, FranceC. Amendola, M. Besancon, F. Couderc, M. Dejardin, D. Denegri, J.L. Faure, F. Ferri, S. Ganjour, A. Givernaud, P. Gras, G. Hamel de Monchenault, P. Jarry, B. Lenzi, E. Locci, J. Malcles, J. Rander, A. Rosowsky, M.Ö. Sahin, A. Savoy-Navarro¹⁵, M. Titov, G.B. Yu**Laboratoire Leprince-Ringuet, CNRS/IN2P3, Ecole Polytechnique, Institut Polytechnique de Paris, Palaiseau, France**

S. Ahuja, F. Beaudette, M. Bonanomi, A. Buchot Perraguin, P. Busson, A. Cappati, C. Charlot, O. Davignon, B. Diab, G. Falmagne, S. Ghosh, R. Granier de Cassagnac, A. Hakimi, I. Kucher, J. Motta, M. Nguyen, C. Ochando, P. Paganini, J. Rembser, R. Salerno, J.B. Sauvan, Y. Sirois, A. Tarabini, A. Zabi, A. Zghiche

Université de Strasbourg, CNRS, IPHC UMR 7178, Strasbourg, FranceJ.-L. Agram¹⁶, J. Andrea, D. Apparou, D. Bloch, G. Bourgatte, J.-M. Brom, E.C. Chabert, C. Collard, D. Darej, J.-C. Fontaine¹⁶, U. Goerlach, C. Grimault, A.-C. Le Bihan, E. Nibigira, P. Van Hove**Institut de Physique des 2 Infinis de Lyon (IP2I), Villeurbanne, France**

E. Asilar, S. Beauceron, C. Bernet, G. Boudoul, C. Camen, A. Carle, N. Chanon, D. Contardo, P. Depasse, H. El Mamouni, J. Fay, S. Gascon, M. Gouzevitch, B. Ille, I.B. Laktineh, H. Lattaud, A. Lesauvage, M. Lethuillier, L. Mirabito, S. Perries, K. Shchablo, V. Sordini, L. Torterotot, G. Touquet, M. Vander Donckt, S. Viret

Georgian Technical University, Tbilisi, GeorgiaI. Lomidze, T. Toriashvili¹⁷, Z. Tsamalaidze¹²**RWTH Aachen University, I. Physikalisches Institut, Aachen, Germany**

L. Feld, K. Klein, M. Lipinski, D. Meuser, A. Pauls, M.P. Rauch, N. Röwert, J. Schulz, M. Teroerde

RWTH Aachen University, III. Physikalisches Institut A, Aachen, Germany

A. Dodonova, D. Eliseev, M. Erdmann, P. Fackeldey, B. Fischer, S. Ghosh, T. Hebbeker, K. Hoepfner, F. Ivone, H. Keller, L. Mastrolorenzo, M. Merschmeyer, A. Meyer, G. Mocellin, S. Mondal, S. Mukherjee, D. Noll, A. Novak, T. Pook, A. Pozdnyakov, Y. Rath, H. Reithler, J. Roemer, A. Schmidt, S.C. Schuler, A. Sharma, L. Vigilante, S. Wiedenbeck, S. Zaleski

RWTH Aachen University, III. Physikalisches Institut B, Aachen, Germany

C. Dziwok, G. Flügge, W. Haj Ahmad¹⁸, O. Hlushchenko, T. Kress, A. Nowack, C. Pistone, O. Pooth, D. Roy, H. Sert, A. Stahl¹⁹, T. Ziemons

Deutsches Elektronen-Synchrotron, Hamburg, Germany

H. Aarup Petersen, M. Aldaya Martin, P. Asmuss, I. Babounikau, S. Baxter, O. Behnke, A. Bermúdez Martínez, S. Bhattacharya, A.A. Bin Anuar, K. Borras²⁰, V. Botta, D. Brunner, A. Campbell, A. Cardini, C. Cheng, F. Colombina, S. Consuegra Rodríguez, G. Correia Silva, V. Danilov, L. Didukh, G. Eckerlin, D. Eckstein, L.I. Estevez Banos, O. Filatov, E. Gallo²¹, A. Geiser, A. Giraldi, A. Grohsjean, M. Guthoff, A. Jafari²², N.Z. Jomhari, H. Jung, A. Kasem²⁰, M. Kasemann, H. Kaveh, C. Kleinwort, D. Krücker, W. Lange, J. Lidrych, K. Lipka, W. Lohmann²³, R. Mankel, I.-A. Melzer-Pellmann, M. Mendizabal Morentin, J. Metwally, A.B. Meyer, M. Meyer, J. Mnich, A. Mussgiller, Y. Otariid, D. Pérez Adán, D. Pitzl, A. Raspereza, B. Ribeiro Lopes, J. Rübenach, A. Saggio, A. Saibel, M. Savitskyi, M. Scham, V. Scheurer, P. Schütze, C. Schwanenberger²¹, A. Singh, R.E. Sosa Ricardo, D. Stafford, N. Tonon, O. Turkot, M. Van De Klundert, R. Walsh, D. Walter, Y. Wen, K. Wichmann, L. Wiens, C. Wissing, S. Wuchterl

University of Hamburg, Hamburg, Germany

R. Aggleton, S. Albrecht, S. Bein, L. Benato, A. Benecke, P. Connor, K. De Leo, M. Eich, F. Feindt, A. Fröhlich, C. Garbers, E. Garutti, P. Gunnellini, J. Haller, A. Hinzmann, G. Kasieczka, R. Klanner, R. Kogler, T. Kramer, V. Kutzner, J. Lange, T. Lange, A. Lobanov, A. Malara, A. Nigamova, K.J. Pena Rodriguez, O. Rieger, P. Schleper, M. Schröder, J. Schwandt, D. Schwarz, J. Sonneveld, H. Stadie, G. Steinbrück, A. Tews, B. Vormwald, I. Zoi

Karlsruher Institut fuer Technologie, Karlsruhe, Germany

J. Bechtel, T. Berger, E. Butz, R. Caspart, T. Chwalek, W. De Boer[†], A. Dierlamm, A. Droll, K. El Morabit, N. Faltermann, M. Giffels, J.o. Gosewisch, A. Gottmann, F. Hartmann¹⁹, C. Heidecker, U. Husemann, P. Keicher, R. Koppenhöfer, S. Maier, M. Metzler, S. Mitra, Th. Müller, M. Neukum, A. Nürnberg, G. Quast, K. Rabbertz, J. Rauser, D. Savoiiu, M. Schnepf, D. Seith, I. Shvetsov, H.J. Simonis, R. Ulrich, J. Van Der Linden, R.F. Von Cube, M. Wassmer, M. Weber, S. Wieland, R. Wolf, S. Wozniewski, S. Wunsch

Institute of Nuclear and Particle Physics (INPP), NCSR Demokritos, Aghia Paraskevi, Greece

G. Anagnostou, G. Daskalakis, T. Gerasis, A. Kyriakis, D. Loukas, A. Stakia

National and Kapodistrian University of Athens, Athens, Greece

M. Diamantopoulou, D. Karasavvas, G. Karathanasis, P. Kontaxakis, C.K. Koraka, A. Manousakis-katsikakis, A. Panagiotou, I. Papavergou, N. Saoulidou, K. Theofilatos, E. Tziaferi, K. Vellidis, E. Vourliotis

National Technical University of Athens, Athens, Greece

G. Bakas, K. Kousouris, I. Papakrivopoulos, G. Tsipolitis, A. Zacharopoulou

University of Ioánnina, Ioánnina, Greece

I. Evangelou, C. Foudas, P. Giannelis, P. Katsoulis, P. Kokkas, N. Manthos, I. Papadopoulos, J. Strologas

MTA-ELTE Lendület CMS Particle and Nuclear Physics Group, Eötvös Loránd University

M. Csanad, K. Farkas, M.M.A. Gadallah²⁴, S. Lökös²⁵, P. Major, K. Mandal, A. Mehta, G. Pasztor, A.J. Rádl, O. Surányi, G.I. Veres

Wigner Research Centre for Physics, Budapest, Hungary

M. Bartók²⁶, G. Bencze, C. Hajdu, D. Horvath²⁷, F. Sikler, V. Veszpremi, G. Vesztergombi[†]

Institute of Nuclear Research ATOMKI, Debrecen, Hungary

S. Czellar, J. Karancki²⁶, J. Molnar, Z. Szillasi, D. Teyssier

Institute of Physics, University of Debrecen

P. Raics, Z.L. Trocsanyi²⁸, B. Ujvari

Karoly Robert Campus, MATE Institute of Technology

T. Csorgo²⁹, F. Nemes²⁹, T. Novak

Indian Institute of Science (IISc), Bangalore, India

J.R. Komaragiri, D. Kumar, L. Panwar, P.C. Tiwari

National Institute of Science Education and Research, HBNI, Bhubaneswar, India

S. Bahinipati³⁰, C. Kar, P. Mal, T. Mishra, V.K. Muraleedharan Nair Bindhu³¹, A. Nayak³¹, P. Saha, N. Sur, S.K. Swain, D. Vats³¹

Panjab University, Chandigarh, India

S. Bansal, S.B. Beri, V. Bhatnagar, G. Chaudhary, S. Chauhan, N. Dhingra³², R. Gupta, A. Kaur, M. Kaur, S. Kaur, P. Kumari, M. Meena, K. Sandeep, J.B. Singh, A.K. Viridi

University of Delhi, Delhi, India

A. Ahmed, A. Bhardwaj, B.C. Choudhary, M. Gola, S. Keshri, A. Kumar, M. Naimuddin, P. Priyanka, K. Ranjan, A. Shah

Saha Institute of Nuclear Physics, HBNI, Kolkata, India

M. Bharti³³, R. Bhattacharya, S. Bhattacharya, D. Bhowmik, S. Dutta, S. Dutta, B. Gomber³⁴, M. Maity³⁵, P. Palit, P.K. Rout, G. Saha, B. Sahu, S. Sarkar, M. Sharan, B. Singh³³, S. Thakur³³

Indian Institute of Technology Madras, Madras, India

P.K. Behera, S.C. Behera, P. Kalbhor, A. Muhammad, R. Pradhan, P.R. Pujahari, A. Sharma, A.K. Sikdar

Bhabha Atomic Research Centre, Mumbai, India

D. Dutta, V. Jha, V. Kumar, D.K. Mishra, K. Naskar³⁶, P.K. Netrakanti, L.M. Pant, P. Shukla

Tata Institute of Fundamental Research-A, Mumbai, India

T. Aziz, S. Dugad, M. Kumar, U. Sarkar

Tata Institute of Fundamental Research-B, Mumbai, India

S. Banerjee, R. Chudasama, M. Guchait, S. Karmakar, S. Kumar, G. Majumder, K. Mazumdar, S. Mukherjee

Indian Institute of Science Education and Research (IISER), Pune, India

K. Alpana, S. Dube, B. Kansal, A. Laha, S. Pandey, A. Rane, A. Rastogi, S. Sharma

Department of Physics, Isfahan University of Technology

H. Bakhshiansohi³⁷, E. Khazaie, M. Zeinali³⁸

Institute for Research in Fundamental Sciences (IPM), Tehran, Iran

S. Chenarani³⁹, S.M. Etesami, M. Khakzad, M. Mohammadi Najafabadi

University College Dublin, Dublin, Ireland

M. Grunewald

INFN Sezione di Bari ^a, Università di Bari ^b, Politecnico di Bari ^c, Bari, Italy

M. Abbrescia^{a,b}, R. Aly^{a,b,40}, C. Aruta^{a,b}, A. Colaleo^a, D. Creanza^{a,c}, N. De Filippis^{a,c}, M. De Palma^{a,b}, A. Di Florio^{a,b}, A. Di Pilato^{a,b}, W. Elmetenawee^{a,b}, L. Fiore^a, A. Gelmi^{a,b}, M. Gul^a, G. Iaselli^{a,c}, M. Ince^{a,b}, S. Lezki^{a,b}, G. Maggi^{a,c}, M. Maggi^a, I. Margjeka^{a,b}, V. Mastrapasqua^{a,b}, J.A. Merlin^a, S. My^{a,b}, S. Nuzzo^{a,b}, A. Pellecchia^{a,b}, A. Pompili^{a,b}, G. Pugliese^{a,c}, A. Ranieri^a, G. Selvaggi^{a,b}, L. Silvestris^a, F.M. Simone^{a,b}, R. Venditti^a, P. Verwilligen^a

INFN Sezione di Bologna ^a, Università di Bologna ^b, Bologna, Italy

G. Abbiendi^a, C. Battilana^{a,b}, D. Bonacorsi^{a,b}, L. Borgonovi^a, L. Brigliadori^a, R. Campanini^{a,b}, P. Capiluppi^{a,b}, A. Castro^{a,b}, F.R. Cavallo^a, M. Cuffiani^{a,b}, G.M. Dallavalle^a, T. Diotallevi^{a,b}, F. Fabbri^a, A. Fanfani^{a,b}, P. Giacomelli^a, L. Giommi^{a,b}, C. Grandi^a, L. Guiducci^{a,b}, S. Lo Meo^{a,41}, L. Lunerti^{a,b}, S. Marcellini^a, G. Masetti^a, F.L. Navarria^{a,b}, A. Perrotta^a, F. Primavera^{a,b}, A.M. Rossi^{a,b}, T. Rovelli^{a,b}, G.P. Siroli^{a,b}

INFN Sezione di Catania ^a, Università di Catania ^b, Catania, Italy

S. Albergo^{a,b,42}, S. Costa^{a,b,42}, A. Di Mattia^a, R. Potenza^{a,b}, A. Tricomi^{a,b,42}, C. Tuve^{a,b}

INFN Sezione di Firenze ^a, Università di Firenze ^b, Firenze, Italy

G. Barbagli^a, A. Cassese^a, R. Ceccarelli^{a,b}, V. Ciulli^{a,b}, C. Civinini^a, R. D'Alessandro^{a,b}, E. Focardi^{a,b}, G. Latino^{a,b}, P. Lenzi^{a,b}, M. Lizzo^{a,b}, M. Meschini^a, S. Paoletti^a, R. Seidita^{a,b}, G. Sguazzoni^a, L. Viliani^a

INFN Laboratori Nazionali di Frascati, Frascati, Italy

L. Benussi, S. Bianco, D. Piccolo

INFN Sezione di Genova ^a, Università di Genova ^b, Genova, Italy

M. Bozzo^{a,b}, F. Ferro^a, R. Mulargia^{a,b}, E. Robutti^a, S. Tosi^{a,b}

INFN Sezione di Milano-Bicocca ^a, Università di Milano-Bicocca ^b, Milano, Italy

A. Benaglia^a, F. Brivio^{a,b}, F. Cetorelli^{a,b}, V. Ciriolo^{a,b,19}, F. De Guio^{a,b}, M.E. Dinardo^{a,b}, P. Dini^a, S. Gennai^a, A. Ghezzi^{a,b}, P. Govoni^{a,b}, L. Guzzi^{a,b}, M. Malberti^a, S. Malvezzi^a, A. Massironi^a, D. Menasce^a, L. Moroni^a, M. Paganoni^{a,b}, D. Pedrini^a, S. Ragazzi^{a,b}, N. Redaelli^a, T. Tabarelli de Fatis^{a,b}, D. Valsecchi^{a,b,19}, D. Zuolo^{a,b}

INFN Sezione di Napoli ^a, Università di Napoli 'Federico II' ^b, Napoli, Italy, Università della Basilicata ^c, Potenza, Italy, Università G. Marconi ^d, Roma, Italy

S. Buontempo^a, F. Carnevali^{a,b}, N. Cavallo^{a,c}, A. De Iorio^{a,b}, F. Fabozzi^{a,c}, A.O.M. Iorio^{a,b}, L. Lista^{a,b}, S. Meola^{a,d,19}, P. Paolucci^{a,19}, B. Rossi^a, C. Sciacca^{a,b}

INFN Sezione di Padova ^a, Università di Padova ^b, Padova, Italy, Università di Trento ^c, Trento, Italy

P. Azzi^a, N. Bacchetta^a, D. Bisello^{a,b}, P. Bortignon^a, A. Bragagnolo^{a,b}, R. Carlin^{a,b}, P. Checchia^a, T. Dorigo^a, U. Dosselli^a, F. Gasparini^{a,b}, U. Gasparini^{a,b}, G. Grosso, S.Y. Hoh^{a,b}, L. Layer^{a,43}, E. Lusiani, M. Margoni^{a,b}, A.T. Meneguzzo^{a,b}, J. Pazzini^{a,b}, M. Presilla^{a,b}, P. Ronchese^{a,b}, R. Rossin^{a,b}, F. Simonetto^{a,b}, G. Strong^a, M. Tosi^{a,b}, H. YARAR^{a,b}, M. Zanetti^{a,b}, P. Zotto^{a,b}, A. Zucchetta^{a,b}, G. Zumerle^{a,b}

INFN Sezione di Pavia ^a, Università di Pavia ^b

C. Aime^{a,b}, A. Braghieri^a, S. Calzaferri^{a,b}, D. Fiorina^{a,b}, P. Montagna^{a,b}, S.P. Ratti^{a,b}, V. Re^a, C. Riccardi^{a,b}, P. Salvini^a, I. Vai^a, P. Vitulo^{a,b}

INFN Sezione di Perugia ^a, Università di Perugia ^b, Perugia, Italy

P. Asenov^{a,44}, G.M. Bilei^a, D. Ciangottini^{a,b}, L. Fanò^{a,b}, P. Lariccia^{a,b}, M. Magherini^b

G. Mantovani^{a,b}, V. Mariani^{a,b}, M. Menichelli^a, F. Moscatelli^{a,44}, A. Piccinelli^{a,b}, A. Rossi^{a,b}, A. Santocchia^{a,b}, D. Spiga^a, T. Tedeschi^{a,b}

INFN Sezione di Pisa ^a, Università di Pisa ^b, Scuola Normale Superiore di Pisa ^c, Pisa Italy, Università di Siena ^d, Siena, Italy

P. Azzurri^a, G. Bagliesi^a, V. Bertacchi^{a,c}, L. Bianchini^a, T. Boccali^a, E. Bossini^{a,b}, R. Castaldi^a, M.A. Ciocci^{a,b}, V. D'Amante^{a,d}, R. Dell'Orso^a, M.R. Di Domenico^{a,d}, S. Donato^a, A. Giassi^a, F. Ligabue^{a,c}, E. Manca^{a,c}, G. Mandorli^{a,c}, A. Messineo^{a,b}, F. Palla^a, S. Parolia^{a,b}, G. Ramirez-Sanchez^{a,c}, A. Rizzi^{a,b}, G. Rolandi^{a,c}, S. Roy Chowdhury^{a,c}, A. Scribano^a, N. Shafiei^{a,b}, P. Spagnolo^a, R. Tenchini^a, G. Tonelli^{a,b}, N. Turini^{a,d}, A. Venturi^a, P.G. Verdini^a

INFN Sezione di Roma ^a, Sapienza Università di Roma ^b, Rome, Italy

M. Campana^{a,b}, F. Cavallari^a, D. Del Re^{a,b}, E. Di Marco^a, M. Diemoz^a, E. Longo^{a,b}, P. Meridiani^a, G. Organtini^{a,b}, F. Pandolfi^a, R. Paramatti^{a,b}, C. Quaranta^{a,b}, S. Rahatlou^{a,b}, C. Rovelli^a, F. Santanastasio^{a,b}, L. Soffi^a, R. Tramontano^{a,b}

INFN Sezione di Torino ^a, Università di Torino ^b, Torino, Italy, Università del Piemonte Orientale ^c, Novara, Italy

N. Amapane^{a,b}, R. Arcidiacono^{a,c}, S. Argiro^{a,b}, M. Arneodo^{a,c}, N. Bartosik^a, R. Bellan^{a,b}, A. Bellora^{a,b}, J. Berenguer Antequera^{a,b}, C. Biino^a, N. Cartiglia^a, S. Cometti^a, M. Costa^{a,b}, R. Covarelli^{a,b}, N. Demaria^a, B. Kiani^{a,b}, F. Legger^a, C. Mariotti^a, S. Maselli^a, E. Migliore^{a,b}, E. Monteil^{a,b}, M. Monteno^a, M.M. Obertino^{a,b}, G. Ortona^a, L. Pacher^{a,b}, N. Pastrone^a, M. Pelliccioni^a, G.L. Pinna Angioni^{a,b}, M. Ruspa^{a,c}, K. Shchelina^{a,b}, F. Siviero^{a,b}, V. Sola^a, A. Solano^{a,b}, D. Soldi^{a,b}, A. Staiano^a, M. Tornago^{a,b}, D. Trocino^{a,b}, A. Vagnerini

INFN Sezione di Trieste ^a, Università di Trieste ^b, Trieste, Italy

S. Belforte^a, V. Candelise^{a,b}, M. Casarsa^a, F. Cossutti^a, A. Da Rold^{a,b}, G. Della Ricca^{a,b}, G. Sorrentino^{a,b}, F. Vazzoler^{a,b}

Kyungpook National University, Daegu, Korea

S. Dogra, C. Huh, B. Kim, D.H. Kim, G.N. Kim, J. Kim, J. Lee, S.W. Lee, C.S. Moon, Y.D. Oh, S.I. Pak, B.C. Radburn-Smith, S. Sekmen, Y.C. Yang

Chonnam National University, Institute for Universe and Elementary Particles, Kwangju, Korea

H. Kim, D.H. Moon

Hanyang University, Seoul, Korea

B. Francois, T.J. Kim, J. Park

Korea University, Seoul, Korea

S. Cho, S. Choi, Y. Go, B. Hong, K. Lee, K.S. Lee, J. Lim, J. Park, S.K. Park, J. Yoo

Kyung Hee University, Department of Physics, Seoul, Republic of Korea

J. Goh, A. Gurtu

Sejong University, Seoul, Korea

H.S. Kim, Y. Kim

Seoul National University, Seoul, Korea

J. Almond, J.H. Bhyun, J. Choi, S. Jeon, J. Kim, J.S. Kim, S. Ko, H. Kwon, H. Lee, S. Lee, B.H. Oh, M. Oh, S.B. Oh, H. Seo, U.K. Yang, I. Yoon

University of Seoul, Seoul, Korea

W. Jang, D.Y. Kang, Y. Kang, S. Kim, B. Ko, J.S.H. Lee, Y. Lee, I.C. Park, Y. Roh, M.S. Ryu, D. Song, I.J. Watson, S. Yang

Yonsei University, Department of Physics, Seoul, Korea

S. Ha, H.D. Yoo

Sungkyunkwan University, Suwon, Korea

M. Choi, Y. Jeong, H. Lee, Y. Lee, I. Yu

College of Engineering and Technology, American University of the Middle East (AUM), Egaila, Kuwait

T. Beyrouthy, Y. Maghrbi

Riga Technical University

T. Torims, V. Veckalns⁴⁵

Vilnius University, Vilnius, Lithuania

M. Ambrozias, A. Carvalho Antunes De Oliveira, A. Juodagalvis, A. Rinkevicius, G. Tamulaitis

National Centre for Particle Physics, Universiti Malaya, Kuala Lumpur, Malaysia

N. Bin Norjoharuddeen, W.A.T. Wan Abdullah, M.N. Yusli, Z. Zolkapli

Universidad de Sonora (UNISON), Hermosillo, Mexico

J.F. Benitez, A. Castaneda Hernandez, M. León Coello, J.A. Murillo Quijada, A. Sehwawat, L. Valencia Palomo

Centro de Investigacion y de Estudios Avanzados del IPN, Mexico City, Mexico

G. Ayala, H. Castilla-Valdez, E. De La Cruz-Burelo, I. Heredia-De La Cruz⁴⁶, R. Lopez-Fernandez, C.A. Mondragon Herrera, D.A. Perez Navarro, A. Sanchez-Hernandez

Universidad Iberoamericana, Mexico City, Mexico

S. Carrillo Moreno, C. Oropeza Barrera, F. Vazquez Valencia

Benemerita Universidad Autonoma de Puebla, Puebla, Mexico

I. Pedraza, H.A. Salazar Ibarguen, C. Uribe Estrada

University of Montenegro, Podgorica, Montenegro

J. Mijuskovic⁴⁷, N. Raicevic

University of Auckland, Auckland, New Zealand

D. Krofcheck

University of Canterbury, Christchurch, New Zealand

S. Bheesette, P.H. Butler

National Centre for Physics, Quaid-I-Azam University, Islamabad, Pakistan

A. Ahmad, M.I. Asghar, A. Awais, M.I.M. Awan, H.R. Hoorani, W.A. Khan, M.A. Shah, M. Shoaib, M. Waqas

AGH University of Science and Technology Faculty of Computer Science, Electronics and Telecommunications, Krakow, Poland

V. Avati, L. Grzanka, M. Malawski

National Centre for Nuclear Research, Swierk, Poland

H. Bialkowska, M. Bluj, B. Boimska, M. Górski, M. Kazana, M. Szleper, P. Zalewski

Institute of Experimental Physics, Faculty of Physics, University of Warsaw, Warsaw, Poland
K. Bunkowski, K. Doroba, A. Kalinowski, M. Konecki, J. Krolikowski, M. Walczak

Laboratório de Instrumentação e Física Experimental de Partículas, Lisboa, Portugal
M. Araujo, P. Bargassa, D. Bastos, A. Boletti, P. Faccioli, M. Gallinaro, J. Hollar, N. Leonardo, T. Niknejad, M. Pisano, J. Seixas, O. Toldaiev, J. Varela

Joint Institute for Nuclear Research, Dubna, Russia
S. Afanasiev, D. Budkouski, I. Golutvin, I. Gorbunov, V. Karjavine, V. Korenkov, A. Lanev, A. Malakhov, V. Matveev^{48,49}, V. Palichik, V. Perelygin, M. Savina, D. Seitova, V. Shalaev, S. Shmatov, S. Shulha, V. Smirnov, O. Teryaev, N. Voytishin, B.S. Yuldashev⁵⁰, A. Zarubin, I. Zhizhin

Petersburg Nuclear Physics Institute, Gatchina (St. Petersburg), Russia
G. Gavrillov, V. Golovtsov, Y. Ivanov, V. Kim⁵¹, E. Kuznetsova⁵², V. Murzin, V. Oreshkin, I. Smirnov, D. Sosnov, V. Sulimov, L. Uvarov, S. Volkov, A. Vorobyev

Institute for Nuclear Research, Moscow, Russia
Yu. Andreev, A. Dermenev, S. Gninenko, N. Golubev, A. Karneyeu, D. Kirpichnikov, M. Kirsanov, N. Krasnikov, A. Pashenkov, G. Pivovarov, D. Tlisov[†], A. Toropin

Institute for Theoretical and Experimental Physics named by A.I. Alikhanov of NRC 'Kurchatov Institute', Moscow, Russia
V. Epshteyn, V. Gavrillov, N. Lychkovskaya, A. Nikitenko⁵³, V. Popov, A. Spiridonov, A. Stepenov, M. Toms, E. Vlasov, A. Zhokin

Moscow Institute of Physics and Technology, Moscow, Russia
T. Aushev

National Research Nuclear University 'Moscow Engineering Physics Institute' (MEPhI), Moscow, Russia
R. Chistov⁵⁴, M. Danilov⁵⁴, A. Oskin, P. Parygin, S. Polikarpov⁵⁴

P.N. Lebedev Physical Institute, Moscow, Russia
V. Andreev, M. Azarkin, I. Dremin, M. Kirakosyan, A. Terkulov

Skobeltsyn Institute of Nuclear Physics, Lomonosov Moscow State University, Moscow, Russia
A. Belyaev, E. Boos, M. Dubinin⁵⁵, L. Dudko, A. Ershov, A. Gribushin, V. Klyukhin, O. Kodolova, I. Lokhtin, S. Obraztsov, S. Petrushanko, V. Savrin, A. Snigirev

Novosibirsk State University (NSU), Novosibirsk, Russia
V. Blinov⁵⁶, T. Dimova⁵⁶, L. Kardapoltsev⁵⁶, A. Kozyrev⁵⁶, I. Ovtin⁵⁶, Y. Skovpen⁵⁶

Institute for High Energy Physics of National Research Centre 'Kurchatov Institute', Protvino, Russia
I. Azhgirey, I. Bayshev, D. Elumakhov, V. Kachanov, D. Konstantinov, P. Mandrik, V. Petrov, R. Ryutin, S. Slabospitskii, A. Sobol, S. Troshin, N. Tyurin, A. Uzunian, A. Volkov

National Research Tomsk Polytechnic University, Tomsk, Russia
A. Babaev, V. Okhotnikov

Tomsk State University, Tomsk, Russia
V. Borshch, V. Ivanchenko, E. Tcherniaev

University of Belgrade: Faculty of Physics and VINCA Institute of Nuclear Sciences, Belgrade, Serbia

P. Adzic⁵⁷, M. Dordevic, P. Milenovic, J. Milosevic

Centro de Investigaciones Energéticas Medioambientales y Tecnológicas (CIEMAT), Madrid, Spain

M. Aguilar-Benitez, J. Alcaraz Maestre, A. Álvarez Fernández, I. Bachiller, M. Barrio Luna, Cristina F. Bedoya, C.A. Carrillo Montoya, M. Cepeda, M. Cerrada, N. Colino, B. De La Cruz, A. Delgado Peris, J.P. Fernández Ramos, J. Flix, M.C. Fouz, O. Gonzalez Lopez, S. Goy Lopez, J.M. Hernandez, M.I. Josa, J. León Holgado, D. Moran, Á. Navarro Tobar, C. Perez Dengra, A. Pérez-Calero Yzquierdo, J. Puerta Pelayo, I. Redondo, L. Romero, S. Sánchez Navas, L. Urda Gómez, C. Willmott

Universidad Autónoma de Madrid, Madrid, Spain

J.F. de Trocóniz, R. Reyes-Almanza

Universidad de Oviedo, Instituto Universitario de Ciencias y Tecnologías Espaciales de Asturias (ICTEA), Oviedo, Spain

B. Alvarez Gonzalez, J. Cuevas, C. Erice, J. Fernandez Menendez, S. Folgueras, I. Gonzalez Caballero, J.R. González Fernández, E. Palencia Cortezon, C. Ramón Álvarez, V. Rodríguez Bouza, A. Trapote, N. Trevisani

Instituto de Física de Cantabria (IFCA), CSIC-Universidad de Cantabria, Santander, Spain

J.A. Brochero Cifuentes, I.J. Cabrillo, A. Calderon, J. Duarte Campderros, M. Fernandez, C. Fernandez Madrazo, P.J. Fernández Manteca, A. García Alonso, G. Gomez, C. Martinez Rivero, P. Martinez Ruiz del Arbol, F. Matorras, P. Matorras Cuevas, J. Piedra Gomez, C. Prieels, T. Rodrigo, A. Ruiz-Jimeno, L. Scodellaro, I. Vila, J.M. Vizan Garcia

University of Colombo, Colombo, Sri Lanka

MK Jayananda, B. Kailasapathy⁵⁸, D.U.J. Sonnadara, DDC Wickramarathna

University of Ruhuna, Department of Physics, Matara, Sri Lanka

W.G.D. Dharmaratna, K. Liyanage, N. Perera, N. Wickramage

CERN, European Organization for Nuclear Research, Geneva, Switzerland

T.K. Aarrestad, D. Abbaneo, J. Alimena, E. Auffray, G. Auzinger, J. Baechler, P. Baillon[†], D. Barney, J. Bendavid, M. Bianco, A. Bocci, T. Camporesi, M. Capeans Garrido, G. Cerminara, S.S. Chhibra, M. Cipriani, L. Cristella, D. d'Enterria, A. Dabrowski, A. David, A. De Roeck, M.M. Defranchis, M. Deile, M. Dobson, M. Dünser, N. Dupont, A. Elliott-Peisert, N. Emriskova, F. Fallavollita⁵⁹, D. Fasanella, A. Florent, G. Franzoni, W. Funk, S. Giani, D. Gigi, K. Gill, F. Glege, L. Gouskos, M. Haranko, J. Hegeman, Y. Iiyama, V. Innocente, T. James, P. Janot, J. Kaspar, J. Kieseler, M. Komm, N. Kratochwil, C. Lange, S. Laurila, P. Lecoq, K. Long, C. Lourenço, L. Malgeri, S. Mallios, M. Mannelli, A.C. Marini, F. Meijers, S. Mersi, E. Meschi, F. Moortgat, M. Mulders, S. Orfanelli, L. Orsini, F. Pantaleo, L. Pape, E. Perez, M. Peruzzi, A. Petrilli, G. Petrucciani, A. Pfeiffer, M. Pierini, D. Piparo, M. Pitt, H. Qu, T. Quast, D. Rabady, A. Racz, G. Reales Gutiérrez, M. Rieger, M. Rovere, H. Sakulin, J. Salfeld-Nebgen, S. Scarfi, C. Schäfer, C. Schwick, M. Selvaggi, A. Sharma, P. Silva, W. Snoeys, P. Sphicas⁶⁰, S. Summers, K. Tatar, V.R. Tavolaro, D. Treille, A. Tsirou, G.P. Van Onsem, J. Wanczyk⁶¹, K.A. Wozniak, W.D. Zeuner

Paul Scherrer Institut, Villigen, Switzerland

L. Caminada⁶², A. Ebrahimi, W. Erdmann, R. Horisberger, Q. Ingram, H.C. Kaestli, D. Kotlinski, U. Langenegger, M. Missiroli, T. Rohe

ETH Zurich - Institute for Particle Physics and Astrophysics (IPA), Zurich, Switzerland

K. Androsov⁶¹, M. Backhaus, P. Berger, A. Calandri, N. Chernyavskaya, A. De Cosa, G. Dissertori, M. Dittmar, M. Donegà, C. Dorfer, F. Eble, K. Gedia, F. Glessgen, T.A. Gómez Espinosa, C. Grab, D. Hits, W. Lusterhmann, A.-M. Lyon, R.A. Manzoni, C. Martin Perez, M.T. Meinhard, F. Nessi-Tedaldi, J. Niedziela, F. Pauss, V. Perovic, S. Pigazzini, M.G. Ratti, M. Reichmann, C. Reissel, T. Reitenspiess, B. Ristic, D. Ruini, D.A. Sanz Becerra, M. Schönenberger, V. Stampf, J. Steggemann⁶¹, R. Wallny, D.H. Zhu

Universität Zürich, Zurich, Switzerland

C. Amsler⁶³, P. Bäertschi, C. Botta, D. Brzhechko, M.F. Canelli, K. Cormier, A. De Wit, R. Del Burgo, J.K. Heikkilä, M. Huwiler, W. Jin, A. Jofrehei, B. Kilminster, S. Leontsinis, S.P. Liechti, A. Macchiolo, P. Meiring, V.M. Mikuni, U. Molinatti, I. Neutelings, A. Reimers, P. Robmann, S. Sanchez Cruz, K. Schweiger, Y. Takahashi

National Central University, Chung-Li, Taiwan

C. Adloff⁶⁴, C.M. Kuo, W. Lin, A. Roy, T. Sarkar³⁵, S.S. Yu

National Taiwan University (NTU), Taipei, Taiwan

L. Ceard, Y. Chao, K.F. Chen, P.H. Chen, W.-S. Hou, Y.y. Li, R.-S. Lu, E. Paganis, A. Psallidas, A. Steen, H.y. Wu, E. Yazgan, P.r. Yu

Chulalongkorn University, Faculty of Science, Department of Physics, Bangkok, Thailand

B. Asavapibhop, C. Asawatangtrakuldee, N. Srimanobhas

Çukurova University, Physics Department, Science and Art Faculty, Adana, Turkey

F. Boran, S. Damarseckin⁶⁵, Z.S. Demiroglu, F. Dolek, I. Dumanoglu⁶⁶, E. Eskut, Y. Guler, E. Gurpinar Guler⁶⁷, I. Hos⁶⁸, C. Isik, O. Kara, A. Kayis Topaksu, U. Kiminsu, G. Onengut, K. Ozdemir⁶⁹, A. Polatoz, A.E. Simsek, B. Tali⁷⁰, U.G. Tok, S. Turkcapar, I.S. Zorbakir, C. Zorbilmez

Middle East Technical University, Physics Department, Ankara, Turkey

B. Isildak⁷¹, G. Karapinar⁷², K. Ocalan⁷³, M. Yalvac⁷⁴

Bogazici University, Istanbul, Turkey

B. Akgun, I.O. Atakisi, E. Gülmez, M. Kaya⁷⁵, O. Kaya⁷⁶, Ö. Özçelik, S. Tekten⁷⁷, E.A. Yetkin⁷⁸

Istanbul Technical University, Istanbul, Turkey

A. Cakir, K. Cankocak⁶⁶, Y. Komurcu, S. Sen⁷⁹

Istanbul University, Istanbul, Turkey

S. Cerci⁷⁰, B. Kaynak, S. Ozkorucuklu, D. Sunar Cerci⁷⁰

Institute for Scintillation Materials of National Academy of Science of Ukraine, Kharkov, Ukraine

B. Grynyov

National Scientific Center, Kharkov Institute of Physics and Technology, Kharkov, Ukraine

L. Levchuk

University of Bristol, Bristol, United Kingdom

D. Anthony, E. Bhal, S. Bologna, J.J. Brooke, A. Bundock, E. Clement, D. Cussans, H. Flacher, J. Goldstein, G.P. Heath, H.F. Heath, M.I. Holmberg⁸⁰, L. Kreczko, B. Krikler, S. Paramesvaran, S. Seif El Nasr-Storey, V.J. Smith, N. Stylianou⁸¹, K. Walkingshaw Pass, R. White

Rutherford Appleton Laboratory, Didcot, United Kingdom

K.W. Bell, A. Belyaev⁸², C. Brew, R.M. Brown, D.J.A. Cockerill, C. Cooke, K.V. Ellis, K. Harder,

S. Harper, J. Linacre, K. Manolopoulos, D.M. Newbold, E. Olaiya, D. Petyt, T. Reis, T. Schuh, C.H. Shepherd-Themistocleous, I.R. Tomalin, T. Williams

Imperial College, London, United Kingdom

R. Bainbridge, P. Bloch, S. Bonomally, J. Borg, S. Breeze, O. Buchmuller, V. Cepaitis, G.S. Chahal⁸³, D. Colling, P. Dauncey, G. Davies, M. Della Negra, S. Fayer, G. Fedi, G. Hall, M.H. Hassanshahi, G. Iles, J. Langford, L. Lyons, A.-M. Magnan, S. Malik, A. Martelli, D.G. Monk, J. Nash⁸⁴, M. Pesaresi, D.M. Raymond, A. Richards, A. Rose, E. Scott, C. Seez, A. Shtipliyski, A. Tapper, K. Uchida, T. Virdee¹⁹, M. Vojinovic, N. Wardle, S.N. Webb, D. Winterbottom

Brunel University, Uxbridge, United Kingdom

K. Coldham, J.E. Cole, A. Khan, P. Kyberd, I.D. Reid, L. Teodorescu, S. Zahid

Baylor University, Waco, USA

S. Abdullin, A. Brinkerhoff, B. Caraway, J. Dittmann, K. Hatakeyama, A.R. Kanuganti, B. McMaster, N. Pastika, M. Saunders, S. Sawant, C. Sutantawibul, J. Wilson

Catholic University of America, Washington, DC, USA

R. Bartek, A. Dominguez, R. Uniyal, A.M. Vargas Hernandez

The University of Alabama, Tuscaloosa, USA

A. Buccilli, S.I. Cooper, D. Di Croce, S.V. Gleyzer, C. Henderson, C.U. Perez, P. Rumerio⁸⁵, C. West

Boston University, Boston, USA

A. Akpınar, A. Albert, D. Arcaro, C. Cosby, Z. Demiragli, E. Fontanesi, D. Gastler, J. Rohlf, K. Salyer, D. Sperka, D. Spitzbart, I. Suarez, A. Tsatsos, S. Yuan, D. Zou

Brown University, Providence, USA

G. Benelli, B. Burkley, X. Coubez²⁰, D. Cutts, M. Hadley, U. Heintz, J.M. Hogan⁸⁶, G. Landsberg, K.T. Lau, M. Lukasik, J. Luo, M. Narain, S. Sagir⁸⁷, E. Usai, W.Y. Wong, X. Yan, D. Yu, W. Zhang

University of California, Davis, Davis, USA

J. Bonilla, C. Brainerd, R. Breedon, M. Calderon De La Barca Sanchez, M. Chertok, J. Conway, P.T. Cox, R. Erbacher, G. Haza, F. Jensen, O. Kukral, R. Lander, M. Mulhearn, D. Pellett, B. Regnery, D. Taylor, Y. Yao, F. Zhang

University of California, Los Angeles, USA

M. Bachtis, R. Cousins, A. Datta, D. Hamilton, J. Hauser, M. Ignatenko, M.A. Iqbal, T. Lam, W.A. Nash, S. Regnard, D. Saltzberg, B. Stone, V. Valuev

University of California, Riverside, Riverside, USA

K. Burt, Y. Chen, R. Clare, J.W. Gary, M. Gordon, G. Hanson, G. Karapostoli, O.R. Long, N. Mangano, M. Olmedo Negrete, W. Si, S. Wimpenny, Y. Zhang

University of California, San Diego, La Jolla, USA

J.G. Branson, P. Chang, S. Cittolin, S. Cooperstein, N. Deelen, D. Diaz, J. Duarte, R. Gerosa, L. Giannini, D. Gilbert, J. Guiang, R. Kansal, V. Krutelyov, R. Lee, J. Letts, M. Masciovecchio, S. May, M. Pieri, B.V. Sathia Narayanan, V. Sharma, M. Tadel, A. Vartak, F. Würthwein, Y. Xiang, A. Yagil

University of California, Santa Barbara - Department of Physics, Santa Barbara, USA

N. Amin, C. Campagnari, M. Citron, A. Dorsett, V. Dutta, J. Incandela, M. Kilpatrick, J. Kim,

B. Marsh, H. Mei, M. Oshiro, M. Quinnan, J. Richman, U. Sarica, F. Setti, J. Sheplock, D. Stuart, S. Wang

California Institute of Technology, Pasadena, USA

A. Bornheim, O. Cerri, I. Dutta, J.M. Lawhorn, N. Lu, J. Mao, H.B. Newman, T.Q. Nguyen, M. Spiropulu, J.R. Vlimant, C. Wang, S. Xie, Z. Zhang, R.Y. Zhu

Carnegie Mellon University, Pittsburgh, USA

J. Alison, S. An, M.B. Andrews, P. Bryant, T. Ferguson, A. Harilal, C. Liu, T. Mudholkar, M. Paulini, A. Sanchez, W. Terrill

University of Colorado Boulder, Boulder, USA

J.P. Cumalat, W.T. Ford, A. Hassani, E. MacDonald, R. Patel, A. Perloff, C. Savard, K. Stenson, K.A. Ulmer, S.R. Wagner

Cornell University, Ithaca, USA

J. Alexander, S. Bright-thonney, Y. Cheng, D.J. Cranshaw, S. Hogan, J. Monroy, J.R. Patterson, D. Quach, J. Reichert, M. Reid, A. Ryd, W. Sun, J. Thom, P. Wittich, R. Zou

Fermi National Accelerator Laboratory, Batavia, USA

M. Albrow, M. Alyari, G. Apollinari, A. Apresyan, A. Apyan, S. Banerjee, L.A.T. Bauerdick, D. Berry, J. Berryhill, P.C. Bhat, K. Burkett, J.N. Butler, A. Canepa, G.B. Cerati, H.W.K. Cheung, F. Chlebana, M. Cremonesi, K.F. Di Petrillo, V.D. Elvira, Y. Feng, J. Freeman, Z. Gecse, L. Gray, D. Green, S. Grünendahl, O. Gutsche, R.M. Harris, R. Heller, T.C. Herwig, J. Hirschauer, B. Jayatilaka, S. Jindariani, M. Johnson, U. Joshi, T. Klijnsma, B. Klima, K.H.M. Kwok, S. Lammel, D. Lincoln, R. Lipton, T. Liu, C. Madrid, K. Maeshima, C. Mantilla, D. Mason, P. McBride, P. Merkel, S. Mrenna, S. Nahn, J. Ngadiuba, V. O'Dell, V. Papadimitriou, K. Pedro, C. Pena⁵⁵, O. Prokofyev, F. Ravera, A. Reinsvold Hall, L. Ristori, B. Schneider, E. Sexton-Kennedy, N. Smith, A. Soha, W.J. Spalding, L. Spiegel, S. Stoynev, J. Strait, L. Taylor, S. Tkaczyk, N.V. Tran, L. Uplegger, E.W. Vaandering, H.A. Weber

University of Florida, Gainesville, USA

D. Acosta, P. Avery, D. Bourilkov, L. Cadamuro, V. Cherepanov, F. Errico, R.D. Field, D. Guerrero, B.M. Joshi, M. Kim, E. Koenig, J. Konigsberg, A. Korytov, K.H. Lo, K. Matchev, N. Menendez, G. Mitselmakher, A. Muthirakalayil Madhu, N. Rawal, D. Rosenzweig, S. Rosenzweig, K. Shi, J. Sturdy, J. Wang, E. Yigitbasi, X. Zuo

Florida State University, Tallahassee, USA

T. Adams, A. Askew, R. Habibullah, V. Hagopian, K.F. Johnson, R. Khurana, T. Kolberg, G. Martinez, H. Prosper, C. Schiber, O. Viazlo, R. Yohay, J. Zhang

Florida Institute of Technology, Melbourne, USA

M.M. Baarmand, S. Butalla, T. Elkafrawy⁸⁸, M. Hohlmann, R. Kumar Verma, D. Noonan, M. Rahmani, F. Yumiceva

University of Illinois at Chicago (UIC), Chicago, USA

M.R. Adams, H. Becerril Gonzalez, R. Cavanaugh, X. Chen, S. Dittmer, O. Evdokimov, C.E. Gerber, D.A. Hangal, D.J. Hofman, A.H. Merrit, C. Mills, G. Oh, T. Roy, S. Rudrabhatla, M.B. Tonjes, N. Varelas, J. Viinikainen, X. Wang, Z. Wu, Z. Ye

The University of Iowa, Iowa City, USA

M. Alhousseini, K. Dilsiz⁸⁹, R.P. Gandrajula, O.K. Köseyan, J.-P. Merlo, A. Mestvirishvili⁹⁰, J. Nachtman, H. Ogul⁹¹, Y. Onel, A. Penzo, C. Snyder, E. Tiras⁹²

Johns Hopkins University, Baltimore, USA

O. Amram, B. Blumenfeld, L. Corcodilos, J. Davis, M. Eminizer, A.V. Gritsan, S. Kyriacou, P. Maksimovic, J. Roskes, M. Swartz, T.Á. Vámi

The University of Kansas, Lawrence, USA

A. Abreu, J. Anguiano, C. Baldenegro Barrera, P. Baringer, A. Bean, A. Bylinkin, Z. Flowers, T. Isidori, S. Khalil, J. King, G. Krintiras, A. Kropivnitskaya, M. Lazarovits, C. Lindsey, J. Marquez, N. Minafra, M. Murray, M. Nickel, C. Rogan, C. Royon, R. Salvatico, S. Sanders, E. Schmitz, C. Smith, J.D. Tapia Takaki, Q. Wang, Z. Warner, J. Williams, G. Wilson

Kansas State University, Manhattan, USA

S. Duric, A. Ivanov, K. Kaadze, D. Kim, Y. Maravin, T. Mitchell, A. Modak, K. Nam

Lawrence Livermore National Laboratory, Livermore, USA

F. Rebassoo, D. Wright

University of Maryland, College Park, USA

E. Adams, A. Baden, O. Baron, A. Belloni, S.C. Eno, N.J. Hadley, S. Jabeen, R.G. Kellogg, T. Koeth, A.C. Mignerey, S. Nabili, C. Palmer, M. Seidel, A. Skuja, L. Wang, K. Wong

Massachusetts Institute of Technology, Cambridge, USA

D. Abercrombie, G. Andreassi, R. Bi, S. Brandt, W. Busza, I.A. Cali, Y. Chen, M. D'Alfonso, J. Eysermans, C. Freer, G. Gomez Ceballos, M. Goncharov, P. Harris, M. Hu, M. Klute, D. Kovalskyi, J. Krupa, Y.-J. Lee, B. Maier, C. Mironov, C. Paus, D. Rankin, C. Roland, G. Roland, Z. Shi, G.S.F. Stephans, J. Wang, Z. Wang, B. Wyslouch

University of Minnesota, Minneapolis, USA

R.M. Chatterjee, A. Evans, P. Hansen, J. Hiltbrand, Sh. Jain, M. Krohn, Y. Kubota, J. Mans, M. Revering, R. Rusack, R. Saradhy, N. Schroeder, N. Strobbe, M.A. Wadud

University of Nebraska-Lincoln, Lincoln, USA

K. Bloom, M. Bryson, S. Chauhan, D.R. Claes, C. Fangmeier, L. Finco, F. Golf, C. Joo, I. Kravchenko, M. Musich, I. Reed, J.E. Siado, G.R. Snow[†], W. Tabb, F. Yan, A.G. Zecchinelli

State University of New York at Buffalo, Buffalo, USA

G. Agarwal, H. Bandyopadhyay, L. Hay, I. Iashvili, A. Kharchilava, C. McLean, D. Nguyen, J. Pekkanen, S. Rappoccio, A. Williams

Northeastern University, Boston, USA

G. Alverson, E. Barberis, Y. Haddad, A. Hortiangtham, J. Li, G. Madigan, B. Marzocchi, D.M. Morse, V. Nguyen, T. Orimoto, A. Parker, L. Skinnari, A. Tishelman-Charny, T. Wamorkar, B. Wang, A. Wisecarver, D. Wood

Northwestern University, Evanston, USA

S. Bhattacharya, J. Bueghly, Z. Chen, A. Gilbert, T. Gunter, K.A. Hahn, Y. Liu, N. Odell, M.H. Schmitt, M. Velasco

University of Notre Dame, Notre Dame, USA

R. Band, R. Bucci, A. Das, N. Dev, R. Goldouzian, M. Hildreth, K. Hurtado Anampa, C. Jessop, K. Lannon, J. Lawrence, N. Loukas, D. Lutton, N. Marinelli, I. Mcalister, T. McCauley, C. Mcgrady, F. Meng, K. Mohrman, Y. Musienko⁴⁸, R. Ruchti, P. Siddireddy, A. Townsend, M. Wayne, A. Wightman, M. Wolf, M. Zarucki, L. Zygala

The Ohio State University, Columbus, USA

B. Bylsma, B. Cardwell, L.S. Durkin, B. Francis, C. Hill, M. Nunez Ornelas, K. Wei, B.L. Winer, B.R. Yates

Princeton University, Princeton, USA

F.M. Addesa, B. Bonham, P. Das, G. Dezoort, P. Elmer, A. Frankenthal, B. Greenberg, N. Haubrich, S. Higginbotham, A. Kalogeropoulos, G. Kopp, S. Kwan, D. Lange, M.T. Lucchini, D. Marlow, K. Mei, I. Ojalvo, J. Olsen, D. Stickland, C. Tully

University of Puerto Rico, Mayaguez, USA

S. Malik, S. Norberg

Purdue University, West Lafayette, USA

A.S. Bakshi, V.E. Barnes, R. Chawla, S. Das, L. Gutay, M. Jones, A.W. Jung, S. Karmarkar, M. Liu, G. Negro, N. Neumeister, G. Paspalaki, C.C. Peng, S. Piperov, A. Purohit, J.F. Schulte, M. Stojanovic¹⁵, J. Thieman, F. Wang, R. Xiao, W. Xie

Purdue University Northwest, Hammond, USA

J. Dolen, N. Parashar

Rice University, Houston, USA

A. Baty, M. Decaro, S. Dildick, K.M. Ecklund, S. Freed, P. Gardner, F.J.M. Geurts, A. Kumar, W. Li, B.P. Padley, R. Redjimi, W. Shi, A.G. Stahl Leiton, S. Yang, L. Zhang, Y. Zhang

University of Rochester, Rochester, USA

A. Bodek, P. de Barbaro, R. Demina, J.L. Dulemba, C. Fallon, T. Ferbel, M. Galanti, A. Garcia-Bellido, O. Hindrichs, A. Khukhunaishvili, E. Ranken, R. Taus

Rutgers, The State University of New Jersey, Piscataway, USA

B. Chiarito, J.P. Chou, A. Gandrakota, Y. Gershtein, E. Halkiadakis, A. Hart, M. Heindl, O. Karacheban²³, I. Laflotte, A. Lath, R. Montalvo, K. Nash, M. Osherson, S. Salur, S. Schnetzer, S. Somalwar, R. Stone, S.A. Thayil, S. Thomas, H. Wang

University of Tennessee, Knoxville, USA

H. Acharya, A.G. Delannoy, S. Fiorendi, S. Spanier

Texas A&M University, College Station, USA

O. Bouhali⁹³, M. Dalchenko, A. Delgado, R. Eusebi, J. Gilmore, T. Huang, T. Kamon⁹⁴, H. Kim, S. Luo, S. Malhotra, R. Mueller, D. Overton, D. Rathjens, A. Safonov

Texas Tech University, Lubbock, USA

N. Akchurin, J. Damgov, V. Hegde, S. Kunori, K. Lamichhane, S.W. Lee, T. Mengke, S. Muthumuni, T. Peltola, I. Volobouev, Z. Wang, A. Whitbeck

Vanderbilt University, Nashville, USA

E. Appelt, S. Greene, A. Gurrola, W. Johns, A. Melo, H. Ni, K. Padeken, F. Romeo, P. Sheldon, S. Tuo, J. Velkovska

University of Virginia, Charlottesville, USA

M.W. Arenton, B. Cox, G. Cummings, J. Hakala, R. Hirosky, M. Joyce, A. Ledovskoy, A. Li, C. Neu, B. Tannenwald, S. White, E. Wolfe

Wayne State University, Detroit, USA

N. Poudyal

University of Wisconsin - Madison, Madison, WI, USA

K. Black, T. Bose, C. Caillol, S. Dasu, I. De Bruyn, P. Everaerts, F. Fienga, C. Galloni, H. He, M. Herndon, A. Hervé, U. Hussain, A. Lanaro, A. Loeliger, R. Loveless, J. Madhusudanan Sreekala, A. Mallampalli, A. Mohammadi, D. Pinna, A. Savin, V. Shang, V. Sharma, W.H. Smith, D. Teague, S. Trembath-reichert, W. Vetens

†: Deceased

1: Also at TU Wien, Wien, Austria

2: Also at Institute of Basic and Applied Sciences, Faculty of Engineering, Arab Academy for Science, Technology and Maritime Transport, Alexandria, Egypt

3: Also at Université Libre de Bruxelles, Bruxelles, Belgium

4: Also at Universidade Estadual de Campinas, Campinas, Brazil

5: Also at Federal University of Rio Grande do Sul, Porto Alegre, Brazil

6: Also at University of Chinese Academy of Sciences, Beijing, China

7: Also at Department of Physics, Tsinghua University, Beijing, China

8: Also at UFMS, Nova Andradina, Brazil

9: Also at Nanjing Normal University Department of Physics, Nanjing, China

10: Now at The University of Iowa, Iowa City, USA

11: Also at Institute for Theoretical and Experimental Physics named by A.I. Alikhanov of NRC 'Kurchatov Institute', Moscow, Russia

12: Also at Joint Institute for Nuclear Research, Dubna, Russia

13: Also at Cairo University, Cairo, Egypt

14: Now at British University in Egypt, Cairo, Egypt

15: Also at Purdue University, West Lafayette, USA

16: Also at Université de Haute Alsace, Mulhouse, France

17: Also at Tbilisi State University, Tbilisi, Georgia

18: Also at Erzincan Binali Yildirim University, Erzincan, Turkey

19: Also at CERN, European Organization for Nuclear Research, Geneva, Switzerland

20: Also at RWTH Aachen University, III. Physikalisches Institut A, Aachen, Germany

21: Also at University of Hamburg, Hamburg, Germany

22: Also at Department of Physics, Isfahan University of Technology, Isfahan, Iran

23: Also at Brandenburg University of Technology, Cottbus, Germany

24: Also at Physics Department, Faculty of Science, Assiut University, Assiut, Egypt

25: Also at Karoly Robert Campus, MATE Institute of Technology, Gyongyos, Hungary

26: Also at Institute of Physics, University of Debrecen, Debrecen, Hungary

27: Also at Institute of Nuclear Research ATOMKI, Debrecen, Hungary

28: Also at MTA-ELTE Lendület CMS Particle and Nuclear Physics Group, Eötvös Loránd University, Budapest, Hungary

29: Also at Wigner Research Centre for Physics, Budapest, Hungary

30: Also at IIT Bhubaneswar, Bhubaneswar, India

31: Also at Institute of Physics, Bhubaneswar, India

32: Also at G.H.G. Khalsa College, Punjab, India

33: Also at Shoolini University, Solan, India

34: Also at University of Hyderabad, Hyderabad, India

35: Also at University of Visva-Bharati, Santiniketan, India

36: Also at Indian Institute of Technology (IIT), Mumbai, India

37: Also at Deutsches Elektronen-Synchrotron, Hamburg, Germany

38: Also at Sharif University of Technology, Tehran, Iran

39: Also at Department of Physics, University of Science and Technology of Mazandaran, Behshahr, Iran

-
- 40: Now at INFN Sezione di Bari ^a, Università di Bari ^b, Politecnico di Bari ^c, Bari, Italy
- 41: Also at Italian National Agency for New Technologies, Energy and Sustainable Economic Development, Bologna, Italy
- 42: Also at Centro Siciliano di Fisica Nucleare e di Struttura Della Materia, Catania, Italy
- 43: Also at Università di Napoli 'Federico II', Napoli, Italy
- 44: Also at Consiglio Nazionale delle Ricerche - Istituto Officina dei Materiali, PERUGIA, Italy
- 45: Also at Riga Technical University, Riga, Latvia
- 46: Also at Consejo Nacional de Ciencia y Tecnología, Mexico City, Mexico
- 47: Also at IRFU, CEA, Université Paris-Saclay, Gif-sur-Yvette, France
- 48: Also at Institute for Nuclear Research, Moscow, Russia
- 49: Now at National Research Nuclear University 'Moscow Engineering Physics Institute' (MEPhI), Moscow, Russia
- 50: Also at Institute of Nuclear Physics of the Uzbekistan Academy of Sciences, Tashkent, Uzbekistan
- 51: Also at St. Petersburg State Polytechnical University, St. Petersburg, Russia
- 52: Also at University of Florida, Gainesville, USA
- 53: Also at Imperial College, London, United Kingdom
- 54: Also at P.N. Lebedev Physical Institute, Moscow, Russia
- 55: Also at California Institute of Technology, Pasadena, USA
- 56: Also at Budker Institute of Nuclear Physics, Novosibirsk, Russia
- 57: Also at Faculty of Physics, University of Belgrade, Belgrade, Serbia
- 58: Also at Trincomalee Campus, Eastern University, Sri Lanka, Nilaveli, Sri Lanka
- 59: Also at INFN Sezione di Pavia ^a, Università di Pavia ^b, Pavia, Italy
- 60: Also at National and Kapodistrian University of Athens, Athens, Greece
- 61: Also at Ecole Polytechnique Fédérale Lausanne, Lausanne, Switzerland
- 62: Also at Universität Zürich, Zurich, Switzerland
- 63: Also at Stefan Meyer Institute for Subatomic Physics, Vienna, Austria
- 64: Also at Laboratoire d'Annecy-le-Vieux de Physique des Particules, IN2P3-CNRS, Annecy-le-Vieux, France
- 65: Also at Şırnak University, Sirnak, Turkey
- 66: Also at Near East University, Research Center of Experimental Health Science, Nicosia, Turkey
- 67: Also at Konya Technical University, Konya, Turkey
- 68: Also at Istanbul University - Cerrahpasa, Faculty of Engineering, Istanbul, Turkey
- 69: Also at Piri Reis University, Istanbul, Turkey
- 70: Also at Adiyaman University, Adiyaman, Turkey
- 71: Also at Ozyegin University, Istanbul, Turkey
- 72: Also at Izmir Institute of Technology, Izmir, Turkey
- 73: Also at Necmettin Erbakan University, Konya, Turkey
- 74: Also at Bozok Universititesi Rektörlüğü, Yozgat, Turkey
- 75: Also at Marmara University, Istanbul, Turkey
- 76: Also at Milli Savunma University, Istanbul, Turkey
- 77: Also at Kafkas University, Kars, Turkey
- 78: Also at Istanbul Bilgi University, Istanbul, Turkey
- 79: Also at Hacettepe University, Ankara, Turkey
- 80: Also at Rutherford Appleton Laboratory, Didcot, United Kingdom
- 81: Also at Vrije Universiteit Brussel, Brussel, Belgium
- 82: Also at School of Physics and Astronomy, University of Southampton, Southampton, United Kingdom

- 83: Also at IPPP Durham University, Durham, United Kingdom
- 84: Also at Monash University, Faculty of Science, Clayton, Australia
- 85: Also at Università di Torino, TORINO, Italy
- 86: Also at Bethel University, St. Paul, Minneapolis, USA, St. Paul, USA
- 87: Also at Karamanoğlu Mehmetbey University, Karaman, Turkey
- 88: Also at Ain Shams University, Cairo, Egypt
- 89: Also at Bingol University, Bingol, Turkey
- 90: Also at Georgian Technical University, Tbilisi, Georgia
- 91: Also at Sinop University, Sinop, Turkey
- 92: Also at Erciyes University, KAYSERI, Turkey
- 93: Also at Texas A&M University at Qatar, Doha, Qatar
- 94: Also at Kyungpook National University, Daegu, Korea, Daegu, Korea